Density Functional Studies of Nanomaterials with Applications in Electronic Devices and Hydrogen Storage

Henry Morgan Stewart

A dissertation submitted in partial fulfilment
of the requirements for the degree of
Doctor of Philosophy
of
University College London

Abstract

We present density functional calculations investigating two different nanomaterials: a titanium carbide nanocluster and few-layered black phosphorus. The titanium carbide nanocluster, Ti_8C_{12}, has properties that are well suited to applications in hydrogen storage, while few-layered black phosphorus has recently been used in the fabrication of novel field effect transistors. Chapter 1 provides some background information regarding hydrogen storage and electronic devices, with Chapter 2 introducing the computational methods used throughout subsequent chapters.

In Chapter 3, we investigate the thermodynamic and kinetic profile of H_2 dissociation by Ti_8C_{12} under a range of conditions. Our results show that that Ti_8C_{12} is able to reversibly dissociate H_2 with an unusually low activation barrier. In Chapter 4, we introduce few-layered black phosphorus, dubbed phosphorene. The use of black-phosphorus exfoliates in FETs is potentially important given the fast approaching limits of transistor miniaturization using current technologies. Phosphorene appears to have properties necessary for use in next generation FETs, and has therefore attracted enormous experimental and theoretical attention. Our work on phosphorene contributes to an ever growing body of information, with Chapter 5 investigating the effects of deforming monolayer and bilayer phosphorene and Chapter 6 investigating the properties of phosphorene nanoribbons.

In Chapter 5, we show that compressing bilayer phosphorene normal to its surface dramatically increases *n*-type mobility and modulates the band gap. The compressions required to increase *n*-type mobility by a factor of 10^2 are modest, meaning that our results are experimentally relevant. We also investigate the effects of bending of phosphorene, which has a highly anisotropic bending modulus.

Our work on phosphorene nanoribbons in Chapter 6 shows that in-plane quantum confinement effects lead to a significant increase in the band gap. We replicate this effect by applying periodic boundary conditions to the bulk and derive a formula relating the band gap of phosphorene nanoribbons to phosphorene's band edge effective masses. We also show that the band gap and mobility of phosphorene nanoribbons can be modified through the application of linear strain.

Chapter 7 concludes the main body of this thesis, summarising its outcomes and giving a direction for future work. We also include an brief investigation into a family of semiconducting quaternary oxynitride compounds in the Appendix. These compounds are of interest given that their band gaps fall within the visible light region.

Acknowledgements

First and foremost, I would like to thank my supervisors, Richard and Xiao. I could not have asked for better guidance, and will always be grateful to have been given the opportunity to work as part of their research groups. Special thanks is reserved for Stephen, whose daily advice, guidance and friendship was pivotal to the completion of this thesis. While I have kept my acknowledgements brief so as not to dilute the importance of those mentioned, thank you to all of my other colleagues for their support. Finally, I would like to thank EPSRC for making such an amazing experience possible.

Table of Contents

Page

List of Figures

List of Tables

List of Publications

1. Strain and Orientation Modulated Bandgaps and Effective Masses of Phosphorene Nanoribbons. Xiaoyu Han, Henry Morgan Stewart, Stephen A. Shevlin, C. Richard A. Catlow, and Zheng Xiao Guo. *Nano Letters* **2014** *14* (8), 4607-4614

2. Compressive Straining of Bilayer Phosphorene Leads to Extraordinary Electron Mobility at a New Conduction Band Edge. Henry Morgan Stewart, Stephen A. Shevlin, C. Richard A. Catlow, and Zheng Xiao Guo. *Nano Letters* **2015** *15* (3), 2006-2010

3. Reversible hydrogen dissociation with fast kinetics by titanium metallocarbohedrenes (in preparation)

Glossary of Symbols

Å	Ångström
$u_{n,k}$	Blöch Function
k_B	Boltzmann constant
cm	Centimetres
Z	Charge
E_{CB}	Conduction band energy
E_1	Deformation potential constant
m_d	Density of state mass
∇_k	Differential with respect to k
V_{DS}	Drain – Source voltage
$\mathrm{I_D}$	Drain current
m_e	Effective electron mass
m_h	Effective hole mass
m^*	Effective mass
ρ	Electron density
μ	Electron mobility
eV	Electron volts
ψ	Electronic wavefunction
Φ_S	Electrostatic potential
e	Elementary charge
q	Elementary charge
E	Energy

ε_i	Energy of microstate i
S	Entropy
v_{ext}	External electronic potential
E_F	Fermi energy
V_G	Gate voltage
G	Gibb's Free energy
$\mathbf{v}_\mathrm{g}$	Group velocity
$\hat{H}$	Hamiltonian
K	Kelvin
ρ_{KS}	Kohn-Sham density
V_{KS}	Kohn-Sham potential
L	Length
C_β	Longitudinal elastic constant
m	Mass
m	Metre
v	Microcanonical ensemble
I	Moment of intertia
n_e	Number of conduction band charge carriers
n_h	Number of valence band charge carriers
q	Partition function
h	Planck constant
$\hbar$	Planck constant / 2π
$\tilde{\psi}$	Pseudo-wavefunction
k	Rate constant
Γ	Reciprocal space gamma point

k	Reciprocal space vector
$P_{i,k}$	Scattering rate
τ	Scattering time
s	Seconds
Φ	Single electron wavefunction
ATM	Standard pressure
A	Surface area
T	Temperature
m_0	Unitary electron mass
E_{VB}	Valence band energy
Θ	Vibrational temperature
V	Volts
ψ	Wavefunction

Chapter 1

Background

This chapter introduces the broad areas of research relevant to the investigations described in this thesis. Section 1.2 reviews progress towards the development of hydrogen storage materials for vehicular use, relating our study of the dissociation of H_2 by titanium metallocarbohedrene in Chapter 3. Meanwhile, Section 1.4 describes the operation of field effect transistors and other electronic devices, relating to the work on few-layered black phosphorus in Chapters 4, 5 and 6. Finally, Section 1.5 introduces a number of computational approaches that can used to investigate a system's properties.

1.1 Hydrogen storage

At present, our ever increasing demand for energy is primarily satisfied by burning fossil fuels. However, not only are fossil fuels a finite resource, but their combustion produces harmful greenhouse gases. Therefore, the development of a cleaner, more sustainable energy supply is one of the greatest challenges of the 21st Century. While an increasing proportion of electricity is generated by renewable energy sources [1], the use of renewable energy in automobiles is highly limited. While the use battery power has been moderately successful, current technology is limiting in terms of range, charging time and affordability [2]. Another approach is to develop more efficient fuel cell vehicles (FCVs), which use H_2 as a fuel source. However, even though burning H_2 is environmentally harmless, the majority of H_2 is currently produced using energy derived from polluting fossil fuels [3]. In order for the transition from fossil fuel powered automobiles to FCVs to be of net environmental benefit, non-polluting methods of producing large quantities of H_2 must be developed. Given that the vast majority of hydrogen exists in the form of H_2O, efficient methods of producing H_2 from H_2O are key [4]. Alongside issues surrounding the production of H_2, there are a number of other challenges to be overcome before the widespread use of FCVs is feasible. Affordable and reliable hydrogen fuel cells must also be developed alongside the mass scale infrastructure necessary to distribute H_2. Vehicles must also be able to store hydrogen safely on-board at a high volumetric and gravimetric density.

The U.S Department of Energy (DoE) has outlined target metrics that future hydrogen storage materials (HSMs) for use in automotive applications should fulfil. In terms of capacity, HSMs should be able to store hydrogen at a gravimetric density of 7.5 wt% and at a volumetric density of 70 g/L [4]. Furthermore, the kinetics of charging and discharging are also extremely important, with DoE targets stating that depleted hydrogen storage materials should be able to adsorb hydrogen at temperatures of between -40 and 85°C [4]. Therefore, hydrogen storage materials which have a high kinetic barrier to recharging or discharging are not viable for the majority of applications. Targets related to the material's affordability, availability and stability are also vital. To date, none of the hydrogen storage materials investigated has been able to meet DoE targets in their entirety [5-7].

1.1.1 Mechanical storage

In order to increase the volumetric density of molecular hydrogen, H_2 can be compressed or cryogenically cooled. Traditionally, compressed hydrogen has been stored in heavy metal tanks, leading to issues surrounding weight, cost and safety [8]. Even the most advanced storage vessels, which are made from lightweight carbon fibre reinforced plastic (CFRP), fall short of DoE cost and capacity targets [9]. Furthermore, although the volumetric energy density of cryogenic H_2 is almost double that of gaseous H_2 at 690 ATM [8], liquid H_2 must be cooled to 20 K, using 35% of the fuel's energy [10]. Liquid H_2 also evaporates quickly during delivery and pressurizes quickly when on-board and thus requires frequent venting.

The newest hydrogen storage technologies combine both cryogenic storage and compression to produce cryocompressed H_2. Not only does compressing liquid H_2 from 1 ATM to 237 ATM increases its density from 70 g/L to 87 g/L, but cryocompressed vessels can be vented at higher temperatures than uncompressed storage tanks [11]. However, while gravimetric storage capacities of cryocompressed systems meet DOE targets, volumetric capacities fail to meet the ultimate target of 70 g/L. Furthermore, the manufacturing costs of cryocompressed systems are roughly 2 times higher than DOE targets, and well-to-tank efficiency is low. Despite these shortcomings, cryocompressed H_2 storage systems are among the most promising developed to date, and have been used in a number of prototype systems.

1.1.2 Adsorption materials

Molecular H_2 can also be adsorbed by materials which are porous and have a high surface area, including metal organic frameworks (MOF), carbon and other nanostructures [12]. Given the lack of chemical bonds formed upon physisorption, low temperatures and high pressures must be used in order to achieve reasonable storage capacities [3]. For example, while MOF NU-100 can reportedly store 9 wt% H_2, temperatures of 77 K and pressures of 56 bar are required [13], making it unsuitable for use in light duty FCVs. At room temperature, MOFs have low H_2 storage capacities, typical;;y less than 1 wt% and 15 g / L, falling well short of DOE targets [14, 15]. Activated carbons and carbon nanotubes have similar H_2 adsorption properties, only adsorbing significant quantities of H_2 under low temperature, high pressure conditions. For example, while the most effective activated carbon system adsorbs 8 wt% H_2 at 77K / 39 ATM, the same material requires enormous pressures of 493 ATM to adsorb just 6.8 wt% at room temperature [16].

1.1.3 Chemisorption materials

In terms of thermodynamics, systems which chemisorb H_2 are more likely to have high storage capacities under ambient conditions due to the formation of strong chemical bonds [17]. While physisorbed hydrogen has a binding energy of around 0.1 eV, the binding energies of systems which chemisorbed hydrogen can reach values an order of magnitude higher [7, 18].

Metal hydrides have been widely investigated due to their high volumetric and gravimetric storage capacities. For example, MgH_2 stores H_2 at a gravimetric capacity of 7.6 wt%, while AlH_3 stores 10.1 wt% H_2. However, simple metal hydrides often exhibit an undesirably high thermodynamic stability and slow kinetics, hindering the desorption of H_2 at the point of use. While strategies to overcome these problems, including nanostructuring, alloying and doping with catalytic additives, have been successful, none have resulted in a practically useful system [7]. Meanwhile, the lower thermodynamic stability of intermetallic hydrides is better suited to vehicular use, allowing for the adsorption and desorption of H_2 under more moderate conditions [7, 19]. Despite the fact that its gravimetric capacity falls short of DoE targets, sodium alanate is the most heavily investigated intermetallic hydride. While its thermodynamic profile is good, the kinetics of hydrogen desorption and adsorption in un-doped $NaAlH_4$ are slow, and the material's cost is relatively high. Borohydrides have a much higher storage capacity, with $LiBH_4$ storing 18 wt% H_2. However, as with binary metal hydrides, their thermodynamic stability means that H_2 is only released at high temperatures.

Non-metal hydrides, which typically consist of boron, carbon, nitrogen or oxygen in combination with hydrogen, often have high hydrogen storage capacities. For example, ammonia borane has a storage capacity of 19.6 wt% [20]. However, its thermal decomposition requires temperatures in excess of 470 K and results in unwanted borazine by-products. Furthermore, the direct hydrogenation of $(NHBH)_\infty$ to form NH_3BH_3 is slow, proceeding with an activation barrier of 1.89 eV. This is primarily driven by the high activation barrier required for the heterolytic dissociation of H_2, with the isolated dissociation of H_2 into H^+ and H^- proceeding with a huge barrier of 16.9 eV [21]. Given this issue, metal amidoboranes such as $LiNH_2BH_3$ have been suggested as an alternative, and can be synthesised by reacting amidoborane with lithium [22, 23]. Meanwhile, two component systems such as LiH + $LiNH_2$ have been shown to release H_2 with a good thermodynamic profile [24]. However, such systems suffer from a similar problem to that of as NH_3BH_3, requiring high temperatures for charging and discharging owing to the high activation energies needed to heterolytically dissociate H_2 [25, 26].

It is possible to use catalysts to improve the hydrogen adsorption and desorption profiles of hydrogen storage materials with high kinetic barriers. For example, doping sodium alanate with titanium has been shown to improve significantly the kinetics of hydrogen desorption [27], while transition metal clusters act as a source of atomic hydrogen for the chemisorption of hydrogen onto carbon surfaces [28]. For the generation of proton-hydride systems, catalysts should lower the activation energy required for dissociation of H_2 into H^+ and H^-. Complexes containing group VIII to X transition metals with phosphine or amine ligands have succeed in this respect, although the ability of such systems to cooperate with prospective HSMs is limited due to their reliance on proper solvation and their instability in highly reducing environments [29, 30]. Furthermore, the cost of precious transition metals such as Ir, Ru, Pd, Ru and Re is prohibitively high.

If we assume that hydrogenation catalysts dissociate H_2 entirely before acting as a source of atomic or ionic hydrogen, they must adsorb H_2 with a less exothermic binding energy than any cooperating HSM. Meanwhile, it is important that the hydrogenation of HSMs is thermodynamically reversible with respect to free H_2 over a modest range of conditions. The Gibbs free energy change when hydrogen is adsorbed by a prospective hydrogenation catalyst should therefore be zero at some point over the same modest range. This allows the catalyst to be hydrogenated by H_2 and dehydrogenated by any depleted HSM which adsorbs H_2 more strongly.

Furthermore, any hydrogenation catalyst must also dissociate H_2 into atomic or ionic hydrogen with fast kinetics. We investigate the properties of Ti_8C_{12} with respect to this profile in Chapter 3.

1.2 Materials for electronic devices

It is difficult to overstate the impact of electronic devices over the last 50 years. Such progress has been made possible through the continued miniaturization of transistors, with channel regions as small as 14 nm now commercially available [31]. Microprocessors contain billions of silicon based metal oxide semiconductor field-effect transistors (MOSFETs), with Moore's law predicting that the number of transistors per square inch on integrated circuits should approximately double every two years. Moore's prediction was made in 1965 [32], and has proved surprisingly accurate up until now [33]. Housing more transistors per chip results not only in increased processing power, but also in improved efficiency. The Dennard scaling law states that the power density of transistors stays constant as their size is scaled downwards, meaning that chips which are densely packed with transistors are able to produce more computations power per watt of power [34]. However, it is widely acknowledged that the feasibility of Moore's law is reaching a fundamental limit in the absence of a paradigm shift [35]. The continued advancement of processing power depends either on the discovery of novel high performance materials or on the development of new operating principles.

1.2.1 Field Effect Transistors

The concepts behind field effect transistors were proposed in 1925 [36], although it was not until 1960 that the first functioning metal-oxide-semiconductor FET (MOSFET) was fabricated by Kahng and Atalla [37][38]. Transistors are typically used to amplify and switch signals in electronic circuits, with FETs consisting of three terminals: the source, the drain and the gate. The source and drain contacts are connected via a semiconductor, and the gate electrode is separated from the semiconductor by an electrically insulating gate-dielectric. The gate electrode couples capacitively with the semiconductor and controls the electrostatic potential at the semiconductor – dielectric interface [39].

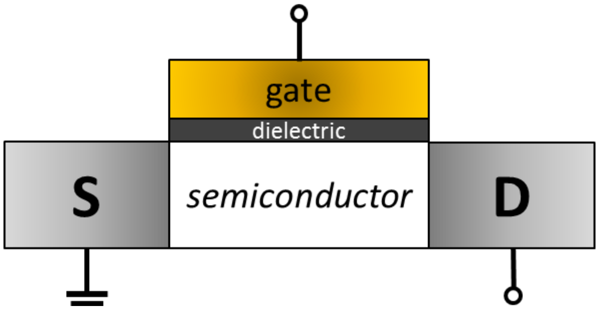

Figure 1.1: A simplified representation of a field-effect transistor.

The drain current can be controlled by varying the electric potentials applied to the three terminals, with the conductivity of the semiconducting channel region modulated by both the gate-source voltage and the drain-source voltage. According to the Drude model, the current along the semiconducting channel, $\mathrm{I_D}$, can be expressed in terms of the cross-sectional area of the conducting channel, A, the channel length, L, the charge-carrier mobility, μ, the number of free charge carriers, n, the voltage applied between the source and drain terminals, V_{DS}, and the elementary charge, q [40]:

$$\mathrm{I_D} = \frac{A}{L}.n.\mu.q.V_{DS}$$

While μ is an inherant property of the channel material, n depends on the energy difference between the Fermi level, E_F, and the valence and conduction band edges in the channel. For example, the number of free electrons in the conduction band under thermal equilibrium can be expressed as follows:

$$n_{e,0} = N_C.exp\left(-\frac{E_{CB} - E_F}{k_B T}\right)$$

A gate voltage can be applied to vary n by means of ‘bending’ the valence and conduction band edges at the semiconductor-gate interface, with Figure 1.2 showing the effect of a negative gate potential V_G.

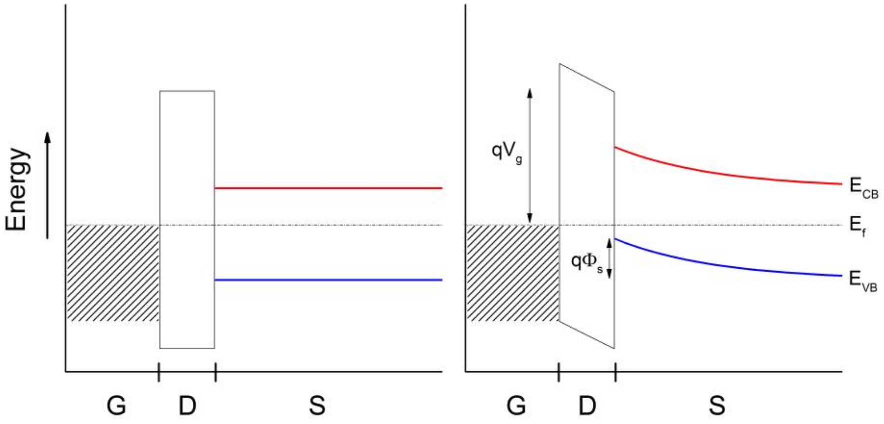

Figure 1.2: The operation of a FET in terms of channel region valence and conduction band edges, in the absence of a gate voltage (left) and when a gate voltage is applied (right).

When V_G is negative, both valence and conduction states in the channel are destabilized leading to an increase in *p*-type charge carriers and a decrease in the number of *n*-type charge carriers. The opposite occurs when a positive V_G is applied, with a decrease in *p*-type charge carriers and an increase in *n*-type charge carriers. Depending on which are the majority charge carriers in the source and drain terminals, this modulates the drain current. The change in the number of free charge carriers can be calculated using the following expression, where Φ_S is the electrostatic potential at the semiconductor / gate interface [39]:

$$n_{e,0} = N_C.exp\left(-\frac{E_{CB} - \mu_c + q\Phi_S}{k_B T}\right) = n_{e,0}.exp\left(-\frac{q.\Phi_S}{k_B T}\right)$$

In order to minimize power consumption, it is desirable for the drain current to be close to zero when the device is idle, at which point the device is said to be in its ‘off’ state. This can only be achieved by using a semiconducting channel region with a moderate band gap, and is particularly important in integrated circuit devices. However, channel regions with a lower band gap can be used in amplifying devices where idle power consumption is less of an issue.

Metal–oxide–semiconductor FETs (MOSFETs) form the basis of complementary metal–oxide–semiconductor (CMOS) logic, and have been used in the vast majority of integrated circuits over the past 30 years. In the most commonly used MOSFET devices, the source and drain terminals are made of a highly doped semiconductor of opposite polarity to the channel region. This arrangement ensures that when no gate voltage is applied, no change carriers pass between the source and channel regions. However, a gate voltage can be applied to change the polarity of the channel region near at the gate-channel interface. This forms an inversion layer through which charge carriers can flow, inducing the MOSFET's 'on' state [41].

Unlike MOSFETs, Schottky barrier FETs have metallic source and drain terminals. As the semiconducting channel region comes into contact with a metal terminal, charge flows across junction, creating an electric field that aligns the two Fermi levels. This buildup of charge results in a potential energy barrier known as the Schottky barrier, which prevents further charge flowing between the source and channel regions [42]. The Schottky barrier can be estimated as being the difference between the metal's work function and the vacuum electron affinity or ionization energy of the semiconductor using the Schottky – Mott rule [43, 44]. However, in reality surface states at the interface result in Fermi pinning, which means that Schottky barriers are largely independent of the metal's work function [45, 46]. Applying a gate voltage can change the channel's valence and conduction band energies through band bending, allowing charge to flow between the source and drain terminals.

1.2.2 Device Performance

The response of FETs to variations in V_G largely defines device performance. For MOSFETs, the transistor is in its off state, $\mathrm{I}_{DS} = \mathrm{I}_{off}$, when $\mathrm{V}_G = 0$ and in its on state, $\mathrm{I}_{DS} = \mathrm{I}_{on}$, when $\mathrm{V}_G = \mathrm{V}_{max}$. The value of V_G at which the FET is on the verge of turning on is known as the threshold voltage (V_T), and its transfer characteristics relate to the variation in I_{DS} with V_G. The subthreshold swing measures the change in $\log(\mathrm{I}_{DS})$ with V_G when approaching the threshold voltage, while the terminal transconductance measures the change in I_{DS} with V_G when $\mathrm{V}_G > \mathrm{V}_T$. Both are important measures in assessing the switching capabilities of a give FET. Furthermore, I_{off} should be as low as possible in order to minimize static power dissipation, with desirable on-off ratios, $\mathrm{I}_{on}/\mathrm{I}_{off}$, ranging between 10^4 and 10^7. On-off ratios of this magnitude typically require channel regions with a sizeable bandgap of 0.4 eV or more [41, 47].

Given that I_{DS} is proportional not only to n, but also to μ and L^{-1}, it follows that its response to V_G is optimized by short, high mobility channel regions. However, ubiquitously used silicon FETs suffer from a number of problems at channel lengths less than 10 nm [48].

1.2.3 Silicon and short-channel effects

While germanium was the favored transistor material up until the 1960s, silicon now dominates the electronics industry. Commercial integrated circuit devices are based around silicon alone, with both p-type and n-type silicon easily fabricated. Pure silicon has a band gap of around 1.1 eV, providing a good balance between static power dissipation and response to moderate gate voltages [49]. Furthermore, transistors based around silicon have so far been able to satisfy Moore's law, with channel lengths now measured on a nanometer scale. However, such progress appears to be unsustainable due to the occurrence of so-called short-channel effects in silicon FETs with sub 10 nm gates [48][50].

In small-geometry MOSFETS, the electrostatic potential throughout the channel region is not only controlled by V_G, but also by V_{DS}. This effect is known as drain induced barrier lowering (DIBL), and means that the conductivity of the channel region is modulated by V_{DS} as well as V_G, which ultimately leads to a loss of control of I_{DS} by the gate. Meanwhile, velocity saturation limits the velocity of charge carriers in short-geometry MOSFETS. Under normal circumstances, electron velocity rises linearly with longitudinal electric field through the relation $\nu_y = \mu_y \varepsilon_y$. However, behaviour in short channels does not obey this relation due to scattering effects, limiting ν_y to a certain velocity. This effect is known as velocity saturation, with the velocity of charge carriers in silicon limited to ~10^5 m^2/s. In n-channel enhancement MOS devices, high ε_y also results in impact ionization, where atoms in the channel are ionized by high velocity electrons. While the resulting electrons travel towards the drain, holes pass into the substrate and towards the source terminal. The corresponding current causes a voltage drop in the substrate, allowing electrons to pass from the source into the substrate, potentially damaging other devices on the chip. Furthermore, 'hot electrons' can also enter and become trapped in the gate dielectric, with the resulting buildup of charge degrading performance and ultimately resulting in device failure. Finally, miniaturization below ~10 nm also means that more charge carriers tunnel through the channel, increasing subthreshold leakage and thus power consumption.

1.2.4 2D Materials

Scaling theory predicts that thin channel regions are immune to the majority of short-channel effects discussed above. However, when ultrathin films of traditional materials such as silicon are used, fluctuations in thickness and surface roughness lead to unpredictable behavior. Exfoliates of layered materials therefore represent a logical choice for use in next generation devices. So-called 2D materials are ultrathin yet uniform, and maintain the electrostatic integrity necessary for sub-10nm transistors. They also have a number of unique properties, allowing for the exploration of new operating principles and device functionality.

The most widely investigated 2D material is graphene, which was first fabricated in 2004 through the mechanical exfoliation of bulk graphite. The mobility of charge carriers in graphene is very high, with a theoretical limit of 200,000 $cm^2/s/V$ at room temperature [51], suggesting a huge potential for use in ultrafast electronic devices. However, while graphene has been used to make efficient radiofrequency devices, its lack of band gap means that graphene's future use in integrated circuits is unlikely [49]. One possible solution lies in the fabrication of graphene nanostructures, some of which have band gaps in excess of 0.2 eV [52]. However, as the band gap of graphene is increased through nanostructuring, its charge carrier mobility falls, with the charge carrier mobility in 10 nm graphene nanoribbons less than 200 $cm^2V^{-1}s^{-1}$, lower than in doped silicon. It appears that carbon nanotubes are more likely to replace silicon in semiconducting applications, with IBM recently reporting progress towards the manufacture of computer chips based on carbon nanotubes [53].

Another promising 2D material investigated in recent years is MoS_2. In its bulk form, MoS_2 is a layered material with an indirect bad gap of 1.29 eV, while monolayer MoS_2 has a direct band gap of around 1.9 eV [54]. As a result of its sizeable band gap, both single and multilayered FETs have high on/off ratios of order 10^8 and good transfer characteristics [55, 56]. However, ultimate charge carrier mobilities in MoS_2 are approximately three orders of magnitude lower than those of graphene [57].

In Chapters 4, 5 and 6 we investigate the properties of phosphorene. The first phosphorene FET devices were reported in 2014, resulting in an explosion of interest in the compound. The performance of early phosphorene devices is discussed in Chapter 4.

1.3 Computational Methods

Computational chemistry can be used to investigate a system's structural, energetic, electronic and chemical properties. It can be predictive, providing a direction for experimental efforts or analytical, explaining misunderstood phenomena. A number of different computational approaches are available, with the suitability of each depending on the size of the system and its properties of interest.

Force field methods treat materials as an array of mechanically connected atoms [58]. Electrons are not treated explicitly but instead in terms of their effect on the attraction between nuclei. Molecular mechanics or energy minimization methods are used to investigate the structure of materials, predicting equilibrium geometries, transition states and the relative energies of different isomers or allotropes. Energy is calculated in terms of parametrized forces between atoms, which are usually fitted to experimental data. While force field methods are computationally undemanding, they come with a number of limitations. Particular force fields are only accurate for a certain systems, which are usually related to those used for parametrization [59]. While force field methods do not give any information regarding chemical or electronic properties, they are powerful in exploring the structure and dynamics of large, complex systems.

The simplest electronic structure method is the tight-binding model, which is able to approximate a material's electronic structure with little computational effort. In the tight-binding model, the wavefunction of solid-state materials is predicted based on the superposition of the wavefunctions of isolated atoms in a process analogous to the linear combination of atomic orbitals (LCAO) [60]. To calculate energies, an approximate form of the Hamiltonian is used, which is expressed in terms of a combination of overlap and on-site matrix elements.

For a more robust description of a system's electronic structure, quantum mechanical (QM) methods known as *ab initio* ("from the beginning") methods can be used. In their purest form, *ab initio* methods require no empirical parameters. Hartree-Fock theory directly solves the Schrodinger equation in the absence of correlation between electrons [61, 62]. However, the results obtained using Hartree-Fock tend to be inaccurate in systems where electron correlation is important. Post- Hartree-Fock methods introduce correlation, relativistic and spin-orbit effects, improving the accuracy of HF solutions at the expense of increased computational cost [63].

Density Functional Theory (DFT) calculates single particle wavefunctions using the system's electron density [64]. While DFT is generally considered to be an *ab initio* method, in reality the majority of functionals are to some extent derived from empirical data [65]. Nevertheless, solutions obtained using DFT are often more accurate than those obtained using standard Hartree-Fock or tight binding methods, and can be achieved at a very reasonable computational costs [66]. The explicit treatment of electrons means that DFT can calculate the electronic structure of solid state materials and assess systems' chemical reactivity. We have used DFT extensively throughout this thesis, and thus it is described in more detail in Chapter 2.

References

1. IEA, *World Energy Outlook 2014*. IEA.

2. Lu, L.G., et al., *A review on the key issues for lithium-ion battery management in electric vehicles.* Journal of Power Sources, 2013. **226**: p. 272-288.

3. Schlapbach, L. and A. Zuttel, *Hydrogen-storage materials for mobile applications.* Nature, 2001. **414**(6861): p. 353-358.

4. Holladay, J.D., et al., *An overview of hydrogen production technologies.* Catalysis Today, 2009. **139**(4): p. 244-260.

5. Stetson, N.T., et al., *US DOE Hydrogen Program: Review of status and performance gaps of on-board hydrogen storage technologies.* Abstracts of Papers of the American Chemical Society, 2009. **238**.

6. Yang, J., et al., *High capacity hydrogen storage materials: attributes for automotive applications and techniques for materials discovery.* Chemical Society Reviews, 2010. **39**(2): p. 656-675.

7. Durbin, D.J. and C. Malardier-Jugroot, *Review of hydrogen storage techniques for on board vehicle applications.* International Journal of Hydrogen Energy, 2013. **38**(34): p. 14595-14617.

8. Jorgensen, S.W., *Hydrogen storage tanks for vehicles: Recent progress and current status.* Current Opinion in Solid State & Materials Science, 2011. **15**(2): p. 39-43.

9. Hua, T.Q., et al., *Technical assessment of compressed hydrogen storage tank systems for automotive applications.* International Journal of Hydrogen Energy, 2011. **36**(4): p. 3037-3049.

10. Wolf, J., *Liquid-hydrogen technology for vehicles.* Mrs Bulletin, 2002. **27**(9): p. 684-687.

11. Ahluwalia, R.K., et al., *Technical assessment of cryo-compressed hydrogen storage tank systems for automotive applications.* International Journal of Hydrogen Energy, 2010. **35**(9): p. 4171-4184.

12. Chae, H.K., et al., *A route to high surface area, porosity and inclusion of large molecules in crystals.* Nature, 2004. **427**(6974): p. 523-527.

13. Farha, O.K., et al., *De novo synthesis of a metal-organic framework material featuring ultrahigh surface area and gas storage capacities.* Nature Chemistry, 2010. **2**(11): p. 944-948.

14. Langmi, H.W., et al., *Hydrogen Storage in Metal-Organic Frameworks: A Review*. Electrochimica Acta, 2014. **128**: p. 368-392.

15. Rowsell, J.L.C., et al., *Hydrogen sorption in functionalized metal-organic frameworks.* Journal of the American Chemical Society, 2004. **126**(18): p. 5666-5667.

16. Jorda-Beneyto, M., et al., *Hydrogen storage on chemically activated carbons and carbon nanomaterials at high pressures.* Carbon, 2007. **45**(2): p. 293-303.

17. Aardahl, C.L. and S.D. Rassat, *Overview of systems considerations for on-board chemical hydrogen storage.* International Journal of Hydrogen Energy, 2009. **34**(16): p. 6676-6683.

18. Gandhi, K., D.K. Dixit, and B.K. Dixit, *Hydrogen desorption energies of Aluminum hydride (AlnH3n) clusters.* Physica B-Condensed Matter, 2010. **405**(15): p. 3075-3081.

19. Satyapal, S., et al., *The US Department of Energy's National Hydrogen Storage Project: Progress towards meeting hydrogen-powered vehicle requirements.* Catalysis Today, 2007. **120**(3-4): p. 246-256.

20. Peng, B. and J. Chen, *Ammonia borane as an efficient and lightweight hydrogen storage medium.* Energy & Environmental Science, 2008. **1**(4): p. 479-483.

21. Nguyen, M.T., et al., *Molecular Mechanism for H2 Release from BH3NH3, Including the Catalytic Role of the Lewis Acid BH3.* The Journal of Physical Chemistry A, 2007. **111**(4): p. 679-690.

22. Xiong, Z.T., et al., *High-capacity hydrogen storage in lithium and sodium amidoboranes.* Nature Materials, 2008. **7**(2): p. 138-141.

23. Sutton, A.D., et al., *Regeneration of Ammonia Borane Spent Fuel by Direct Reaction with Hydrazine and Liquid Ammonia.* Science, 2011. **331**(6023): p. 1426-1429.

24. Chen, P., et al., *Interaction of hydrogen with metal nitrides and imides.* Nature, 2002. **420**(6913): p. 302-304.

25. Sakintuna, B., F. Lamari-Darkrim, and M. Hirscher, *Metal hydride materials for solid hydrogen storage: A review.* International Journal of Hydrogen Energy, 2007. **32**(9): p. 1121-1140.

26. Li, H.W., et al., *Recent Progress in Metal Borohydrides for Hydrogen Storage.* Energies, 2011. **4**(1): p. 185-214.

27. Bogdanovic, B. and M. Schwickardi, *Ti-doped alkali metal aluminium hydrides as potential novel reversible hydrogen storage materials.* Journal of Alloys and Compounds, 1997. **253**: p. 1-9.

28. Prins, R., *Hydrogen Spillover. Facts and Fiction.* Chemical Reviews, 2012. **112**(5): p. 2714-2738.

29. Curtis, C.J., et al., *Measurement of the Hydride Donor Abilities of [HM(diphosphine)2]+ Complexes (M = Ni, Pt) by Heterolytic Activation of Hydrogen.* Journal of the American Chemical Society, 2002. **124**(9): p. 1918-1925.

30. Ohkuma, T., et al., *Practical Enantioselective Hydrogenation of Aromatic Ketones.* Journal of the American Chemical Society, 1995. **117**(9): p. 2675-2676.

31. Intel. *Intel® 14 nm Technology*. 2015 [cited 2015 04/11/2015]; Available from: http://www.intel.com/content/www/us/en/silicon-innovations/intel-14nm-technology.html.

32. Moore, G.E., *Cramming more components onto integrated circuits (Reprinted from Electronics, pg 114-117, April 19, 1965).* Proceedings of the Ieee, 1998. **86**(1): p. 82-85.

33. Moore, G., *Understandng Moore's law: four decades of innovation*, ed. D. Brock. 2006.

34. Dennard, R.H., et al., *Design of ion-implanted MOSFET's with very small physical dimensions (Reprinted from IEEE Journal of Solid-State Circuits, vol 9, pg 256-268, 1974).* Proceedings of the Ieee, 1999. **87**(4): p. 668-678.

35. Markov, I.L., *Limits on fundamental limits to computation.* Nature, 2014. **512**(7513): p. 147-154.

36. Edgar, L.J., *Method and apparatus for controlling electric currents*. 10/08/1926, Edgar, Lilienfeld Julius

37. Dawon, K., *Electric field controlled semiconductor device*. 1963, Google Patents.

38. Kahng, D., *Historical-Perspective on Development of Mos-Transistors and Related Devices.* Ieee Transactions on Electron Devices, 1976. **23**(7): p. 655-657.

39. Zeghbroeck, V., *Principles of Semiconductor Devices and Heterojunctions*. 2007: Prentice Hall PTR.

40. Drude, P., *Zur Elektronentheorie der Metalle.* Annalen der Physik, 1900. **306**(3): p. 566-613.

41. Lundstrom, M. *A Review of MOSFET Fundamentals*. in *NCN@Purdue*. 2008. Indiana, USA.

42. Larson, J.M. and J.P. Snyder, *Overview and status of metal S/D Schottky-barrier MOSFET technology.* Ieee Transactions on Electron Devices, 2006. **53**(5): p. 1048-1058.

43. Schottky, W., *Discrepencies in Ohm's laws in semiconductors.* Physikalische Zeitschrift, 1940. **41**: p. 570-573.

44. Mott, N.F., *The theory of crystal rectifiers.* Proceedings of the Royal Society of London Series a-Mathematical and Physical Sciences, 1939. **171**(A944): p. 0027-0038.

45. Sze, S.M. and K.K. Ng, *Physics of Semiconductor Devices*. 2006: Wiley.

46. Himpsel, F.J., G. Hollinger, and R.A. Pollak, *Determination of the Fermi-Level Pinning Position at Si(111) Surfaces.* Physical Review B, 1983. **28**(12): p. 7014-7018.

47. Schwierz, F., *Graphene transistors.* Nat Nano, 2010. **5**(7): p. 487-496.

48. Agostino, F. *Short-channel effects in MOSFETs*. 2000 05/11/2015]; Available from: www0.cs.ucl.ac.uk/staff/ucacdxq/projects/vlsi/report.pdf.

49. Jacoboni, C., et al., *A review of some charge transport properties of silicon.* Solid-State Electronics, 1977. **20**(2): p. 77-89.

50. Chaudhry, A. and M.J. Kumar, *Controlling short-channel effects in deep-submicron SOI MOSFETs for improved reliability: A review.* Ieee Transactions on Device and Materials Reliability, 2004. **4**(1): p. 99-109.

51. Shishir, R.S., D.K. Ferry, and S.M. Goodnick, *Intrinsic Mobility Limit in Graphene at Room Temperature.* 2009 9th Ieee Conference on Nanotechnology (Ieee-Nano), 2009: p. 21-24.

52. Dutta, S. and S.K. Pati, *Novel properties of graphene nanoribbons: a review.* Journal of Materials Chemistry, 2010. **20**(38): p. 8207-8223.

53. Orcutt, M. *IBM Reports Breakthrough on Carbon Nanotube Transistors*. 2015 05/11/2015]; Available from: technologyreview.com/news/541921/ibm-reports-breakthrough-on-carbon-nanotube-transistors/.

54. Ganatra, R. and Q. Zhang, *Few-Layer MoS2: A Promising Layered Semiconductor.* Acs Nano, 2014. **8**(5): p. 4074-4099.

55. RadisavljevicB, et al., *Single-layer MoS2 transistors.* Nat Nano, 2011. **6**(3): p. 147-150.

56. Yoon, Y., K. Ganapathi, and S. Salahuddin, *How Good Can Monolayer MoS2 Transistors Be?* Nano Letters, 2011. **11**(9): p. 3768-3773.

57. Bao, W.Z., et al., *High mobility ambipolar MoS2 field-effect transistors: Substrate and dielectric effects.* Applied Physics Letters, 2013. **102**(4).

58. Allinger NL, B.U., *Molecualr Mechanics. An American Chemical Society Publication*. 1982.

59. Bowen, J.P. and N.L. Allinger, *Molecular Mechanics: The Art and Science of Parameterization*, in *Reviews in Computational Chemistry*. 2007, John Wiley & Sons, Inc. p. 81-97.

60. Harrison, W.A., *Electronic structure and the properties of solids: the physics of the chemical bond*. 1989: Dover Publications.

61. Echenique, P. and J.L. Alonso, *A mathematical and computational review of Hartree–Fock SCF methods in quantum chemistry*. Molecular Physics, 2007. **105**(23-24): p. 3057-3098.

62. Magnasco, V., *Elementary Methods of Molecular Quantum Mechanics*. 2006: Elsevier Science.

63. Bartlett, R.J. and J.F. Stanton, *Applications of Post-Hartree—Fock Methods: A Tutorial*, in *Reviews in Computational Chemistry*. 2007, John Wiley & Sons, Inc. p. 65-169.

64. Burke, K. *The ABC of DFT, http://dft.uci.edu/book/gamma/g1.pdf*. 2007; Available from: http://dft.uci.edu/book/gamma/g1.pdf.

65. Perdew, J.P. and K. Schmidt, *Jacob's ladder of density functional approximations for the exchange-correlation energy*. Density Functional Theory and Its Application to Materials, 2001. **577**: p. 1-20.

66. Xiao, B., et al., *Testing the Jacob's ladder of density functionals for electronic structure and magnetism of rutile VO2*. Physical Review B, 2014. **90**(8).

Chapter 2

Theoretical Background

This chapter will discuss the principles of Density Functional Theory along with aspects of electronic structure theory, thermodynamics and kinetics. The information contained is relevant to many of the subsequent chapters of this thesis. A number of standard texts have been referenced throughout, and should be consulted where more details are required [1-5].

2.1 Density Functional Theory

2.1.1 The Many-Body Schrödinger Equation

The properties of matter are governed by the laws of quantum mechanics, with the non-relativistic Schrödinger Equation used to determine a system's behavior. The ultimate aim of *ab-initio* methods is to solve the many-body Schrödinger equation, thereby determining the system's ground state wavefunction and energy. The Schrödinger equation can be written as follows:

$$i\frac{\partial}{\partial t}\,\psi(\boldsymbol{r},t) = \widehat{H}\psi(\boldsymbol{r},t)$$

where $\widehat{H}$ is the Hamiltonian and $\psi(\boldsymbol{r},t)$ is the wavefunction expressed in terms of spatial coordinates and time. When considering a static system, the Schrödinger equation can be separated into spatial, $\psi(r)$, and time dependent, $\Phi(t)$, components.

$$\Psi(\boldsymbol{r},t) = \Phi(t)\psi(r)$$

$$i\frac{d\Phi(t)}{dt} = E\Phi(t)$$

$$\hat{H}\psi(r) = E\psi(r)$$

Throughout this work, we have investigated the properties of ground state systems, and therefore only consider time independent solutions of the Schrödinger equation. The time-independent Schrödinger equation (TISE) can be solved in order to find the ground state wavefunction and energy of a system by using the following Hamiltonian:

$$\hat{H} = -\frac{1}{2}\sum_{i} \nabla_i^2 - \frac{1}{2m_A}\sum_{A} \nabla_A^2 + \sum_{A>B} \frac{Z_A Z_B}{R_{AB}} - \sum_{A,i} \frac{Z_A}{r_{Ai}} + \sum_{i>j} \frac{1}{r_{ij}}$$

The first term calculates the kinetic energy of electron i, while the second term calculates the kinetic energy of nucleus A with mass m_A. The third term calculates the energy of the interaction between nucleus A and nucleus B, which have charges Z_A and Z_B respectively and are separated by the distance R_{AB}. The fourth term calculates the energy of the interaction between the nucleus A of charge Z_A and electron i, which are separated by the distance r_{Aj}. The fifth term calculates the energy of the interaction between electrons i and j, which are separated by the distance r_{ij}.

Under the Born Oppenheimer approximation, both the above Hamiltonian and corresponding many-body wavefunction can be simplified. The Born Oppenheimer approximation allows electronic and nuclear degrees of freedom to be decoupled under the assumption that electrons respond instantaneously to the movement of nuclei. Therefore, the TISE can be solved for a set of electrons with a wavefunction depending on both electronic and nuclear positions, $\psi(\{\boldsymbol{r_i}\};\{\boldsymbol{R_A}\})$, surrounding a set of static nuclei with wavefunction $\Phi(\{\boldsymbol{R_A}\})$.

$$\psi(\{\boldsymbol{r_i}\},\{\boldsymbol{R_A}\}) = \psi(\{\boldsymbol{r_i}\};\{\boldsymbol{R_A}\})\Phi(\{\boldsymbol{R_A}\})$$

$$\hat{H} = -\frac{1}{2}\sum_{i} \nabla_i^2 - \sum_{A,i} \frac{Z_A}{r_{Ai}} + \sum_{i>j} \frac{1}{r_{ij}}$$

While the above Hamiltonian can be solved analytically, for all but the simplest systems the computational effort required to do so is enormous given the complexity of many-body electronic wavefunctions and the two electron operator, $\frac{1}{r_{ij}}$. The complexity of both ψ and $\frac{1}{r_{ij}}$ arises as a result of the coupling between electrons required to account for exchange and correlation effects. While the variational principle allows for the solution of the TISE for simple atomic systems, more efficient methods are required to model systems of a practically useful size.

2.1.2 Variational Principle

The variational principle is a simple but very important concept utilised by the majority of computational methods that set out to solve the many-body problem. The variational principle states that the best guess ground state wavefunction is the wavefunction which produces the lowest energy when acted on by the Hamiltonian.

$$E_{min} = \langle \psi_0 | \hat{H} | \psi_0 \rangle \leq \langle \psi | \hat{H} | \psi \rangle$$

The above expression justifies trying a large number of wavefunctions and choosing the one which gives the lowest energy as the ground state wavefunction.

2.1.3 Hartree-Fock Theory

As discussed in Section 2.2.1, the main difficulties in solving the TISE are a result of the complexity of the many-electron wavefunction, $\psi(r_1 \dots r_N)$ and the two electron operator, $\frac{1}{r_{ij}}$. Hartree-Fock theory manages to simplify both $\psi(r_1 \dots r_N)$ and $\frac{1}{r_{ij}}$, and was proposed by Douglas Hartree in 1927 before being modified by Vladimir Fock in 1930 [6].

As a basis for the simplification of $\psi(r_1 \dots r_N)$, Hartree theory assumes that the full N-body wavefunction can be written as a product of N single-electron wavefunctions, $\Phi_k(\boldsymbol{r}_N)$, in an expression known as a Hartree-Product:

$$\psi(r_1 \dots r_N) = \Phi_i(\boldsymbol{r}_1) \dots \Phi_k(\boldsymbol{r}_N)$$

In contrast with true many-body wavefunctions, the resultant single electron probability distributions are not interdependent and are relatively simple to work with. However, wavefunctions represented in this way are not correlated and are asymmetric with respect to fermion exchange, disobeying the Pauli Exclusion Principle.

For example, in a two electron case:

$$\psi(r_2, r_1) \neq -\psi(r_1, r_2)$$

The Pauli Exclusion Principle can be satisfied if a linear combination of each of the allowed Hartree products is taken, resulting in a Slater Determinant which is asymmetric with respect to electron exchange [7]:

$$\psi(r_1, r_2) = \frac{1}{\sqrt{2}}\{\Phi_1(\boldsymbol{r}_1)\Phi_2(\boldsymbol{r}_2) - \Phi_1(\boldsymbol{r}_2)\Phi_2(\boldsymbol{r}_1)\} = \frac{1}{\sqrt{2}}\begin{vmatrix} \Phi_1(\boldsymbol{r}_1) & \Phi_1(\boldsymbol{r}_2) \\ \Phi_1(\boldsymbol{r}_2) & \Phi_2(\boldsymbol{r}_2) \end{vmatrix}$$

Furthermore, the Hartree-Fock method rewrites the Hamiltonian in order to account for electron-electron interactions in a mean field way, eliminating the troublesome $\frac{1}{r_{ij}}$ term in the TISE Hamiltonian [8, 9].

$$\hat{H} = -\frac{1}{2}\sum_i \nabla_i^2 - \sum_{A,i}\frac{Z_A}{r_{Ai}} + \sum_{A>B}\frac{Z_A Z_B}{R_{AB}} + \sum_{i,j}\int dr' \frac{\left|\Psi_j(r')\right|^{\mathbf{2}}}{|(r-r')|} - \sum_{i,j}\sigma_i\sigma_j\int dr' \frac{\left|\Psi_j^*(r')\Psi_i(r')\right|}{|(r-r')|}$$

where r and r' represent the spatial coordinates of electrons i and j respectively, Z_A is the charge of ionic core A, R_{AB} is the distance between ionic cores A and B and r_{Ai} is the distance between ionic core A and electron i. The first, second and third terms account for the kinetic energy, electron-ion potential and the ion-ion potential respectively. The fourth term accounts for the electron-electron potential, and includes an unphysical self-interaction of electrons when $i = j$. This error is cancelled by the fifth term, known as the exchange term, which ensures that electrons of equivalent spin avoid one another. The $\sigma_i\sigma_j$ term equals zero when the spins of electrons i and j are opposite and one when they are equal.

The variational principle can be used to determine the ground state wavefunction and corresponding energy of the Hartree-Fock Hamiltonian. Minimization of the Hartree-Fock Hamiltonian is carried out under the constraint of orbitals orthogonality, $\langle\Phi_i|\Phi_j\rangle = \delta_{ij}$, in order to ensures that the total number of electrons in the system remains constant. While the Hartree-

Fock method allows for the investigation of systems far larger than would be solvable using the TISE and full wavefunction, the computational effort required still scales as approximately N^4. More importantly, Hartree-Fock theory neglects electron correlation entirely, meaning that the solutions obtained are limited when correlation effects are significant. Most notably, the wavefunctions obtained using Hartree-Fock are highly localized, resulting in the considerable overestimation of the band gap in semiconductors.

2.1.4 Thomas-Fermi Theory

In the same year that Hartree-Fock theory was proposed, Llewellyn Thomas and Enrico Fermi developed the first electronic structure theory to use the electron density, $\rho(\boldsymbol{r})$, as the central variable as opposed to the wavefunction [10, 11]. The energy functional in Thomas-Fermi theory is as follows:

$$E^{TF}[\rho(\boldsymbol{r})] = C_F \int \rho(\boldsymbol{r})^{5/3} d\mathbf{r} + \int \rho(\boldsymbol{r}) v_{ext}(\boldsymbol{r}) d\mathbf{r} + \frac{1}{2} \int \int \frac{\rho(\boldsymbol{r})\rho(\boldsymbol{r}')}{|\boldsymbol{r}-\boldsymbol{r}'|} d\mathbf{r} d\mathbf{r}'$$

where $v_{ext}(\boldsymbol{r})$ is the external potential felt by electrons, typically the result of surrounding ionic cores, and C_F is a constant. The first term accounts for the non-interacting kinetic energy, and is derived through the integration of the kinetic energy density of a homogeneous electron gas. The second term is the classical Coulomb interaction between $\rho(\boldsymbol{r})$ and $v_{ext}(\boldsymbol{r})$. Finally, the third term accounts for electron-electron repulsions, resulting in the Hartree energy.

To obtain the ground state, the Tomas-Fermi functional can be minimized using the variational principle subject to the constraint of constant $\rho(\boldsymbol{r})$. However, the Thomas-Fermi model yields poor results, failing to reproduce even the most basic features such as shell structures in atoms. While the main source of error in Thomas-Fermi theory is the poor approximation of kinetic energy, electron correlation and exchange energies are also neglected entirely. Despite the addition of an exchange energy functional by Paul Dirac in 1928, Thomas-Fermi-Dirac theory remains inaccurate in the majority of instances [12].

2.1.5 The Hohenberg-Kohn Theorems

Density Functional Theory originated in 1964 when Pierre Hohenberg and Walter Kohn proved that all of a system's properties can be calculated through knowledge of its ground state electron density [13]. This assertion is based on two theorems, which are outlined below.

Theorem I: A particular external potential can only give rise to one ground state electron density. Conversely, a particular ground state electron density must be the result of one external potential (for example, a fixed arrangement of nuclei). Therefore, the external potential is a unique functional of electron density.

Proof: Assume the existence of two potentials, $V_{ext}^{(1)}(\boldsymbol{r})$ and $V_{ext}^{(2)}(\boldsymbol{r})$, which differ by more than a constant factor. Assume also that $V_{ext}^{(1)}(\boldsymbol{r})$ and $V_{ext}^{(2)}(\boldsymbol{r})$ give rise to the same ground state electron density, $\rho_0(\boldsymbol{r})$. Two distinct Hamiltonians, $H_{ext}^{(1)}(\boldsymbol{r})$ and $H_{ext}^{(2)}(\boldsymbol{r})$ also exist, along with two distinct wavefunctions, $\psi_{ext}^{(1)}(\boldsymbol{r})$ and $\psi_{ext}^{(2)}$. According to the variational principle:

$$\mathrm{E}^{(1)} = \langle \psi^{(1)} | H^{(1)} | \psi^{(1)} \rangle < \langle \psi^{(2)} | H^{(1)} | \psi^{(2)} \rangle$$

$$< \langle \psi^{(2)} | H^{(1)} + H^{(2)} - H^{(2)} | \psi^{(2)} \rangle$$

$$< \langle \psi^{(2)} | H^{(1)} - H^{(2)} | \psi^{(2)} \rangle + \langle \psi^{(2)} | H^{(2)} | \psi^{(2)} \rangle$$

$$\mathrm{E}^{(1)} < \int d\mathbf{r} \left[V_{ext}^{(2)}(\boldsymbol{r}) - V_{ext}^{(1)}(\boldsymbol{r}) \right] \rho_0(\boldsymbol{r}) + \mathrm{E}^{(2)}$$

This can be repeated, exchanging (1) and (2) to give:

$$\mathrm{E}^{(2)} < \int d\mathbf{r} \left[V_{ext}^{(1)}(\boldsymbol{r}) - V_{ext}^{(2)}(\boldsymbol{r}) \right] \rho_0(\boldsymbol{r}) + \mathrm{E}^{(1)}$$

Combining the above equations, we arrive at the following contradiction, thus proving *Theorem I* by *reductio ad absurdum*.

$$\mathrm{E}^{(1)} + \mathrm{E}^{(2)} < \mathrm{E}^{(2)} + \mathrm{E}^{(1)}$$

There cannot be two V_{ext} that result in the same $\rho_0(\boldsymbol{r})$, and each V_{ext} therefore must give a unique $\rho_0(\boldsymbol{r})$.

Theorem II: A universally applicable energy functional can be defined in terms of $\rho(\boldsymbol{r})$, and is independent of the external potential, V_{ext}. Furthermore, the electron density that minimizes this functional, $E[\rho(\boldsymbol{r})]$, is the ground state density.

Proof: A universal functional, $F[\rho(\boldsymbol{r})]$, can be written as follows:

$$F[\rho(\boldsymbol{r})] = T[\rho(\boldsymbol{r})] + E_{int}[\rho(\boldsymbol{r})]$$

where $T[\rho(\boldsymbol{r})]$ is the kinetic energy functional and $E_{int}[\rho(\boldsymbol{r})]$ is the functional which calculates the electron interaction energy. Meanwhile, the energy functional defined in terms of the wavefunction can be written as follows:

$$E\left[\psi^{(1)}\right] = \left\langle\psi^{(1)}\middle|H^{(1)}\middle|\psi^{(1)}\right\rangle = \left\langle\psi^{(1)}\middle|\hat{T} + \hat{V}_{int} + \hat{V}_{ext}\middle|\psi^{(1)}\right\rangle$$

According to *Theorem I*, $\psi^{(1)}$ corresponds to a specific electron density $\rho^{(1)}(\boldsymbol{r})$ and a specific external potential $V_{ext}^{(1)}(\boldsymbol{r})$. Therefore, $E\left[\psi^{(1)}\right]$ is a functional of $\rho^{(1)}(\boldsymbol{r})$.

$$\begin{aligned}
E\left[\psi^{(1)}\right] &= \left\langle\psi^{(1)}\middle|\hat{T} + \hat{V}_{int} + \hat{V}_{ext}\middle|\psi^{(1)}\right\rangle \\
&= E\left[\rho^{(1)}(\boldsymbol{r})\right] \\
&= \int d\mathbf{r}\left[V_{ext}^{(1)}(\boldsymbol{r})\right]\rho^{(1)}(\boldsymbol{r}) + F\left[\rho^{(1)}(\boldsymbol{r})\right] \\
&\geq E[\psi_0] \\
&= \int d\mathbf{r}\left[V_{ext}^{(1)}(\boldsymbol{r})\right]\rho_0(\boldsymbol{r}) + F[\rho_0(\boldsymbol{r})] \\
&= E[\rho_0(\boldsymbol{r})]
\end{aligned}$$

This proves that the energy functional $E[\rho(\boldsymbol{r})]$ is lower in energy when evaluated using the ground state density $\rho_0(\boldsymbol{r})$ than when it is evaluated using any other density, $\rho(\boldsymbol{r})$. Therefore, minimizing the total energy functional with respect to $\rho(\boldsymbol{r})$ results in the correct ground state electron density and the correct ground state energy.

2.1.6 The Kohn-Sham Equations

The Hohenberg-Kohn theorems justify the minimization of energy with respect to electron density as a means to solving the many-body Schrödinger equation. However, the practical framework used by the majority of DFT codes was introduced by Walter Kohn and Lu Jeu Sham in 1965 [14]. Kohn-Sham density functional theory (KS-DFT) proposes that the real many-body system can be represented by a reference system of non-interacting wavefunctions, ψ_i, with the same ground state density as the true, interacting electronic system.

$$\rho_{KS}(\boldsymbol{r}) = \sum_{\boldsymbol{i}}^{\boldsymbol{N}} |\psi_i(\boldsymbol{r})|^{\mathbf{2}} = \rho(\boldsymbol{r})$$

where ψ_i are the single electron orbitals of the non-interacting system, $\rho_{KS}(\boldsymbol{r})$ is the density of the non-interacting system, and $\rho(\boldsymbol{r})$ is the actual electron density of the many-body system. In KS-DFT, energy is calculated as a functional of particle density:

$$E_{KS}[\rho(\mathbf{r})] = T_{KS}[\rho(\mathbf{r})] + E_{ext}[\rho(\mathbf{r})] + E_{har}[\rho(\mathbf{r})] + E_{xc}[\rho(\mathbf{r})]$$

While the exact form of the kinetic energy functional, $T[\rho(\mathbf{r})]$, is unknown, KS-DFT calculates the kinetic energy of the non-interacting system as a proxy. This approach is a significant improvement on the approached used in the Thomas-Fermi model, where kinetic energy is calculated by integrating the kinetic energy density of a homogenous electron gas.

$$T_{KS}[\rho(\mathbf{r})] = -\frac{1}{2}\sum_{i}^{N}\langle\psi_i|\nabla^2|\psi_i\rangle$$

$E_{ext}[\rho(\mathbf{r})]$ accounts for interactions with the external potential, V_{ext}. In the majority of cases, V_{ext} is the result of ionic cores of charge Z_A. The strength of the interaction between $\rho(\mathbf{r})$ and Z_A depends on the magnitude of Z_A and the distance between $\boldsymbol{r}$ and Z_A, $\boldsymbol{r_{Ai}}$.

$$E_{ext}[\rho(\mathbf{r})] = \int V_{ext}\rho(\boldsymbol{r})d\boldsymbol{r} = -\int \sum_{A}^{M} \frac{Z_A}{\boldsymbol{r_{Ai}}} \rho(\boldsymbol{r})d\boldsymbol{r}$$

The Hartree interaction, $E_{har}[\rho(\boldsymbol{r})]$, can be calculated explicitly using the same technique as is used in Thomas-Fermi theory, see Section 2.1.4.

$$E_{har}[\rho(\boldsymbol{r})] = \frac{1}{2}\int\int \frac{p(\boldsymbol{r}')p(\boldsymbol{r})}{|\boldsymbol{r}-\boldsymbol{r}'|} d\mathbf{r}d\mathbf{r}'$$

$E_{xc}[\rho(\mathbf{r})]$ is formally defined as the sum of the errors induced through the neglect of many-body correlation and exchange effects. While $E_{xc}[\rho_{KS}(\boldsymbol{r})]$ has no explicitly solvable form, a wide array of approximate functionals have been proposed [5], which are discussed in detail in Section 2.3.1.

$$E_{xc}[\rho(\mathbf{r})] = (T[\rho(\mathbf{r})] - T_{KS}[\rho_{KS}(\mathbf{r})]) + (E_{e-e}[\rho(\mathbf{r})] - E_{har}[\rho_{KS}(\boldsymbol{r})])$$

The Kohn-Sham equations can be minimized using the variational principle under the constraint of orthonormality of the single electron orbitals. In order to maintain orthonormality, the following Lagrangian expression is obtained:

$$\Omega_{KS}[\rho(\mathbf{r})] = E_{KS}[\rho(\mathbf{r})] - 2\sum_{i}^{N/2}\sum_{j}^{N/2} \varepsilon_{ij}\left(\int \Phi_i(\boldsymbol{r})\Phi_j(\boldsymbol{r})d\mathbf{r} - \delta_{ij}\right)$$

For information on Lagrangian expressions, see the Appendix at the end of this Chapter. The above Lagrangian can be minimized with respect to Φ_j using the following chain rule:

$$\frac{\delta\Omega_{KS}}{\delta\Phi_j(\boldsymbol{r})} = \frac{\delta\Omega_{KS}}{\delta\rho(\mathbf{r})}.\frac{\delta\rho(\mathbf{r})}{\delta\Phi_j(\boldsymbol{r})} = \frac{\delta\Omega_{KS}}{\delta\rho(\mathbf{r})}.2\Phi_j(\boldsymbol{r})$$

$$\frac{\delta\Omega_{KS}}{\delta\Phi_j(\boldsymbol{r})} = 2\frac{\delta T_{KS}}{\delta\Phi_j(\boldsymbol{r})} + 2\left[\frac{\delta E_H}{\delta\rho(\mathbf{r})} + \frac{\delta E_{ext}}{\delta\rho(\mathbf{r})} + \frac{\delta E_{xc}}{\delta\rho(\mathbf{r})}\right] - 2\sum_{i=1}^{N/2} \varepsilon_{ij}\Phi_j(\boldsymbol{r}) = 0$$

The derivative of E_H with respect to $\rho(\mathrm{r})$ gives the Hartree potential, V_{har}, while the derivative of E_{XC} gives the exchange correlation potential, V_{xc}.

$$V_{har} = \frac{\delta E_H}{\delta \rho(\mathbf{r})} = \int \frac{p(\boldsymbol{r}')}{|\boldsymbol{r} - \boldsymbol{r}'|} d\mathbf{r}'$$

$$V_{xc} = \frac{\delta E_{xc}}{\delta \rho(\mathbf{r})}$$

This leaves us with a set of potentials, V_{har}, V_{ext} and V_{xc}, the sum of which equals the Kohn-Sham potential, V_{KS}. The Kohn-Sham potential accounts for both interactions with external charges and inter-electronic interactions. Furthermore, the Kohn-Sham equations can be expressed as shown below, where single electron wavefunctions exist under the influence of V_{KS}.

$$\left[\frac{\hbar^2}{2m_e} \nabla_i^2 + V_{KS}\right] \psi_i = \varepsilon_i \psi_i$$

The *N* single electron wavefunctions are effectively coupled through V_{har} and V_{xc}. Given that V_{har} and V_{xc} both depend on ψ_i and vice versa, the Kohn-Sham equations are best solved using a self-consistent loop, as ilustrated in Figure 2.1.

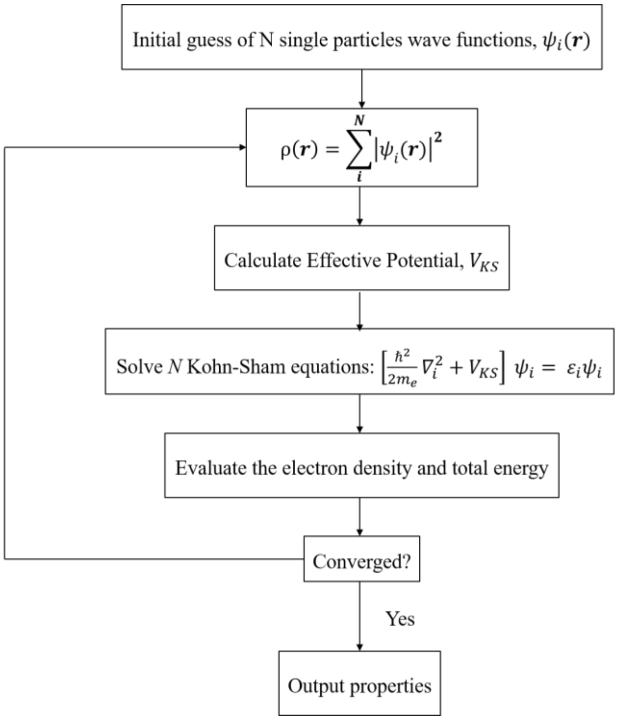

Figure 2.1: The self-consistency scheme used to solve the Kohn Sham equations

The self-consistent procedure begins with an initial guess at the system's ground state wavefunction, usually a superposition of the wavefunctions of the system's constituent atoms. The resulting charge density is used to calculate the KS potential, allowing the solution of N single particle equations. The charge density of the N single particle wavefunctions is calculated and used to define a new KS potential and a new set of N single particle wavefunctions. If the energies of the old and new set of N single particle wavefunctions are similar to within a predefined threshold, the calculation is considered to be converged and the final properties of the system are returned. If the energies of the old and new wavefunctions are not similar to within the said threshold, a new charge density is calculated and the self-consistent loop continues.

The upshot of KS-DFT is that highly demanding N electron problems are transformed into N single electron problems, greatly increasing computationally affordability. KS-DFT is used by the vast majority of DFT codes, including VASP, the code used throughout this thesis.

2.2 Implementation of Density Functional Theory

2.2.1 Functionals

The exchange correlation energy, E_{xc}, accounts for the errors induced through the neglect of many-body exchange and correlation effects. While the exact form of the functional which calculates E_{xc} is not known, a number of different approaches have been developed. [15, 16]

The local density approximation (LDA) is the simplest approach used to calculate E_{xc}. Developed by Kohn and Sham [17], the LDA assumes that $E_{xc}(\boldsymbol{r})$ is equal to the exchange correlation energy of an electron gas with a uniform density, E_{xc}^{unif}. This approximation is surprisingly accurate for systems which have a uniform electron density, e.g. metals. However, the LDA fails when $\rho(\boldsymbol{r})$ changes more rapidly.

$$E_{xc}^{LDA}[\rho(\boldsymbol{r})] = \int \rho(\boldsymbol{r}) E_{xc}^{unif} \rho(\boldsymbol{r})\, d\boldsymbol{r}$$

While the form of exchange for a uniform electron gas has been known since 1930, Monte Carlo simulations of the uniform gas have been used to parametrize correlation effects [18]. Widely used correlation functionals have been developed by Vosko and Perdew [19, 20].

$$E_x^{unif} = -\frac{4}{3}\cdot\left(\frac{3}{\pi}\right)^{1/3}\int \rho^{4/3} d\boldsymbol{r}$$

While LDA has not been used in this work, it provides a vital basis for semi-local techniques such as the generalized gradient approximation (GGA), which includes a gradient expansion describing a varying electron gas. Simple expansions in terms of the dimensionless reduced gradient, $x = \nabla\rho/\rho^{4/3}$, work well in systems where $\rho(\boldsymbol{r})$ varies slowly and consistently.

$$E_x^{GEA} = -\int \rho^{4/3}\left[\frac{4}{3}\cdot\left(\frac{3}{\pi}\right)^{1/3} + \frac{7}{432\pi(3\pi^2)^{1/3}} + \cdots\right] d\boldsymbol{r}$$

However, in chemical problems x becomes poorly defined. Towards atomic tails, $\rho(\boldsymbol{r})$ decays exponentially and $x \to \infty$, causing the approximation to break down. The solution was the development of the GGA.

$$E_x^{GGA}[p, x] = \int \rho^{4/3} F(x) d\boldsymbol{r}$$

There are many forms of $F(x)$, but the one used throughout this work was developed by Perdew, Burke and Ernzerhof (PBE) [21]:

$$E_x^{PBE} = -\int \rho^{4/3}\left[\frac{4}{3}\cdot\left(\frac{3}{\pi}\right)^{1/3} + \frac{\mu s^2}{1 + \mu s^2/\kappa}\right] d\boldsymbol{r}$$

Correlation contributions are more complex, and there are two main functionals which are used; LYP and PBE [21, 22].

Relaxing structures using local and semi-local functionals often results in very accurate geometries and relative energies. However, LDA and GGA both fail to accurately describe a number of important properties. Namely, and of particular importance to this work, they tend underestimate reaction barriers and electronic band gaps. Both issues are caused by delocalization errors [16, 23], which are the result of dominating Coulomb forces forcing electrons apart.

The way in which delocalization errors manifest in electronic gaps larger than the true band gap of a system can be understood through the consideration fractional charges. The energies of systems with fractional electrons have been calculated exactly [24], with the energy of a system with a fractional number of electrons, $E(N+\delta)$, found to be a linear interpolation between $E(N)$ and $E(N+1)$:

$$E(N+\delta) = (1-\delta)E(N) + \delta E(N+1)$$

Furthermore, the band gap of a material, the difference between the ionization energy, I, and the electron affinity, A, can also be expressed in terms of E and N.

$$E_{gap} = I - A = [E(N-1) - E(N)] - [E(N) - E(N+1)]$$

For functionals which correctly replicate the linear interpolation of fractional charges, the band gap can be accurately expressed in terms of derivatives at N.

$$E_{gap} = E_{gap}^{deriv} = \left.\frac{dE(N)}{dN}\right|_{N+\delta} - \left.\frac{dE(N)}{dN}\right|_{N-\delta}$$

The derivative of total energy with respect to N equals the chemical potential, μ, which is linear with a discontinuity at integer values of N. In KS-DFT, systems are described either by a set of orbitals and occupation numbers, $\{\Phi_i, n_i\}$, or in terms of the local potential and total number of particles, $\{v_r, N\}$. Given that when energy is minimized $dE[v_r, N]/dv_r = 0$,

$$\mu = \left(\frac{dE[v_r, N]}{dN}\right)_{v_{gs}} = \left(\frac{dE[\{\Phi_i, n_i\}]}{dn_f}\right)_{\{\Phi_i\}}$$

where only the frontier level occupation, n_f, is allowed to change with $\delta = \delta n_f$. When $\delta > 0$, $n_f = n_{LUMO}$ and when $\delta < 0$, $n_f = n_{HOMO}$. Assuming KS-DFT functionals satisfy the exact linearity condition:

$$\varepsilon_{HOMO} = -I = \left(\frac{dE[\{\Phi_i, n_i\}]}{dn_{HOMO}}\right)_{\{\Phi_i\}}$$

$$\varepsilon_{LOMO} = -A = \left(\frac{dE[\{\Phi_i, n_i\}]}{dn_{LOMO}}\right)_{\{\Phi_i\}}$$

However, studies investigating fractional charges have repeatedly shown that LDA and GGA functionals do not satisfy the exact linearity condition. Instead, erroneously convex behaviour as a function of fractional charge is observed, and can be explained through the effects of delocalization errors [25].

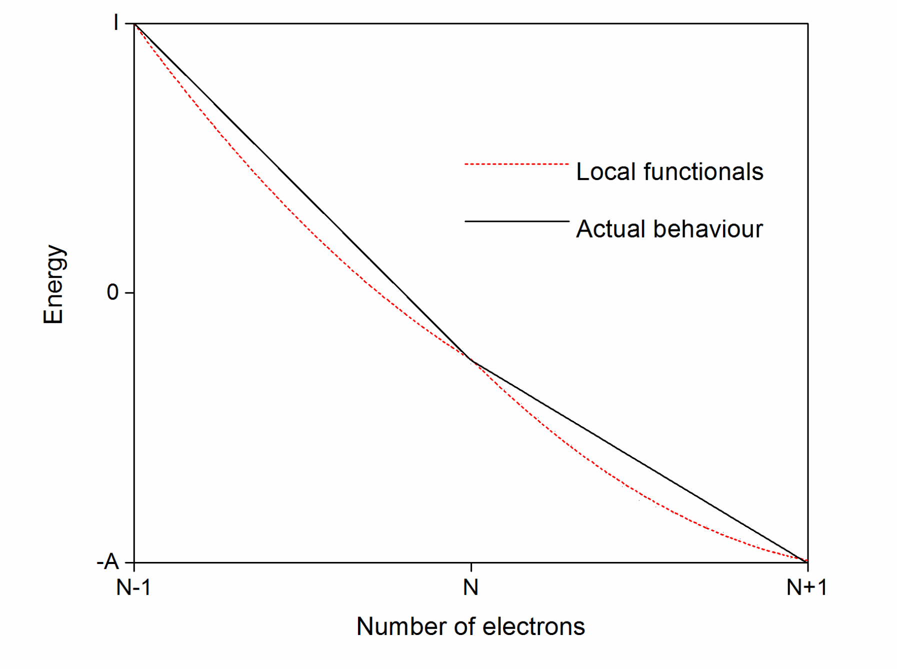

Figure 2.2. A graphical representation of the delocalization errors inherent in DFT when using local and semi-local functionals.

By inspection of Figure 2.2, it can clearly be seen that, at N:

$$\left(\frac{dE[\{\Phi_i, n_i\}]}{dn_{HOMO}}\right)_{\{\Phi_i\}} < I$$

$$\left(\frac{dE[\{\Phi_i, n_i\}]}{dn_{LOMO}}\right)_{\{\Phi_i\}} > A$$

As fractional charge (either positive or negative) is added to the system, it is erroneously delocalised, leading to an overestimation of electron affinity and an underestimation of ionization energy. The net effect of such errors is the underestimation the band gap of semiconductors.

In contrast to local density functionals, the Hartree-Fock approximation has a tendency to localise electrons. This results in electron affinity being underestimated and ionization energy being overestimated, effects which are in directly opposition to the errors experienced when using local and semi-local functionals. Localization errors can also be expressed in terms of the exact linearity condition, and when energy is plotted as a function of fractional charge, erroneously concave behaviour is observed.

Given the opposite effects of the errors induced when using standard DFT and the Hartree-Fock approximation, hybrid density functionals combine the two methods in order to achieve an accurate degree of charge localization. This rationale is formalised through the adiabatic connection, an integral which describes the exchange-correlation energy in terms of the 'turning on' of the coulomb repulsion between electrons [26].

$$E_{xc} = \int_0^1 U_{xc}^{\lambda}\, d\lambda$$

where U_{xc}^{λ} is the potential energy of exchange and correlation at intermediate coupling constant strength λ. At λ=0, U_{xc}^{λ} is the pure exchange energy with no electron correlation whatsoever, as is the case in Hartre-Fock. However, while LDA and GGA are constructed to be accurate for fully interacting systems (λ=1), the λ=0 limit is misrepresented. Therefore, a weighted sum of E_{xc} at λ=1 (GGA or LDA) and at λ=0 (Hartree-Fock exchange) is used to approximate the integral.

$$E_x = aE_{Fock} + bE_{GGA}$$

The B3LYP functional, which combines a fraction of exact exchange energy with the B88 gradient correction for exchange and the PW91 gradient coaction for correlation [26], is often used to model chemical processes.

$$E_{xc}^{B3LYP} = E_{xc}^{LSDA} + a_0(E_x^{exact} - E_x^{LSDA}) + a_x \mathit{\Delta} E_x^{B88} + a_c \mathit{\Delta} E_c^{PW91}$$

However, functionals such as B3LYP, which calculate exact exchange between each possible electron pair, are prohibitively expensive when using a plane-wave basis set (see Section 2.2.3), especially when dealing with larger systems. The modelling of bulk systems is particularly expensive due to long-range Hartree Fock interactions. Screened hybrid functionals, such as the Heyd–Scuseria–Ernzerhof screened Coulomb hybrid functional (HSE), allow more efficient calculations in bulk systems as they do not calculate long range exchange energies exactly [27]. The HSE06 functional has been found to significantly improve the band gap prediction for a wide range of solids with accuracy comparable to more expensive methods [28].

$$E_{xc}^{HSE03} = \frac{1}{4} E_x^{sr,exact} + \frac{3}{4} E_x^{sr,PBE} + E_x^{lr,PBE} + E_c^{PBE}$$

2.2.2 Calculating Forces

While the ground state electronic wavefunction can be calculated using the electronic relaxation scheme shown in Figure 2.1, the forces between individual atoms must be calculated in order to determine the ground state atomic structure. Inter atomic forces, $\boldsymbol{F}$, are defined through the following expression, where $E(\boldsymbol{R})$ is the ground state energy of the system with atomic spatial coordinates $\boldsymbol{R}$.

$$\boldsymbol{F} = -\nabla_R E(\boldsymbol{R})$$

In DFT, the Hellman-Feynman theorem can be used to calculate an expression for the force at given spatial coodinates [29].

$$\frac{\partial E}{\partial R} = \left\langle \psi \middle| \frac{\partial \hat{H}}{\partial R} \middle| \psi \right\rangle$$

Hellman-Feynman theorem is valid when the wavefunction, ψ, is an exact eigenstate of the Hamiltonian, $\hat{H}$. It is important to note that if the basis functions are dependent on atomic positions, $\boldsymbol{R}$, then Pulay forces will be included in the form of additional terms and inaccuracies when relaxing unit cell volumes. It is therefore advisable to relax the volume of unit cells using a Murnaghan fitting scheme.

2.2.3 Basis Sets

In order to be computationally solvable, single-electron wavefunctions are expanded in terms of a basis. A basis set may take a number of forms, with real space, atom-centered functions most commonly during studies of molecular systems [30]. However, using real space basis sets to study bulk materials requires the simulation of enormous systems containing a vast number of electrons. This necessity can be avoided by simulating a periodically repeating unit cell using a plane-wave basis set [31]. Bloch's theorem states that the wavefunctions of electrons in a periodic potential can be written as the product of a cell periodic function modulated by a plane wave [32].

$$\psi_{n,k} = e^{ikr} u_{n,k}$$

where the Bloch function, $u_{n,k}$, has the same periodicity as the crystal and e^{ikr} is the equation of a plane wave. As is the case with all periodic functions, $u_{n,k}$ can be expanded into a Fourier series of plane waves.

$$u_{n,k} = \sum_{G} \tilde{u}_{G,n,k} e^{iG.r}$$

where G are reciprocal lattice vectors defined through $G = \frac{2\pi m}{a_i}$, where a_i is a real space lattice vector. The electronic wavefunction can be written as a linear combination of plane waves.

$$\psi_{n,k} = \sum_{G} \tilde{u}_{G,n,k} e^{i(k+G).r}$$

While G can take an unlimited number of values corresponding to increasingly small wavelengths, high frequency components are less important due to their high kinetic energy. The series can therefore by truncated in accordance with the below condition:

$$|k + G|^2 \frac{\hbar^2}{2m_e} < E_{cut}$$

It is important that the cut-off energy is large enough so as not to compromise the accuracy of results, and therefore the properties of interest should be carefully converged with respect to E_{cut}. While imposing a cutoff energy limits the range of G at a given k-point, modelling an infinitely large periodic solid theoretically requires wavefunctions to be calculated over an infinite number of k-points. The Born von Karmen boundary conditions can be used to circumvent this issue [33].

$$\psi(\boldsymbol{r} + N_i a_i) = \psi(r)$$

where N_i is the number of lattice points considered. Therefore, wavefuncitons must satisfy the condition:

$$\psi(\boldsymbol{r} + N_i a_i) = e^{iN_i k_i . a_i}\, \psi(\boldsymbol{r})$$

The only k-points for which this is true give the exponential an argument value equal to $2n\pi$, where n is an integer.

$$k_i = \frac{2\pi n}{N_i}$$

When $N_i \rightarrow \infty$, an infinitely dense set of k-points emerges. However, given that energy is a smooth functional with respect to k and that Bloch wave solutions are only unique within the first Brillouin zone, it suffices to take a weighted average over a finite number of k-points within the first Brillouin zone provided the measured properties are converged with respect to k [34]. It is important to note that when energy changes rapidly with respect to k (e.g. in metals), a much finer sampling of k-space is required to reach convergence.

2.2.4 Pseudopotentials

The strong Coulomb potentials felt in regions closely surrounding nuclei give rise to extremely high kinetic energies. This means that a very large basis set is required in order to converge a system's properties. The basis sets required correspond to a high E_{cut} and result in prohibitively expensive calculations. However, core electrons are almost entirely independent of the surrounding environment and are not involved in the bonding or properties of the parent compound. This means that they do not have to be modelled explicitly in every calculation.

Pseudopotentials have been constructed for each atomic species in order to reduce computational cost. The use of pseudopotentials assumes that core electrons in any system have the same distribution as those in an isolated atom. Ideally, pseudopotential should precisely reproduce the effect of core electrons on those involved in bonding across a range of environments. Using pseudopotentials not only means that calculations can be converged with a smaller basis set, but also means that less eigenstates need to be calculated for any given system.

While there are several different types of pseudopotential, the work presented in this thesis uses the projector augmented wave (PAW) method [35, 36]. The PAW method uses a linear transformation to transform the fictitious pseudo-wavefunction ($\tilde{\psi}$) onto the all electron wavefunction (ψ).

$$T\tilde{\psi} = \psi$$

$$T = 1 + \sum_{R} \hat{S}_R$$

The operator T transforms the smooth pseudo-wavefunctions used in the pseudopotential onto the true, all electron wavefunction. Given that $\tilde{\psi}$ and ψ should only differ near the ion cores, T can be expressed in terms of a sum of $\hat{S}_R$ which are zero outside a spherical augmentation region Ω_R enclosing atom R.

2.3.5 The Vienna Ab initio Simulation Package

The Vienna Ab initio Simulation Package (VASP) is the code used most frequently throughout this thesis [35, 37]. Using a plane-wave basis set and periodic boundary conditions, VASP can solve the Kohn-Sham equations using standard DFT, hybrid DFT and other post-DFT techniques such as GW and RPA [38, 39]. VASP models the interaction between ionic cores and valence electrons using either ultra-soft Vanderbilt (US-PP) or PAW pseudopotentials [40][41]. While designed to be used to study bulk systems, the nature of periodic boundary conditions means that isolated systems can also be studied provided a sufficient vacuum region between images is used

VASP calculates the electronic ground state using a self-consistent loop, see Figure 2.1, with initial charge densities taken as a superposition of constituent atomic charge densities. Within each loop, wavefunctions are optimized iteratively until they closely resemble the ground state wavefunction of the Hamiltonian. The algorithms used to optimize wavefunctions are based on iterative matrix-diagonalization schemes, and include the Block Davidson scheme, the conjugate gradient scheme, or residual minimization scheme-direct inversion in the iterative subspace (RMM-DIIS) [42][43]. Old and new charge densities are mixed using efficient Broyden and Pulay mixing schemes. Once the electronic ground state is determined, geometry optimization is performed by self-consistently modifying structures until all forces fall below a predefined threshold. Forces are calculated using Hellmann-Fenyman theorem, and geometries are relaxed using either a conjugate gradient relaxation scheme or a RMM-DIIS scheme.

VASP performs well on massively parallel machines such as ARCHER, the current UK high end computing system, given that it is possible to parallelize the code over bands, plane wave coefficients and k-points.

2.3 Electronic Structure

Once the ground state wavefunctions have been determined, the electronic properties of the system can be calculated [33]. According to Bloch's theorem, the wavefunctions of a periodic solid can be written as a function of the reciprocal space coordinate, k.

$$\psi_{n,k} = e^{ikr} u_{n,k}$$

$$\hat{H}\psi_{n,k} = E\psi_{n,k}$$

The electronic band structure is a useful way of visualizing the allowed energy states of a given system. The band structure plots the energies of allowed electronic states along reciprocal space vectors running between highly symmetric points in the Brillouin zone. The energy of ψ_n varies smoothly with k, forming a band of allowed electronic states along reciprocal space vectors. The band gap of an N electron system is simply the energy difference the top of band $N/2$ and the bottom of band $N/2+1$. Furthermore, the dispersion of energy bands is also important, giving insights into the mobility of occupant charge carriers. The relationship between band dispersion and charge carrier mobility is formalized through the calculation of effective mass, which, along with scattering time, τ, can be used to estimate charge carrier mobility, μ:

$$\mu = \frac{q}{m*}\tau$$

2.3.1 Effective mass theory

The effective mass is a convenient way of describing the motion of a band of electrons subject to an external force. In Bloch theory, the electronic wavefunction is defined as a superposition of a set of plane waves, known as a wavepacket. The concept of a group velocity, $\mathbf{v}_\mathrm{g}$, can be used to calculate the effective mass. Group velocity describes the velocity at which a wave propagates through space via the following relation:

$$\mathbf{v}_\mathrm{g} = \frac{1}{\hbar}.\nabla_k E(\boldsymbol{k})$$

where $E(\boldsymbol{k})$ is a function of energy with respect to $\boldsymbol{k}$. When an external force, F_{ext}, is applied to a band electron the force will do work.

$$\delta E = F_{ext}\delta x = F_{ext}\mathbf{v}_{\mathrm{g}}\delta t$$

From the equation for group velocity, δE can also be expressed as follows:

$$\delta E = \hbar\mathbf{v}_{\mathrm{g}}\delta\boldsymbol{k}$$

Combining the above two equations, dividing through by δt and considering the limit $\delta t \to 0$:

$$F_{ext} = \hbar\frac{\delta\boldsymbol{k}}{\delta t} = \hbar\frac{d\boldsymbol{k}}{dt}$$

Given that, classically, $F_{ext} = dp/dt$, $\hbar\boldsymbol{k}$ is known as the crystal momentum. This result relates the rate of change in $\boldsymbol{k}$ to the external force acting on an electron, and provides the basis for effective mass theory. The rate of change of velocity with time is:

$$a = \frac{d\mathbf{v}_{\mathrm{g}}}{dt} = \frac{1}{\hbar}.\frac{d^2E}{d\boldsymbol{k}dt} = \frac{1}{\hbar}.\frac{d^2E}{d\boldsymbol{k}^2}.\frac{d\boldsymbol{k}}{dt}$$

Combining with the expression for F_{ext} gives:

$$F_{ext} = \frac{d\mathbf{v}_{\mathrm{g}}}{dt}.\hbar^2.\left(\frac{d^2E}{d\boldsymbol{k}^2}\right)^{-1}$$

Given that classically $F = ma$, we can define the ‘effective mass’ as:

$$m^* = \hbar^2.\left(\frac{d^2E}{d\boldsymbol{k}^2}\right)^{-1}$$

2.3.2 Scattering and the deformation potential approximation

When under an electric field, charge carriers are ballistically accelerated according their effective mass until an external event leads to a change in direction or energy. These external events are known as scattering, and are most commonly the result of ionized impurities or coupling with phonons. The scattering rate, $P_{i,k}$, for the electronic state (i,k) can be described by Fermi's golden rule [44]:

$$P_{i,k} = \frac{2\pi}{h}\sum_{j,k}|M(ik,jk)|^2\,\delta[\varepsilon_i(k) - \varepsilon_i(k')]$$

where the matrix element $M(ik,jk) = \langle j,k|\Delta V|i,k\rangle$, which describes scattering from state (i,k) to state (j,k') by a perturbation of the periodic potential, ΔV. Such perturbations can arise as a result of atomic displacements associated with a phonon, or due to the presence of a charged defect or impurity. The scattering time, τ, is defined as being $1/P_{i,k}$. Throughout this thesis, we assume a defect free structure and consider scattering as a result of electron-phonon coupling only.

The deformation potential approximation (DPA) was proposed by Bardeen and Shockley in the 1950s to describe charge transport in non-polar semiconductors [45], and has since been adapted for use in low-dimensional materials [46]. The DPA is based around a comparison of the wavelength of charge carriers and the wavelength of typical lattice phonons. The wavelength of charge carriers with energy k_bT can be calculated using the de Broglie relation, $\lambda = \hbar/mv$. At room temperature, λ = 7 nm, much larger than a typical lattice constant. Therefore, the DPA assumes that charge carriers are scattered only by acoustic phonons, and do not couple to higher frequency optical phonons.

The DPA also assumes that perturbations to the lattice potential as a result of acoustic phonons, $\Delta V(\boldsymbol{r})$, are linearly dependent on the accompanying volume change, $\Delta(\boldsymbol{r})$, through the relation:

$$\Delta V(\boldsymbol{r}) = E_1\Delta(\boldsymbol{r})$$

where E_1 is the deformation potential constant.

The displacement associated with the acoustic phonon with wavevector $\boldsymbol{q}$ is**:**

$$u(\boldsymbol{r}) = \frac{1}{\sqrt{N}}\boldsymbol{e_q}\left[a_{\boldsymbol{q}}e^{i\boldsymbol{qr}} + a_q^* e^{-i\boldsymbol{qr}}\right]$$

where N is the number of lattice sites per unit volume, and $\boldsymbol{e_q}$ and $a_{\boldsymbol{q}}$ are the unit vector and amplitude of the phonon $\boldsymbol{q}$ respectively. Furthermore, the relative volume change, $\Delta(\boldsymbol{r})$ can be expressed in terms of the displacement function $u(\boldsymbol{r})$:

$$\Delta(\boldsymbol{r}) = \frac{du(\boldsymbol{r})}{d\boldsymbol{r}} = \frac{i}{\sqrt{N}}\boldsymbol{q}.\boldsymbol{e}_q\left[a_{\boldsymbol{q}}e^{i\boldsymbol{qr}} - a_q^* e^{-i\boldsymbol{qr}}\right]$$

Only longitudinal acoustic (LA) phonons contribute to the deformation $\Delta(\boldsymbol{r})$. The matrix lattice element for electrons to be scattered from Bloch state $|i,k\rangle$ to $|i,k'\rangle$ can be calculated using the formula:

$$|M(ik,ik')|^2 = |\langle ik|\Delta V|ik'\rangle|^2 = \frac{1}{N}{E_1}^2 q^2 {a_q}^2$$

where $q = \pm(k - k')$. When the lattice is fully excited, the amplitude of the phonon wave is given by $a^2 = k_B T/2mq^2{v_a}^2$, where m is the total mass of the unit cell and v_a is the velocity of the phonon. It follows that the average scattering probability and relaxation time are:

$$\langle|M(ik,ik')|^2\rangle = \frac{k_B T{E_1}^2}{Nm{v_a}^2} = \frac{k_B T{E_1}^2}{C_\beta}$$

$$\frac{1}{\tau} = \frac{2\pi k_B T{E_1}^2}{\hbar C_\beta}\sum_{k'}\delta[\varepsilon_i(k) - \varepsilon_i(k')]\left[1 - \frac{v_\beta(i,k')}{v_\beta(i,k)}\right]$$

where $C_\beta = Nm{v_a}^2$, the elastic constant for the longitudinal strain in the direction of propagation of the LA wave. Meanwhile, $\left[1 - \frac{v_\beta(i,k')}{v_\beta(i,k)}\right]$ describes the scattering angle weighting factor, which, assuming parabolic bands can be replaced with $(1 - \cos(\theta))$. The expression can be further simplified using the effective mass approximation. Given that band edge energies can be written in terms of the band edge energy and the effective mass, m^*.

$$\varepsilon(k) - \varepsilon_0 = \frac{\hbar^2 k^2}{2m^*}$$

In the 2D systems that are studied extensively throughout this thesis, the expression for scattering time derived using the DPA is as follows:

$$\tau_i = \frac{\hbar^3 C_{2D,i}}{k_B T m_d E_{1,i}^2}$$

where m_d is the equivalent density-of-state mass, $m_d = \sqrt{m_x m_y}$.

2.4 Stability and Reactivity

Using DFT to solve the Schrodinger equation gives information about the electronic ground state properties of a material. However, given that time-independent DFT only directly calculates electronic energies, relative stabilities are valid at 0 K only. At non-zero temperatures, the assessment of a compound's stability requires the calculation of its Gibbs free energy. The Gibbs free energy includes electronic, vibrational, rotational and translational energy and entropy and can be calculated using statistical mechanics, as described in Section 2.4.1.

Meanwhile, the assessment of a compound's reactivity requires knowledge of the energy barrier between reactant and product states. The basic concepts of transition state theory (TST) and the implementation of TST in VASP will be discussed in Section 2.4.2.

2.4.1 Statistical Mechanics

While VASP and most other DFT codes only calculate electronic energies, ΔE_{elec}, other contributions to ΔG_{sys} can be calculated using statistical mechanics. The starting point for this process is to calculate the relevant partition function, q. The partition function is also the normalization constant in the Boltzmann distribution:

$$p_i = \frac{e^{-\varepsilon_i / k_B T}}{q}$$

$$q = \sum_j e^{-\varepsilon_j/k_B T}$$

where ε_i is the energy of microstate i and p_i is the probability of the system being in microstate i. The partition function can be used to calculate all macroscopic properties of the system, including energy and entropy. For example, the average energy is:

$$\langle E\rangle = \sum_i \varepsilon_i p_i = \frac{\sum_i \varepsilon_i e^{-\varepsilon_i/k_B T}}{\sum_j e^{-\varepsilon_j/k_B T}}$$

$$= k_B T^2 \left(\frac{\partial \ln(q)}{\partial T}\right)_V$$

However, calculating entropy from the partition function is less trivial. First, one must determine the number of ways of arranging microstates within the ensemble. Overall, the ensemble has v copies and v_i copies in the i^{th} microstate, so the number of ways of arranging these, Ω_v is:

$$\Omega_v = \frac{v!}{v_1!\, v_2!\, v_3! \ldots}$$

Using Stirling's approximation, $\ln(x!) = xln(x) - x$:

$$ln(\Omega_v) = vln(v) - v - \sum\nolimits_i (v_i \ln(v_i) - v_i)$$

$$= -\sum\nolimits_i v_i(\ln(v) - \ln(v_i))$$

$$= -\sum\nolimits_i (v_i \ln(v_i/v))$$

$$= -v \sum\nolimits_i p_i \ln(p_i)$$

Therefore, the ensemble entropy is $S_v = -k_B \sum_i \Omega_v$, and thus the system entropy is:

$$\langle S\rangle = -k_B \sum_i p_i \ln(p_i)$$

For systems at a constant temperature:

$$\langle S \rangle = -k_B \sum_i p_i(-\,\varepsilon_i k_B T - \ln(q))$$

$$= -k_B(\langle E \rangle k_B T + \ln(q))$$

$$= \frac{\langle E \rangle}{T} + k_B \ln(q)$$

Apart from ΔE_{elec} which is calculated using DFT, the above equations for energy and entropy can be used to calculate vibrational, rotational, translational and electronic energies and entropies. The specific equations can be found in Table 1.1, and while their derivations are not shown here they can be found in a number of standard texts [1-5]. All terms for energy and entropy can be derived simply by substituting the appropriate partition function, q_x, into the equations derived above, with energy equal to $k_B T^2 \left(\frac{\partial \ln(q)}{\partial T}\right)_V$ and entropy equal to $\frac{\langle E \rangle}{T} + k_B \ln(q)$. Among the non-standard terms, $\theta_{r,x}$, used in the calculation of the rotational partition function, q_r, is equal to $\frac{h^2}{8\pi^2 I k_B}$, where I is the moment of intertial about the x-axis and σ_r is the rotational symmetry factor. Meanwhile, $\Theta_{v,K}$ is the vibrational temperature of vibrational mode K, and is used in the calculation of the vibrational partition function, q_v. Finally, w_i, used in the calculation of the electronic partition function, q_e , is simply the degeneracy of electronic state i.

	Energy, E_x	**Entropy, S_x**	**Partition function, q_x**
Translational, t	$\frac{3}{2} k_b T$	$R\, ln\left(q_t + \frac{5}{2}\right)$	$\left(\frac{2\pi m k_b T}{h^2}\right)^{3/2} \frac{k_b T}{P}$
Rotational, r	$k_b T$	$R\, ln(q_r + 3/2)$	$\frac{\pi^{1/2}}{\sigma_r}\left(\frac{T^{3/2}}{(\theta_{r,x}\theta_{r,y}\theta_{r,z})}\right)$
Electronic, e	E_e	$R\left(ln(q_e) + T\left(\frac{\mathrm{d}\, ln(q_e)}{\mathrm{d}T}\right)_V\right)$	$\sum_i w_i e^{-\varepsilon_0/k_B T}$
Vibrational, v	$R\sum_K \Theta_{v,K}\left(\frac{1}{2} + \frac{1}{e^{\Theta_{v,K}/T} - 1}\right)$	$R\sum_K\left(\frac{\Theta_{v,K}/T}{e^{\Theta_{v,K}/T} - 1} - ln(1 - e^{\Theta_{v,K}/T})\right)$	$\prod_K \frac{1}{1 - e^{\Theta_{v,K}/T}}$

Table 2.1: The equations used to calculate the total internal energy and entropy of a system.

2.4.2 Transition State Theory

The rate at which a reaction proceeds can be estimated using the Eyring equation [47], which assumes that all reactions proceed via the transition state, $R^{\#}$, the highest energy state encountered during the transition between reactants and products. The rate at which the product, P, is formed depends on the concentration of $R^{\#}$ and the rate at which $R^{\#}$ is turned into P.

$$\frac{\mathrm{d}[P]}{dt} = k[R^{\#}]$$

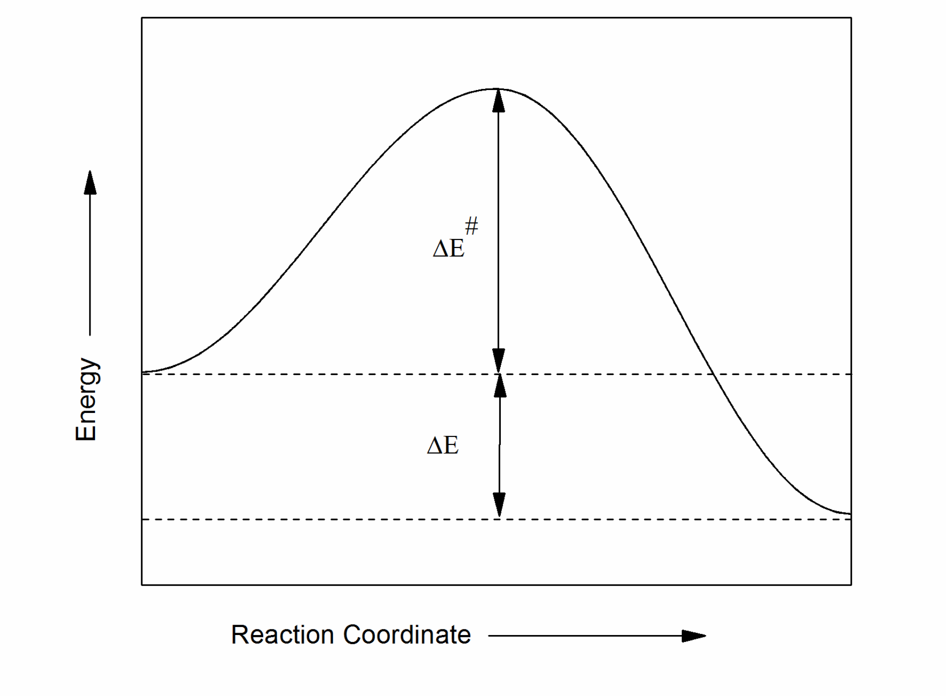

Figure 2.3: A graphical representation of the energy profile of a chemical reaction.

If we assume that a pre-equilibrium between R and $R^{\#}$ is established, where $K^{\#} = [R^{\#}]/[R]$, we can write the rate equation in terms of [R].

$$\frac{\mathrm{d}[P]}{dt} = k[R] = k.K^{\#}[R]$$

Furthermore, $K^{\#} = \frac{q'^{\#}}{q} = e^{-\Delta G_0^{\#}/RT}$, where $q^{\#}$ and q are the partition functons of $R^{\#}$ and R respectively and $\Delta G_0^{\#}$ is the difference in Gibbs free energy between $R^{\#}$ and R.

$$\frac{\mathrm{d}[P]}{dt} = k.e^{-\Delta G_0^{\#}/_{RT}}[R]$$

The rate at which $R^{\#}$ is converted into P and thus k can be estimated by assuming that the reaction coordinate is representative of a vibrational mode, and that the reaction is attempted with a frequency equal to that of the vibration. As the vibrational mode representing the reaction coordinate is extremely low in energy in the transition state complex, the partition function of this mode can be approximated as $\frac{k_B T}{h}$.

$$\frac{\mathrm{d}[P]}{dt} = \frac{k_B T}{h} e^{-\Delta G_0^{\#}/_{RT}}[R]$$

In order to identify the transition state, VASP uses the nudged elastic band (NEB) method [48]. The NEB method finds the minimum energy path (MEP) by relaxing a set of images, derived by a linear interpolation between reactant and product structures, under the constraint of spring forces between successive images.

The original elastic band (EB) method suffers from two critical problems. When the spring constant between images is low, the true potential force parallel to the MEP means that the distance between images becomes high around the saddle point, resulting in a problematically low image resolution. However, when higher spring constants are used, the spring force component perpendicular to the path pulls the images away from the true MEP. This effect is known as ‘corner cutting’, and results in the EB method missing the MEP. It is not possible to avoid both problems at once, and therefore the NEB method was developed.

In the NEB method, the perpendicular component of the spring force and the parallel component of the true force are projected out. In NEB, the total force on each image is the sum of the true potential force perpendicular to the local tangent and the spring force parallel to the local tangent. Once the spring forces are minimized, the mimicked elastic band is the true MEP. Furthermore, the climbing image modification drives the highest energy image up to the saddle point. Climbing image nudged elastic band (CI-NEB) takes the highest energy image and removes the spring force and inverts the true potential force along the path, thus relaxing the image to its local maxima [49].

2.5.3 Heitler-London model

The Heitler-London model expresses the energy of bonding and antibonding states in H_2 according to the following equations:

$$E_{bonding} = 2E_0 + \frac{e^2}{R} + \frac{K+H}{1+S^2}$$

$$E_{antibonding} = 2E_0 + \frac{e^2}{R} + \frac{K-H}{1-S^2}$$

where E_0 is the atomic energy, K is the sum of classical electron-electron and electron-ion Coulomb energies, S is the overlap between atomic orbitals and H is the exchange integral term. The magnitude of S must be smaller than 1, with the square of S is even smaller. Furthermore, in general, the magnitude of the coulomb energy is small, with changes in H dominating trends in energy.

$$H = \int\int \psi_a^*(r_1)\psi_b^*(r_2)\left(\frac{1}{r_{12}} - \frac{1}{r_{2a}} - \frac{1}{r_{1b}}\right) \times \psi_b(r_1)\psi_a(r_2)dr_1dr_2$$

where non-classical electron-electron ($\frac{1}{r_{12}}$) contributions are positive and electron-ion interactions ($-\frac{1}{r_{12}}$ and $-\frac{1}{r_{12}}$) are negative. In all non-localized cases, the electron-ion contributions dominate over electron-electron contributions. As the bond length shortens, H decreases and vice versa. Although developed for H_2 specifically, the implications of the the Heitler-London hold true for more complex bonding arrangements; bond shortening through the application of compressive strain stabilises $E_{bonding}$ and destabilises $E_{antibonding}$, whereas bond lengthening through the application of tensile strain destabilises $E_{bonding}$ and stabilises $E_{antibonding}$. These effects are relevant to work in Chapters 5 and 6.

2.5 Appendix: Lagrange Multipliers

It is often necessary to find the extrema of a function or functional under particular constraints. This can be achieved by using Lagrange multipliers. For example, to find the minimum of a function $f(x, y)$ under the condition $g(x, y) = 0$.

$$f(x, y) = x + 2y$$

$$g(x, y) = x^2 + y^2 - 1$$

A new function can be written which consists of the old ln. function plus the function which is subject to numerical constrains multiplied by a number called a Lagrange multiplier.

$$h(x, y) = f(x, y) + \lambda g(x, y)$$

To find the extrema of our new function with respect to either x or y, simple derivatives can be taken.

$$\frac{\partial h}{\partial x} = 1 + 2\lambda\, x = 0$$

$$\frac{\partial h}{\partial y} = 1 + 2\lambda\, y = 0$$

Along with the constraint $g(x, y) = 0$, this gives us three equations and three unknowns, x, y and λ, and thus can solve the minimization problem. Furthermore, functionals can be minimized in an analogous way.

References

1. Kittel, C., *Introduction to Solid State Physics*. 2004: Wiley.

2. Ashcroft, N.W. and N.D. Mermin, *Solid state physics*. 1976: Saunders College.

3. Parr, R.G., *Density-Functional Theory of Atoms and Molecules*. 1989: Oxford University Press, USA.

4. Sabin, J.R., et al., *Advances in Density Functional Theory*. 1998: Elsevier Science.

5. Perdew, J.P. and K. Schmidt, *Jacob's ladder of density functional approximations for the exchange-correlation energy*. Density Functional Theory and Its Application to Materials, 2001. **577**: p. 1-20.

6. Fock, V., *Approximation method for the solution of the quantum mechanical multibody problems.* Zeitschrift Fur Physik, 1930. **61**(1-2): p. 126-148.

7. Slater, J.C., *A Simplification of the Hartree-Fock Method.* Physical Review, 1951. **81**(3): p. 385-390.

8. Echenique, P. and J.L. Alonso, *A mathematical and computational review of Hartree–Fock SCF methods in quantum chemistry*. Molecular Physics, 2007. **105**(23-24): p. 3057-3098.

9. Magnasco, V., *Elementary Methods of Molecular Quantum Mechanics*. 2006: Elsevier Science.

10. Thomas, L.H., *The calculation of atomic fields.* Proceedings of the Cambridge Philosophical Society, 1927. **23**: p. 542-548.

11. Fermi, E., *A statistical Method for Determining some Properties of the Atoms and its Application to the Theory of the periodic Table of Elements.* Zeitschrift Fur Physik, 1928. **48**(1-2): p. 73-79.

12. Stich, W., et al., *Accurate Solution of the Thomas-Fermi-Dirac-Weizsacker Variational Equations for the Case of Neutral Atoms and Positive-Ions.* Zeitschrift Fur Physik a-Hadrons and Nuclei, 1982. **309**(1): p. 5-11.

13. Hohenberg, P. and W. Kohn, *Inhomogeneous Electron Gas.* Physical Review B, 1964. **136**(3B): p. B864.

14. Kohn, W. and L.J. Sham, *Self-Consistent Equations Including Exchange and Correlation Effects.* Physical Review, 1965. **140**(4A): p. 1133.

15. Perdew, J.P., *Climbing the ladder of density functional approximations.* Mrs Bulletin, 2013. **38**(9): p. 743-750.

16. Cohen, A.J., P. Mori-Sanchez, and W.T. Yang, *Challenges for Density Functional Theory.* Chemical Reviews, 2012. **112**(1): p. 289-320.

17. Dirac, P.A.M., *Note on exchange phenomena in the Thomas atom.* Proceedings of the Cambridge Philosophical Society, 1930. **26**: p. 376-385.

18. Ceperley, D.M. and B.J. Alder, *Ground-State of the Electron-Gas by a Stochastic Method.* Physical Review Letters, 1980. **45**(7): p. 566-569.

19. Vosko, S.H., L. Wilk, and M. Nusair, *Accurate Spin-Dependent Electron Liquid Correlation Energies for Local Spin-Density Calculations - a Critical Analysis.* Canadian Journal of Physics, 1980. **58**(8): p. 1200-1211.

20. Perdew, J.P. and Y. Wang, *Accurate and Simple Analytic Representation of the Electron-Gas Correlation-Energy.* Physical Review B, 1992. **45**(23): p. 13244-13249.

21. Perdew, J.P., K. Burke, and M. Ernzerhof, *Generalized Gradient Approximation Made Simple.* Physical Review Letters, 1996. **77**(18): p. 3865-3868.

22. Lee, C.T., W.T. Yang, and R.G. Parr, *Development of the Colle-Salvetti Correlation-Energy Formula into a Functional of the Electron-Density.* Physical Review B, 1988. **37**(2): p. 785-789.

23. Cohen, A.J., P. Mori-Sanchez, and W.T. Yang, *Insights into current limitations of density functional theory.* Science, 2008. **321**(5890): p. 792-794.

24. Perdew, J.P., et al., *Density-Functional Theory for Fractional Particle Number - Derivative Discontinuities of the Energy.* Physical Review Letters, 1982. **49**(23): p. 1691-1694.

25. Mori-Sanchez, P., A.J. Cohen, and W.T. Yang, *Localization and delocalization errors in density functional theory and implications for band-gap prediction.* Physical Review Letters, 2008. **100**(14).

26. Becke, A.D., *Density-Functional Thermochemistry .3. The Role of Exact Exchange.* Journal of Chemical Physics, 1993. **98**(7): p. 5648-5652.

27. Heyd, J. and G.E. Scuseria, *Efficient hybrid density functional calculations in solids: Assessment of the Heyd-Scuseria-Ernzerhof screened Coulomb hybrid functional.* Journal of Chemical Physics, 2004. **121**(3): p. 1187-1192.

28. Janesko, B.G., T.M. Henderson, and G.E. Scuseria, *Screened hybrid density functionals for solid-state chemistry and physics.* Physical Chemistry Chemical Physics, 2009. **11**(3): p. 443-454.

29. Feynman, R.P., *Forces in molecules.* Physical Review, 1939. **56**(4): p. 340-343.

30. Davidson, E.R. and D. Feller, *Basis Set Selection for Molecular Calculations.* Chemical Reviews, 1986. **86**(4): p. 681-696.

31. Kresse, G. and J. Furthmuller, *Efficient iterative schemes for ab initio total-energy calculations using a plane-wave basis set.* Physical Review B, 1996. **54**(16): p. 11169-11186.

32. Bloch, F., *Über die Quantenmechanik der Elektronen in Kristallgittern.* Zeitschrift für Physik, 1929. **52**(7-8): p. 555-600.

33. Singleton, J., *Band Theory and Electronic Properties of Solids*. 2001: OUP Oxford.

34. Monkhorst, H.J. and J.D. Pack, *Special points for Brillouin-zone integrations.* Physical Review B, 1976. **13**(12): p. 5188-5192.

35. Blochl, P.E., *Projector Augmented-Wave Method.* Physical Review B, 1994. **50**(24): p. 17953-17979.

36. Blochl, P.E., *The projector augmented wave (PAW) method: Basics and applications.* Abstracts of Papers of the American Chemical Society, 1999. **217**: p. U690-U690.

37. Kresse, G. and J. Furthmuller, *Efficiency of ab-initio total energy calculations for metals and semiconductors using a plane-wave basis set.* Computational Materials Science, 1996. **6**(1): p. 15-50.

38. Aulbur, W.G., L. Jonsson, and J.W. Wilkins, *Quasiparticle calculations in solids.* Solid State Physics: Advances in Research and Applications, Vol. 54, 2000. **54**: p. 1-218.

39. Ren, X., et al., *Random-phase approximation and its applications in computational chemistry and materials science.* Journal of Materials Science, 2012. **47**(21): p. 7447-7471.

40. Vanderbilt, D., *Soft Self-Consistent Pseudopotentials in a Generalized Eigenvalue Formalism.* Physical Review B, 1990. **41**(11): p. 7892-7895.

41. Tackett, A.R., N.A.W. Holzwarth, and G.E. Matthews, *A Projector Augmented Wave (PAW) code for electronic structure calculations, Part II: pwpaw for periodic solids in a plane wave basis.* Computer Physics Communications, 2001. **135**(3): p. 348-376.

42. Press, W.H., *Numerical Recipes 3rd Edition: The Art of Scientific Computing*. 2007: Cambridge University Press.

43. Pulay, P., *Convergence Acceleration of Iterative Sequences - the Case of Scf Iteration.* Chemical Physics Letters, 1980. **73**(2): p. 393-398.

44. Dirac, P.A.M., *The quantum theory of the emission and absorption of radiation.* Proceedings of the Royal Society of London Series a-Containing Papers of a Mathematical and Physical Character, 1927. **114**(767): p. 243-265.

45. Bardeen, J. and W. Shockley, *Deformation Potentials and Mobilities in Non-Polar Crystals.* Physical Review, 1950. **80**(1): p. 72-80.

46. Xi, J., et al., *First-principles prediction of charge mobility in carbon and organic nanomaterials.* Nanoscale, 2012. **4**(15): p. 4348-69.

47. Eyring, H., *The activated complex in chemical reactions.* Journal of Chemical Physics, 1935. **3**(2): p. 107-115.

48. Henkelman, G., G. Jóhannesson, and H. Jónsson, *Methods for Finding Saddle Points and Minimum Energy Paths*, in *Theoretical Methods in Condensed Phase Chemistry*, S. Schwartz, Editor. 2002, Springer Netherlands. p. 269-302.

49. Henkelman, G., B.P. Uberuaga, and H. Jonsson, *A climbing image nudged elastic band method for finding saddle points and minimum energy paths.* Journal of Chemical Physics, 2000. **113**(22): p. 9901-9904.

Chapter 3

Hydrogen adsorption by Ti_8C_{12}

3.1 Background

In this chapter, we investigate the reversible hydrogenation of titanium metallocarbohedrene, Ti_8C_{12}. We show that when all contributions to the Gibbs free energy are considered, Ti_8C_{12} can reversibly dissociate H_2 with fast kinetics over a modest range of conditions to form a variety of products. While our results suggest that the ultimate H_2 storage capacity of Ti_8C_{12} is lower than previously reported, its ability to reversibly dissociate H_2 with a low kinetic barrier suggests its potential use as a catalyst to regenerate depleted HSMs.

As discussed in Chapter 1, it is important to find materials that are able to reversibly store H_2. However, high capacity HSMs usually chemisorb hydrogen, meaning that their regeneration is often prohibitively slow given the high activation energy needed to dissociate H_2. Materials which dissociate H_2 with a low activation barrier are therefore potentially useful for the catalytic regeneration of high capacity HSMs. However, potential catalysts must bind hydrogen less strongly than the HSM itself, implying that they must reversibly dissociate hydrogen over a range of practical operating conditions.

In the search for a catalyst fitting this profile, Maj and Grochala investigated the hydrogenation of cubane like $M_4Nm_4H_8$ (M=V,Ti, Zr, Hf, Nm= Si, C, B, N) nanoparticles [1]. They found that their properties can be tailored to have low activation energies and Gibbs free adsorption energies close to zero. However, experimental studies have shown that clusters with an M_4Nm_4 stoichiometry are unstable [2]. It is for this reason that we have investigated the closely related Ti_8C_{12} metal-carbon cluster. M_8C_{12} (M = Ti, V) clusters have been experimentally and theoretically shown to be exceptionally stable following the synthesis of Ti_8C_{12} in 1992 [3-10]. Both ionic and neutral forms of M_8C_{12} can be synthesized through plasma reactions between metals and small hydrocarbon molecules including methane, ethane, ethane and propane using laser vaporization techniques. The ground state of Ti_8C_{12} is thought to resemble a distorted tetrahedron [11-14].

Previous Density Functional studies have suggested that Ti_8C_{12} has the potential to be used as a hydrogen storage material (HSM), with reported hydrogen storage capacities ranging between 2.5 and 15 wt%. Akman *et al*. reported a storage capacity of 5.8% in 2006 based around the physisorbtion of 16 × H_2 molecules, each bound to a titanium atom with an average electronic binding energy of 0.28 eV [15]. However, not only did this study neglect important entropic effects, but its calculations used a GGA exchange-correlation functional known to overestimate charge transfer binding energies. More recently, Banerjee *et al*. used ab-initio molecular dynamics to show that at 0 K Ti_8C_{12} adsorbs 15.06 wt% of H_2, with a 10.06 wt% reversible storage capacity [16]. However, at higher temperatures storage capacities were lower, less than 3 wt%, and furthermore an inaccurate GGA exchange-correlation functional was used to model H_2 physisorption.

Most relevant to our work is a study by Zhou *et al* which reports that H_2 is dissociated by Ti_8C_{12} with a very low electronic activation energy of around 0.2 eV relative to the physisorbed state [17]. However, this study also used a GGA exchange-correlation functional, which, as well as having a tendency to overestimate charge transfer binding energies, are also known to significantly underestimate activation barriers. Furthermore, Zhou *et al.* also described the behaviour of Ti_8C_{12} + H_2 at zero temperature only, neglecting translational, rotational and vibrational energy and entropy. Regardless of the issues cited, the low energy dissociation of H_2 reported is still potentially important, and therefore we have carried out a more extensive investigation into the hydrogenation of Ti_8C_{12}.

3.2 Methodology

Density functional calculations were performed using the VASP code. We used a plane-wave basis set truncated at 400 eV and PAW pseudopotentials to treat core electrons. More information about plane-wave DFT and pseudopotentials can be found in Section 2.2. Exchange and correlation contributions to the electronic energy, E_{xc}, are accounted for using the B3LYP hybrid functional. Hybrid exchange-correlation functionals such as B3LYP generally provide more accurate activation barriers than local and semi-local functionals, see Section 2.2.1. Meanwhile, we found that additional inclusion of van der Waals corrections made little difference to either physisorption or chemisorption energies, with differences in H_2 binding energies less than 3 meV. We used a conjugate gradient algorithm to relax structures until all interatomic forces fell below 0 .01 eV/Å, with $Ti_8C_{12}H_x$ relaxed within a 25 × 25 × 25 $Å^3$ box. This provided a large separation between images of Ti_8C_{12} to ensure that the interaction between neighbouring images remained negligible. Furthermore, the Brillouin zone was sampled at the Γ point only.

Full entropic, translational, vibrational and rotational contributions to the Gibbs free energy were calculated using equations derived using statistical mechanics, see Section 2.4.1. The required vibrational analyses were performed by calculating the Hessian matrix, which includes the second derivatives of energy with respect to atomic positions. To ensure that atomic displacements fell within the harmonic region, we used a small ionic displacement of 0.015Å.To calculate activation barriers, we used NEB, see Section 2.4.2. When performing NEB calculations, the forces between consecutive images were minimized to less than 0.01 eV/Å. The climbing image method was used to ensure that the true activation energy was found.

3.3 Ground state Ti_8C_{12}

Previous studies have consistently reported that Ti_8C_{12} has approximate T_d symmetry, and therefore we used a T_d structure as a starting point for our investigations. The T_d form of Ti_8C_{12}, shown in Figure 3.1, is based around a pair of interlocking tetrahedra with titanium atoms positioned at each vertex. The tetrahedra are arranged so that the titanium atoms at the vertices of the smaller tetrahedron cap the faces of the larger tetrahedron. Throughout this study, we refer to titanium atoms at the vertices of the larger tetrahedron as Ti_α and titanium atoms at the vertices of the smaller tetrahedron as Ti_β. Six C_2 units run parallel to the edges of the large tetrahedron, with Ti_α and Ti_β coordinated to three and six carbon atoms respectively.

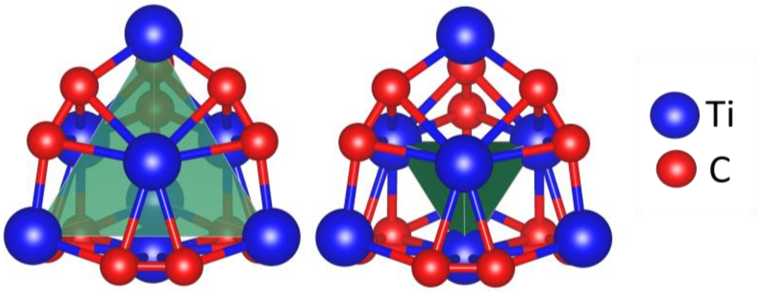

Figure 3.1: Two representations of T_d Ti_8C_{12}, with highlighting the tetrahedron with Ti_α (left) at its vertices and highlighting the tetrahedron with Ti_β at its vertices (right)

When relaxed under the constraints of T_d symmetry, Ti_8C_{12} has a degenerate electronic $^3T_2$ ground state. Jahn-Teller theorem says that structures with a degenerate electronic state are unstable with respect to structural distortions. Indeed, in the absence of symmetry constraints ground state Ti_8C_{12} is stabilised by 0.12eV with respect to the T_d isomer. Upon inspection, ground state Ti_8C_{12} is distorted with respect to the T_d isomer through a compression along one of four C_3 symmetry axes, resulting in a structure with approximate C_{3v} symmetry. We found that this distortion lifts the degeneracy of the T_2 valence orbital and results in the emergence of a ^3E frontier orbital. Meanwhile, elongating along the same C_3 axis also stabilises the structure with respect to the T_d isomer, lifting the degeneracy of the T_2 valence orbital through the emergence of a ^1A electronic ground state.

	Term Symbol	Relative Energy
T_d	$^3T_2$	0.00 eV
C_{3v}	$^1A_1$	-0.05eV
C_{3v}	^3E	-0.12 eV

Table 3.1: The relative energy and electronic term symbols of structural isomers of Ti_8C_{12}.

We note that the average carbon-carbon bond length of 1.32Å is comparable to that of a typical carbon-carbon double bond. Carbon - α-titanium distances, meanwhile, are only marginally elongated with respect to bulk titanium carbide, with carbon - β-titanium distances elongated by a further 10%.

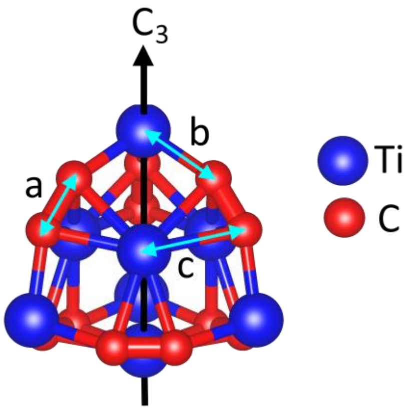

Figure 3.2: The structure of C_{3v} Ti_8C_{12} with the C_3 symmetry axis and key bond lengths labelled: (a) C-C, (b) Ti_α and (c) $Ti_{\beta.}$

The decomposed density of states (DoS), see Figure 3.3, shows that both the highest occupied molecular orbital (HOMO) and the lowest unoccupied molecular orbital (LUMO) predominantly consist of titanium orbital character. The fact that titanium orbitals dominate both HOMO and LUMO states suggests the favourable formation of dihydrogen complexes centred around titanium. In dihydrogen complexes, H_2 acts simultaneously as a σ-donor and a σ-acceptor, meaning that it is favourable to have a high energy HOMO and a low energy LUMO based around the same species. The electronic structure of Ti_8C_{12} fits this criteria well given that the HOMO – LUMO gap is very small.

The DoS also reveals that the lowest energy occupied states predominantly consist of carbon orbital character, whereas there is more titanium orbital character in unoccupied states. The unequal distribution of occupied and unoccupied states manifests in an unequal charge distribution between titanium and carbon species. Bader charge analysis confirms this, with carbon atoms carrying, on average, a -0.87 *e* charge, Ti_β atoms carrying a +1.37 *e* charge and Ti_β atoms carrying a +1.24 *e* charge. Such heterogeneous charge distribution between titanium and carbon species suggests a suitability for heterolyitc splitting of H_2.

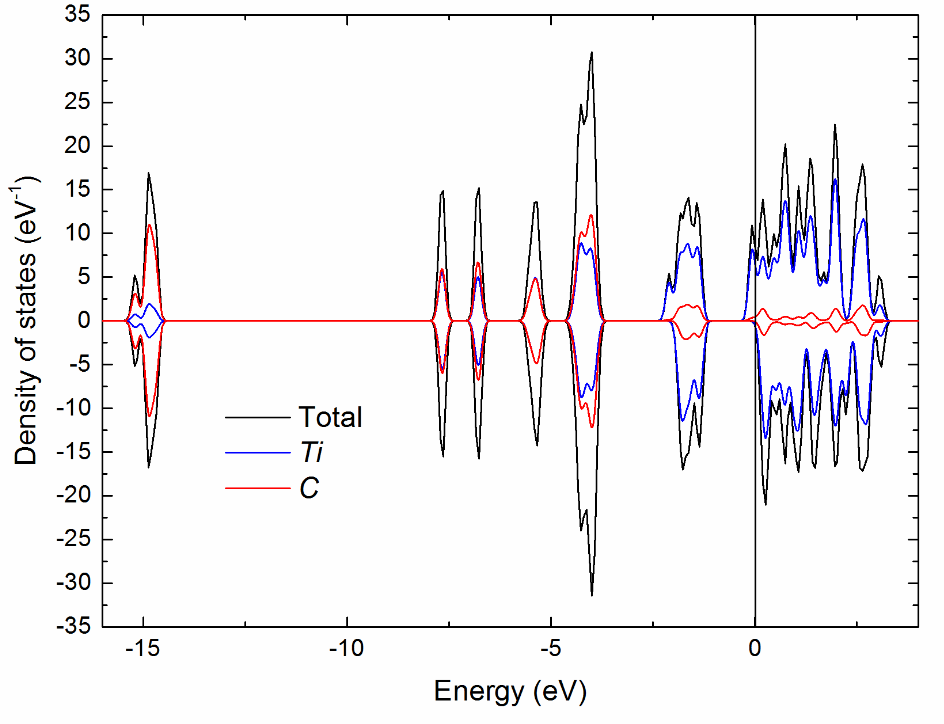

Fig 3.3: The species decomposed density of states of C_{3v} Ti_8C_{12}.

3.4 Thermodynamics of hydrogen adsorption

3.4.1 Physisorption

In order to model the physisorption of H_2 by Ti_8C_{12}, we coordinated H_2 to the T_d isomer of Ti_8C_{12} before allowing the structure to relax with unrestricted symmetry. This approach greatly reduces the number of possible starting configurations, which grows exponentially as more H_2 molecules are added. H_2 can be physisorbed at either of the two unique titanium positions present in T_d Ti_8C_{12} to form either α-Ti_8C_{12}–H_2 or β-Ti_8C_{12}–H_2.

We found that H_2 is physisorbed at Ti_α with an exothermic electronic binding energy, ΔE_{elec}, of −0.235 eV/H_2. Meanwhile, H_2 is physisorbed at the more coordinated Ti_β species with a far less exothermic ΔE_{elec} of −0.038 eV/H_2. Both of these binding energies are significantly less exothermic than those reported in previous studies, −0.39 eV/H_2 and −0.24 eV/H_2 when H_2 is physisorbed at Ti_α and Ti_β respectively [15]. This discrepancy can be attributed to the overestimation of charge transfer binding energies when using semi-local exchange-correlation functionals.

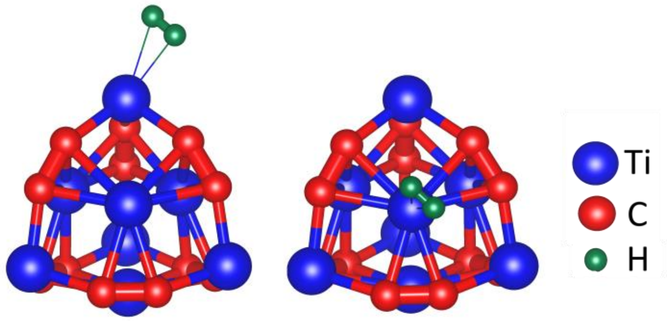

Figure 3.4: The relaxed structure of Ti_8C_{12} with H_2 physisorbed at Ti_α (left) and Ti_β (right).

In order to ascertain the thermodynamic stability of α-Ti_8C_{12}–H_2 and β-Ti_8C_{12}–H_2 with respect to Ti_8C_{12} and H_2, we calculated the Gibbs free energy change, ΔG_{phys}, at temperatures of between 170 K and 370 K and at pressures of between 0.1 ATM and 100 ATM. Table 3.2 shows the contributing changes in electronic, rotational, vibrational and translational energy and entropy when H_2 is physisorbed to form α-Ti_8C_{12}–H_2 at standard conditions (298 K / 1 ATM), 170 K / 100 ATM and 370K / 0.1 ATM.

	170 K / 100 ATM	**298 K / 1 ATM**	**370 K / 0.1 ATM**
$\Delta E_{electronic}$	-0.235 eV	-0.235 eV	-0.235 eV
$T \times \Delta S_{electronic}$	0.0 eV	-0.0 eV	-0.0 eV
$\Delta E_{translational}$	-0.022 eV	-0.039 eV	-0.048 eV
$T \times \Delta S_{translational}$	-0.119 eV	-0.363 eV	-0.541 eV
$\Delta E_{vibrational}$	0.135 eV	0.165 eV	0.186 eV
$T \times \Delta S_{vibrational}$	0.046 eV	0.117 eV	0.170 eV
$\Delta E_{rotational}$	-0.022 eV	-0.039 eV	-0.048 eV
$T \times \Delta S_{rotational}$	-0.014 eV	-0.039 eV	-0.055 eV
$\Delta G_{phys,\alpha}$	-0.057 eV	0.137 eV	0.281 eV

Table 3.2: The contributions to the Gibbs free energy change when H_2 is physisorbed at Ti_α.

Overall, entropy is lost when H_2 is adsorbed, meaning that decreasing temperature favours H_2 adsorption. This is primarily driven by the decrease in translational entropy when H_2 is adsorbed and loses its translational independence. Given that the translational entropy of H_2 is highest at low pressures, high pressure conditions also favour H_2 adsorption. The corresponding fall in translational energy when H_2 is adsorbed is low and independent of pressure, just $\frac{3}{2}kT$. Meanwhile, vibrational entropy and energy both increase when H_2 is adsorbed as a new bond is formed between Ti_8C_{12} and H_2. Changes in rotational energy and entropy are both small and slightly negative given the loss of hydrogen's rotational independence.

Overall, $\Delta G_{phys,\alpha}$ is endothermic under standard conditions, +0.137 eV, and therefore the formation of α-Ti_8C_{12}–H_2 is not thermodynamically favourable. However, $\Delta G_{phys,\alpha}$ can be made exothermic by increasing pressure and lowering temperature. For example, at 170 K / 100 ATM, $\Delta G_{phys,\alpha}$ = -0.057 eV. Figure 3.5 shows $\Delta G_{phys,\alpha}$ over the range of temperatures and pressures investigated; red areas signify that $\Delta G_{phys,\alpha}$ is endothermic and that the physisorption of H_2 at Ti_α is not thermodynamically favourable, whereas green areas signify that $\Delta G_{phys,\alpha}$ is exothermic and that the physisorption of H_2 at Ti_α is thermodynamically favourable. While α-Ti_8C_{12}–H_2 is only stable under high pressure / low temperature conditions, any increase in pressure and decrease in temperature increases the stability of α-Ti_8C_{12}–H_2, an intermediate in the chemisorption process discussed later.

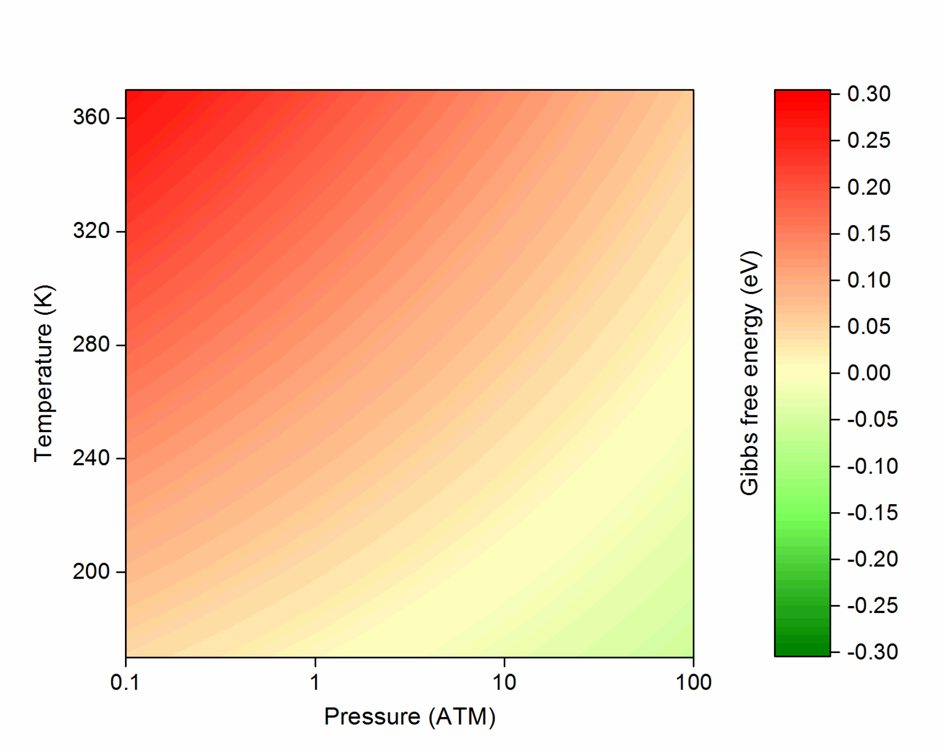

Figure 3.5: The Gibbs free energy change when H_2 is physisorbed at Ti_α under various conditions.

We also calculated the Gibbs free energy change when H_2 is physisorbed at Ti_β to form β-Ti_8C_{12}–H_2, $\Delta G_{phys,\beta}$. Table 3.3 shows the contributions to the Gibbs free energy and Figure 3.6 shows $\Delta G_{phys,\beta}$ over a range of temperatures and pressures. In contrast with $\Delta G_{phys,\alpha}$, $\Delta G_{phys,\beta}$ remains endothermic over the entire range of conditions studied given that ΔE_{elec} is almost 0.2 eV more endothermic than when H_2 is physisorbed at Ti_α. Most of the other contributions to $\Delta G_{phys,\beta}$ are similar to those contributing to $\Delta G_{phys,\alpha}$, although changes in vibrational energy are slightly lower and changes in vibrational entropy are higher as a result of a weaker Ti_β – H_2 bond.

	170 K / 100 ATM	298 K / 1 ATM	370 K / 0.1 ATM
$\Delta E_{electronic}$	-0.038	-0.038	-0.038
$T \times \Delta S_{electronic}$	-0.010	-0.018	-0.022
$\Delta E_{translational}$	-0.022	-0.039	-0.048
$T \times \Delta S_{translational}$	-0.119	-0.363	-0.541
$\Delta E_{vibrational}$	0.108	0.148	0.174
$T \times \Delta S_{vibrational}$	0.072	0.175	0.249
$\Delta E_{rotational}$	-0.022	-0.039	-0.048
$T \times \Delta S_{rotational}$	-0.014	-0.039	-0.055
ΔG_{total}	0.087	0.259	0.387

Table 3.3: The contributions to the Gibbs free energy change when H_2 is physisorbed at Ti_β.

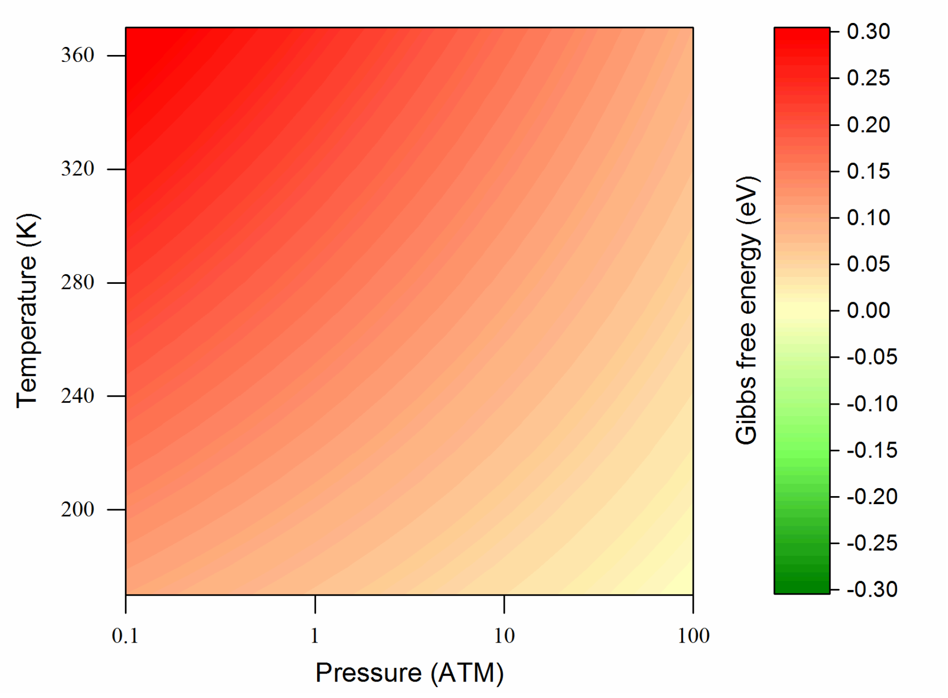

Figure 3.6: The Gibbs free energy change when H_2 is physisorbed at Ti_β under various conditions

The fact that $\Delta G_{phys,\beta}$ is moderately endothermic even under low temperature / high pressure conditions means that no appreciable quantities of β-Ti_8C_{12}–H_2 will exist at any conditions of interest. Therefore, we did not investigate the physisorption of subsequent H_2 molecules at any Ti_β site. We found that subsequent H_2 molecules are barely bound to hydrogenated Ti_α species, with $\Delta E_{elec} = -0.06$ eV and -0.04 eV for the second and third H_2 physisorption, with corresponding changes in Gibbs free energy highly endothermic even under low temperature / high pressure conditions. Our findings are in contrast to previous studies which reported electronic binding energies of -0.32 eV and -0.13 eV for the second and third H_2 physisorption, a difference that can again be attributed to the overestimation of charge transfer binding energies when using semi-local exchange-correlation functionals. Meanwhile, we did find that H_2 binds exothermically to non-hydrogenated Ti_α sites in α-Ti_8C_{12}–H_2; under standard conditions, $\Delta G_{phys,\alpha}$ = +0.142, and at 170K / 100 bar ΔG_{phys} = -0.027 eV, similar to physisorbtion of Ti_α by α-Ti_8C_{12}, +0.137 eV and -0.057 eV.

Our investigations into the physisorbtion of H_2 by Ti_8C_{12} suggest that the high storage capacities reported in previous studies, which are reliant on the mass physisorbtion of H_2, are unrealistic. We found that even at low temperature, high pressure conditions, each Ti_α species can only physisorb one H_2 molecule, and that H_2 is not physisorbed at all by Ti_β at all.

3.4.2 Chemisorption

In this section we investigate the stability of the isomers of $Ti_8C_{12}H_2$ resulting from the chemisorption 2 × H_2 molecules by Ti_8C_{12}. In each case, we used a stable physisorbed state as a starting configuration before dissociating H_2 between neighbouring atoms. When H_2 physisorbed at Ti_α is dissociated between Ti_α and carbon, α-$Ti_8C_{12}H_2$ is formed, whereas when H_2 physisorbed at Ti_β is dissociated between Ti_β and carbon, β-$Ti_8C_{12}H_2$ is formed. Both structures are shown in Figure 3.7.

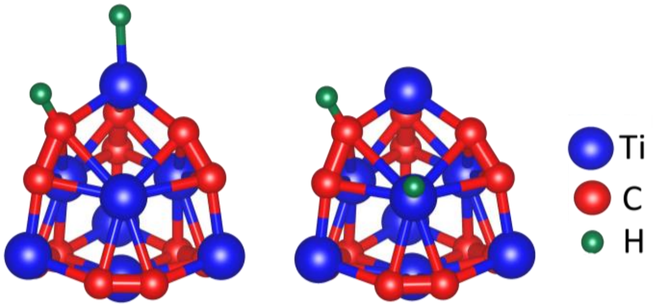

Figure 3.7: The relaxed structure of α-$Ti_8C_{12}H_2$ (left) and β-$Ti_8C_{12}H_2$ (right).

The formation α-$Ti_8C_{12}H_2$ is energetically favourable over the formation of β-$Ti_8C_{12}-H_2$, with $\Delta E_{elec} = -0.447$ eV when forming α-$Ti_8C_{12}H_2$ and $\Delta E_{elec} = -0.063$ eV when forming β-$Ti_8C_{12}-H_2$. The weak binding of atomic hydrogen to Ti_β is consistent with the weak binding of H_2 to Ti_β, with both atomic hydrogen and H_2 binding much more strongly to Ti_α, see Section 3.4.1.

We calculated the changes in Gibbs free energy when H_2 is chemisorbed. The change in Gibbs free energy when H_2 is chemisorbed by Ti_α and carbon to form α-$Ti_8C_{12}H_2$, $\Delta G_{chem,\alpha}$, will be discussed first. Non-electronic contributions to the Gibbs free energy follow a similar pattern to those when H_2 is physisorbed: upon chemisorption, translational entropy falls while vibrational entropy and energy increase. However, in addition, electronic entropy is also lost as the spin degeneracy of Ti_8C_{12} is lifted. Full contributions to $\Delta G_{chem,\alpha}$ are shown in Table 3.4.

As can be seen in Figure 3.8, $\Delta G_{chem,\alpha}$ is exothermic over a wide range of conditions, reaching to -0.180 eV at 170 K / 100 ATM. Under standard conditions $\Delta G_{chem} = +0.068$ eV, and thus becomes exothermic when pressure is slightly increased and/or temperature is slightly decreased. Thus, in terms of thermodynamics, Ti_8C_{12} can be reversibly hydrogenated to form α-$Ti_8C_{12}H_2$ over a very modest range of conditions.

	170 K / 100 ATM	298 K / 1 ATM	370 K / 0.1 ATM
$\Delta E_{electronic}$	-0.447	-0.447	-0.447
$T \times \Delta S_{translational}$	-0.020	-0.036	-0.044
$\Delta E_{translational}$	-0.022	-0.039	-0.048
$T \times \Delta S_{translational}$	-0.119	-0.363	-0.541
$\Delta E_{vibrational}$	0.155	0.174	0.190
$T \times \Delta S_{vibrational}$	-0.003	0.019	0.042
$\Delta E_{rotational}$	-0.022	-0.039	-0.048
$T \times \Delta S_{rotational}$	-0.014	-0.039	-0.055
ΔG_{total}	-0.180	0.068	0.245

Table 3.4: The contributions to the Gibbs free energy change when H_2 is chemisorbed by Ti_α and carbon.

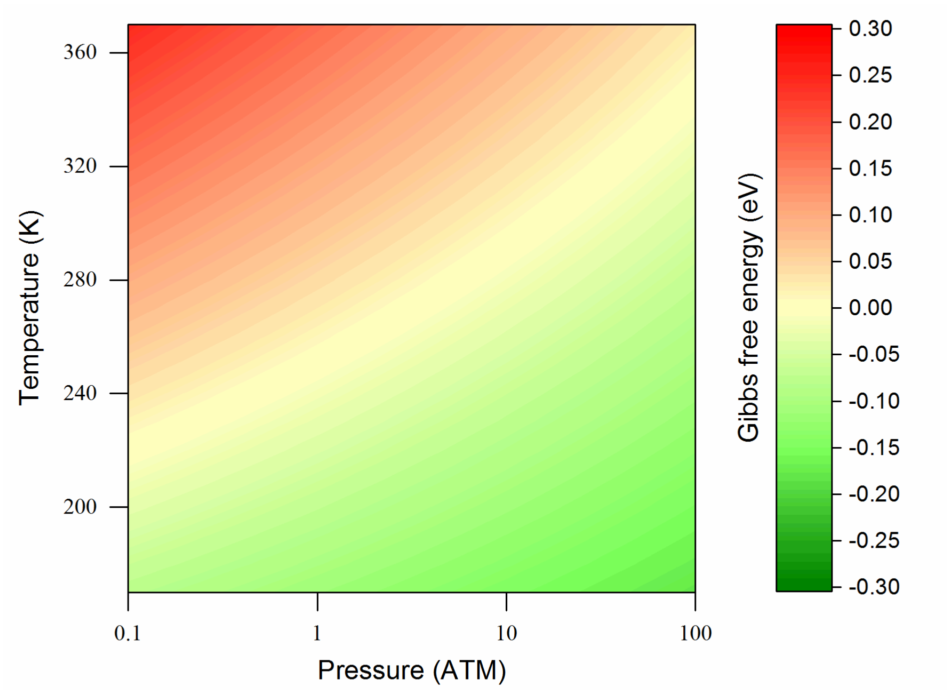

Figure 3.8: The Gibbs free energy change when H_2 is chemisorbed by Ti_α and carbon under various conditions.

We also calculated the Gibbs free energy change when H_2 is chemisorbed by Ti_β and carbon, $\Delta G_{chem,\beta}$. Given the magnitude of $\Delta E_{electronic}$, it is unsurprising that $\Delta G_{chem,\beta}$ remains positive over the entire range of conditions studied. Even when $\Delta G_{chem,\beta}$ is minimized at 170 K / 100 ATM, $\Delta G_{chem,\beta}$ is still highly endothermic, +0.211 eV. We conclude that no appreciable quantity of β-$Ti_8C_{12}H_2$ will exist under the conditions of interest, and have ignored the possibility of the chemisorption of subsequent H_2 by β-$Ti_8C_{12}H_2$.

We did, however, investigate the subsequent hydrogenation of α-$Ti_8C_{12}H_2$ to $Ti_8C_{12}H_4$. The hydrogenation of α-$Ti_8C_{12}H_2$ can proceed to form five possible isomers, as shown in Figure 3.9. We found that isomer A is significantly more stable than any other isomer, with ΔE_{elec} far more exothermic than when Ti_8C_{12} is hydrogenated to form α-$Ti_8C_{12}H_2$. This implies the relative instability of partially hydrogenated C_2 units, C_2H, relative to fully hydrogenated C_2 units, C_2H_2. If C_2 units are assumed to be similar to alkenes, see Section 3.3, then partially hydrogenated C_2H species have unstable dangling bonds that are not present in C_2H_2. However, while the carbon-carbon bond length in hydrogenated C_2H_2 units is elongated with respect to C_2 (1.39 Å vs. 1.32 Å), it does not approach the length of a typical carbon-carbon single bond (~1.5 Å). Interestingly, our results suggest that partially hydrogenated C_2H species are stabilised when positioned adjacently, as in isomer C, the next most stable isomer of $Ti_8C_{12}H_4$.

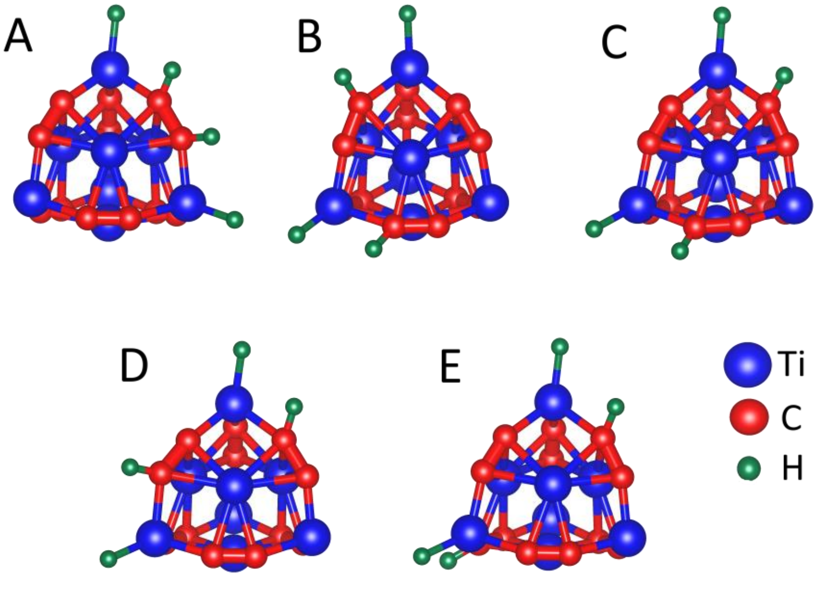

Figure 3.9: Structural isomers of $Ti_8C_{12}H_4$

	$T_8C_{12} \rightarrow Ti_8C_{12}H_4$		**$T_8C_{12}H_2 \rightarrow Ti_8C_{12}H_4$**	
	ΔE_{elec} (eV/H_2)	**ΔG_{ads} (eV/H_2)**	**ΔE_{elec} (eV)**	**ΔG_{ads} (eV)**
A	−0.558	−0.112	-0.669	-0.292
B	−0.330	+0.117	-0.213	0.166
C	−0.487	−0.028	-0.527	-0.124
D	−0.317	+0.130	-0.187	0.192
E	−0.344	+0.102	-0.240	0.136

Table 3.5. The electronic and Gibbs free changes for the adsorption of (i) 2 ×H_2 by Ti_8C_{12} and (ii) H_2 by Ti_8C_{12} to form the isomeric forms of $Ti_8C_{12}H_4$ (a) – (e).

We calculated the Gibbs free energy change for the formation of isomer A from both Ti_8C_{12} and α-$Ti_8C_{12}H_2$, see Figure 3.10. The formation of isomer A from Ti_8C_{12}, ΔG_{chem} / H_2 can be exothermic or endothermic depending on the conditions. For example, while the formation of isomer A from Ti_8C_{12} is exothermic under standard conditions (ΔG_{chem} = -0.112 eV / H_2), at 370 K / 0.1 ATM it is endothermic (G_{chem} = +0.054 eV / H_2). Therefore, we conclude the chemisorption of 2 × H_2 is thermodynamically reversible between 298 K / 1.0 ATM and 370 K / 0.1 ATM.

While the stability of α-$Ti_8C_{12}H_4$ with respect to α-$Ti_8C_{12}H_2$ only amounts to a kinetic barrier to the full dehydrogenation of α-$Ti_8C_{12}H_4$, if α-$Ti_8C_{12}H_4$ were to be used as a hydrogenation catalyst it would severely limit the range of compatible HSMs. Compatible HSMs must bind H_2 with a more exothermic Gibbs free energy than $Ti_8C_{12}H_2$. Therefore, under standard conditions, compatible HSMs must bind H_2 with ΔG < -0.246 eV.

One possible solution would be to prevent the formation for $Ti_8C_{12}H_4$ through the blocking of Ti_{α} sites, preventing the formation of α-$Ti_8C_{12}H_4$. Zhao et al. suggest that Ti_8C_{12} dimerizes with a binding energy of 1.8 eV / molecule. The same study suggests that larger polymeric structures are likely to form, with certain surfaces leaving exposed desirable Ti_{α}-C units.

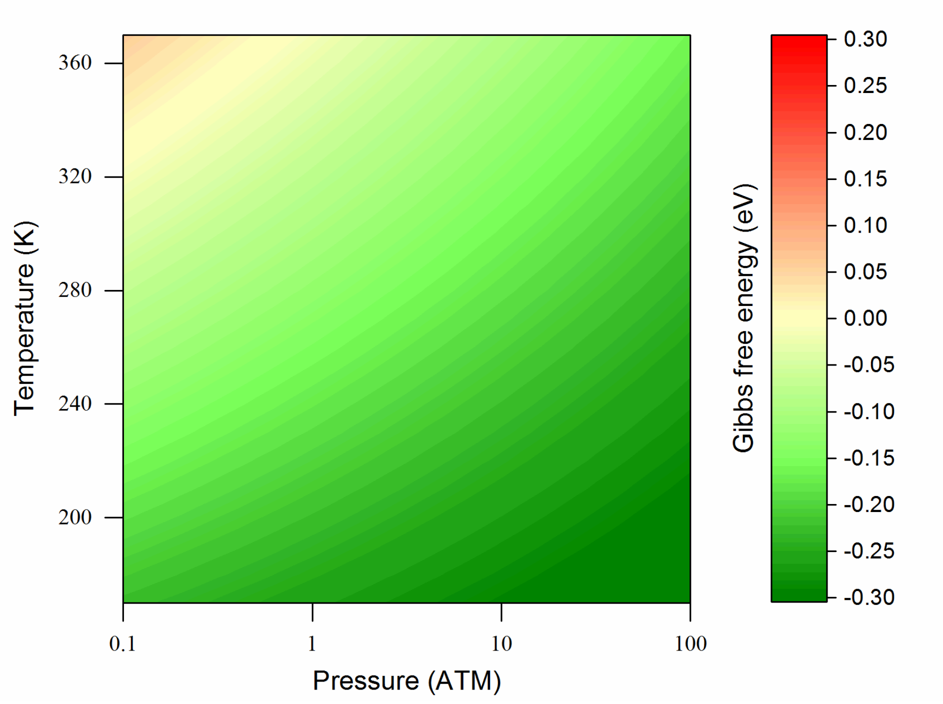

Figure 3.10: The Gibbs free energy change per H_2 when 2 × H_2 are chemisorbed by Ti_8C_{12} to form isomer A under various conditions.

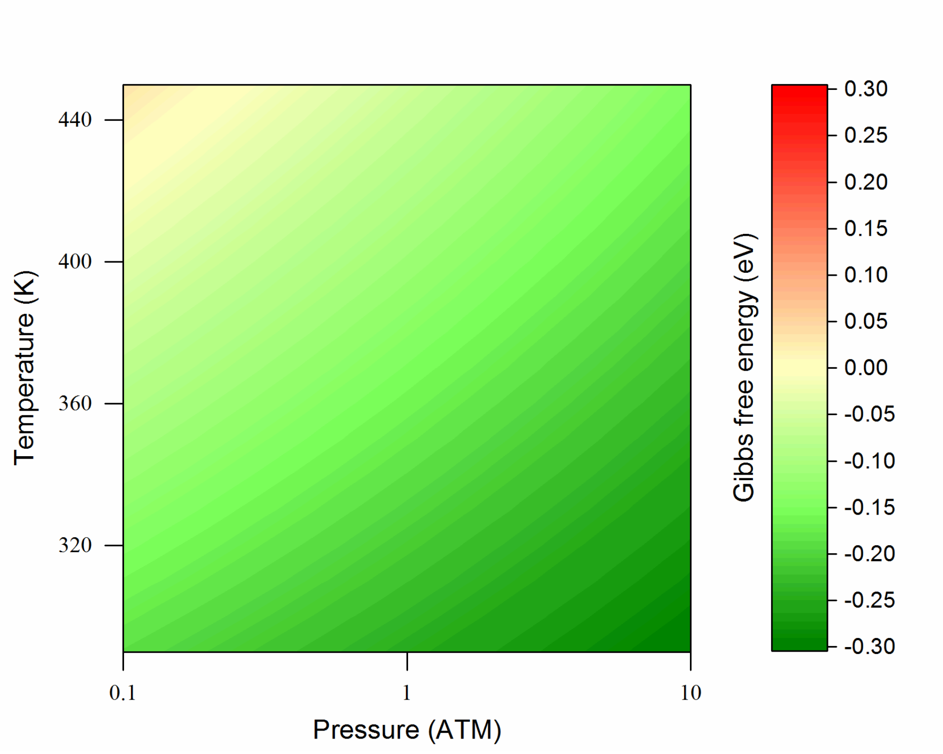

Figure 3.11: The Gibbs free energy change when H_2 is chemisorbed by $Ti_8C_{12}H_2$ to form isomer A under various conditions.

3.5 Kinetics of hydrogen adsorption

In order to understand the kinetics of H_2 dissociation by Ti_8C_{12}, we used the nudged elastic band (NEB) method, which finds the minimum energy pathway (MEP) between reactants and products in terms of the system's electronic energy. We investigated the hydrogenation of Ti_8C_{12} to $Ti_8C_{12}H_4$ by performing NEB relaxations between five different intermediates: [$Ti_8C_{12} + 2 \times H_2$], [$\alpha$-$T_8C_{12}$–$H_2$ + H_2], [α-$T_8C_{12}H_2$ + H_2], [α-$T_8C_{12}H_2$–H_2] and [α-$T_8C_{12}H_2$]. Figure 3.12 shows the reaction profile for the hydrogenation of Ti_8C_{12} to $Ti_8C_{12}H_4$ in terms of electronic energy.

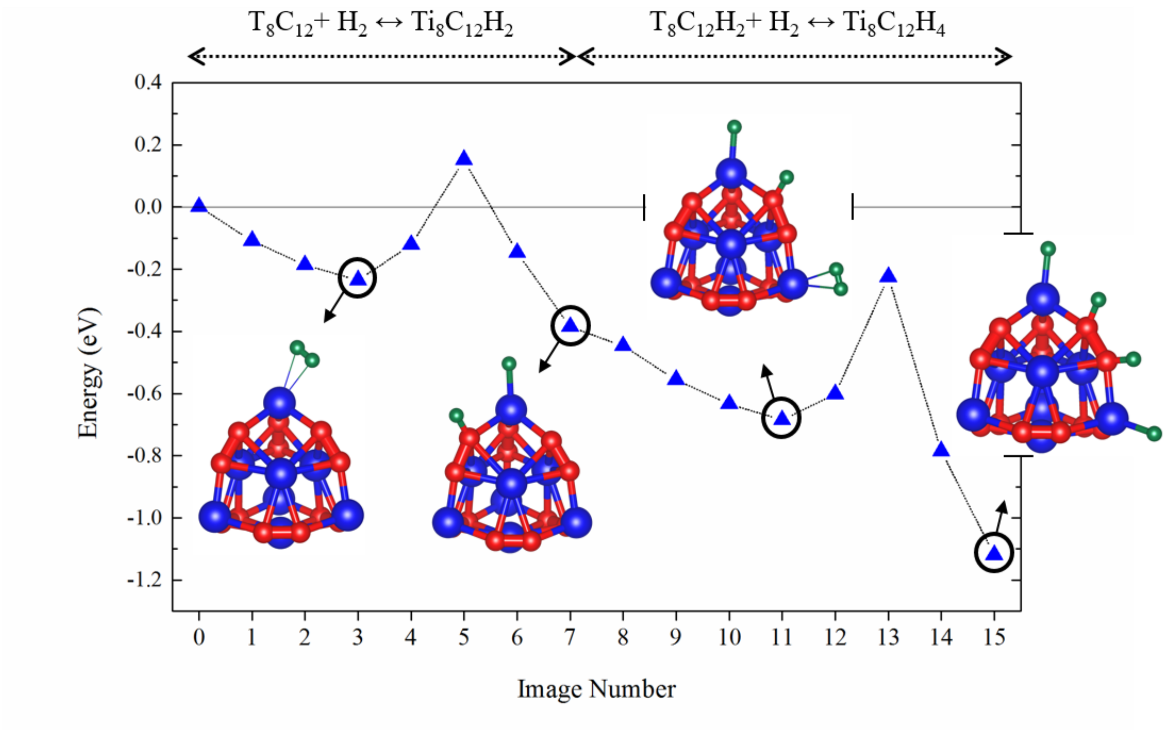

Figure 3.12: The reaction profile in terms of electronic energy for the consecutive chemisorption of two H_2 molecules by Ti_8C_{12}.

Between images 0 and 3, H_2 is physisorbed at Ti_α with no electronic energy barrier to form the stable intermediate α-T_8C_{12}–H_2. Between images 3 and 8, H_2 is dissociated between Ti_α and carbon to form α-$T_8C_{12}H_2$ with an electronic activation battier of 0.387 eV, significantly higher than previously reported results obtained using the PBE functional, a GGA functional known to underestimate activation barriers. Between images 8 and 11, H_2 is physisorbed at Ti_α with no electronic energy barrier. Between images 11 and 15, H_2 is dissociated between Ti_α and carbon to form α-$T_8C_{12}H_2$ with an electronic energy battier of 0.460 eV.

However, reaction kinetics are not determined by the electronic energy barrier alone. The Eyring equation uses the Gibbs free energy barrier, $\Delta G^{\#}$, to calculate pre-exponential factors. Figure 3.13 which shows MEP between Ti_8C_{12} and $Ti_8C_{12}H_4$ in terms of the intermediates' Gibbs free energy at 170 K / 100 ATM, 298 K / 1.0 ATM and 370 K / 0.1 ATM.

/

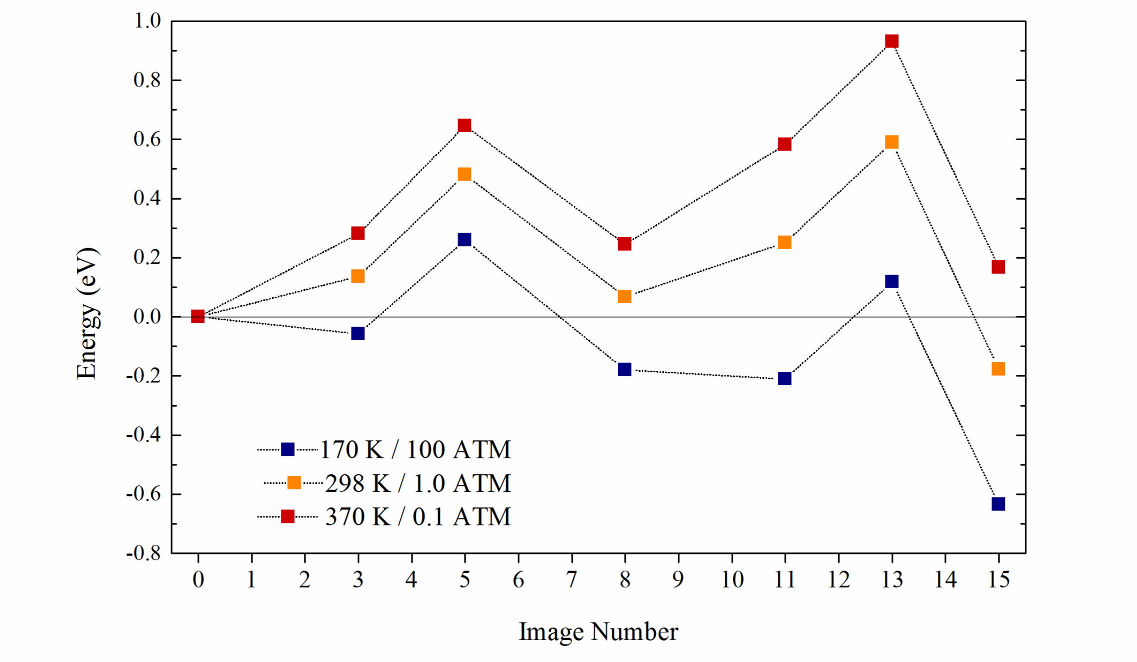

Figure 3.13: The reaction profile in terms of the Gibbs free energy for the consecutive chemisorption of two H_2 molecules by Ti_8C_{12}.

Under standard conditions, physisorbed states (i.e. α-T_8C_{12}-H_2 and α-$T_8C_{12}H_2$-H_2, images 3 and 11) are not stable intermediates. Therefore, $\Delta G^{\#}$ for the hydrogenation of T_8C_{12} is the barrier between images 1 and 8 (0.480 eV) and $\Delta G^{\#}$ for the hydrogenation of α-$Ti_8C_{12}H_2$ is the barrier between images 8 and 15 (0.522 eV).

However, high pressure / low temperature conditions (170 K / 100 ATM) minimise $\Delta G^{\#}$ for both hydrogenations. Under these conditions, both physisorbed states are stable intermediates, and therefore $\Delta G^{\#}$ for the hydrogenation of T_8C_{12} is the barrier between images 3 and 8 (0.316 eV) and $\Delta G^{\#}$ for the hydrogenation of α-$Ti_8C_{12}H_2$ is the barrier between images 11 and 15 (0.329 eV). Both barriers are far lower than those under standard conditions, 0.480 eV and 0.522 eV respectively. Therefore, high pressure, low temperature conditions not only thermodynamically favour the formation $Ti_8C_{12}H_4$ but also minimise the activation barrier.

Meanwhile, for the dehydrogenation of $Ti_8C_{12}H_4$ and $Ti_8C_{12}H_2$, $\Delta G^{\#}$ = 0.768 eV and 0.412 eV respectively under standard conditions. Given that the number of independent particles and total bonds are unchanged in the transition state with respect to $Ti_8C_{12}H_4$ and $Ti_8C_{12}H_2$, $\Delta S^{\#}_{trans}$ and $\Delta S^{\#}_{vib}$ are both low, and so changes in temperature and pressure do not significantly affect $\Delta G^{\#}$

Figure 3.13 also reiterates some of our results discussed in Section 3.4. Under standard conditions, the Gibbs free energy of α-$T_8C_{12}H_4$ (image 15) is lower than that of Ti_8C_{12} (image 0), meaning that α-$T_8C_{12}H_4$ is stable with respect to dehydrogenation. However, at 370 K / 0.1 ATM, the Gibbs free energy of α-$T_8C_{12}H_4$ is higher than that of Ti_8C_{12}, meaning that α-$T_8C_{12}H_4$ is unstable with respect to dehydrogenation.

While the relative Gibbs free energy of the hydrogenated and dehydrogenated species determines their thermodynamic stability, $\Delta G^{\#}$ determines kinetic stability**.** The rate at which hydrogen is adsorbed and desorbed can be calculated using the Eyring equation, see Section 2.4.2:

$$k_{TST} = \frac{k_B T}{h} e^{-\Delta G^{\#}/RT}$$

Table 3.6 shows k_{TST} and $\Delta G^{\#}$ for all hydrogenation and dehydrogenation processes described below:

$$Ti_8C_{12}\ (M) \underset{-1}{\overset{1}{\rightleftharpoons}} Ti_8C_{12}H_2\ (MH_2)$$

$$Ti_8C_{12}H_2 \underset{-2}{\overset{2}{\rightleftharpoons}} Ti_8C_{12}H_4\ (MH_4)$$

	170 K / 100 ATM		298 K / 1.0 ATM		370 K / 0.1 ATM	
	$\Delta G^{\#}$	$\mathbf{k_x}$	$\Delta G^{\#}$	$\mathbf{k_x}$	$\Delta G^{\#}$	$\mathbf{k_x}$
1	0.316	1.52×10^{3} s^{-1}	0.480	4.73×10^{4} L/mol/s	0.646	1.22×10^{4} L/mol/s
-1	0.439	3.43×10^{-1} s^{-1}	0.412	6.69×10^{5} s^{-1}	0.401	2.66×10^{7} s^{-1}
2	0.329	6.25×10^{2} s^{-1}	0.522	9.23×10^{3} L/mol/s	0.685	3.60×10^{3} L/mol/s
-2	0.752	1.80×10^{-10} s^{-1}	0.768	6.38×10^{-1} s^{-1}	0.763	3.16×10^{2} s^{-1}

Table 3.6: The Gibbs free transition energy and rate constants for the hydrogenation of Ti_8C_{12} and the dehydrogenation of reactions of $Ti_8C_{12}H_4$.

Given that the initial hydrogenation of Ti_8C_{12} and dehydrogenation of $Ti_8C_{12}H_2$ are both fast under standard conditions compared with the hydrogenation of $Ti_8C_{12}H_2$, we can assume that Ti_8C_{12} (M) and $Ti_8C_{12}H_2$ (MH_2) form a pre-equilibrium prior to formation of α-$T_8C_{12}H_4$ (MH_4). Under this approximation, the rate of formation of α-$T_8C_{12}H_4$ is:

$$\frac{d[\mathrm{MH_4}]}{dt} = k_2[\mathrm{MH_2}][\mathrm{H_2}] - k_{-2}[\mathrm{MH_4}]$$

$$= k_2.\frac{k_1}{k_{-1}}.[\mathrm{M}][\mathrm{H_2}][\mathrm{H_2}] - k_{-2}[\mathrm{MH_4}]$$

Unless $[\mathrm{MH_4}]$ is very large (i.e. close to equilibrium under standard conditions), $k_{-2}[\mathrm{MH_4}]$ is small compared to $k_2.\frac{k_1}{k_{-1}}.[\mathrm{M}][\mathrm{H_2}][\mathrm{H_2}]$, and therefore:

$$\frac{d[\mathrm{MH_4}]}{dt} = k_2.\frac{k_1}{k_{-1}}.[\mathrm{M}][\mathrm{H_2}]^2$$

$$= k'.[\mathrm{M}][\mathrm{H_2}]^2$$

where k' = 6.52×10^{2} s^{-1} L^{2} mol^{-2} under standard conditions. This effective rate constant is very high, and thus $Ti_8C_{12}H_4$ will form quickly under standard conditions. The inclusion of $\frac{k_1}{k_{-1}}$ in the expression for k' reflects the fact that the rate of hydrogenation of Ti_8C_{12} is limited by the supply of $[\mathrm{MH_2}]$.

Meanwhile, at 370 K / 0.1 ATM, α-$T_8C_{12}H_4$ is unstable with respect to dehydrogenation. Under these conditions, the initial dehydrogenation of $Ti_8C_{12}H_4$ to $Ti_8C_{12}H_2$ is the rate determining step, with $Ti_8C_{12}H_2$ forming slowly. Under the steady state approximation, we assume that $Ti_8C_{12}H_2$ exists in a steady concentration:

$$\frac{d[\mathrm{M}H_2]}{dt} = 0 = k_1[\mathrm{M}][H_2] + k_{-2}[\mathrm{MH_4}] - k_{-1}[\mathrm{MH_2}] - k_2[\mathrm{MH_2}][\mathrm{H_2}]$$

$$[\mathrm{MH_2}] = \frac{k_1[\mathrm{M}][H_2] + k_{-2}[\mathrm{MH_4}]}{k_{-1} + k_2[\mathrm{H_2}]}$$

Furthermore, the rate of formation of Ti_8C_{12} + 2 × H_2 from $Ti_8C_{12}H_4$ is:

$$\frac{d[\mathrm{M}]}{dt} = k_{-1}[\mathrm{MH_2}] - k_1[\mathrm{M}][H_2]$$

$$= k_{-1}\left(\frac{k_1[\mathrm{M}][H_2] + k_{-2}[\mathrm{MH_4}]}{k_{-1} + k_2[\mathrm{H_2}]}\right) - k_1[\mathrm{M}][H_2]$$

Given that $k_{-1} \gg k_2$:

$$\frac{d[\mathrm{M}]}{dt} = k_{-1}\left(\frac{k_1[\mathrm{M}][H_2] + k_{-2}[\mathrm{MH_4}]}{k_{-1}}\right) - k_1[\mathrm{M}][H_2]$$

$$= k_{-2}[\mathrm{MH_4}]$$

The dehydrogenation of α-$T_8C_{12}H_4$ is determined solely by k_{-2}, which is considerably lower than the effective rate constant for the hydrogenation of Ti_8C_{12}. This suggests that α-$T_8C_{12}H_4$ is not only thermodynamically stable but also kinetically stable with respect to dehydrogenation. However, for catalytic purposes, the direct desorption of H_2 is not desirable. The catalytic hydrogenation of HSMs would proceed via an alternative pathway, making use of the fast, low energy dissociation of H_2 by Ti_8C_{12}.

3.6 Fully hydrogenated Ti_8C_{12}

While Sections 3.4 and 3.5 have investigated the behavior of $Ti_8C_{12} + 2 \times H_2$, we are ultimately interested in the behavior of Ti_8C_{12} in an excess of H_2. Assuming that hydrogen dissociates between Ti_α and neighbouring carbon atoms only, $Ti_8C_{12}H_8$ is the most hydrogenated form of Ti_8C_{12} achievable. Using α-$T_8C_{12}H_4$ centred around a T_d Ti_8C_{12} interior as a starting point, we identified four possible isomers of $Ti_8C_{12}H_8$, shown in Figure 3.14.

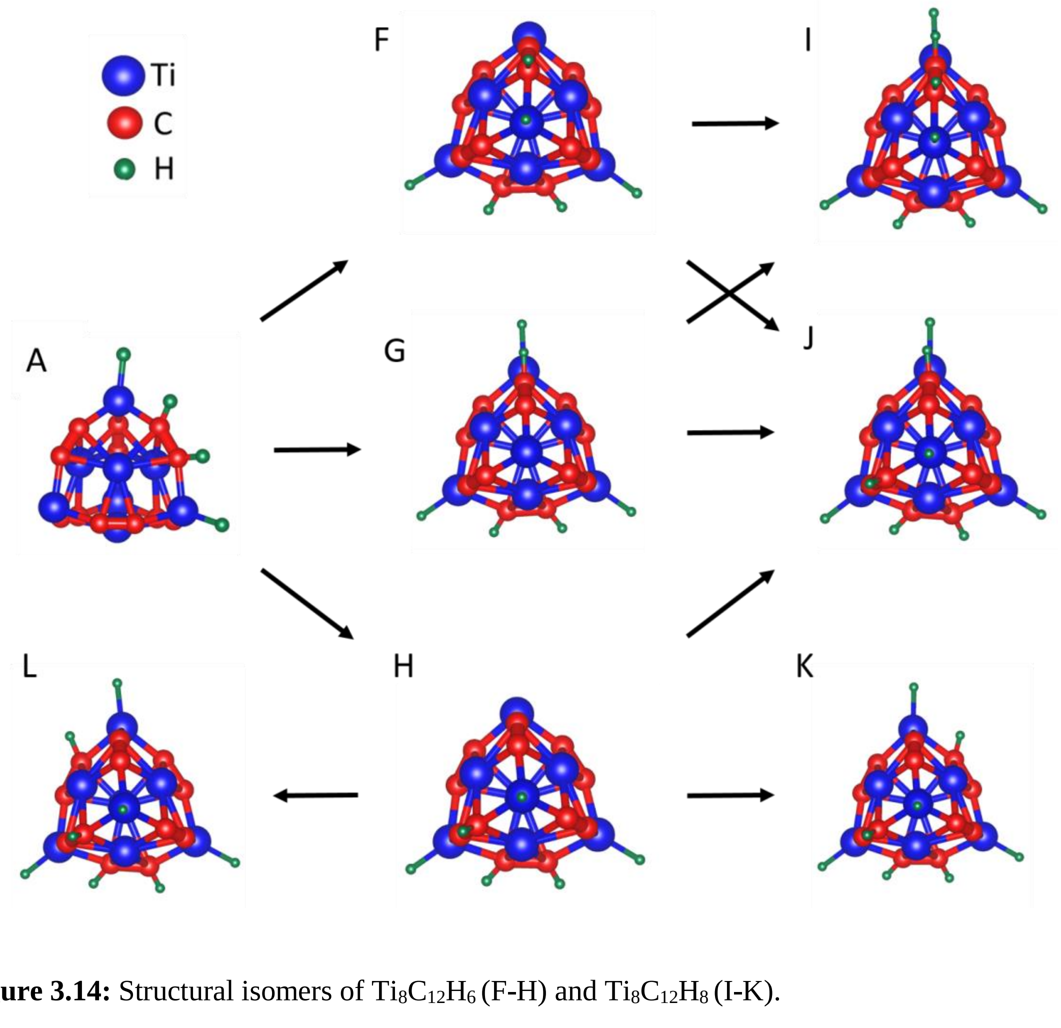

Figure 3.14: Structural isomers of $Ti_8C_{12}H_6$ (F-H) and $Ti_8C_{12}H_8$ (I-K).

		ΔG_{chem} (eV/H_2)		
	ΔE_{chem} (eV / H_2)	170 K / 100 ATM	298 K / 1 ATM	370 K / 0.1 ATM
F	-0.079	0.168	0.400	0.569
G	-0.077	0.170	0.402	0.571
H	-0.350	-0.103	0.129	0.298
I	-0.279	-0.053	0.163	0.324
J	-0.249	-0.002	0.230	0.399
K	-0.207	0.040	0.272	0.441
L	-0.135	0.112	0.344	0.513

Table 3.7: The electronic and Gibb's free energy changes for the formation of isomers of $Ti_8C_{12}H_6$ and $Ti_8C_{12}H_8$ from α-$Ti_8C_{12}H_4$.

We found that isomer I is the most stable isomer of $Ti_8C_{12}H_8$, with the hydrogenation of α-$T_8C_{12}H_4$ proceeding with ΔE_{elec} = -0.280 eV / H_2 and ΔG = +0.163 eV / H_2 under standard conditions and -0.053 eV at 170 K / 100 ATM. Importantly, the dehydrogenation of isomer I to form either isomer F or isomer G proceeds with an endothermic ΔG = +0.07 eV under standard conditions. Thus, in terms of thermodynamics, isomer I ideally fits the Gibbs free energy requirements for a hydrogenation catalyst, hydrogenating any HSM which adsorbs H_2 with ΔG < -0.07 eV under standard conditions. However, the formation of isomer I requires the formation $Ti_8C_{12}H_6$ as an intermediate, with only isomers F and G suitable (see Figure 3.14). Both are highly unstable with respect to α-$T_8C_{12}H_4$, even at 170 K / 100 ATM when ΔG = +0.17 eV. Therefore, the formation of the required isomers of $Ti_8C_{12}H_6$ acts as a significant barrier to the formation of isomer I. We carried out an NEB calculation to profile the transition barrier between α-$T_8C_{12}H_4$ and isomer I, with the electronic energy profile shown in Figure 3.15 and the same profile shown in terms of Gibbs free energy profile in Figure 3.16.

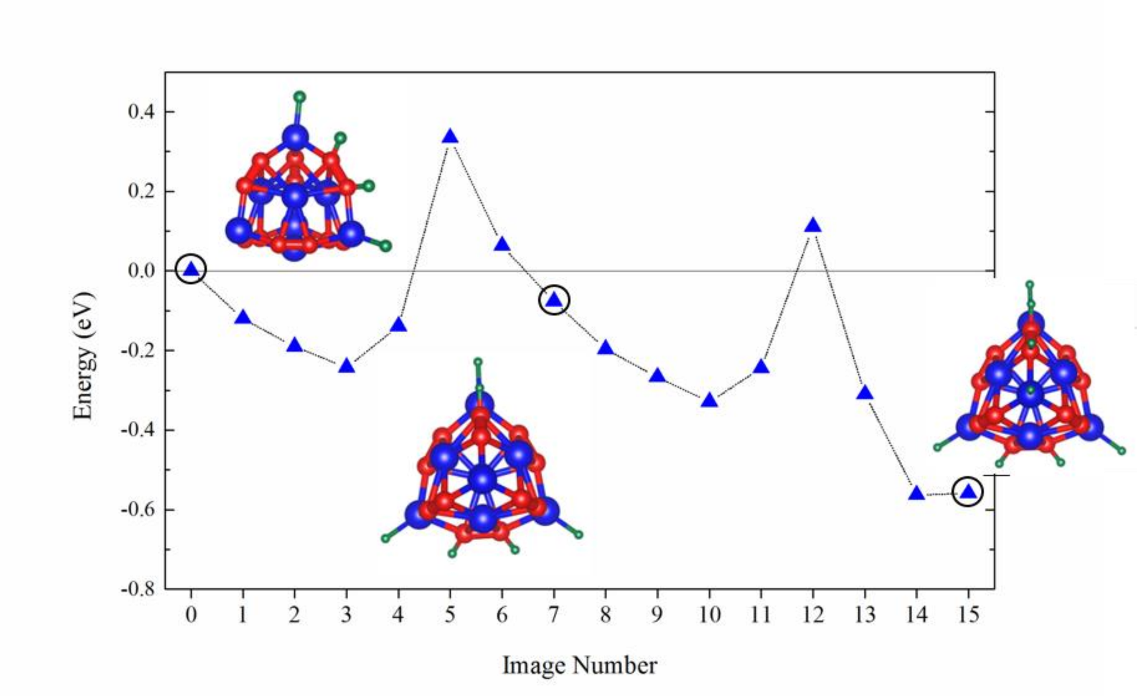

Figure 3.15: The reaction profile in terms of electronic energy for the consecutive chemisorption of two H_2 molecules by $Ti_8C_{12}H_4$ to form isomer I.

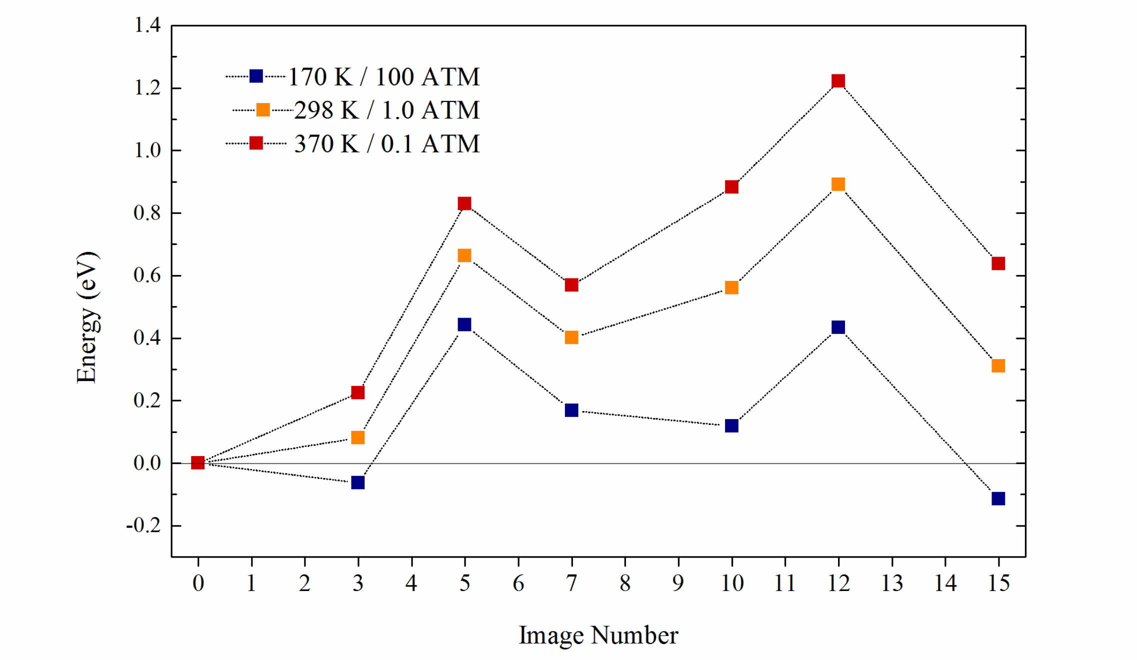

Figure 3.16: The reaction profile in terms of electronic energy for the consecutive chemisorption of two H_2 molecules by $Ti_8C_{12}H_4$ to form isomer I.

We calculated the Gibbs free activation barriers and the corresponding rate constants for the conversion of $Ti_8C_{12}H_4$ to isomer I via isomer G.

$$\mathrm{Ti_8C_{12}}\ (\mathrm{M}) \underset{-1}{\overset{1}{\rightleftharpoons}} \mathrm{Ti_8C_{12}H_2}\ (\mathrm{MH_2}) \underset{-2}{\overset{2}{\rightleftharpoons}} \mathrm{Ti_8C_{12}H_4}\ (\mathrm{MH_4})$$

	170 K / 100 ATM		**298 K / 1.0 ATM**		**370 K / 0.1 ATM**	
	$\Delta G^{\#}$	$\mathbf{k_x}$ **(s^{-1})**	$\Delta G^{\#}$	$\mathbf{k_x}$ **(s^{-1})**	$\Delta G^{\#}$	$\mathbf{k_x}$ **(s^{-1})**
1	0.504	$3.92 \times 10^{-3}\ s^{-1}$	0.663	3.86×10^{1} L/mol/s	0.829	3.99×10^{1} L/mol/s
-1	0.273	$2.81\times 10^{4}\ s^{-1}$	0.262	$2.28\times 10^{8}\ s^{-1}$	0.260	$2.20\times 10^{9}\ s^{-1}$
2	0.315	$1.58\times 10^{3}\ s^{-1}$	0.490	3.25×10^{4} L/mol/s	0.653	9.93×10^{3} L/mol/s
-2	0.548	$1.99\times 10^{-4}\ s^{-1}$	0.580	$9.59\times 10^{4}\ s^{-1}$	0.584	8.52×10^{4} L/mol/s

Table 3.8: The Gibbs free transition energy and rate constants for the hydrogenation of $Ti_8C_{12}H_4$ and the dehydrogenation of reactions of $Ti_8C_{12}H_8$.

Given that the rate of the formation of isomer G is significantly slower than the reverse process, we assume that assume that isomer F exists at a stable concentration throughout and utilise the steady state approximation:

$$\frac{d[\mathrm{M}H_6]}{dt} = 0 = k_1[\mathrm{M}H_6][H_2] + k_{-2}[\mathrm{MH_8}] - k_{-1}[\mathrm{MH_6}] - k_2[\mathrm{MH_6}][\mathrm{H_2}]$$

$$[\mathrm{MH_6}] = \frac{k_1[\mathrm{M}H_4][H_2] + k_{-2}[\mathrm{MH_8}]}{k_{-1} + k_2[\mathrm{H_2}]}$$

Furthermore, the rate of formation of isomer I is:

$$\frac{d[\mathrm{M}H_8]}{dt} = k_2[\mathrm{MH_6}] - k_{-2}[\mathrm{M}H_8]$$

$$= k_2\left(\frac{k_1[\mathrm{M}H_4][H_2] + k_{-2}[\mathrm{MH_8}]}{k_{-1} + k_2[\mathrm{H_2}]}\right) - k_{-2}[\mathrm{M}H_8]$$

At 170 K / 100 ATM, the only conditions which thermodynamically favour the formation of isomer I, $k_1 \gg k_{-2}$, and $k_{-1} \ll k_2$:

$$\frac{d[\mathrm{M}H_8]}{dt} = k_2\left(\frac{k_1[\mathrm{M}H_4][H_2]}{k_{-1}}\right)$$

$$= k''[\mathrm{M}H_4][H_2]$$

The above equation reflects that the rate of reaction is limited by the reversible hydrogenation of $Ti_8C_{12}H_4$ to $Ti_8C_{12}H_6$ given that k_1/k_{-1} is very small.

Meanwhile, while isomers F and G are both unstable over the entire range of conditions studied, the most stable form of $Ti_8C_{12}H_6$, isomer H, forms with ΔG = +0.129 eV under standard conditions and ΔG = -0.103 eV at 170 K / 100 ATM. The subsequent hydrogenation of isomer H to form isomers J, K and L has an endothermic Gibbs free energy over the entire range of conditions studied, meaning that at 170 K / 100 ATM isomer H is stable with respect to both hydrogenation and dehydrogenation. Furthermore, isomer H catalytically compatible with HMSs which adsorb hydrogen with a room temperature ΔG < +0.129 eV (-0.103 eV at 170 K / 100 ATM).

$$Ti_8C_{12}H_4\,(MH_4) \underset{-1}{\overset{1}{\rightleftharpoons}} Ti_8C_{12}H_6\,(MH_6)$$

NEB calculations show that the hydrogenation of α-$T_8C_{12}H_4$ to isomer H proceeds with a Gibbs free activation barrier of 0.504 eV at 170 K / 100 ATM. The rate equation for the formation of Isomer H (MH_6) from $Ti_8C_{12}H_4$ is simple:

$$\frac{d[\mathrm{M}H_6]}{dt} = k_1[\mathrm{M}H_4] - k_{-1}[\mathrm{M}H_6]$$

Given that $k_1 \gg k_{-1}$:

$$\frac{d[\mathrm{M}H_6]}{dt} = k_1[\mathrm{M}H_4]$$

where k_1 = 1.25 s^{-1} at 170 K / 100 ATM, suggesting that isomer H will form far more rapidly than $Ti_8C_{12}H_8$ (isomer I), where the effective rate constant is over an order of magnitude lower.

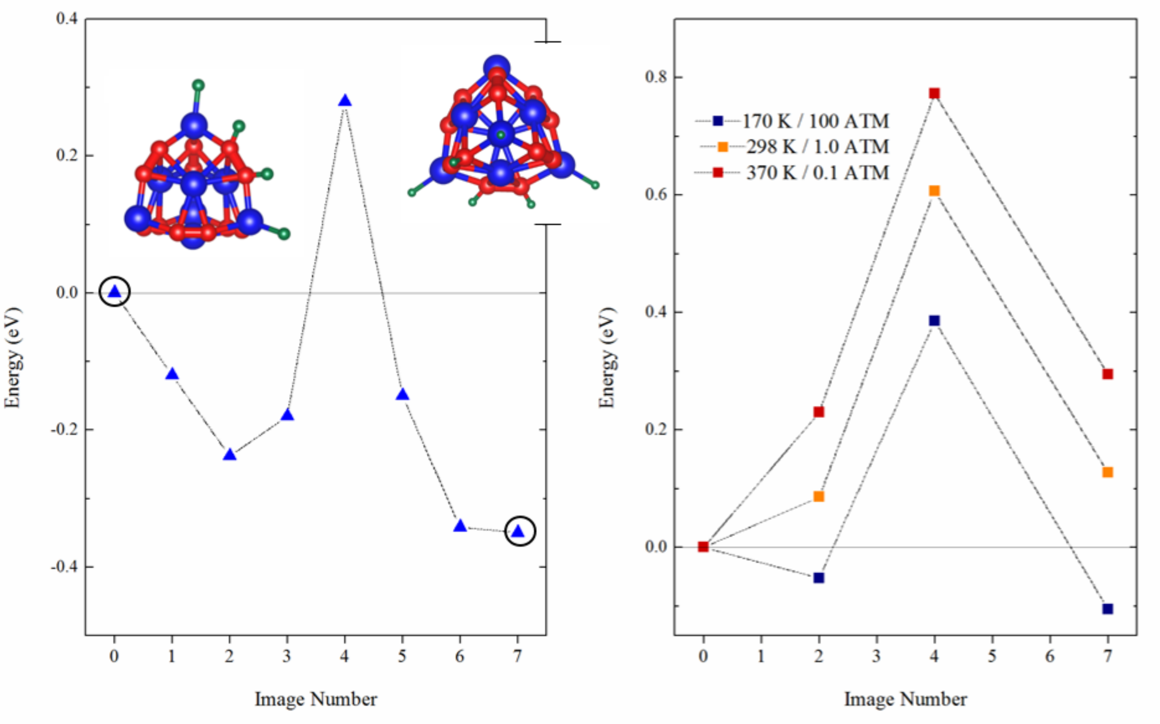

Figure 3.17: The reaction profile in terms of electronic energy (left) and Gibb's free energy (right) for the chemisorption of H_2 by $Ti_8C_{12}H_4$ to form isomer H.

3.6.1 Equilibrium populations

The relative populations of hydrogenated forms of Ti_8C_{12} can be calculated according to their Boltzmann populations.

$$p_i = \frac{e^{-G_i/kT}}{\sum_j e^{-G_j/kT}}$$

where p_i is the population of species i and G_i is the absolute Gibb's free energy of species i, as calculated using the equations in Table 2.1. We found that in an excess of H_2, only Ti_8C_{12}, $Ti_8C_{12}H_2$, $Ti_8C_{12}H_4$ (isomer A), $Ti_8C_{12}H_4$ (isomer C), $Ti_8C_{12}H_6$ (isomer H) and $Ti_8C_{12}H_8$ (isomer I) exist in any appreciable equilibrium concentration at the conditions studied.

	Ti_8C_{12}	**Isomer A**	**Isomer C**	**Isomer H**	**Isomer I**
170 K / 100 ATM	0.00%	0.04%	0.00%	44.88%	55.08%
298 K / 1.0 ATM	0.02%	99.13%	0.20%	0.65%	0.00%
370 K / 0.1 ATM	99.64%	0.35%	0.00%	0.00%	0.00%

Table 3.9: The equilibrium populations of Ti_8C_{12} and its most stable hydrogenated forms.

Under standard conditions, isomer A exists in a large excess, whereas Ti_8C_{12} is fully dehydrogenated under high temperature / low pressure conditions. Under low temperature / high pressure conditions, isomers H and I ($Ti_8C_{12}H_6$ and $Ti_8C_{12}H_8$) exist in roughly equal quantities. However, as discussed above their production is slow compared to isomer A, which is the kinetic product under such conditions.

3.7 Summary

In summary, we have investigated the thermodynamics and kinetics involved in the dissociation of H_2 by Ti_8C_{12} nanoclusters over a range of desirable operating temperatures and pressures using hybrid density functional theory. The dissociation of H_2 by Ti_8C_{12} and its partially hydrogenated forms proceeds with an exceptionally low activation barrier. Given the difference in charge between carbon and titanium species in Ti_8C_{12}, the dissociation of H_2 by Ti_8C_{12} is heterolyitc, and therefore is a potential source of hydrogen for the regeneration of heterolyitc HSMs.

We have shown that, under standard conditions, Ti_8C_{12} is rapidly hydrogenated to form $Ti_8C_{12}H_4$, which can be dehydrogenated by increasing temperature and/or reducing pressure. Furthermore, in terms of thermodynamics $Ti_8C_{12}H_4$ would hydrogenate any depleted HSM which binds H_2 with a standard Gibbs free energy less than -0.246 eV / H_2

The subsequent hydrogenation of $Ti_8C_{12}H_4$ is less favourable, with no isomers of $Ti_8C_{12}H_6$ or $Ti_8C_{12}H_8$ stable under standard conditions. However, isomer H ($Ti_8C_{12}H_6$) and isomer I ($Ti_8C_{12}H_8$) are both stable at 170 K / 100 ATM and other low temperature / high pressure conditions. Although isomer H and isomer I are similarly stable, isomer I forms much more slowly Furthermore, isomer I is thermodynamically compatible with HSMs which adsorb hydrogen a standard Gibbs free energy less than -0.07 eV while isomer H is compatible with HSMs with a standard Gibbs free energy less than +0.129 eV. However, it is the fast kinetics of H_2 dissociation that are most interesting. Electronic activation barriers for the dissociation of H_2 by $Ti_8C_{12}H_x$ (x = 0, 2, 4, 6) are consistently < 0.3 eV with respect to free H_2 and < 0.5 eV with respect to physisorbed H_2.

References

1. Maj, Ł. and W. Grochala, *Theoretical Design of Catalysts for the Heterolytic Splitting of H2.* Advanced Functional Materials, 2006. **16**(16): p. 2061-2076.
2. Pilgrim, J.S. and M.A. Duncan, *Metallo-carbohedrenes: chromium, iron, and molybdenum analogs.* Journal of the American Chemical Society, 1993. **115**(15): p. 6958-6961.
3. Guo, B.C., et al., *Metallo-Carbohedrenes [M8c12+ (M = V, Zr, Hf, and Ti)] - a Class of Stable Molecular Cluster Ions.* Science, 1992. **256**(5056): p. 515-516.
4. Wei, S., et al., *Metallocarbohedrenes as a Class of Stable Neutral Clusters - Formation Mechanism of M8c12 (M = Ti and V).* Journal of Physical Chemistry, 1992. **96**(11): p. 4166-4168.
5. Cartier, S.F., B.D. May, and A.W. Castleman, *Formation, structure, and stabilities of metallocarbohedrenes.* Journal of Physical Chemistry, 1996. **100**(20): p. 8175-8179.
6. Rohmer, M.M., et al., *Ab-Initio Scf and Ci Investigations on Titanium Carbon Clusters - Metallocarbohedrenes Ti8c12 and Fcc Crystallites Ti14c13.* Journal of the American Chemical Society, 1995. **117**(1): p. 508-517.

7. Chen, H., et al., *Stability, Bonding, and Geometric Structure of Ti8c12, Ti8n12, V8c12, and Zr8c12.* Physical Review Letters, 1993. **71**(11): p. 1732-1735.

8. Castleman, A.W., B. Guo, and S. Wei, *Metallo-Carbohedrenes - a New Class of Molecular Clusters.* International Journal of Modern Physics B, 1992. **6**(23-24): p. 3587-3594.

9. Hou, H., et al., *Computational Study of the Geometry and Properties of the Metcars Ti8C12 and Mo8C12.* The Journal of Physical Chemistry A, 2003. **107**(44): p. 9344-9356.

10. Guo, B.C., K.P. Kerns, and A.W. Castleman, *Ti8c12+-Metallo-Carbohedrenes - a New Class of Molecular Clusters.* Science, 1992. **255**(5050): p. 1411-1413.

11. Gueorguiev, G.K. and J.M. Pacheco, *Structural Identification of Metcars.* Physical Review Letters, 2002. **88**(11): p. 115504.

12. Baruah, T., et al., *Predicted infrared and Raman spectra for neutral ${\mathrm{Ti}}_{8}{\mathrm{C}}_{12}$ isomers.* Physical Review A, 2002. **66**(5): p. 053201.

13. Sobhy, M.A., A.W. Castleman, and J.O. Sofo, *A density-functional study of the structural, electronic, magnetic, and vibrational properties of Ti8C12 metallocarbohedrynes.* The Journal of Chemical Physics, 2005. **123**(15): p. 154106.

14. Deng, K., W. Duan, and B. Gu, *Theoretical studies on the electronic structure of Ti8C12 isomers.* The Journal of Chemical Physics, 2004. **121**(9): p. 4123-4126.

15. Akman, N., et al., *Hydrogen storage capacity of titanium met-cars.* Journal of Physics-Condensed Matter, 2006. **18**(41): p. 9509-9517.

16. Banerjee, S., C.G.S. Pillai, and C. Majumder, *High capacity reversible hydrogen storage by metallo-carbohedrenes: An ab initio molecular dynamics simulation study.* Applied Physics Letters, 2013. **102**(7): p. 073901.

17. Zhao, Y.F., et al., *Self-catalyzed hydrogenation and dihydrogen adsorption on titanium carbide nanoparticles.* Chemical Physics Letters, 2006. **425**(4-6): p. 273-277.

Chapter 4

Phosphorenes

4.1 Background

Few-layered black phosphorus has been the subject of huge attention since the exfoliation of bulk black phosphorus in early 2014 and the subsequent assembly of the first black phosphorus field effect transistors (BP-FETs). The performance of early BP-FETs is encouraging, with their performance satisfying many of the requirements for next generation FETs discussed in Chapter 1. A theoretical understanding of the properties of black phosphorus exfoliates is important not only to aid the optimization of BP-FETs, but also to explore other potentially useful properties relating to optoelectronic, photovoltaic, thermoelectric and battery applications.

In this Chapter, we review the performance of early black phosphorus devices and investigate the ground state properties of bulk and few-layered black phosphorus using DFT. Our findings are generally in excellent agreement with results published elsewhere, and provide a context for the investigations discussed in Chapters 5 and 6.

4.1.1 Black phosphorus

Black phosphorus is the most thermodynamically and kinetically stable allotrope of elemental phosphorus under standard conditions [1, 2]. It has an orthorhombic structure consisting of puckered layers of interlinked six membered rings, as shown in Figure 4.1. The buckled layers of black phosphorus are in contrast with the planar layers of graphite. While graphite contains planar sp^2 carbon atoms and a delocalized network of π bonds, atoms in black phosphorus are sp^3 hybridized with lone pair electrons, with the geometric arrangement around each phosphorus atoms similar to the trigonal pyramidal structure of ammonia [3].

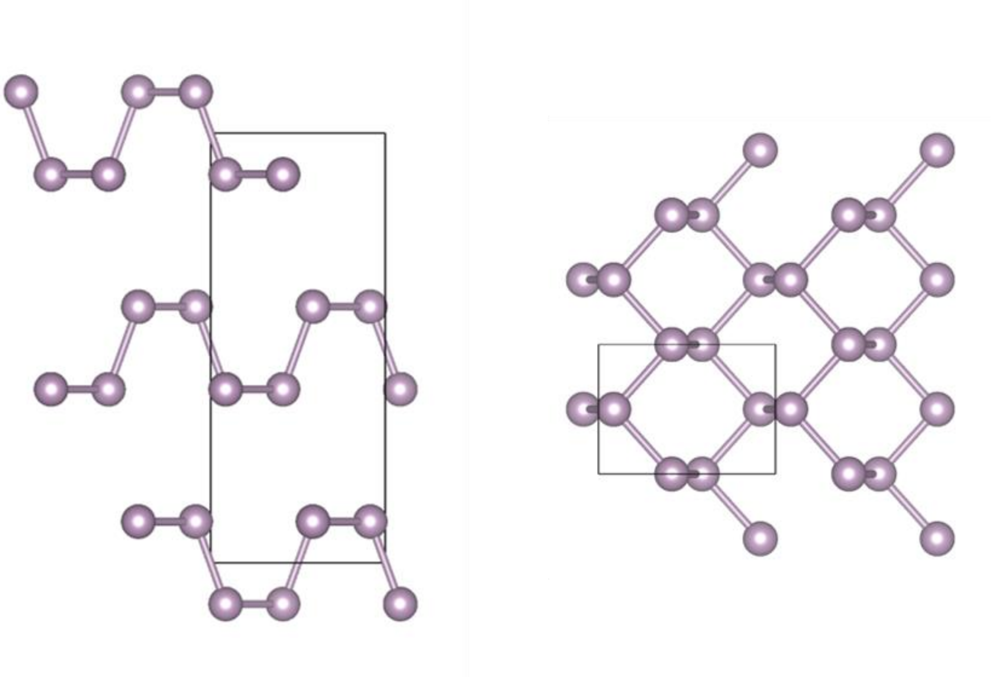

Figure 4.1: Side view of bulk black phosphorus (left) and the top view of one layer of bulk black phosphorus (right).

In terms of electronic structure, black phosphorus is a narrow-gap semiconductor with an experimentally determined band gap of between 0.31 and 0.33 eV [4, 5]. Theoretical and experimental studies have found that both conduction and valence band edges are located at Z in the Brillouin zone corresponding to the primitive unit cell of bulk black phosphorus. At room temperature, its average hole and electron mobilities are 350 cm^2 V^{-1} s^{-1} and 220 cm^2 V^{-1} s^{-1} respectively [5, 6]. Both hole and electron mobilities vary with $T^{-2/3}$, suggesting that scattering occurs mainly as a result of lattice vibrations. Furthermore, many studies have highlighted the anisotropic mobility of charge carriers in black phosphorus [7-9]. Charge carriers travelling perpendicular black phosphorus's quasi-planar layers (i.e. in the *z*-direction) show the lowest mobility, while charge carriers travelling in the *y*-direction (the 'armchair' direction) show the highest mobility. However, the low mobility of charge carriers in the *z*-direction does not tally with experimental or theoretical measurements of effective mass [10]. The effective masses of charge carriers travelling in the *z*-direction are significantly lower than of those travelling in the *x*, or 'zigzag', direction, despite showing lower mobility.

Early syntheses of black phosphorus involved heating white phosphorus to approximately 473 K under ~12 kilobars of pressure [11-13]. A later synthesis reported the preparation of single crystals of black phosphorus by slowly cooling a solution of white phosphorus in liquid bismuth from 673K to room temperature [4, 14]. However, the most recently reported synthesis uses Au_3SnP_7 to catalyze the conversion of red phosphorus to black phosphorus under low pressure, high temperature conditions [15]. So, while it is still challenging to produce yields of black phosphorus large enough for industrial applications, the recent interest in the compound will no doubt stimulate research into more efficient syntheses.

4.1.2 Early black phosphorus devices

The first BP-FETs were simultaneously reported by Liu *et al.* and Li *et al.* in 2014. Both devices used a back gate configuration with metal terminals, a Si / SiO_2 substrate and an exfoliated black phosphorus channel region [16, 17]. Samples of few-layered black phosphorus were collected using mechanical exfoliation techniques similar to those used to obtain graphene from graphite. The thickness of exfoliate used ranged between 2 and 50 nm, corresponding to between 4 and ~100 layers. Both studies found that the thickness of the black phosphorus channel had an enormous impact on device performance. Liu *et al*. reported that the on/off ratio decreased linearly with increasing channel thickness, from 10^5 at 2nm to 10^1 at 20 nm. Li *et al*. reported similar results, with the on/off also reaching 10^5 for samples thinner than 7.5 nm. The decrease in on/off ratio with increasing thickness can be easily explained; the back-gate configuration means that carrier concentrations are only changed in the bottom layers of the channel as gate voltages are applied, meaning that charge carriers are ever present in the upper layers of thicker channels. Furthermore, the band gap of few-layered black phosphorus decreases with increased thickness, also contributing to a decline in the on-off ratio [18, 19]. While the highest on-off ratios achieved to date are three order of magnitude lower than those reported for transition metal dichalcogenide (TMD) devices, they are far higher than those achieved in graphene devices, where semi-metallic character leads to on/off ratios in the order of 10^1.

In terms of charge carrier mobility, BP-FETs already outperform TMD devices. Even the best performing TMD devices have a modest *n*-type charge carrier mobility of 200 $cm^2 V^{-1} s^{-1}$, limiting their potential usefulness [20]. Meanwhile, BP-FETs have a much higher *p*-type charge carrier mobility, with Li *et al* reporting a field-effect mobility of 1,000 $cm^2 V^{-1} s^{-1}$ at 120 K and a room temperature mobility of 600 $cm^2 V^{-1} s^{-1}$. Meanwhile, Liu *et al.* and a number of other studies report a peak room temperature mobility of ~300 $cm^2 V^{-1} s^{-1}$ for devices with a channel thickness of ~10 nm. As the channel thickness is increased past 10 nm, the interlayer resistance steadily reduces net mobility, an effect that is particularly pronounced in back-gated devices where charge carriers must travel between layers in order to reach the gated layers. When the channel thickness is less than 10 nm, it has been postulated that scattering by charge impurities at the gate interface limits mobility [21].

While mobility in ~10 nm thick devices is already reasonable, there is a consensus that performances can be significantly improved through tuning. In order to increase mobility in thinner channels, it may be possible to use a top-gate configuration in conjunction with a capping high-*k* dielectric to screen charge impurities [22]. Furthermore, it has been suggested that charge carrier mobility is also adversely affected by chemisorbed species, contact resistance and the electronic anisotropy of black phosphorus. Liu *et al*. also reported a strong angular dependence on drain current, with a 50% anisotropy between orthogonal directions. Along with a similar trend in transconductance, this obervation suggests a large mobility variation in the *x*-*y* plane, and therefore careful channel orientation is necessary to ensure optimal mobility.

Interestingly, BP-FETs exhibit ambipolar behavior. Li *et al.* reported *p*-type conductance at gate voltages < -20 V and *n*-type mobility at gate voltages > 40 V. The ambipolar behavior observed is attributed to the narrow band gap of 8 nm thick black phosphorus used. While the Schottky barrier at the valence band edge is smaller than at the conduction band edge, both can be overcome through the application of a sufficient gate voltage. A later study investigating the effect of channel lengths and contact resistances on device performance found that *n*-type mobility is significantly enhanced at short channel lengths [23]. Ultimately, there is hope that the ambipolar nature of BP-FETs could be used to construct single material CMOS devices.

Overall, FET devices based around a black phosphorus channel show great promise. Charge carrier mobility and drain currents surpass those achieved in TMD devices, with the resulting fast operation meaning that gigahertz frequency levels have been achieved [24]. Furthermore, their on / off ratios and current saturation characteristics are vastly superior to those achieved using graphene. However, the future development of black phosphorus FETs faces a number of significant challenges. From a practical standpoint, the biggest problem faced is the surface instability of black phosphorus. Several studies have shown that few-layered black phosphorus samples degrade over time, wrecking device performance [25, 26][27]. The exact mechanism of this degradation remains unclear, with degradation pathways involving water, oxidation and photo-oxidation all suggested [28-30]. The most promising solution thus far has been to cap the channel region with an air-stable material. For example, recent studies have shown that device lifetimes can be lengthened by capping the channel with Al_2O_3 or 2D compounds such as graphene and boron nitride [31-33]. This early progress suggests that the stability issues encountered are not insurmountable, and furthermore new fabrication methods are likely to improve the quality of phosphorenes, reducing instability with respect to defect nucleated degradation [34]. Another consideration in optimizing phosphorene devices is the balance between mobility and the on/off ratio. Theoretically, thin flakes of black phosphorus in combination with a screening dielectric to counteract scattering by charge impurities should provide the best overall performance [35], and thus it is sensible to focus theoretical effects on the properties of phosphorenes with a low number of layers.

4.2 Simulations of bulk black phosphorus

While it is few-layered black phosphorus that has been the subject of so much recent attention, we began by investigating the bulk. It is important to understand which properties are inherent to the bulk and which emerge as a result of quantum confinement and other nanoscale effects when black phosphorus is exfoliated. Furthermore, given that bulk black phosphorus has been well characterized experimentally, we used simulations of the bulk to ascertain the accuracy of different exchange-correlation functionals. We worked under the assumption that methodologies which accurately reproduce the structure and electronic properties of bulk black phosphorus are likely to be more accurate in predicting the properties of its few-layered derivatives.

4.2.2 Methodology

Density functional calculations were performed using the VASP code, a plane-wave basis set truncated at 400 eV and PAW pseudopotentials to treat core electrons. More information about plane-wave DFT and pseudopotentials can be found in Section 2.2. We relaxed internal geometries using a conjugate gradient relaxation scheme until all interatomic forces were < 0.01 eV/Å, while lattice parameters were obtained using a Murnaghan fitting scheme [36]. For seven cell volumes between 91.2% and 109.2% of experiment, we relaxed the cell shape and internal geometry. The ground state cell volume was then obtained by fitting a parabola to the plot of energy versus cell volume. Regardless of the functional used, we found that the properties of bulk black phosphorus where converged when sampling *k*-space using a Monkhorst-Pack mesh of

8×8×3 [37]. For electronic structure calculations, a *k*-point density equivalent to that of a 100×100×50 Monkhorst-Pack mesh.

4.2.3 Comparison of functionals

We tested three exchange-correlation functionals: PBE [38], which uses the generalized gradient approximation (GGA) to calculate E_{xc}, PBEsol [39], a modified version of the PBE functional tailored for use in the solid state, and HSE06 [40], a screened hybrid functional which has been shown to predict accurately the electronic structure of semiconducting solids. A more detailed discussion of exchange-correlation functionals can be found in Chapter 2.

We found that relaxing the structure of black phosphorus using PBEsol underestimates the cell volume by over 7% with respect to experiment, while PBE and HSE06 overestimate cell volume by 10.5% and 5.7% respectively. However, in the case of PBE and HSE06, the majority of error in cell volume can be attributed to the overestimation of the c_0 lattice parameter, which is likely due to the neglect of van der Waals in standard DFT. Given the layered structure of bulk black phosphorus, it is reasonable to assume that van der Waals forces play an important role in determining the length of c_0. Given that standard time-independent DFT functionals do not account for van der Waals forces, we tested the effect of two different dispersion correction schemes. The D3 method of Grimme *at al.* provides an empirical energy correction, E_{disp}, for a given structure through the summation of empirical pair potentials between increasingly distant atomic pairs until convergence is reached [41]. Meanwhile, the vdW-DF functional of Langreth, Lundqvist *et al*. introduces a non-local, long-range part of the correlation functional, expressed in terms of a density-density interaction formula [42]. It is important to note that while both dispersion corrections can influence the geometry relaxation of a compound, once the structure's geometry is fully relaxed they do not affect electronic structure.

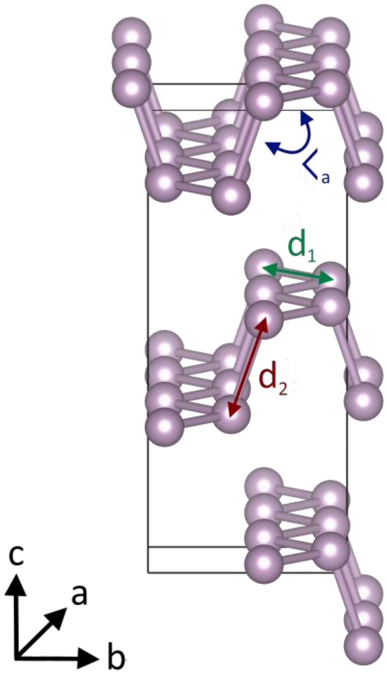

Figure 4.2: The relaxed structure of bulk black phosphorus.

	PBE	**PBEsol**	**HSE06**	**PBE-D3**	**HSE-D3**	**PBE-DF**	**HSE-DF**	**Exp.**
a (Å)	3.31	3.33	3.29	3.32	3.29	3.34	3.32	3.31
b (Å)	4.54	4.11	4.47	4.44	4.39	4.45	4.51	4.38
c (Å)	11.18	10.31	10.92	10.47	10.52	10.68	10.80	10.48
d_1 (Å)	2.23	2.23	2.23	2.22	2.21	2.22	2.23	2.22
d_2 (Å)	2.26	2.27	2.26	2.26	2.23	2.26	2.26	2.24
Angle (°)	103.4	103.4	103.4	102.6	102.8	103.1	103.2	102.1°

Table 4.1: The structural parameters and electronic band gap of bulk black phosphorus using a variety of functionals.

As seen in Table 4.1, structural relaxation using either PBE or HSE06 in conjunction with the DFT-D3 dispersion correction scheme (referred to as PBE-D3 and HSE-D3 respectively) accurately reproduced the experimentally measured geometry of bulk black phosphorus [43], with all parameters precise to within 1%. The use of the DFT-D3 correction scheme particularly improved the accuracy of the c_0 lattice parameter, mainly as a result of a decreased interlayer spacing. While the vdW-DF correction scheme also improved the accuracy of the c_0 lattice parameter it did not perform as well as DFT-D3, with PBE-DF and HSE-DF overestimating c_0 by 2% and 3% respectively. We therefore decided to use the DFT-D3 correction scheme throughout this study.

Given the potential applications of black phosphorus derivatives in electronic devices it is vital to calculate their electronic structure accurately. We tested the performance of PBE and HSE06 functionals in predicting the band gap of bulk black phosphorus. We found that using PBE-D3 to relax both the geometry and electronic structure of black phosphorus fails to recognize it as a semiconductor. Meanwhile, using HSE-D3 to perform the same calculations results in a band gap of 0.31 eV, which is in excellent agreement with the experimentally measured value of 0.30 eV. The contrasting performance of PBE and HSE06 in determining the electronic structure of black phosphorus is an example of the systematic errors that occur when ones assumes the equivalence of the Kohn-Sham gap calculated using local and semi-local functionals and the true band gap.

Our findings are in contrast with those initially reported in the literature, which suggest that an accurate band gap can only be obtained by increasing the proportion of exact exchange used in the HSE06 functional. However, we suggest that as long as an accurate geometry is obtained through the inclusion of dispersion corrections, the HSE06 functional with its default exchange contribution performs well.

While using HSE-D3 to relax both the geometry and the electronic structure of bulk black phosphorus provides a reassuringly accurate band gap, it is important to recognize the accuracy of the geometry obtained using PBE-D3 and to question whether it makes practical sense to use a computationally more expensive hybrid functional to obtain a very similar structure. Indeed, we found that using HSE06 to calculate the electronic structure of the geometry obtained using PBE-D3 correctly identifies the compound’s semiconducting nature and returns a reasonable band gap of 0.36 eV. Moreover, aside from a rigid shift in the relative energies of valence and conduction bands, the nature of the bands obtained using PBE-D3 and HSE-D3 derived geometries are very similar, with Table 4.2 showing that the effective masses calculated using the two methods are similar to within 4%.

	HSE-D3 / HSE06	PBE-D3 / HSE06
$m_{h,x}$	0.643	0.651
$m_{h,y}$	0.111	0.107
$m_{h,z}$	0.272	0.271
$m_{e,x}$	1.110	1.109
$m_{e,y}$	0.123	0.119
$m_{e,z}$	0.133	0.130
gap (eV)	0.314	0.356

Table 4.2: The hole and electron effective masses and band gap of bulk black phosphorus relaxed using HSE-D3.

Overall, we consider that in the interests of computational efficiency it is, in most cases, a reasonable compromise to perform geometry relaxations using PBE-D3 before using the HSE06 functional to investigate the structure's electronic properties. For larger systems, we will use the PBE functional to calculate both structural and electronic properties with the understanding that band gaps will be significantly underestimated.

4.2.4 Geometry and stacking effects

While the experimental ground state of black phosphorus has its layers arranged in an alternating AB arrangement, it is important to test the stability of other stacking arrangements. We identified a total of four likely arrangements, AA, AB, AC and AD, as shown in Figure 4.3. In the AA arrangement, the second layer is simply a replica of the first, rigidly shifted in the z-direction. In the ground state AB arrangement, the second layer is offset relative to the first by half a unit cell in the x-direction. In the AC arrangement, the second layer is reflected in the xy plane relative to the first, meaning that the zigzag channels in neighboring layers are directly opposing one another. This is the equivalent of offsetting the second layer by half a unit cell in both the x and y-directions. In the AD arrangement, the second layer is offset relative to the first by half a unit cell in the y-direction only.

We relaxed the both the unit cell and atomic coordinates of each stacking arrangement using PBE-D3. In each case, the initial stacking arrangement persisted following relaxation, suggesting that all of the arrangements tested are kinetically stable.

	AA	**AB**	**AC**	**AD**
a_0 (Å)	3.31	3.32	3.31	3.32
a_0 (Å)	4.42	4.44	4.50	4.46
Interlayer	3.44	3.09	3.70	3.29
ΔE (eV / atom)	0.026	0.000	0.040	0.015

Table 4.3: The structural parameters of four different stacking arrangements of black phosphorus.

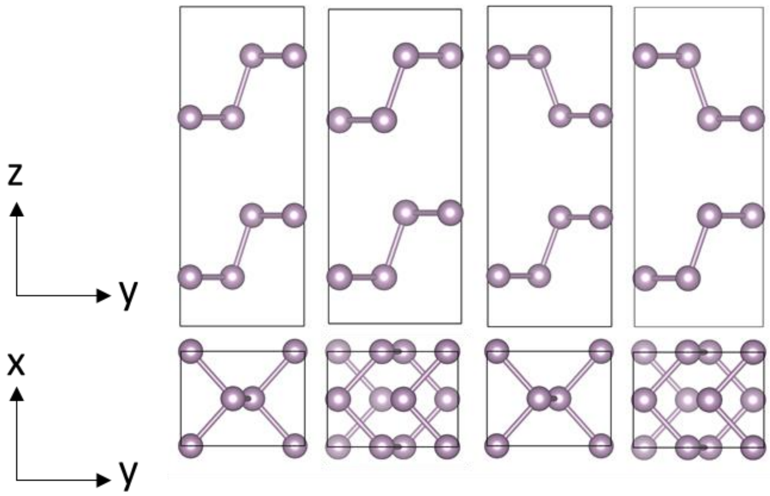

Figure 4.3: The lattice parameters, interlay spacing and relative energy of four stacking arrangements of bulk black phosphorus.

Our calculations confirm that the AB stacking arrangement is the most stable configuration, with the next most stable AD configuration 15 meV/atom higher in energy than AB. The AA configuration is the next most stable, 26 meV/atom higher in energy than AB. The AC configuration is the least stable, 40 meV/atom higher in energy than AB. There is a clear linear trend between relative stability and interlayer separation, and thus we conclude that there is more interlayer bonding in the AB structure than in any other structure.

By comparing the energies of pairs of configurations with respective layers offset by either ½ a or ½ b, it appears that offsetting the top layer by ½ a with respect to the bottom layer has a stabilizing effect of ~0.025 eV / atom, and that offsetting the top layer by ½ b with respect to the bottom layer has a consistent destabilizing effect of ~0.015 eV / atom. Overall, given that the absolute differences in energy between stacking arrangements are small, we predict a degree of stacking disorder in bulk black phosphorus. Furthermore, while we have studied only the most stable AB configuration, we suggest that fully investigating the effects of stacking disorder would be a useful exercise.

4.2.3 Density of states and band structure

The density of states (DoS), shown in Figure 4.4, shows that states around the valence band maximum (VBM) mainly comprise p_z orbital character, whereas states around the conduction band minimum (CBM) comprise a relatively even mixture of $p_{x,y,z}$ and s character. Meanwhile, the total density of states rises more rapidly when moving away from the CBM than when moving away from the VBM. A higher density of states around the CBM is potentially important given that current is directly proportional to the density of carrier states (see Section 2.3) favoring *n*-type conductivity over *p*-type conductivity.

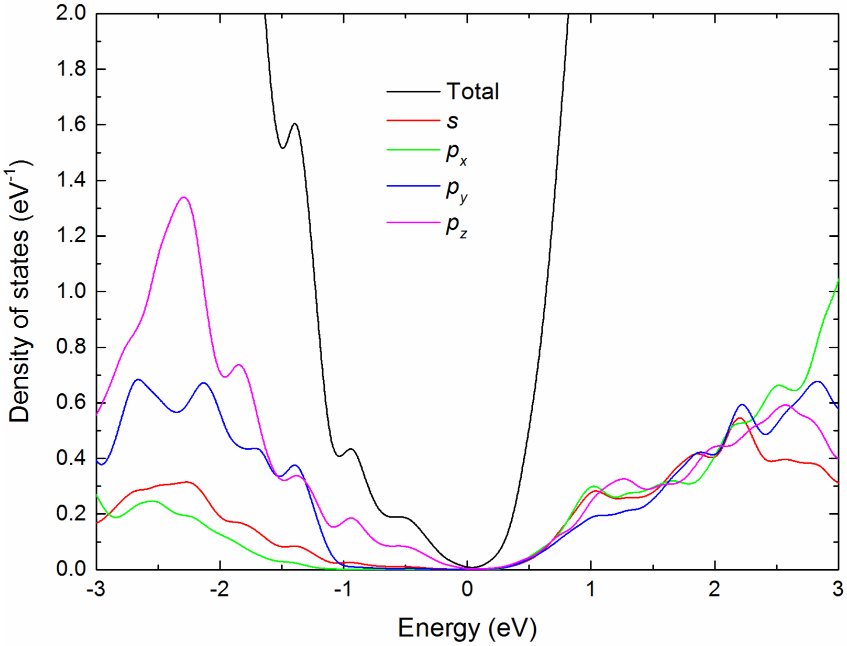

Figure 4.4: The orbital decomposed density of states of bulk black phosphorus.

The band structure of black phosphorus, shown in Figure 4.5, reveals that black phosphorus' band edges are more dispersive between Γ and Y/ Z than between Γ and X. This reflects the compound's structural and electronic anisotropy, and results in the highly anisotropic effective masses shown in Table 4.2. Electron and hole effective masses are low in the *y* and *z* directions, with m_h equal to 0.107 and 0.271 m_0 and m_e equal to 0.119 and 0.130 m_0 respectively. However, *x* direction effectively masses are far higher, with m_h equal to 0.651 and m_e equal to 1.109 m_0, suggesting low zigzag direction charge carrier mobility. The average effective mass $(m_x m_y m_z)^{1/3}$ of electrons is 0.258 m_0 and 0.266 m_0 for holes.

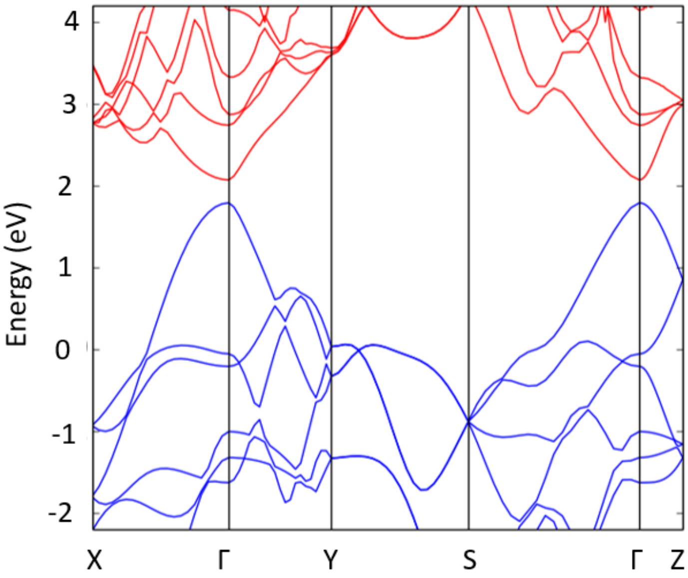

Figure 4.5: The band structure of bulk black phosphorus, calculated using the HSE06 functional.

Overall, our calculations are in good agreement with theoretical and experimental reports of effective masses in black phosphorus. They do not, however, directly correspond with measurements of charge carrier mobility in the *z*-direction. Under the assumption that scattering times are constant with respect to the direction of charge transport, our results imply that the conductivity is lower in the *x* direction than it is the *y* and *z* directions. However, experimental charge carrier mobilities are lower in the *z*-direction than in the *x*-direction, which suggests that scattering times are anisotropic and play an important role in determining overall mobility.

Meanwhile, the implications of the high band dispersion between Γ and Z extend beyond low *z*-direction effective masses. It suggests that the layers in black phosphorus are chemically coupled, which has important implications regarding the electronic structure of black phosphorus exfoliates. The manifesting quantum confinement effects are central to the properties of few-layered black phosphorus, as will be explored in Section 4.3.

4.3 Few layered black phosphorus

Monolayer black phosphorus has been dubbed phosphorene, something of a misnomer given the absence of π-bonding. The devices discussed in Section 4.1.2 used few-layered black phosphorus flakes between 2 and 50 nm thick, corresponding to between approximately 4 and 100 layers of phosphorene. However, it is likely that thinner channels will ultimately result in the best device performance, and therefore we have investigated one, two and three layered phosphorene compounds.

4.3.1 Methodology

As in Section 4.2, we performed DFT calculations using VASP with a plane-wave basis set truncated at 400 eV and PAW pseudopotentials to treat core electrons, see Chapter 2. Following our investigation of bulk black phosphorus, we used PBE-D3 to perform structural relaxations of few-layered phosphorenes and HSE06 to investigate their electronic properties. When relaxing crystal lattices and internal atomic positions, we used a conjugate gradient algorithm until all interatomic forces fell below 0.01 eV/Å. A vacuum region of over 20 Å was maintained perpendicular to the *xy* plane, with an additional 20 Å vacuum region separating the periodic images of PNRs within the plane. The geometries obtained were fully converged when *k*-space was sampled using a 9×9×1 Monkhorst-Pack mesh. For electronic structure calculations, a *k*-point density equivalent to that of a 100×100×1 Monkhorst-Pack mesh. Absolute band energies were calculated by subtracting the total local potential found directly in the middle of the vacuum region from the eigenvalues computed using DFT.

4.3.2 Geometry

The geometry of few-layered phosphorene remains similar to that of bulk black phosphorus, as can be seen in Table 4.4. The lattice constant running in the 'armchair' direction changes the most as the number of layers is decreased, with b_0 3% longer in phosphorene than in bulk black phosphorus. Meanwhile, all bond lengths remained constant when rounded to the nearest 0.01 Å, while the marked bond angle increased slightly when the number of layers is decreased.

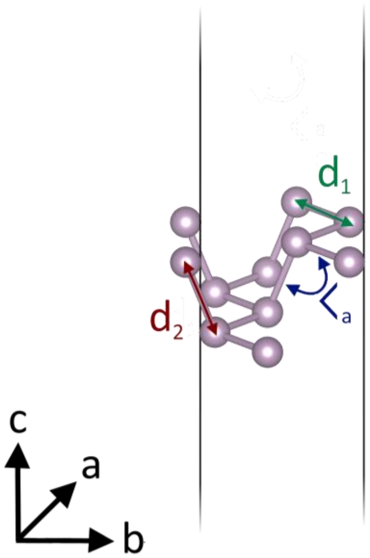

Figure 4.6: The structure of monolayer black phosphorus, phosphorene, relaxed using the PBE-DF functional.

	Monolayer	Bilayer	Trilayer	Bulk
a (Å)	3.294	3.304	3.309	3.320
b (Å)	4.604	4.523	4.479	4.441
d_1 (Å)	2.223	2.221	2.221	2.218
d_2 (Å)	2.264	2.262	2.260	2.258
Angle (°)	103.9	103.2	102.9	102.6
Interlayer (Å)	N/A	3.223	3.207	3.010

Table 4.4: The structural parameters of few-layered phosphorenes.

4.3.3 Exfoliation energy

In order to ascertain the exfoliation energy of black phosphorus, we calculated the relative energies of n-layered black phosphorus compounds, E_n, varying n between 1 and 7. The exfoliation energy for n-layered black phosphorus was calculated using the following formula:

$$E_{ex,n} = (E_{n-1} + E_1) - E_n$$

Our results show that E_{ex} tends towards 0.322 eV per unit cell as n → ∞, equating to exfoliation energy of 0.339 Jm^{-2}, comparable to the exfoliation energy of graphene, 0.390 Jm^{-2}. When dispersion forces are neglected, the exfoliation energy of black phosphorus is found to be an unrealistic 0.05 Jm^{-2}, highlighting the importance of van der Waals effects when modelling black phosphorus derivatives.

4.3.4 Band Gap

While the geometry of phosphorenes remains relatively similar to that of the bulk, their electronic properties change dramatically due to quantum confinement effects. We calculated the electronic structure of n-layered black phosphorus compounds for n = 1 – 6, and found that the band gap increases exponentially as $n \rightarrow 1$.

As shown in Figure 4.7, bulk black phosphorus has a band gap of 0.36 eV and monolayer black phosphorus has a band gap is 1.53 eV, close to the experimentally measured optical gap of 1.55 eV. However, optical gaps also include exciton binding effects, which are considerable in quasi-2D compounds but are in not accounted for in standard DFT. The actual band gap of phosphorene is therefore likely to be significantly higher than 1.55 eV, and indeed state of the art GW calculations report that phosphorene's band gap is around 2.2 eV, with an exciton binding energy of around 0.6 eV predicted using the Bethe-Salpeter Equation (BSE) [44]. The band gap of black phosphorus exfoliates can therefore be tailored to be between 0.30 and 2.2 eV, suggesting a suitability for use in number of electronic and optoelectronic applications.

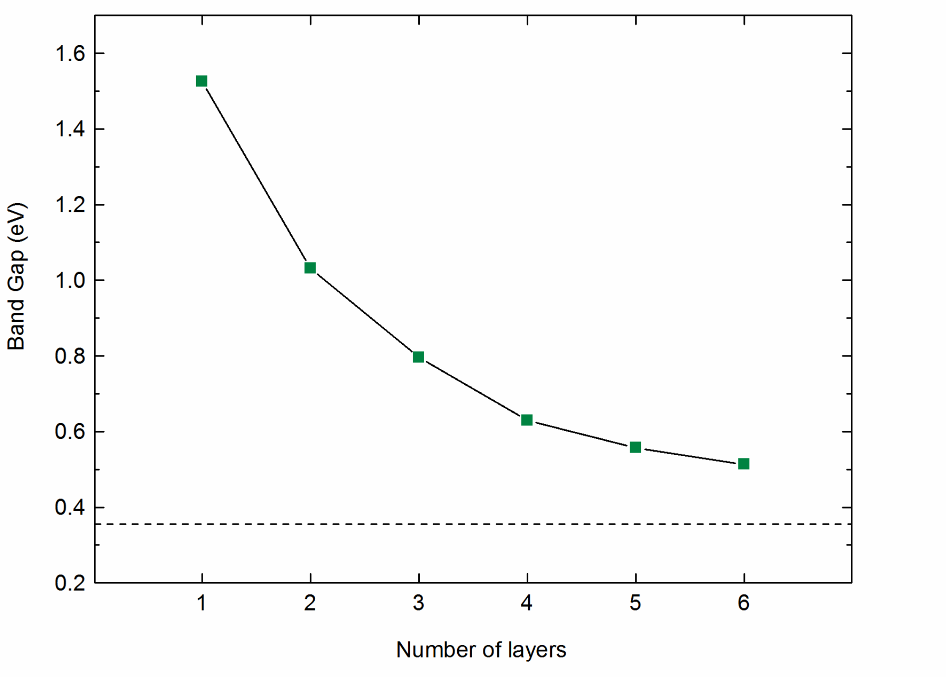

Figure 4.7: The band gap of *n*-layered black phosphorus (*n* = 1-6). The dotted green line marks the band gap of bulk black phosphorus (n = ∞).

Exfoliating bulk black phosphorus to produce *N*-layered phosphorene effectively confines electronic wavefunctions along the z axis between z and $z+\frac{N}{2}c_0$. We explored the effect of confining bulk wavefunctions by applying periodic boundary conditions (PBCS). When the bulk is confined between z and $z+\frac{N}{2}c_0$, only electronic states at *k*-points defined by the below equation are allowed:[1]

$$k_z = \frac{\pi}{c_0} . \frac{n}{\mathrm{N}/2} \qquad n = 1 \ \ldots \mathrm{N}/2$$

We sampled the Brillouin zone of bulk black phosphorus at the *k*-points allowed according to the above condition. For each value of *N*, the highest energy valence state and the lowest energy conduction state were found when *n* = 1, which is unsurprising given that both band edges of bulk black phosphorus are located at the Γ-point ($k = 0$). We found that applying PBCs to the bulk

---

[1] Note that the factor of $1/2$ arises as each unit cell of black phosphorus consists of two layers

results in a significantly higher band gap than is calculated by directly modelling *N*-layered phosphorene, see Figure 4.8.

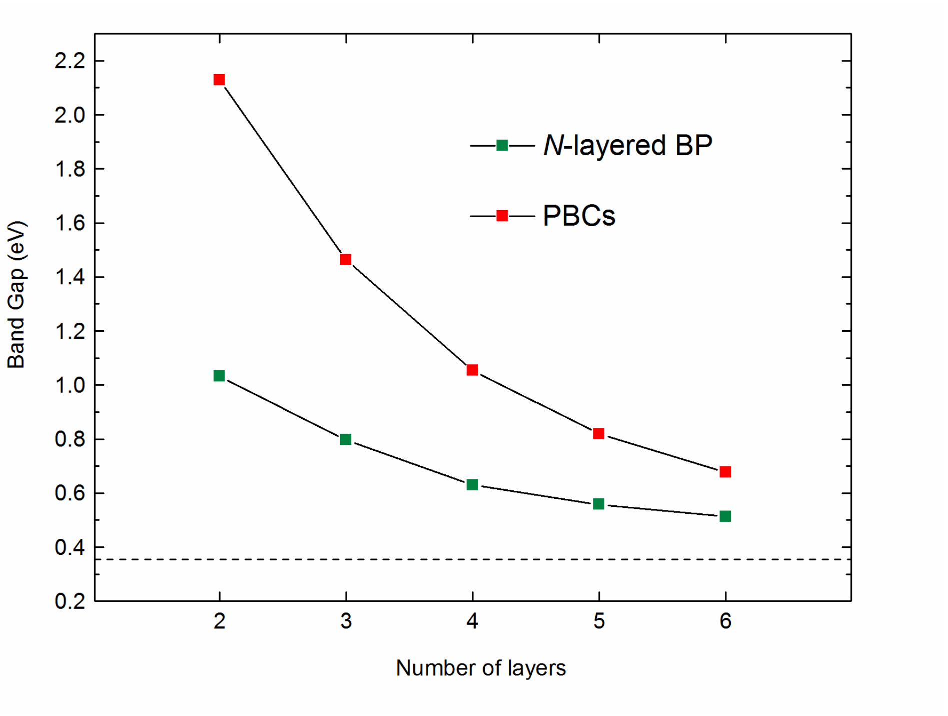

Figure 4.8: The band gap of *n*-layered black phosphorus (*n* = 1-6), calculated using DFT and PBCs. The dotted green line marks the band gap of bulk black phosphorus (n = ∞).

The differences between band gaps calculated by directly modelling few-layered phosphorenes and those calculated by applying PBCs to the bulk can, however, be explained. When PBCs are applied to the bulk, confined wavefunctions are zero at z and $z + \frac{N}{2}c_0$, whereas in few-layered compounds the wavefunction tends to zero as the vacuum level is approached. Also, the structure of the bulk is slightly different from that of few layered compounds, see Table 4.4. Both effects are more considerable when *N* is small, and hence as *N* increases the difference between the band gap predicted using PBCs and the band gap predicted by directly modelling *N*-layered phosphorene becomes smaller. We therefore suppose that applying PBCs to the bulk represents a good way of predicting the band gap of many-layered black phosphorus, particularly given that the direct modelling of large systems can be computationally demanding.

4.3.5 Band structure and effective mass

The band structure of few-layered phosphorene reveals a direct band gap located at the Γ-point. As can be seen in Figure 4.9, both conduction and valence band edges are relatively flat moving from Γ to X but are highly dispersive moving from Γ to Y, leading to the highly anisotropic effective masses.

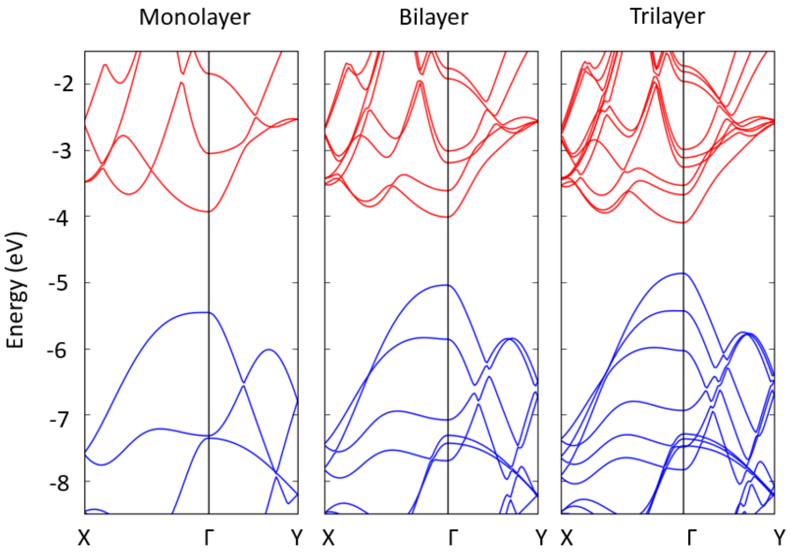

Figure 4.9: The band structures of monolayer, bilayer and trilayer phosphorenes, with band energies aligned to the vacuum level.

As seen in Table 4.5, both electron and hole effective masses are low in the armchair direction in monolayer, bilayer and trilayer phosphorene, ranging between 0.16 and 0.19 m_0. While these masses are slightly higher than the corresponding bulk effective masses, it is clear that the high charge carrier mobility in the armchair direction is maintained when exfoliating down from the bulk to monolayer phosphorene. Moreover, effective masses < 0.2 m_0 are very low when compared to other quasi-2D compounds: studies of monolayer MoS2 report that electron and hole effective masses are both higher, 0.54 m_0 and 0.44 m_0 respectively [45].

Zigzag direction effective masses are significantly higher than armchair direction effective masses. Our results are not only in good agreement with a number of other theoretical studies, but also with the experimentally reported angular dependence of charge carrier mobility. Electron effective masses in the zigzag direction were relatively consistent regardless of the number of layers, ranging between 1.21 m_0 in monolayer phosphorene to 1.16m_0 in trilayer phosphorene and 1.11 m_0 in the bulk. However, the hole effective mass in the zigzag direction, $m_{h,x}$, increases dramatically when N is small. In agreement with other calculations [44], this effect is most dramatic in monolayer phosphorene, where $m_{h,x}$ ~ 6 m_0. Such a high effective mass is the result of an unusually flat region around the VBM, as shown in Figure 4.10. In bilayer and trilayer phosphorene, $m_{h,x}$ falls towards the bulk value of $m_{h,x}$ = 0.68 m_0. The fact that $m_{h,x}$ falls with increasing N is important, particularly given that black phosphorus is naturally *p*-type. Our results suggest that, subject to isotropic scattering times, the degree of anisotropy in charge carrier mobility is likely to increase as the number of layers is reduced and $m_{h,x}$ rises.

	Monolayer	**Bilayer**	**Trilayer**	**Bulk**
$\boldsymbol{m_{h,x}}$ **(VBM)**	6.12 m_0	1.213 m_0	1.01 m_0	0.651 m_0
$\boldsymbol{m_{h,y}}$ **(VBM)**	0.17 m_0	0.16 m_0	0.16 m_0	0.107 m_0
$\boldsymbol{m_{e,x}}$ **(CBM)**	1.21 m_0	1.18 m_0	1.16 m_0	1.109 m_0
$\boldsymbol{m_{e,y}}$ **(CBM)**	0.19 m_0	0.19 m_0	0.18 m_0	0.119 m_0

Table 4.5: The hole and electron effective masses of monolayer and bilayer phosphorene

.

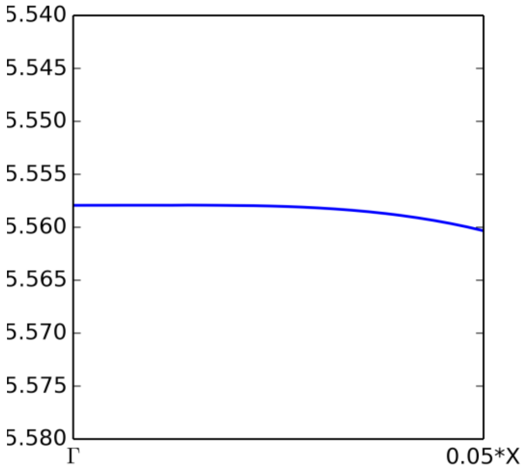

Figure 4.10: The band structure of monolayer black phosphorus at high resolution between Γ and 0.1 × X.

Other recent studies not only calculated the effective mass but also predicted charge carrier mobility using the deformation potential approximation. Despite the high corresponding effective mass, Qiao *et al.* reported an enormous room temperature hole mobility of 26,000 cm^{2}V^{-1}s^{-1} in the zigzag direction of phosphorene, a result attributed to an extremely low acoustic phonon scattering [44]. Meanwhile, in the armchair direction, $\mu_{h,y}$ = 700 cm^{2}V^{-1}s^{-1} despite a much lower hole effective mass. For multi-layered phosphorenes, hole mobilities $\mu_{h,y}$ and $\mu_{h,x}$ were found to be similar, reaching 2,800 and 2,200 cm^{2}V^{-1}s^{-1} respectively. In terms of electron mobilities at the CBM, $\mu_{e,y}$ and $\mu_{e,x}$ have been calcualted in the range of 1,100 – 2,100 and 80 – 200 cm^{2}V^{-1}s^{-1} respectively [44, 46].

4.3.6 Density of states

The DoS of monolayer phosphorene is relatively similar to that of bulk black phosphorus, albeit with a significantly enlarged band gap. The composition of valence states closely resembles that of the bulk, with a strong contribution from the p_z orbitals. However, p_z orbitals also contribute most strongly to phosphorene's shallow conduction states, whereas in the bulk all three p states contribute equally.

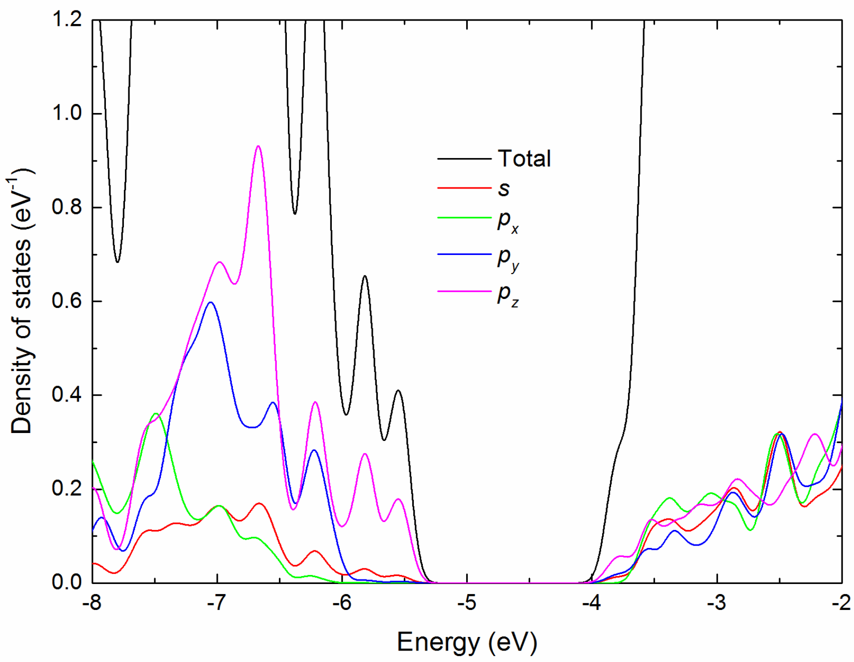

Figure 4.11: The orbital decomposed density of states of monolayer phosphorene.

The orbital decomposed contributions to wavefunctions at the VBM and CBM reveal that both band edges are indeed dominated by p_z character, with smaller contributions from p_y and s orbitals. There is no contribution whatsoever from p_x orbitals at either band edge, which helps to explain phosphorene's high x direction charge carrier masses. The site decomposed phase factors of the p_z orbitals, as shown in Figure 4.12, reveal that orbitals making up the VBM are bonding in the z-direction whereas the orbitals making up the CBM are anti-bonding in the z-direction. The importance of the relative bonding character of electronic states at the VBM and CBM will become apparent in Chapter 5.

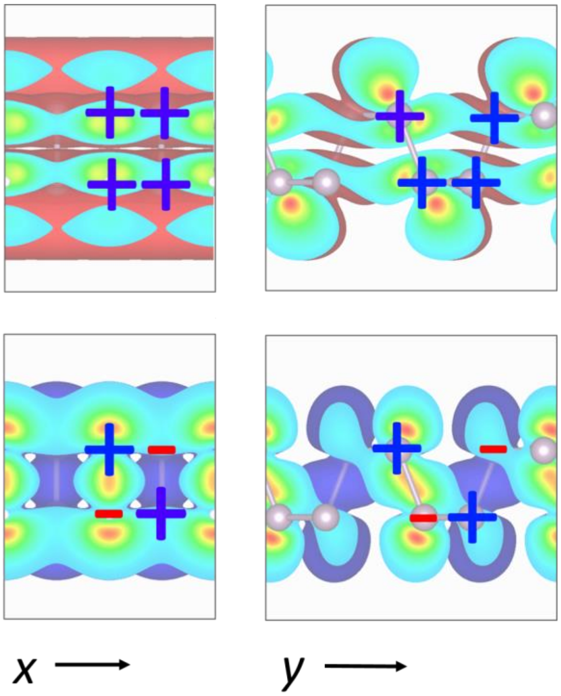

Figure 4.12: The charge density of electronic states at phosphorene's VBM (bottom) and CBM (top) viewed along the zigzag (left) and armchair (right) directions. The phase factors of the constituent p_z orbitals are also marked, + or −.

4.4 Summary

We tested various exchange-correlation functionals on their ability to reproduce the experimentally measured properties of bulk black phosphorus. We found that using the PBE functional in combination with the DFT-D3 van der Waals correction scheme accurately reproduces the geometry of bulk black phosphorus. However, the PBE functional predicts that black phosphorus is a metal, whereas the HSE06 functional accurately predicts a band gap in the region of 0.3 eV. We therefore used PBE-D3 to perform structural relaxations and HSE06 to calculate electronic structure when investigating few-layered phosphorenes.

The band gaps of few-layered phosphorenes are increased with respect to the bulk and can be tuned by varying the number of layers. The range within which the band gap can be tuned, from ~0.3 eV in the bulk to 1.53 eV in monolayer phosphorene, is potentially useful for an array of applications.

The low armchair direction charge carrier effective masses of bulk black phosphorus are maintained upon exfoliation. However, zigzag direction hole effective mass increases dramatically from 0.65 m_0 in bulk black phosphorus to > 6 m_0 in monolayer phosphorene, suggesting that anisotropy increases as the number of layers is decreased.

Given the recent advent of interest in few-layered black phosphorus compounds, many of their properties remain unexplored, making it a rich new field of research. The next two chapters of this thesis therefore focus on few-layered black phosphorus, with Chapter 4 investigating the effects of deforming few-layered phosphorenes and Chapter 5 investigating the properties of phosphorene nanoribbons.

References

1. Wiberg, E., N. Wiberg, and A.F. Holleman, *Inorganic chemistry*. 2001, San Diego; Berlin; New York: Academic Press ; De Gruyter.

2. Chang, K.J. and M.L. Cohen, *Structural Stability of Phases of Black Phosphorus.* Physical Review B, 1986. **33**(9): p. 6177-6186.

3. Charlier, J.C., et al., *Tight-Binding Model for the Electronic-Properties of Simple Hexagonal Graphite.* Physical Review B, 1991. **44**(24): p. 13237-13249.

4. Maruyama, Y., et al., *Synthesis and Some Properties of Black Phosphorus Single-Crystals.* Physica B & C, 1981. **105**(1-3): p. 99-102.

5. Keyes, R.W., *The Electrical Properties of Black Phosphorus.* Physical Review, 1953. **92**(3): p. 580-584.

6. Liu, H., et al., *Semiconducting black phosphorus: synthesis, transport properties and electronic applications.* Chemical Society Reviews, 2015. **44**(9): p. 2732-2743.

7. Shirotani, I., *Growth of Large Single Crystals of Black Phosphorus at High Pressures and Temperatures, and its Electrical Properties.* Molecular Crystals and Liquid Crystals, 1982. **86**(1): p. 203-211.

8. Akahama, Y.E., S; Narita, S, *Electrical properties of single-crystal black phosphorus under pressure.* Physica B+C, 1986. **139-140**: p. 397.

9. Narita, S., et al., *Electrical and Optical-Properties of Black Phosphorus Single-Crystals.* Physica B & C, 1983. **117**(Mar): p. 422-424.

10. Narita, S., et al., *Far-Infrared Cyclotron-Resonance Absorptions in Black Phosphorus Single-Crystals.* Journal of the Physical Society of Japan, 1983. **52**(10): p. 3544-3553.

11. Warschauer, D.M., *Electrical and Optical Properties of Crystalline Black Phosporus.* Journal of Applied Physics, 1963. **34**(7): p. 1853-&.

12. Ellis, R.C. and D.M. Warschauer, *Synthesis of Semiconducting Black Phosphorus.* Journal of the Electrochemical Society, 1962. **109**(8): p. C207-C207.

13. Bridgman, P.W., *Two new modifications of phosphorus.* Journal of the American Chemical Society, 1914. **36**: p. 1344-1363.

14. Brown, A. and Rundqvis.S, *Refinement of Crystal Structure of Black Phosphorous.* Acta Crystallographica, 1965. **19**: p. 684-&.

15. Lange, S., P. Schmidt, and T. Nilges, *Au3SnP7@black phosphorus: An easy access to black phosphorus.* Inorganic Chemistry, 2007. **46**(10): p. 4028-4035.

16. Liu, H., et al., *Phosphorene: An Unexplored 2D Semiconductor with a High Hole Mobility.* ACS Nano, 2014. **8**(4): p. 4033-4041.

17. Li, L., et al., *Black phosphorus field-effect transistors.* Nat Nano, 2014. **9**(5): p. 372-377.

18. Zhang, S., et al., *Extraordinary Photoluminescence and Strong Temperature/Angle-Dependent Raman Responses in Few-Layer Phosphorene.* ACS Nano, 2014. **8**(9): p. 9590-9596.

19. Tran, V., et al., *Layer-controlled band gap and anisotropic excitons in few-layer black phosphorus.* Physical Review B, 2014. **89**(23): p. 235319.

20. Yoon, Y., K. Ganapathi, and S. Salahuddin, *How Good Can Monolayer MoS2 Transistors Be?* Nano Letters, 2011. **11**(9): p. 3768-3773.

21. Das, S., et al., *High Performance Multilayer MoS2 Transistors with Scandium Contacts.* Nano Letters, 2013. **13**(1): p. 100-105.

22. Jena, D. and A. Konar, *Enhancement of carrier mobility in semiconductor nanostructures by dielectric engineering.* Physical Review Letters, 2007. **98**(13).

23. Du, Y.C., et al., *Device Perspective for Black Phosphorus Field-Effect Transistors: Contact Resistance, Ambipolar Behavior, and Scaling.* Acs Nano, 2014. **8**(10): p. 10035-10042.

24. Wang, H., et al., *Black Phosphorus Radio-Frequency Transistors.* Nano Letters, 2014. **14**(11): p. 6424-6429.

25. Castellanos-Gomez, A., et al., *Isolation and characterization of few-layer black phosphorus.* 2D Materials, 2014. **1**(2).

26. Island, J.O., et al., *Environmental instability of few-layer black phosphorus.* 2d Materials, 2015. **2**(1).

27. Koenig, S.P., et al., *Electric field effect in ultrathin black phosphorus.* Applied Physics Letters, 2014. **104**(10).

28. Utt, K.L., et al., *Intrinsic Defects, Fluctuations of the Local Shape, and the Photo-Oxidation of Black Phosphorus.* ACS Central Science, 2015. **1**(6): p. 320-327.

29. Ziletti, A., et al., *Oxygen Defects in Phosphorene.* Physical Review Letters, 2015. **114**(4).

30. Carvalho, A. and A.H.C. Neto, *Phosphorene: Overcoming the Oxidation Barrier.* ACS Central Science, 2015. **1**(6): p. 289-291.

31. Luo, X., et al., *Temporal and Thermal Stability of Al2O3-Passivated Phosphorene MOSFETs.* Ieee Electron Device Letters, 2014. **35**(12): p. 1314-1316.

32. Kim, J.S., et al., *Toward air-stable multilayer phosphorene thin-films and transistors.* Scientific Reports, 2015. **5**.

33. Doganov, R.A., et al., *Transport properties of pristine few-layer black phosphorus by van der Waals passivation in an inert atmosphere.* Nature Communications, 2015. **6**.

34. Lu, W., et al., *Plasma-assisted fabrication of monolayer phosphorene and its Raman characterization.* Nano Research, 2014. **7**(6): p. 853-859.

35. Lam, K.T., Z.P. Dong, and J. Guo, *Performance Limits Projection of Black Phosphorous Field-Effect Transistors.* Ieee Electron Device Letters, 2014. **35**(9): p. 963-965.

36. Birch, F., *Finite Elastic Strain of Cubic Crystals.* Physical Review, 1947. **71**(11): p. 809-824.

37. Monkhorst, H.J. and J.D. Pack, *Special points for Brillouin-zone integrations.* Physical Review B, 1976. **13**(12): p. 5188-5192.

38. Perdew, J.P., K. Burke, and M. Ernzerhof, *Generalized Gradient Approximation Made Simple.* Physical Review Letters, 1996. **77**(18): p. 3865-3868.

39. Perdew, J.P., et al., *Restoring the Density-Gradient Expansion for Exchange in Solids and Surfaces.* Physical Review Letters, 2008. **100**(13): p. 136406.

40. Heyd, J. and G.E. Scuseria, *Efficient hybrid density functional calculations in solids: Assessment of the Heyd-Scuseria-Ernzerhof screened Coulomb hybrid functional.* Journal of Chemical Physics, 2004. **121**(3): p. 1187-1192.

41. Grimme, S., et al., *A consistent and accurate ab initio parametrization of density functional dispersion correction (DFT-D) for the 94 elements H-Pu.* The Journal of Chemical Physics, 2010. **132**(15): p. 154104.

42. Dion, M., et al., *Van der Waals Density Functional for General Geometries.* Physical Review Letters, 2004. **92**(24): p. 246401.

43. Brown, A. and S. Rundqvist, *Refinement of the crystal structure of black phosphorus.* Acta Crystallographica, 1965. **19**(4): p. 684-685.

44. Qiao, J., et al., *High-mobility transport anisotropy and linear dichroism in few-layer black phosphorus.* Nat Commun, 2014. **5**.

45. Kadantsev, E.S. and P. Hawrylak, *Electronic structure of a single MoS2 monolayer.* Solid State Communications, 2012. **152**(10): p. 909-913.

46. Fei, R. and L. Yang, *Strain-Engineering the Anisotropic Electrical Conductance of Few-Layer Black Phosphorus.* Nano Letters, 2014. **14**(5): p. 2884-2889.

Chapter 5

Deforming Phosphorenes

5.1 Background

In this chapter, we investigate the response of phosphorene to different types of strain. Our work complements a number of studies investigating the effects of in-plane strain on phosphorene which studies report that, by virtue of its puckered structure, phosphorene can be strained with relative ease and has a large critical strain [1-3].

The structural anisotropy of phosphorene results in an orientation dependent Young's modulus of 44 GPa in the armchair direction and 166 GPa in the zigzag direction, with corresponding in-plane stiffness of 105.2 GPa nm and 22.4 GPa nm respectively [4]. While this observation suggests that strain is easier to apply in the armchair direction than in the zigzag direction, both Young's moduli are significantly lower than the Young's moduli of graphene (1000 GPa) [5], monolayer MoS_2 (330 GPa) [6], and monolayer h-BN (250 GPa) [7]. Furthermore, phosphorene's reported critical strain is large: 27% in the armchair direction and 30% zigzag directions – much higher than the 6 – 11% reported for MoS_2 [1] [8].

Phosphorene's structural anisotropy also leads to interesting electronic effects on straining. Peng *et al.* found that a direct to indirect band gap transition can be induced through the application of strains $\varepsilon < -2$ % or $\varepsilon > 8\%$ in the zigzag direction and $\varepsilon < -8\%$ or $\varepsilon > 8\%$ in the armchair direction [3]. The same study also reported the variation in phosphorene's band gap under uniaxial strains in the range $-12\% < \varepsilon < +12\%$. Phosphorene's band gap can be varied between 0.05 eV and 1.00 eV through the application of zigzag direction strains, and between 0.2 eV and 1.1 eV through the application of armchair direction strains. The fact that the band gap can be modulate by ~ 1 eV through the application of uniaxial strain suggests that straining could be used to tailor phosphorene for use in different electronic devices.

However, it is not only the size of the phosphorene's band gap that can be modified through the application of strain. The changing nature of its valence and conduction band edges means that both hole and electron charge carrier mobilities can be varied. For example, Fei and Yang investigated the properties of a new conduction band edge that emerges when phosphorene is strained by more than +3% in the zigzag direction [4]. At the emergent CBM, the zigzag direction effective mass is almost an order of magnitude lower than the armchair direction effective mass. This anisotropy is the exact opposite of the anisotropy observed in ground state phosphorene, and results in an accompanying change in orientation dependent electron mobility. In ground state phosphorene, the zigzag direction electron mobility, $\mu_{e,x}$, is < 200 $cm^2V^{-1}s^{-1}$ and the armchair direction electron mobility, $\mu_{e,y}$, is > 2000 $cm^2V^{-1}s^{-1}$. In strained phosphorene, $\mu_{e,x}$ rises to almost 2000 $cm^2V^{-1}s^{-1}$ and $\mu_{e,y}$ falls to < 200 $cm^2V^{-1}s^{-1}$. Given that hole transport remains unaffected, strains greater than +3% in the zigzag direction rotate the preferred direction for electron transport by 90° with respect to the preferred direction for hole transport.

While the literature has focussed on the effects of in-plane straining, it is important to consider other, lower energy responses to in-plane forces. Furthermore, we have investigated a possible phase transformation when phosphorene is subject to extensive strain in Section 5.4, and an alternative response to compressive strain, bending, in Section 5.3. However, first of all, we look at the effects of subjecting bilayer phosphorene to normal compression.

5.2 Compressing Bilayer Phosphorene

Despite the interesting effects of in-plain straining on the electronic properties of phosphorene, the application of such strains is experimentally challenging. Meanwhile, compressions perpendicular to the surface of few-layered materials are more easily realised. We therefore investigated the effects of normal strain on bilayer phosphorene.

5.2.1 Methodology

Density functional calculations were performed using the VASP code. We used a plane-wave basis set truncated at 400 eV and PAW pseudopotentials to treat core electrons. More information about plane-wave DFT and pseudopotentials can be found in Section 2.2. Having shown in Chapter 4 that it is not necessary to use computationally expensive hybrid functionals in order to obtain accurate geometries, we used the PBE functional in combination with the DFT-D3 dispersion correction scheme to relax crystal lattices and internal atomic positions. Furthermore, we used a conjugate gradient algorithm to relax structures until all interatomic forces fell below 0.01 eV/Å, with a vacuum region of over 20 Å maintained perpendicular to the *xy* plane in order to avoid spurious interactions between images. The geometries obtained were fully converged when *k*-space was sampled using a 10×10×1 Monkhorst-Pack mesh. Meanwhile, when investigating bilayer phosphorene's electronic structure, we used the HSE06 functional. For these calculations, we used a *k*-point density equivalent to that of a 100×100×1 Monkhorst-Pack mesh. Absolute band energies were obtained by subtracting the total local potential found directly in the middle of the vacuum region from the eigenvalues computed using DFT [9].

5.2.2 Ground state bilayer phosphorene

We investigated the stability of four different stacking arrangements of bilayer phosphorene, AA, AB, AC and AD. These arrangements, shown in Figure 5.1, are analogous to the bulk stacking arrangements investigated in Section 4.3. In the AA arrangement, the second layer is a replica of the first layer, rigidly translated along the *z* axis. In the AB arrangement, the second layer is offset relative to the first by half a unit cell in the *x*-direction. In the AC arrangement, the second layer is offset relative to the first by half a unit cell in both the *x*-direction and the *y*-direction, meaning that the zigzag channels in neighboring layers are directly opposing one another. In the AD arrangement the second layer is offset relative to the first by half a unit cell in the *y*-direction only. The relaxed a_0 lattice parameter is similar across all four stacking arrangements, varying by just 0.003 Å. The b_0 lattice parameter is, however, slightly lower in the AA and AB stacking arrangements than in the AC and AD stacking arrangements.

We found that bilayer phosphorene is most stable in its AB stacking arrangement, which is 8.5 meV per atom more stable than the next most stable AD stacking arrangement, with the AA arrangement 9.3 meV per atom less stable and the AC stacking arrangement 16.3 meV per atom less stable. The relationship between interlayer distance and stability is approximately linear, with less stable stacking arrangements having a higher interlayer spacing. For example, the ground state interlayer spacing in bilayer phosphorene is lowest in the most stable AB arrangement, 3.20 Å, and rises to 3.82 Å in the AC arrangement where ΔE = 16.3 meV. This is consistent with the assumption that the relative stability of stacking arrangements is determined by the extent of interlayer bonding. Given that the AB arrangement is not only the most stable arrangement of bilayer phosphorene but is also the produced through the exfoliation of bulk black phosphorus, we will disregard other stacking arrangements for the remainder of this investigation.

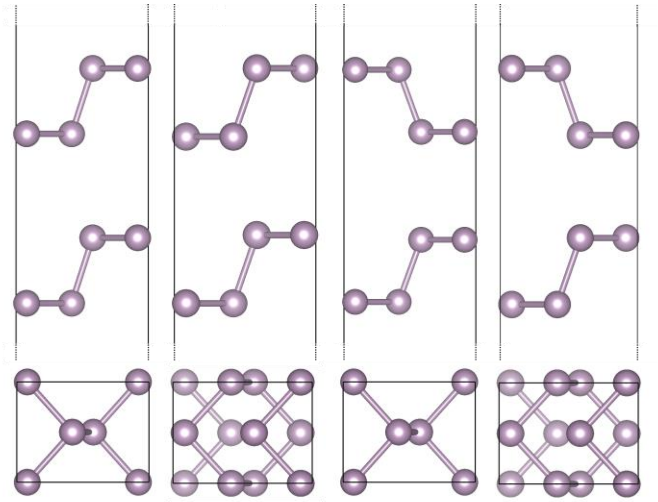

Figure 5.1: The structure of four stacking arrangements of bilayer phosphorene: AA, AB, AC, AD (from left to right).

	AA	**AB**	**AC**	**AD**
a (Å)	3.299	3.302	3.299	3.300
b (Å)	4.511	4.503	4.554	4.541
***Interlayer* (Å)**	3.519	3.204	3.815	3.461
ΔE / atom	9.3 meV	0 meV	16.3 meV	8.5 meV

Table 5.1: The structural parameters and relative energy of four stacking. arrangements of bilayer phosphorene.

The electronic structure of ground state bilayer phosphorene was investigated in Chapter 3. In summary, we found that bilayer phosphorene has a direct band gap of 1.05 eV, with anisotropic electron and hole effective masses of $m_{h,x/y}$ = 1.213 / 0.160 m_0 and $m_{e,x/y}$ = 1.187 / m_0 respectively. The ground state band structure is later in Figure 5.6.

5.2.3 Normal Compression of bilayer phosphorene

We investigated the effects of compressing bilayer phosphorene by varying the bilayer distance, *d* and fixing the *z* coordinate of the top and.bottom phosphorus atoms. For each value of *d*, we relaxed both in-plane lattice parameters and unfixed internal atomic positions.

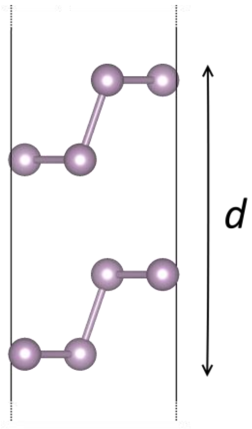

Figure 5.2: The structure of bilayer phosphorene with the bilayer distance, *d*, marked.

5.2.4 Energetics

We found that the ground state energy of bilayer phosphorene at 1.00 d_0 is 0.32 eV lower per unit cell (8 atoms) than the energy of two isolated monolayers. Van der Waals interactions dominate interlayer bonding; when bilayer phosphorene was relaxed without including van der Waals effects, we found that the binding energy was less than 0.10 eV. The changes in energy as *d* is varied are typical of a layered material, and are shown in Figure 5.3. Approximately parabolic behaviour is observed close to 1.00 d_0 before ΔE tends towards zero as *d* is increased.

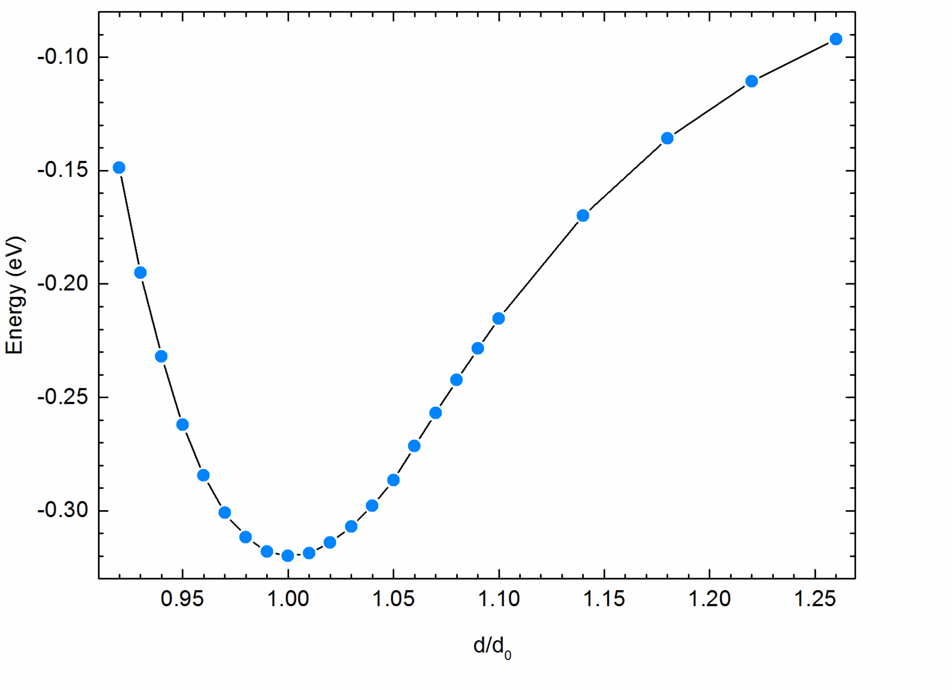

Figure 5.3: The change in energy of bilayer black phosphorus relative to two infinitely separated phosphorene monolayers as d_1 is varied.

Given that we are most interested in experimentally realisable compressions, we calculated the surface pressures necessary to compress bilayer phosphorene by calculating the stress, σ, at strains of between d_0 =1.00 d_0 and 0.92 d_0 using the following formula:

$$\sigma = F_N . A^{-1} = \frac{\partial E}{\partial d} . A^{-1}$$

where F_N is the normal force component, A is the surface area of bilayer phosphorene, E is energy and d is the bilayer distance. Given that the change in energy with compressive strain is parabolic between 1.00 and 0.92 d_0, the resulting stress-strain relationship is linear, as shown in Figure 5.4. We found that a pressure of around 1.2 GPa is required to compress d by 2%, with pressures of just under 5 GPa resulting in an 8% compression. While gigapascal pressures are high, the effects of applying pressures approaching 40 GPa normal to a material's surface have been investigated experimentally [10].

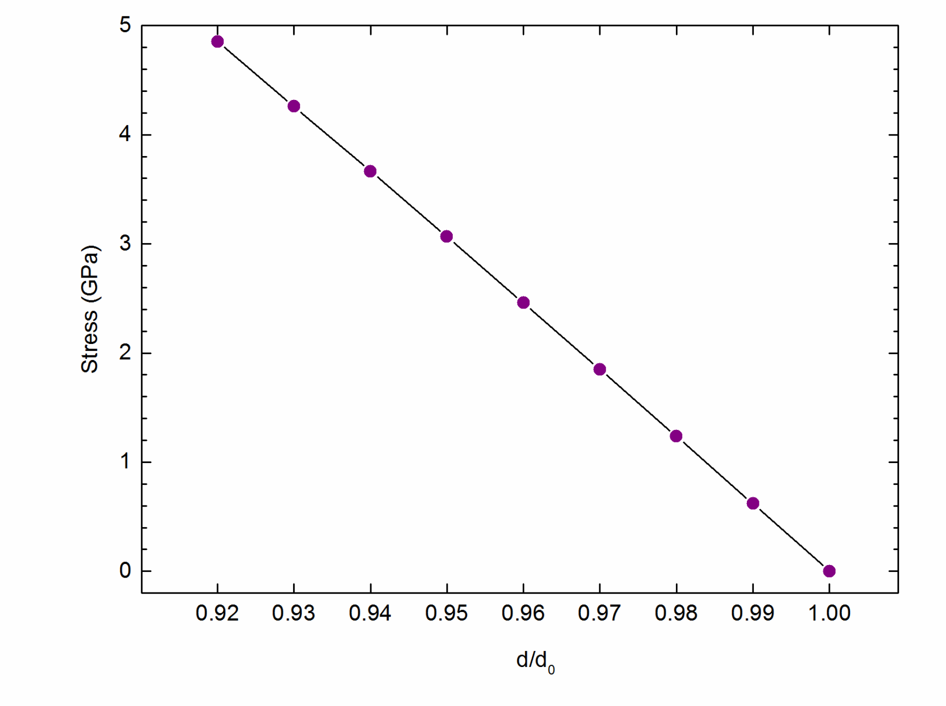

Figure 5.4: The stress induced in bilayer phosphorene under a range of compressions of d.

5.2.5 Geometry

We found that when bilayer phosphorene is compressed, it is mainly the interlayer distance that changes as opposed to the intralayer distance. For example, when d is compressed from 1.00 d_0 to 0.96 d_0, the interlayer distance is reduced by 8.32% and the intralayer distance is reduced by only 0.73%. This is because reducing the intralayer distance results in the shortening of chemical bonds and reducing the interlayer distance does not, with van der Waals bonds far weaker and therefore easier to distort than chemical bonds.

Meanwhile, the ground state surface area, $a \times b$, increases when bilayer phosphorene is compressed, as shown Figure 5.5. On further inspection, it is primarily the b lattice parameter which increases, reaching 4.62 Å when $d = 0.90\ d_0$ compared to 4.50 Å in the ground state. The zigzag direction lattice parameter, a, varies by less than 0.01 Å across all investigated compressions. Our findings tally with the Young's moduli calculated in the armchair and zigzag directions: the strain induced when bilayer phosphorene is compressed normal to its surface is released through an increase in b, which corresponds to the direction with a lower Young's modulus.

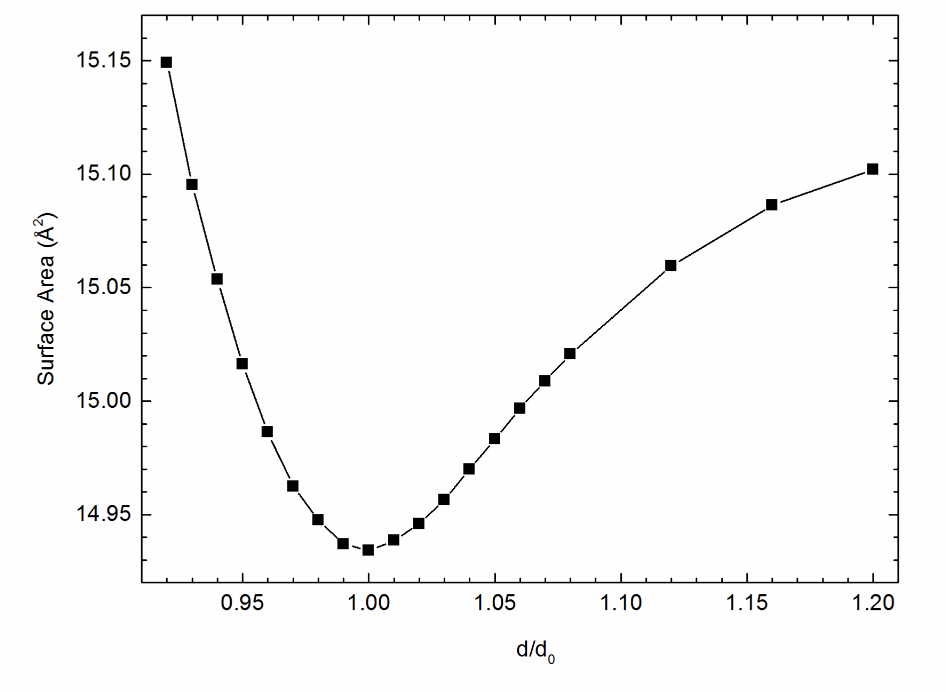

Figure 5.5: The surface area, $a_1 \times b_1$, of bilayer phosphorene under a range of compressions of d.

5.2.6 Band Gap

We found that as d is compressed from 1.00 to 0.92 d_0, the overall band gap of bilayer phosphorene decreases from 1.05 to 0.59 eV. Meanwhile, when d is increased from 1.00 to 1.20 d_0, the band gap increases to 1.34 eV.

The trend in band gap with changing d can be understood by inspection of Figure 5.6, which shows the energy of two valence to conduction band transitions, both of which originate at the VBM (Γ_{VB}). At values of $d > 0.98\ d_0$, the band gap is direct, from $\Gamma_{VB} - \Gamma_{CB}$, but when $d \leq 0.98$ d_0, the band gap becomes indirect as a new CBM emerges at X^*, [0.3, 0.0, 0.0].(2π/a) m^{-1}. The CB at X^* is stabilised with normal compressive strain, and between d = 1.00 and 0.92 d_0, Γ_{VB} - X^*_{CB} falls from 1.19 to 0.59 eV. Over the same range, there is a concurrent increase in the $\Gamma_{VB} - \Gamma_{CB}$ gap, from 1.05 to 1.24 eV.

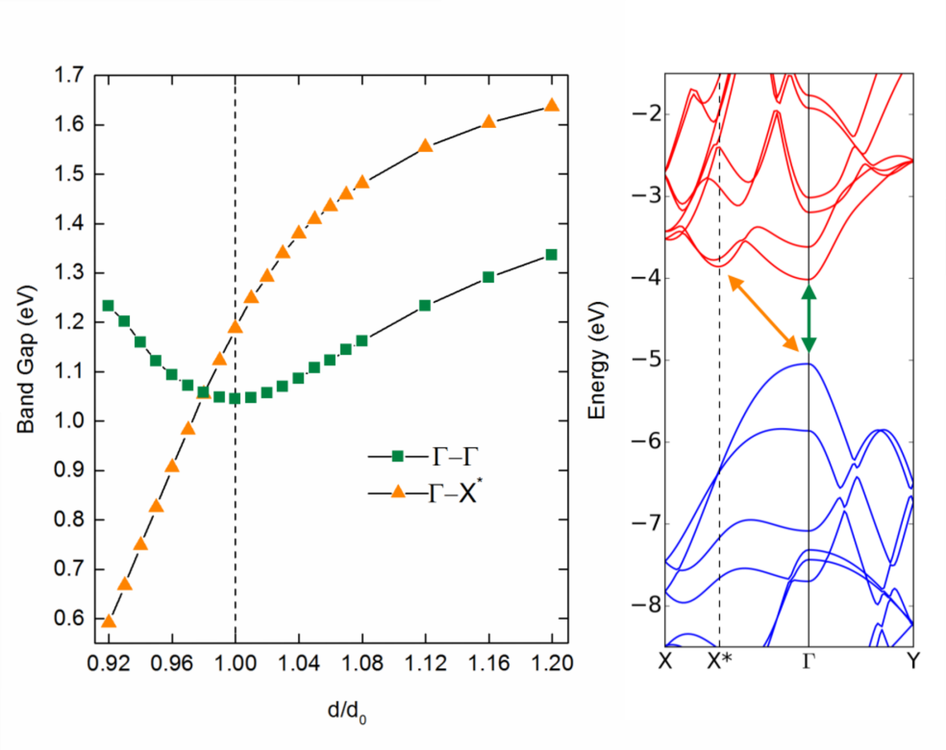

Figure 5.6: The variation of $VB_{\Gamma V}$- CB_{Γ} (green) and VB_{Γ}-CB_{M} (orange) transition energies under a range of compressions of *d* (left) and the electronic band structure of ground state bilayer phosphorene (right).

On first inspection, the direct to indirect band gap transition appears to be analogous to the direct to indirect band gap transition that occurs as bulk black phosphorus is compressed along the c_0 lattice parameter [11]. However, in that case the emergent CBM is located between Z and U in reciprocal space and therefore corresponds to electronic states which do not exist in quasi-2D black phosphorus derivatives.

In order to understand the origins of the behaviour seen in Figure 5.6, we calculated the absolute band energies of the VB and CB at Γ (Γ_{VB} and Γ_{CB}) and the CB at X^* (X^*_{CB}). We found that X^*_{CB} is stabilised and Γ_{CB} is destabilised with compressive strain. While Γ_{VB} is also destabilised with compressive strain, Γ_{CB} is destabilised more rapidly meaning that the $\Gamma_{VB} - \Gamma_{CB}$ band gap rises. Given that X^*_{CB} is stabilised and Γ_{VB} is destabilised with compressive strain, the $\Gamma_{VB} - X^*_{CB}$ band gap quickly decreases.

The spd- and site-projected phase factors of the electronic states at X^*_{CB}, Γ_{CB} and Γ_{VB} explain their changes in energy with compressive strain. Both Γ_{CB} and Γ_{VB} consist predominantly of p_z orbitals, which, as can be seen by looking at the phase factors of these orbitals in Figure 5.7 are arranged in a manner that manifests an anti-bonding interlayer interaction. As bilayer phosphorene is compressed and the interlayer distance decreases, the anti-bonding Γ_{CB} and Γ_{VB} orbitals are destabilised.

Meanwhile, the X^*_{CB} consists of p_x and p_y orbitals in equal measure. Their arrangement manifests a bonding interlayer interaction, with Figure 5.7 showing the bonding interaction between both the p_y and p_x components.

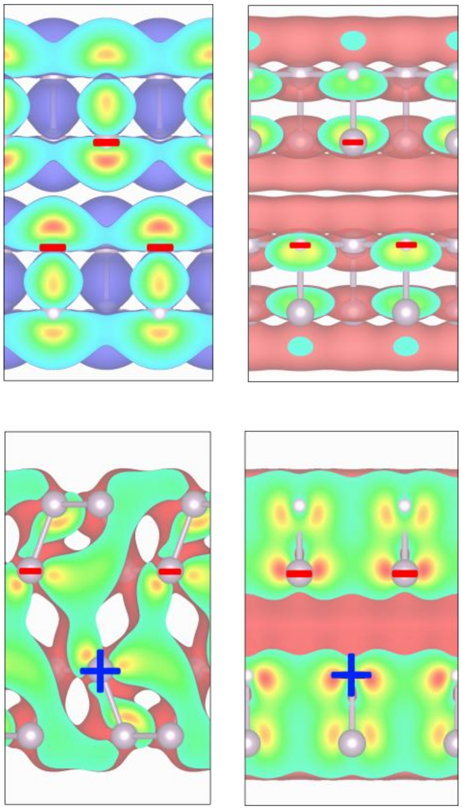

Figure 5.7: The charge density of the electronic states at VB_{Γ} (top left) and CB_{Γ} (top right) and CB_{X^*} (bottom left and right). The phase factors of constituent p_z orbitals are also marked, + or −.

Despite the fact that the overall band gap falls as *d* is compressed, the imaginary part of the dielectric constant, ϵ_{zz}, is blue shifted as a result of the rising Γ- Γ direct band gap, as seen in Figure 5.8, implying an increased optical band gap. While the indirect Γ- X* band gap falls with compression, indirect optical excitations are forbidden in the absence of phonon coupling. Furthermore, indirect radiative recombination is also forbidden, and therefore electron-hole recombination is far slower in indirect semiconductors.

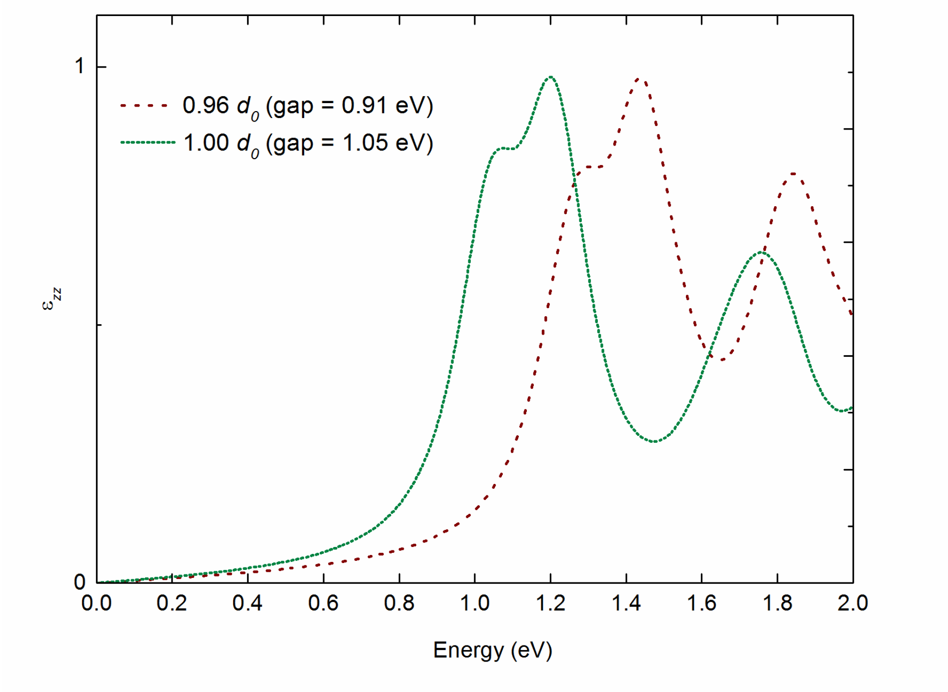

Figure 5.8: The imaginary dielectric constant, ε_{yy}, for bilayer phosphorene when $d = 0.94\ d_0$ and $d = 1.00\ d_0$.

5.2.7 Effective Mass

In uncompressed bilayer phosphorene, both band edges are located at the Γ-point. We calculated hole effective masses of $m_{h,x}$ = 1.21 m_0 and $m_{h,y}$ = 0.16 m_0 and electron effective masses of $m_{e,x}$ = 1.18 m_0 and $m_{e,y}$ = 0.19 m_0. Furthermore, given that the VBM remains at the Γ-point at all times, hole effective masses vary smoothly as *d* is compressed. Between *d* = 1.03 d_0 and 0.95 d_0, $m_{h,x}$ falls from 1.38 m_0 to 1.00 m_0, while $m_{h,y}$ rises from 0.16 m_0 to 0.18 m_0. These trends can be seen in Figure 5.9.

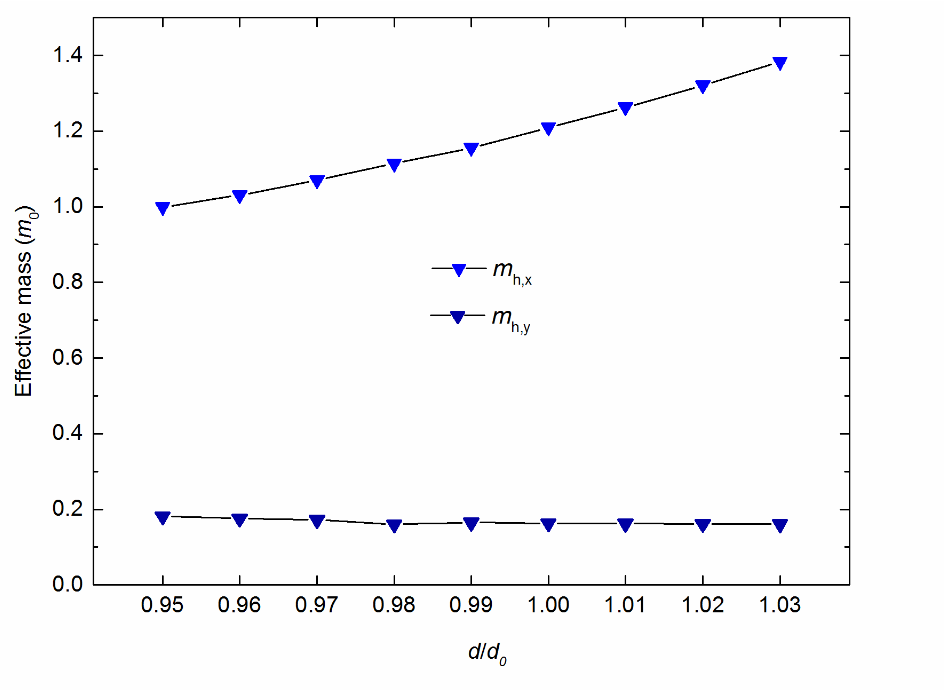

Figure 5.9: The hole effective masses, $m_{h,x}$ and $m_{h,y}$, in bilayer phosphorene under a range of compressions of *d*.

Given that the CBM moves from Γ to X^* when $d < 0.99\, d_0$, electron effective masses change more abruptly. In particular, $m_{e,x}$ is far lower at X^* than it is at the Γ-point, and therefore when *d* is reduced from 1.00 d_0 to 0.98 m_0, $m_{e,x}$ falls from 1.17 $m_0$to 0.32 m_0. Meanwhile, $m_{e,y}$ is slightly higher at X^* then it is at Γ, and when *d* is reduced from 1.00 d_0 to 0.98 d_0 $m_{e,y}$ rises from 0.18 m_0 to 0.25 m_0. As discussed in Section 5.2.6, the CB_{X^*} is made up of both p_x and p_y orbitals and therefore there is strong overlap in both *x*- and *y*- directions. This means that the energy dispersion of the CB around X* is isotopically high and $m_{e,x}/m_{e,y}$ = 1.29 m_0. The changing nature of the CBM upon compression can be appreciated by inspection of Figure 5.11.

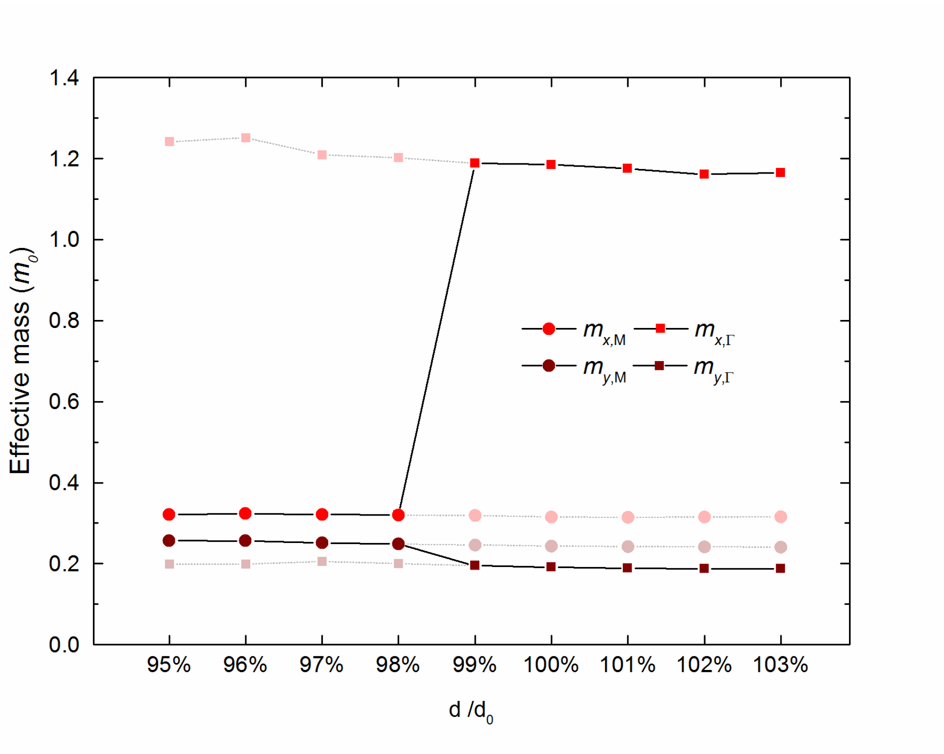

Figure 5.10: The electron effective mass, $m_{e,x}$ and $m_{e,y}$, in bilayer phosphorene at reciprocal space points Γ and X under a range of compressions of d.

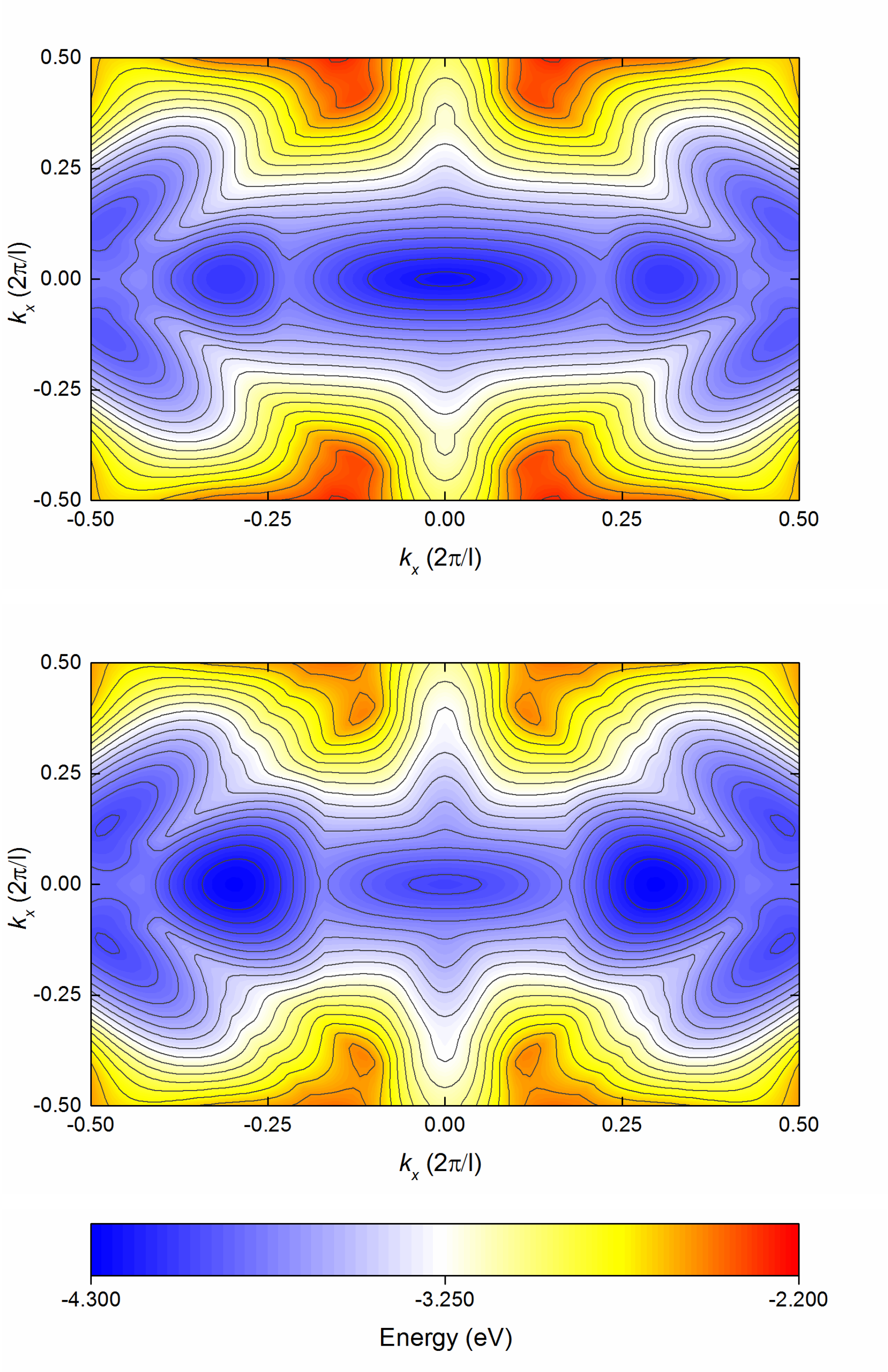

Figure 5.11: The energy of the first conduction band with respect to k when d = 1.00 (top) and 0.96 d_0 (bottom).

5.2.8 Mobility

Given the changing nature of the CBM under compression, we also investigated the overall mobility of electrons using a simplistic model that assumes that charge carrier velocity is randomised after each scattering event. Under this assumption, the charge carrier mobility, μ, can be expressed as:

$$\mu = \frac{q}{m_e}\tau$$

where τ is equal to the average time between scattering events. We used the deformation potential approximation (DPA), as discussed in Chapter 2, to calculate scattering times:

$$\tau = \frac{\hbar^3 C_{2D}}{k_B T m_d E_1^2}$$

where the deformation potential constant, $E_{1,}$ is the rate of change in the absolute energy of the CBM as the lattice is deformed, C_{2D} is the elastic modulus of longitudinal strain in the transport direction, and m_d is the average effective mass, $(m_x m_y)^{\frac{1}{2}}$. In uncompressed bilayer phosphorene, we calculated Γ-point electron scattering times of τ_x = 126 fs and τ_y = 137 fs, findings that are in good agreement with a number of other studies of few-layered black phosphorus. Meanwhile, we found that scattering times at the competing band minima at X^* are significantly longer as a result of low values of E_1 and m_d, with τ_x = 1,041 fs and τ_y = 15,713 fs. In the *x* direction, both E_1 and m_d are approximately halved at X^* with respect to Γ, reflecting lower electron-phonon coupling and a greater average band dispersion. Meanwhile, in the y direction E_1 is over an order of magnitude lower at X* than it is at Γ, 0.28 eV versus 3.66 eV. As discussed in Chapter 2, E_1 is calculated by straining the lattice parameter corresponding to the direction of charge transport between 0.99 l_0 and 1.01 l_0 and looking at the rate at which the electronic state of interest changes energy.

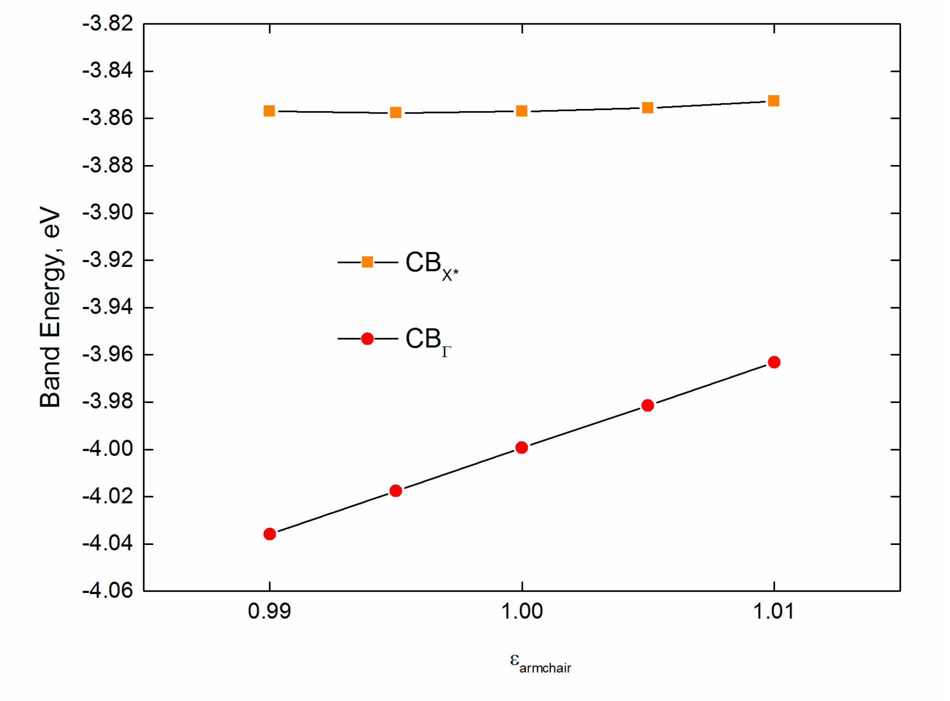

Figure 5.12: The energies of CB_{Γ} and CB_{X*} under armchair direction strains of between 0.99 and 1.01.

As can be seen in Figure 5.12, the electronic state at X* changes energy less rapidly when bilayer phosphorene is strained along b_0 than the electronic state at Γ, suggesting that there is less coupling between the electronic state at X* and the *y* direction LA phonon. Examining the values of E_1 for conduction states around X* gives insight into why E_1 is so low at X* specifically. When k_x < X*, E_1 is negative as the conduction band at k_x is stabilised when the lattice is stretched in the *y* direction. Meanwhile, when k_x > X*, E_1 is positive as the conduction band at k_x is destabilised when the lattice is stretched in the *y* direction. Therefore, at X*, the CB is neither stabilised nor destabilised when the lattice is stretched in the *y* direction and E_1 is close to zero. Furthermore, the lack of coupling can be qualitatively understood by inspection of Figure 5.7, where it is apparent that the bulk of bonding character at X* occurs between the layers rather than in the armchair direction along which the acoustic phonon propagates. While such a low value of E_1 is surprising, it is not unprecedented; an even lower deformation potential constant of ~0.15 eV was previously calculated for holes at the VBM of monolayer phosphorene.

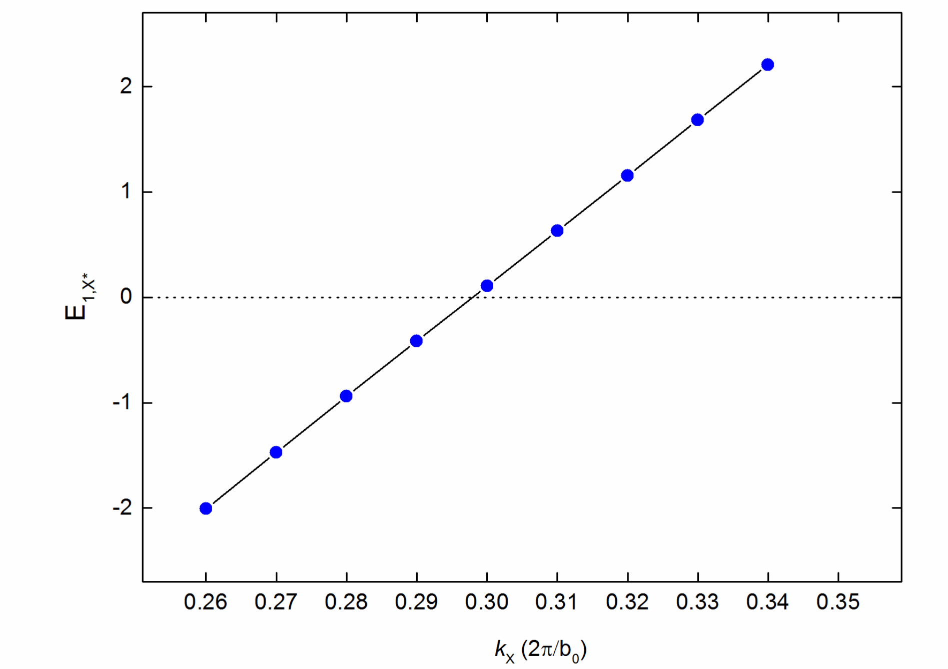

Figure 5.13: The electronic deformation potential constant of bilayer phosphorene at reciprocal points around X*.

As bilayer phosphorene is compressed, we found that electron scattering times at both X* and the Γ-point remain relatively constant. However, as discussed extensively in Section 5.2.6, the conduction band at X* is stabilised with respect to the conduction band at the Γ-point with compression. By calculating the relative occupancy of states X* and the Γ-point, we predicted the overall electron mobility using the following equation:

$$\mu_{x/y,e}(T) = \frac{\sum_k \mu_{x/y,k} \,.\, n_k . e^{-E_k/k_BT}}{\sum_k e^{-E_k/k_BT}}$$

where $\mu_{x/y,k}$ is the electron mobility in the *x* / *y* direction at *k*-point *k*, n_k is the degeneracy of *k* and E_k is the energy of the electronic state at *k* relative to the CBM. We found that when calculated using the above formula, both *x*- and *y*- direction electron mobilities increase dramatically when *d* is decreased.

When $d = 1.00\ d_0$, $\mu_{e,x}$(298K) = 219 cm^{2}V^{-1}s^{-1} and $\mu_{e,y}$ (298K) = 1,362 cm^{2}V^{-1}s^{-1}, numbers which are comparable to the literature. As *d* is compressed, $\mu_{e,y}$(298K) rises rapidly as the occupancy of the conduction band valley around X* is increased, plateauing around 60,000 cm^{2}V^{-1}s^{-1} when d = 0.98 d_0. At X* specifically, electron mobility reaches an enormous 2.38×10^5 cm^2/V/s, almost an order of magnitude higher than the upper limit of phosphorene's hole mobility calculated by Qiao et al. [12]. Meanwhile, $\mu_{e,x}$(298K) plateaus between 4,000 and 5,000 cm^{2}V^{-1}s^{-1} as X* is stabilised, higher than any room temperature electron mobility calculated for a black phosphorus derived structure.

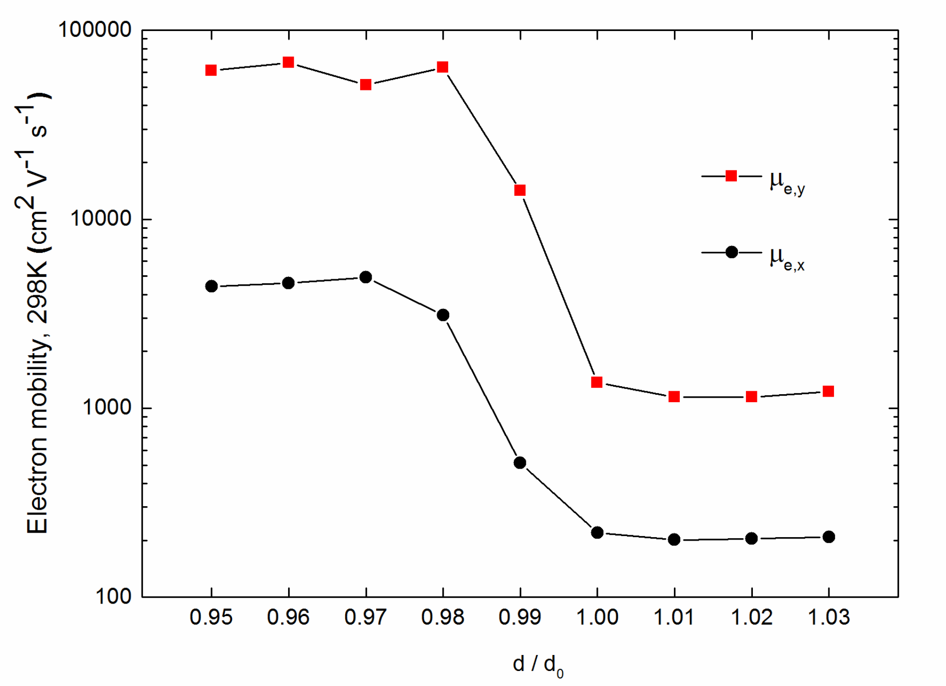

Figure 5.14: The electron mobility of bilayer phosphorene under a range of compressions of d.

It is, however, important to reiterate that mobility calculated using the DPA is limited solely by coupling to LA phonons. The viability of this approximation becomes more questionable when the acoustic phonon scattering time is very high and other forms of scattering are likely to dominate. Therefore mobility calculated using the DPA should be considered as an upper limit.

5.2.9 Compressing bilayer phosphorene: Summary

We have that a new CBM emerges when bilayer phosphorene is subjected to a modest compression. The effective electronic mass at X* is far more isotropic than it is at Γ, with $m_{e,x}$ = 0.32 m_0 and $m_{e,y}$ = 0.25 m_0. We have also shown that the electronic states around X* are scarcely coupled to acoustic phonons in the armchair direction, with the mobility of states at X* peaking at 2.38×10^{5} $cm^{2}V^{-1}s^{-1}$. Through the stabilisation of these highly mobile states located in the vicinity of X*, we have shown that relatively small compressions can increase the overall mobility of bilayer phosphorene by approaching two order of magnitude, reaching 7×10^{4} $cm^{2}V^{-1}s^{-1}$ in the armchair direction and 5×10^{3} $cm^{2}V^{-1}s^{-1}$ in the zigzag direction.

5.3 Phase transformation to blue phosphorus

While previous studies have reported that phosphorene has very high critical strains of 27% in the armchair direction and 30% in the zigzag direction [12], it is possible that some of the states identified as being stable are not the global minimum structures. Given the recent identification of a number of new forms of monolayer phosphorus, it is important to consider the stability of strained phosphorene with respect to other phases with the same lattice parameters. In this section, we compare the stability of strained phosphorene to that of monolayer blue phosphorus.

5.3.1 Methodology

As in Section 5.2, we performed DFT calculations using VASP with a plane-wave basis set truncated at 400 eV and PAW pseudopotentials to treat core electrons, see Chapter 2. Given that, in this section, we are only interested in the structural and energetic properties of monolayer blue phosphorus and phosphorene, we have used the PBE functional in combination with the DFT-D3 dispersion correction scheme throughout. We relaxed the structure of both monolayer blue phosphorus and monolayer phosphorene using a conjugate gradient algorithm until all interatomic forces fell below 0.01 eV/Å. A vacuum region greater than 20 Å was maintained perpendicular to the *xy* plane in order to avoid spurious interactions between images. We found that sampling *k*-space using a 10×10×1 Monkhorst-Pack mesh fully converged the geometry and energy of both compounds.

5.3.2 Blue Phosphorus

Following the isolation of few-layered black phosphorus, an alternative layered phase of phosphorus was theoretically identified [13]. The compound, named blue phosphorus, has an in-plane hexagonal structure, and when calculated using the PBE functional, its monolayer has an indirect band gap of approximately 2 eV. These properties are in contrast with those of phosphorene, which has a direct band gap of around 0.9 eV and in-plane rectangular symmetry. Despite these differences, monolayer blue phosphorus and phosphorene are energetically equivalent to within 1 meV per atom, with phosphorene only marginally more stable. In light of this, it is important to determine the circumstances where phosphorene is unstable with respect to monolayer blue phosphorus. Given that the in-plane surface area per atom in monolayer blue phosphorus is significantly higher than it is in phosphorene, it is likely that phosphorene is unstable with respect to monolayer blue phosphorus when subjected to in-plane extensive strains.

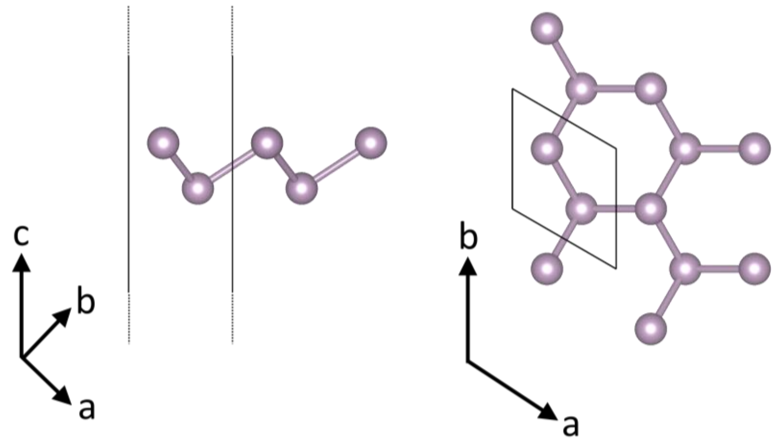

Figure 5.15: The relaxed structure of monolayer blue phosphorus.

While the primitive unit cells of monolayer blue phosphorus and phosphorene are not commensurate, it is possible to represent that structure of monolayer blue phosphorus using a cubic unit cell, as shown in Figure 5.16. Under this representation, the a_0 parameters of the two phases are similar, whereas the b_0 lattice parameter in monolayer blue phosphorus is around 20% greater than in phosphorene. We therefore investigated the effect of applying strain along the b_0 lattice parameter on the relative stability of phosphorene and monolayer blue phosphorus.

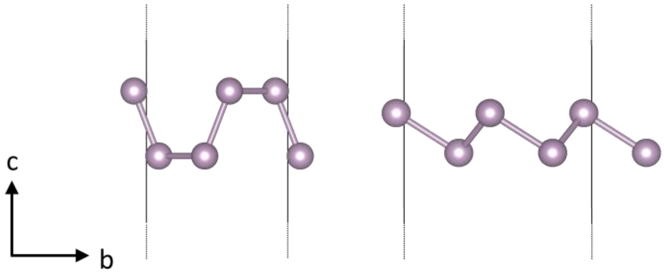

Figure 5.16: The relaxed structure of phosphorene (left) and monolayer blue phosphorus (right), both represented using a cubic unit cell.

	Phosphorene	**Monolayer Blue Phosphorus**
a (Å)	3.294 Å	3.310 Å
b (Å)	4.602 Å	5.671 Å
Area / atom	3.790 Å^2	4.692 Å^2
Energy / atom	0 meV	1 meV

Table 5.2 A comparison of the cubic unit cells of phosphorene and monolayer blue phosphorus.

5.3.3 Straining Monolayer Phosphorus

Phosphorene and monolayer blue phosphorus are energetically equivalent to within 1 meV per atom when both are relaxed to their ground state, $b_{black} = b_{0,black}$ and $b_{blue} = b_{0,blue}$. If we stretch b_{black}, phosphorene becomes less stable, and if we compress b_{blue}, monolayer blue phosphorus becomes less stable. Given that $b_{0,blue} > b_{0,black}$, there must exist a shared lattice parameter, b_1, where monolayer blue phosphorus and phosphorene are energetically equivalent and furthermore when $b_{black} > b_1$ phosphorene is unstable with respect to monolayer blue phosphorus. The position of b_1 between $b_{0,blue}$ and $b_{0,black}$ depends on relative in-plane stiffness of phosphorene and monolayer blue phosphorus.

Given that $b_{black} < b_1 < b_{blue}$, we investigated the extension of phosphorene and the compression of monolayer blue phosphorus along the b lattice parameter. In both cases we calculated the in-plane stiffness, C_{2D}, using the following formula:

$$C_{2D} = \frac{1}{A_0}\left(\frac{\partial^2 E}{\partial \varepsilon^2}\right)$$

where E, ε and A_0 correspond to energy, linear strain and the equilibrium surface area respectively. C_{2D} is related to the Young's modulus, C_{3D}, through the relationship $C_{3D} = \frac{C_{2D}}{c_0}$, where c_0 is the lattice parameter perpendicular to the plane on which the monolayer lies, and therefore quantifies the relationship between strain and energy.

In good agreement with previous studies, we found that in the case of phosphorene, $C_{2D,y}$ = 17.07 GPa nm. Such a low in-plane stiffness confirms that is it exceptionally easy to stretch phosphorene in the armchair direction. In the case of monolayer blue phosphorus, we found that $C_{2D,y}$ = 58.58 GPa nm. While the in-plane stiffness of monolayer blue phosphorus is still low compared to other monolayer compounds, the fact that it is significantly higher than it is for phosphorene implies that b_1 is closer to b_{blue} than b_{black}.

While the a_0 lattice parameters of phosphorene and monolayer blue phosphorus are similar, it is important to consider how a changes when b is extended or compressed. When strain is applied along one lattice parameter, it is often possible to release some of the induced surface tension by relaxing other lattice parameters. In 2D, this effect is quantified by the Poisson ratio, ν:

$$\nu_b = -\frac{d\varepsilon_a}{d\varepsilon_b}$$

where ε_b is the applied strain along b and ε_a is the spontaneous change along a. We found that the Poisson ratio is much lower in phosphorene that it is in monolayer blue phosphorus, with $\nu_{b,black}$ = 0.10 and $\nu_{b,blue}$ = 0.24.

5.3.4 Phase transition

For both phases of monolayer phosphorus, we varied the b lattice parameter between $b_{0,black}$ and $b_{0,blue}$, relaxing both the internal atomic coordinates and the a lattice parameter in each instance. By plotting the energy of both phases versus b, we identified the value of b_1 and furthermore the range of b within which phosphorene is thermodynamically stable.

Figure 5.17 shows that $b_1 = 5.32$ Å, and that phosphorene is stable when $b < 5.32$ Å, corresponding to values of $\varepsilon < 16\%$. When $\varepsilon > 16\%$, phosphorene becomes unstable with respect to a phase transition to monolayer blue phosphorus. Importantly, this critical strain is significantly lower than phosphorene's previously reported ultimate strain of 31%.

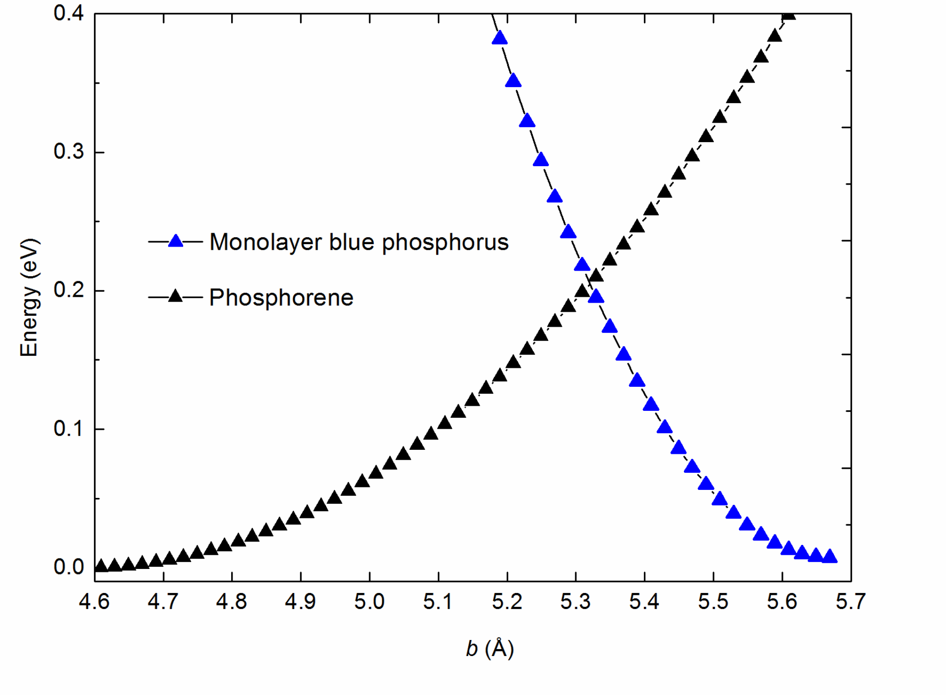

Figure 5.17: The energies of phosphorene and monolayer blue phosphorus, relative to ground state phosphorene when the *b* lattice parameter is varies between 4.7 and 5.7 Å.

5.4 Bending Phosphorene

When modelling the response of 2D materials to compressive in-plane forces, it is important to consider the release of tension through surface buckling. For example, it has been shown experimentally that graphene buckles under compressions > 0.7% [14]. Furthermore, suspended 2D materials may also ripple spontaneously at non-zero temperatures, as was recently found to be the case in a study of suspended graphene [15]. Given the importance of rippling and buckling in other 2D materials, we have investigated the analogous bending of phosphorene.

5.4.1 Methodology

As in Sections 4.2 and 4.3, we performed DFT calculations using VASP with a plane-wave basis set truncated at 400 eV and PAW pseudopotentials to treat core electrons, see Chapter 2. Given the large size of the systems investigated, we used the PBE functional in combination with the DFT-D3 dispersion correction scheme not only during structural relaxations but also when investigating the electronic properties of PNTs. This compromise is necessary in the interest of computational affordability, and means that the band gaps calculated are likely to be underestimated. Despite this caveat, we are confident that the reported trends are representative of the system's true behaviour, with the underestimation of the band gap a relatively consistent effect. When relaxing crystal lattices and internal atomic positions, we used a conjugate gradient algorithm until all interatomic forces fell below 0.01 eV/Å. A vacuum region greater than 20 Å was maintained between periodic images of PNTs in order to avoid spurious interactions A Monkhorst-Pack mesh of 1×9×1 was used when modelling z-PNTs and 9×1×1 when modelling a-PNTs. Absolute band energies were obtained by subtracting the total local potential found directly in the middle of the vacuum region from the eigenvalues computed using DFT.

5.4.2 Geometry and energetics

Given the structural anisotropy of phosphorene, we investigated two principle curvatures: curvature in the zigzag direction and curvature in the armchair direction. A convenient way to investigate bending in 2D materials is to look at the properties of nanotubes [16]: to investigate bending in the zigzag direction we modelled zigzag nanotubes (z-PNTs), and to investigate bending in the armchair direction we modelled armchair nanotubes (a-PNTs). All nanotubes have a constant surface curvature, with the highest curvatures found in nanotubes with smaller radii, r. Therefore, throughout this chapter, we use r^{-1} as a measure of curvature, comparing the properties of PNTs to those of flat phosphorene, where $r^{-1} = 0$.

5.4.2.1 Armchair PNTs

We relaxed eight a-PNTs with circumferences between $8 \times b_0$ and $80 \times b_0$, where b_0 is the armchair direction lattice parameter of monolayer phosphorene. Following relaxation, r^{-1} ranged between 0.017 Å^{-1} (r = 58.5 Å) and 0.190 Å^{-1} (r = 5.2 Å). We measured the internal geometry of each a-PNT and found that three parameters varied considerably over the range of nanotubes studied: d_1, d_2 and a_1, as shown in Figure 5.18. We found that, even for high curvature a-PNTs, all bond lengths remained constant to within 1.2% of the bulk values.

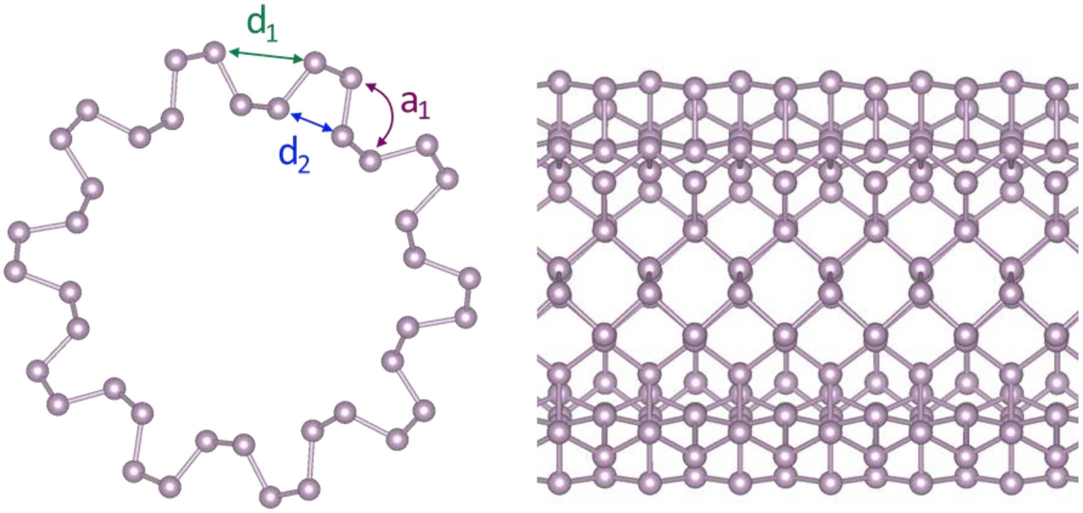

Figure 5.18: The structure of a-PNT with a radius of 8.08 Å viewed along the length of the tube with key structural parameters labelled (left) and from above (right)

Atoms	Radius, r	Curvature, r^{-1}	d_1	d_2	a_1	Energy
32	5.25	0.190	4.48	3.12	113.16	0.073
48	8.08	0.124	4.13	3.22	109.81	0.048
64	10.965	0.091	3.96	3.28	108.26	0.033
80	13.88	0.072	3.87	3.33	107.36	0.019
96	16.815	0.059	3.82	3.36	106.87	0.012
128	22.84	0.044	3.77	3.42	106.36	0.009
160	28.995	0.034	3.76	3.49	105.82	0.006
320	58.525	0.017	3.64	3.50	105.11	0.004
∞	∞	0	3.54	3.54	104.1	0.000

Table 5.3: The structural parameters of a-PNTs with radii between 5.25 and 58.53 Å.

In bulk phosphorene, d_1 and d_2 are equivalent by symmetry, measuring 3.54 Å. As surface curvature is increased, d_1 increases and d_2 decreases. For example, when r^{-1} = 0.017 Å^{-1}, d_1 = 3.64 Å and d_2 = 3.50 Å, whereas when r^{-1} = 0.190 Å^{-1}, d_1 = 4.48 Å and d_2 = 3.12 Å. We found that d_1 increases linearly with r^{-1} over the range of a-PNTs studied, whereas changes in d_2 are not linear with r^{-1}. Meanwhile, the external bond angle does increase linearly with r^{-1}, with a_1 = 104.1° in the bulk, 105.1° when r^{-1} = 0.017 Å^{-1}, and 113.2° when r^{-1} = 0.190 Å^{-1}.

5.4.2.2 Zigzag PNTs

We relaxed eight a-PNTs with circumferences ranging between 12 × a_0 and 80 × a_0. Following relaxation, r^{-1} ranged between 0.025 Å^{-1} (r = 40.16 Å) and 0.167 Å^{-1} (r = 5.99 Å). In contrast with the changes in geometry seen in a-PNTs, two bond lengths varied significantly with surface curvature, d_3 and d_4.

In bulk phosphorene, d_3 and d_4 are both 2.22 Å, and are equivalent by symmetry. As surface curvature is increased, d_3 rises and d_4 falls. We note that d_3 rises more rapidly than d_4 falls as r^{-1} is increased. For example, in the z-PNT with highest surface curvature, r^{-1} = 0.167 Å^{-1}, d_3 = 2.48 Å (+0.26 Å) and d_4 = 2.17 Å (-0.05 Å). At low curvatures, the magnitude of the changes in d_3 and d_4 are more comparable. For example, when r^{-1} = 0.025 Å^{-1}, d_3 = 2.25 Å (+0.03 Å) and d_4 = 2.19 Å (+0.03 Å).

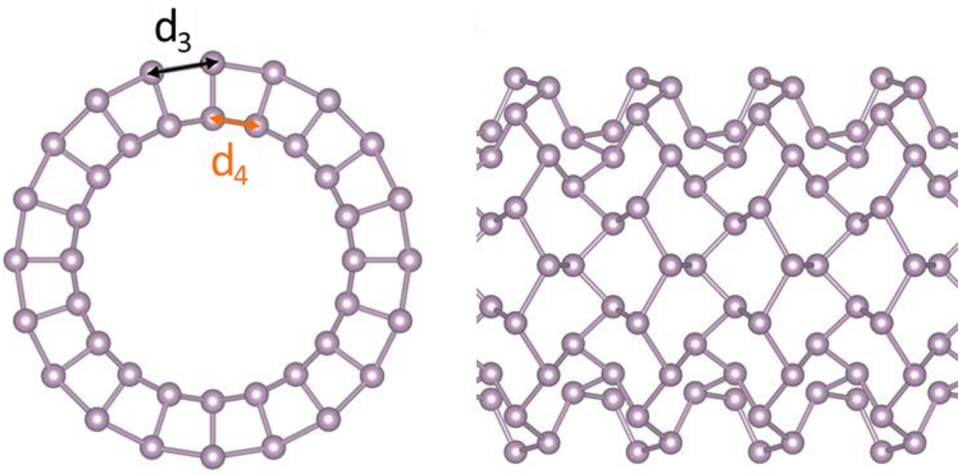

Figure 5.19: The structure of z-PNT with a radius of 4.96 Å from the side, viewed along the length of the tube with key structural parameters labelled (left) and from above (right).

Atoms	Radius,	Curvature	d_3	d_4	Energy
48	5.986	0.167	2.481	2.173	0.247
64	7.931	0.126	2.416	2.173	0.161
80	9.943	0.101	2.372	2.176	0.111
96	11.980	0.083	2.344	2.178	0.081
128	15.993	0.063	2.308	2.184	0.048
160	20.012	0.050	2.287	2.189	0.031
320	40.192	0.025	2.246	2.194	0.011
∞	∞	0	2.224	2.224	0

Table 5.4: The structural parameters of z-PNTs with radii between 5.99 and 40.19 Å.

5.4.2.3 Bending Moduli

We quantified the bending stiffness of phosphorene by calculating bending rigidities, B_M. The energy of a 2D material or membrane which follows the contours of a cylinder or sphere of radius r is governed by the Helfirch Hamiltonian, which was originally developed for the study of lipid bilayers [17, 18]. In the Helfrich Hamiltonian, the configurational energy of a rippled surface is expressed in terms of the energy of a unitary flat surface, γ, the material's bending rigidity, B_M, its mean curvature, C_M, its spontaneous curvature, C_0, its Gaussian curvature, C_G, and finally its Gaussian rigidity, B_G, through the following equation:

$$E = \int [\gamma + 2B_M(C_M - C_0/2)^2 + B_G C_G] dS$$

Both C_M and C_G can be expressed in terms of principle curvatures k_1 and k_2, which are equal to the inverse radius of curvature along the x and y axis respectively.

$$C_M = \frac{(k_1 + k_2)}{2} = \frac{1}{2r_1} + \frac{1}{2r_2}$$

$$C_M = k_1 k_2$$

The bending rigidity of graphene has previously been calculated by modelling graphene nanotubes of varying radii. When a 2D material is deformed to form a nanotube, curvature is non-zero in one direction only, and therefore either k_1 or k_2 must equals zero. Furthermore, under the the approximation $C_0 = 0$:

$$E = \int \left[\gamma + 2B_M \left({}^{k_1}\!/_{2}\right)^2\right] dS$$

$$E_{atom}^{PNT} - E_0 = S_0 B_m r^{-2}/2$$

where E_0 is the energy per atom in ground state phosphorene, and S_0 is the planar footprint of each phosphorus atom in phosphorene. We calculated bending rigidity by plotting atomic energy with respect to bulk phosphorene vs. $S_0 r^{-2}/2$ for both a-PNTs and z-PNTs, as shown in Figure 5.20. We found that B_m is lower for a-PNTs than z-PNTs, with $B_{m,ac}$ = 1.11 eV and $B_{m,zz}$ = 5.28 eV, implying that it is harder to bend phosphorene in the zigzag direction than in the armchair direction. This finding is consistent with the fact that bending phosphorene in the armchair direction does not lead to any large changes in bond length, whereas bending phosphorene in the zigzag direction results in large changes in d_3 and d_4.

Despite the fact that $B_{m,zz}$ is large compared to $B_{m,ac}$, is still lower than the bending rigidities calculated for other quasi-2D compounds such as monolayer MoS_2, where B_m = 9.61 eV. Furthermore, $B_{m,ac}$ is lower than the bending rigidity calculated for graphene using the same methodology, where B_m = 1.45 eV. Given that experimental studies have shown that suspended graphene is intrinsically rippled, our findings suggest that suspended phosphorene is also likely to show spontaneous rippling, and that buckling is likely to be the primary response to compressive in-plane forces.

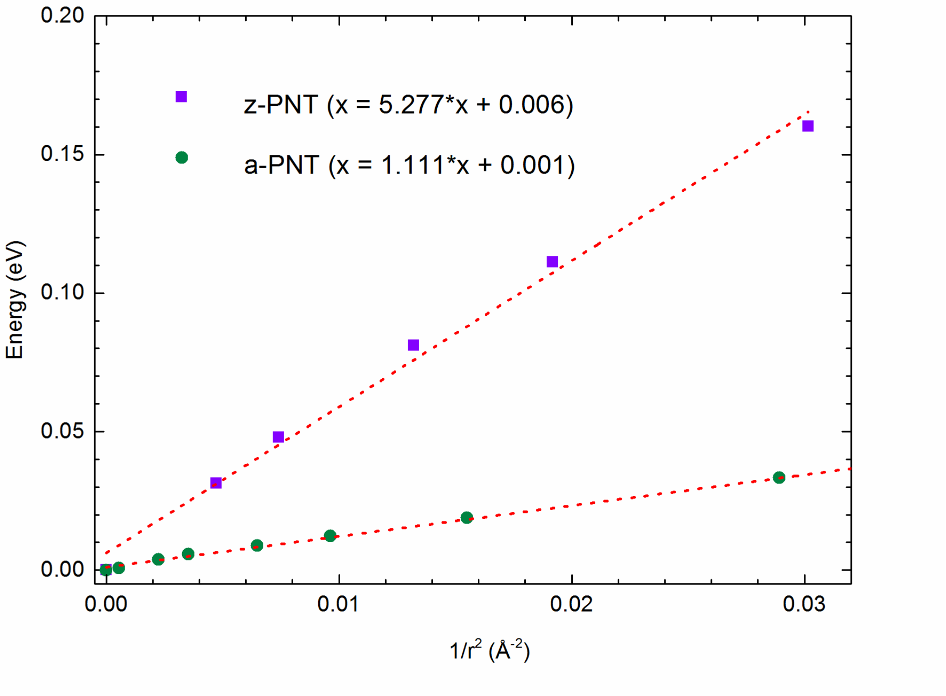

Figure 5.20: The energy of z-PNTs and a-PNTs under a range of values of $S_0 r^{-2}/2$.

5.4.3 Electronic Structure

We investigated the effects of surface curvature on the band gap of phosphorene by calculating the electronic structure of PNTs. In bulk phosphorene, both band edges are located at the Γ-point, where $k_x = 0$ and $k_y = 0$. In contrast to the hard-wall boundary conditions imposed on nanoribbons, see Chapter 6, $k = 0$ is an allowed k-point when wavefunctions are confined to the circumference of a tube:

$$k_n = \frac{2\pi}{a} \cdot \frac{n}{N} \qquad n = -N, -N+1, \dots, N-1, N$$

We are therefore confident that the main trends in band gap that occur as the radii of PNTs are varied are the result of changes in surface curvature rather than changes in the extent of quantum confinement.

5.4.3.1 Armchair PNTs

As shown in Figure 5.21, the band gaps of a-PNTs generally fall when surface curvature is increased. For example, the band gap of a-PNT where r^{-1} = 0.034 $Å^{-1}$ (r = 58.5 Å) is 0.89 eV, whereas when surface curvature is high, r^{-1} = 0.123 $Å^{-1}$ (r = 8.1 Å), the band gap falls to 0.29 eV.

Between r^{-1} = 0.034 $Å^{-1}$ and 0.123 $Å^{-1}$, the variation in band gap with r^{-1} is roughly linear. However, when r^{-1} < 0.034 $Å^{-1}$, the band gap plateaus. In fact, a-PNTs with low surface curvature have band gaps which are slightly higher than that of the bulk. For example, when r^{-1} 0.017 $Å^{-1}$, the band gap is 0.92 eV, 0.03 eV higher than the bulk value of 0.89 eV. While the increases in band gap with respect to the bulk are marginal, the abrupt plateauing of the band gap when r^{-1} < 0.034 $Å^{-1}$ is unequivocal. In summary, it appears that curvatures r^{-1} < 0.034 $Å^{-1}$ have a limited effect on band gap, whereas higher curvatures lead to a significant and linear decreases in the band gap of phosphorene.

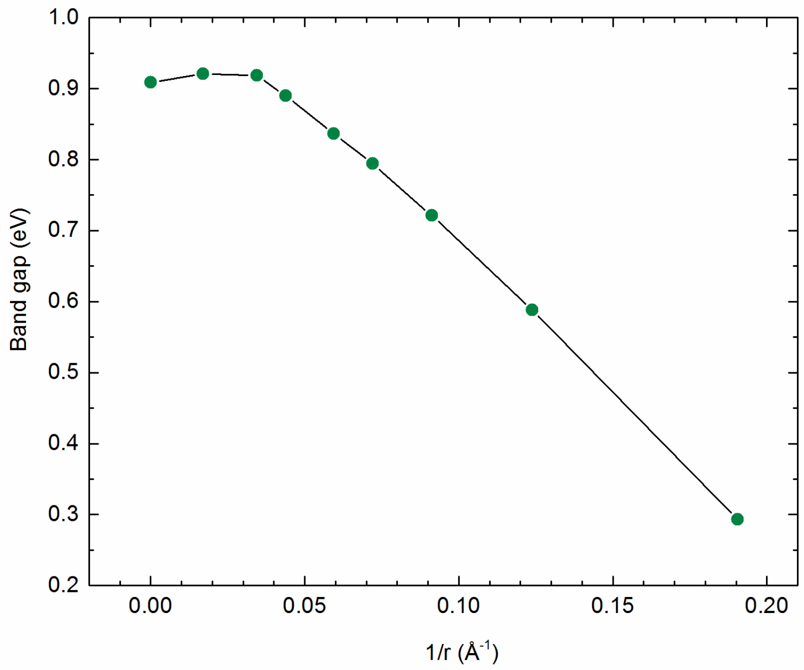

Figure 5.21: The electronic band gap of a-PNT under a range of values of r^{-1}.

The somewhat unusual changes in band gap with increased surface curvature can be understood by examining at the absolute energies of the VBM and CBM. As can be seen in Figure 5.21, the energy of the CBM stays relatively constant, varying by less 0.05 eV over the range of curvatures studied. The changes in band gap are predominantly driven by the destabilisation of the VBM, which rises by 0.67 eV over the same range of curvatures. However, between r^{-1} = 0 and 0.123 Å^{-1}, neither the VBM nor the CBM is destabilised with surface curvature.

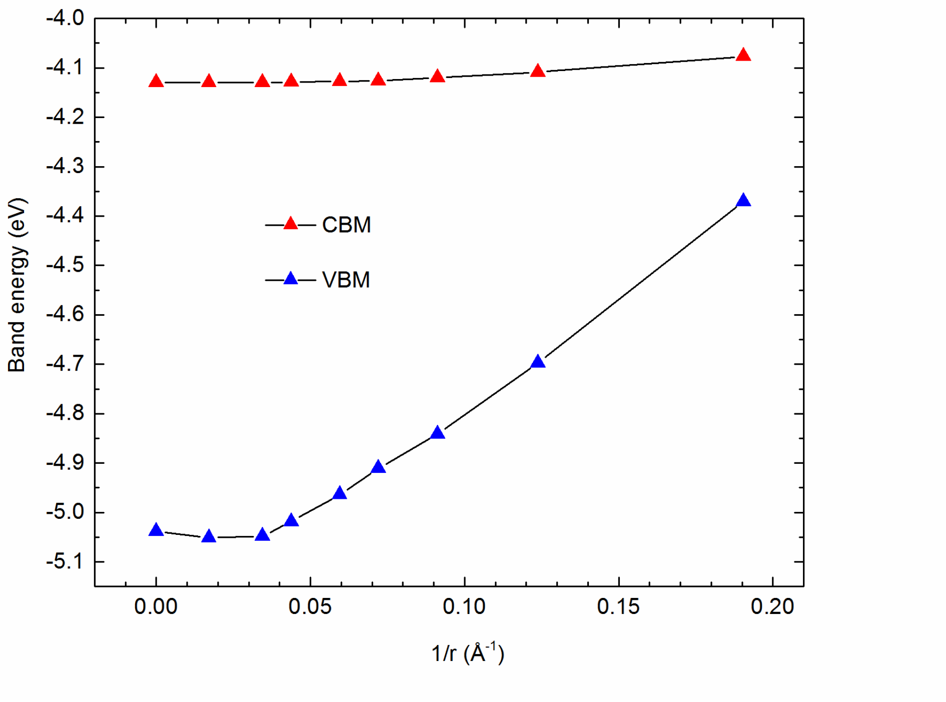

Figure 5.22: The absolute energy of the VBM and CBM under a range of values of r^{-1}.

We examined the character of the electronic state at the VBM by projecting the wavefunction onto *s*, *p* and *d* orbitals at each ionic site. Figure 5.23 shows the phase factors of the p_z orbitals, which account for the majority of the valence band wavefunction. We see that the orbitals separated by d_1 and d_2 are out of phase, manifesting in a π anti-bonding interaction, which means that as d_1 and d_2 decrease, the electronic state is destabilised and vice versa. As shown in Table 5.3, d_1 increases and d_2 decreases with curvature, stabilizing and destabilizing the VBM respectively.

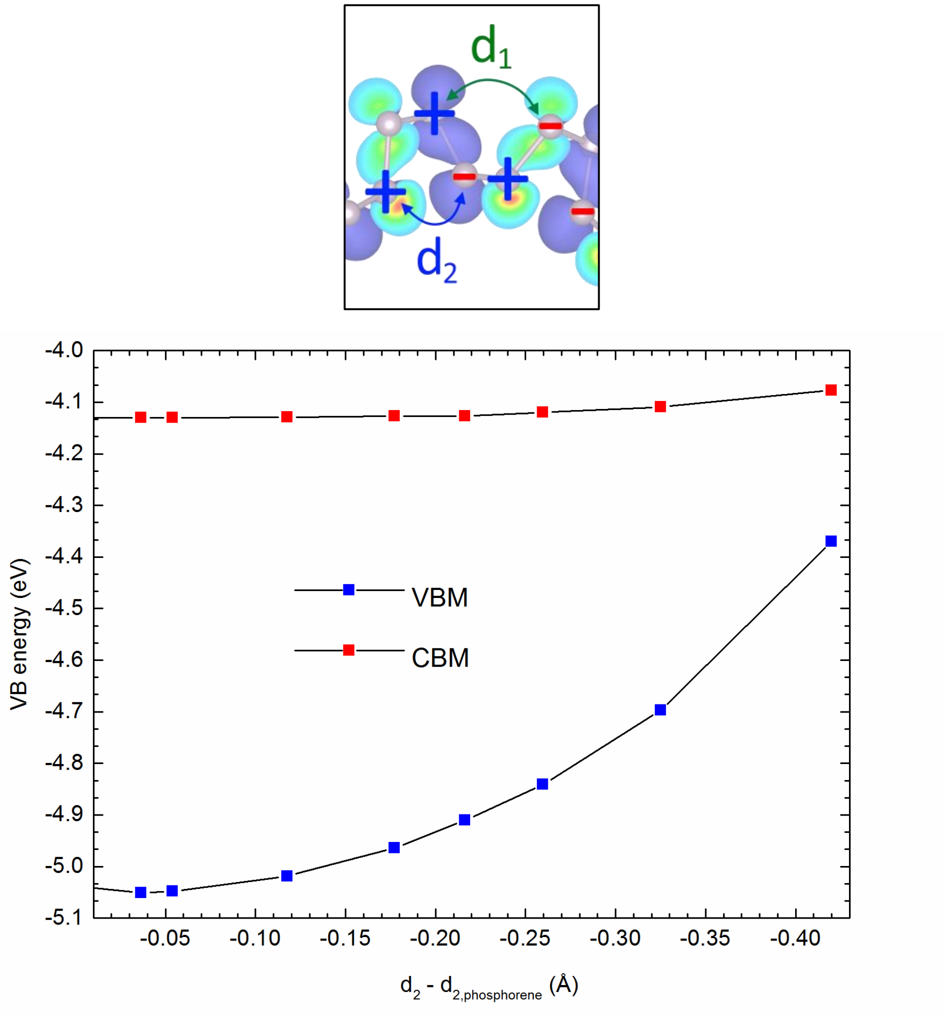

Figure 5.23: The charge density at the VBM of a-PNT with the phase factors of the constituent p_z orbitals (top) and the absolute energy of the VBM and CBM of a-PNT versus r^{-1} (bottom).

It is important to note that the atoms separated by d_1 and d_2 are not chemically bonded, with d_1 and d_2 significantly larger than a typical P-P bond, 3.54 Å vs. 2.22 Å. This separation means that in flat phosphorene, the overlap between orbitals is minimal and $\psi_a^*(r_1)\psi_b^*(r_2)$ is low. Given that d_1 increases with r^{-1}, the interaction between the p_z orbitals quickly becomes negligible. Meanwhile, as d_2 falls with surface curvature the overlap between orbitals separated by d_2 becomes more significant. Therefore, when r^{-1} is high the effect of decreasing d_2 dominates over the effect of increasing d_1. However, when curvature is low and d_1 and d_2 are comparable, the effect of increasing d_1 negates the effect of decreasing d_2, and the energy of the VBM remains constant. Aside from decreasing the band gap, the destabilisation of the VBM is practically important, destabilising phosphorene/ with respect to oxidation, a factor critical to its air stability.

5.4.3.2 Zigzag PNTs

When examining the band structure of z-PNTs, we see that there are two competing band gaps: z-PNTs with high curvature have an indirect band gap, from $VB_\Gamma – CB_{Y*}$, whereas z-PNTs with low curvature have a direct band gap, from $VB_\Gamma – CB_\Gamma$. While VB_Γ and CB_Γ are both located at the Γ-point, CB_{Y*} is located at around [0, 0.3, 0] $2\pi/l$. As can be seen in Figure 5.24, $VB_\Gamma – CB_\Gamma$ rises and $VB_\Gamma – CB_{Y*}$ falls as the curvature increases. The band gap remains direct between r^{-1} = 0 Å^{-1}, when the band gap is 0.89 eV, until around r^{-1} = 0.03 Å^{-1}, when the band gap is 1.09 eV. When r^{-1} > 0.03 Å^{-1}, the band gap becomes indirect, from $VB_\Gamma – CB_{Y*}$. The $VB_\Gamma – CB_{Y*}$ band gap falls with increasing surface curvature, from 1.08 eV when r^{-1} = 0.034 Å^{-1} to 0.21 eV when r^{-1} = 0.123 Å^{-1}. It should be noted that for higher curvature CB_Γ does not necessarily correspond to the lowest Γ-point conduction band, but instead to the electronic state at the CBM in ground state phosphorene.

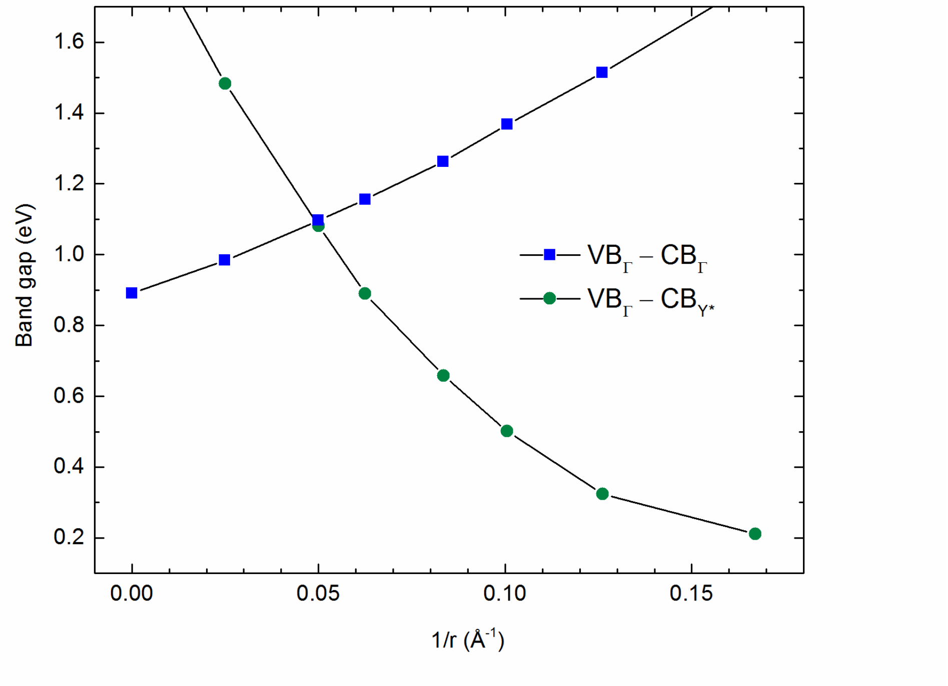

Figure 5.24: The two competing band gap of z-PNT, $VB_\Gamma – CB_{Y*}$ and $VB_\Gamma – CB_\Gamma$ versus r^{-1}.

The fact that both band gaps originate from the same valence state, VB_Γ, suggests that CB_Γ is destabilised with respect to CB_{Y*} with increased curvature. This is confirmed in Figure 5.25, which plots the absolute band energies of CB$_{\Gamma}$, CB$_{Y*}$ and VB$_{\Gamma}$ vs. r^{-1}. The electronic state at CB$_{\Gamma}$ is destabilised while CB$_{Y*}$ and VB$_{\Gamma}$ are both stabilised as surface curvature is increased.

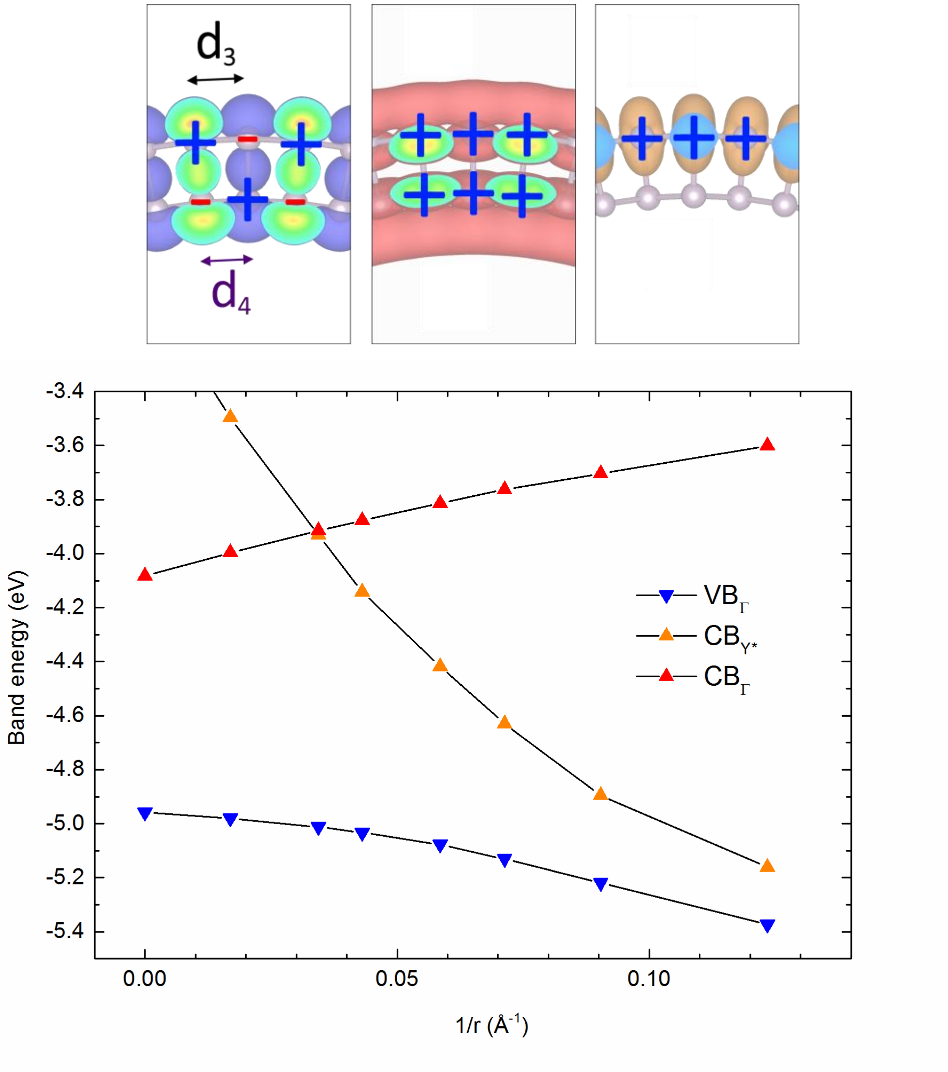

Figure 5.25: The absolute energy of the VB$_{\Gamma}$, CB$_{Y*}$ and CB$_{\Gamma}$ of z-PNT versus r^{-1}.

Examining the phase factors of the atomic orbitals which make up the electronic state at CB$_{\Gamma}$, the constituent p_z orbitals are separated by d_3 and d_4 in-phase, resulting in a bonding interaction. Therefore, when d_3 and d_4 are increased, CB$_{\Gamma}$ is destabilised and when they are decreased CB$_{\Gamma}$ is stabilised. Over the range of z-PNTs studied, d_3 increases and d_4 decreases with increased curvature, and thus the effects of changes in d_3 and d_4 are in direct opposition. However, while d_3 increases by over 10% with respect to the bulk over the range of curvatures studied, d_4 falls by less than 2%. There is therefore a net separation of bonding pairs as r^{-1} is increased, meaning that the overall effect of increasing curvature is to destabilise CB_{Γ}. Conversely, considering the electronic state at VB_{Γ}, the p_z orbitals separated by d_3 and d_4 are out-of-phase, resulting in a bonding interaction. Therefore, increasing r^{-1} stabilises VB_{Γ} in an analogous manner, as can be seen in Figure 5.25.

Meanwhile, the stabilisation of CB_Y with r^{-1} can also be explained by considering the bonding arrangement of the electronic state's constituent atomic orbitals. While the electronic states at CB_{Γ} and VB_{Γ} are dominated by p_z character, the electronic state at CB_Y consists mainly of p_y orbitals separated by d_3. By inspection of Figure 5.26, the orbitals appear to be in-phase. However, in reality the staggered configuration of atoms around the circumference of z-PNT means that the p_y components separated by d_3 are anti-bonding. Therefore, as d_3 rises with r^{-1}, CB_{Y*} is stabilised.

5.4.4 Bending phosphorene: Summary

We have shown through calculation of phosphorene's anisotropic bending moduli that it is far easier to bend phosphorene in the armchair direction than in the zigzag direction. Bending in either direction has a significant effect on the band gap of phosphorene.

When zigzag direction surface curvature is low (r^{-1} < 0.05 Å^{-1}) the band gap rises steadily with r^{-1} as VBM is stabilised and the CBM is destabilised. The simultaneous stabilisation of the VBM and destabilisation of the VBM would protect z-PNTs against both oxidation and reduction relative to the bulk. However, past a critical strain of r^{-1} = 0.05 Å^{-1}, the band gap of z-PNTs becomes indirect following the emergence of a new CBM at reciprocal point Y*. CB_{Y*} is stabilised with r^{-1}, resulting in a falling band gap. Meanwhile, bending in the armchair direction has little effect on the band gap when surface curvature is low (r^{-1} < 0.04 Å^{-1}), with the absolute energy of both band edges remaining relatively constant. At curvatures r^{-1} > 0.04 Å^{-1}, the band gap falls rapidly with increased curvature due to the destabilisation of the VBM. The destabilisation of the VBM makes phosphorene more susceptible to oxidation.

References

1. Wei, Q. and X.H. Peng, *Superior mechanical flexibility of phosphorene and few-layer black phosphorus.* Applied Physics Letters, 2014. **104**(25).

2. Fei, R. and L. Yang, *Strain-Engineering the Anisotropic Electrical Conductance of Few-Layer Black Phosphorus.* Nano Letters, 2014. **14**(5): p. 2884-2889.

3. Peng, X.H., Q. Wei, and A. Copple, *Strain-engineered direct-indirect band gap transition and its mechanism in two-dimensional phosphorene.* Physical Review B, 2014. **90**(8).

4. Wang, L.Q., et al., *Electro-mechanical anisotropy of phosphorene.* Nanoscale, 2015. **7**(21): p. 9746-9751.

5. Lee, C., et al., *Measurement of the Elastic Properties and Intrinsic Strength of Monolayer Graphene.* Science, 2008. **321**(5887): p. 385-388.

6. Castellanos-Gomez, A., et al., *Elastic Properties of Freely Suspended MoS2 Nanosheets.* Advanced Materials, 2012. **24**(6): p. 772-+.

7. Song, L., et al., *Large Scale Growth and Characterization of Atomic Hexagonal Boron Nitride Layers.* Nano Letters, 2010. **10**(8): p. 3209-3215.

8. Bertolazzi, S., J. Brivio, and A. Kis, *Stretching and Breaking of Ultrathin MoS2.* Acs Nano, 2011. **5**(12): p. 9703-9709.

9. Pham, K.T., et al., *Reflectarray Element Based on Variable Line Length for Millimeter-Wave Radar Applications.* 2012 International Conference on Advanced Technologies for Communications (Atc 2012), 2012: p. 218-221.

10. Aksoy, R., et al., *X-ray diffraction study of molybdenum disulfide to 38.8 GPa.* Journal of Physics and Chemistry of Solids, 2006. **67**(9-10): p. 1914-1917.

11. Qin, G., et al., *Hinge-like structure induced unusual properties of black phosphorus and new strategies to improve the thermoelectric performance.* Sci. Rep., 2014. **4**.

12. Qiao, J., et al., *High-mobility transport anisotropy and linear dichroism in few-layer black phosphorus.* Nat Commun, 2014. **5**.

13. Zhu, Z. and D. Tomanek, *Semiconducting Layered Blue Phosphorus: A Computational Study.* Physical Review Letters, 2014. **112**(17).

14. Tsoukleri, G., et al., *Subjecting a Graphene Monolayer to Tension and Compression.* Small, 2009. **5**(21): p. 2397-2402.

15. Meyer, J.C., et al., *The structure of suspended graphene sheets.* Nature, 2007. **446**(7131): p. 60-63.

16. Wei, Y.J., et al., *Bending Rigidity and Gaussian Bending Stiffness of Single-Layered Graphene.* Nano Letters, 2013. **13**(1): p. 26-30.

17. Helfrich, W., *Elastic Properties of Lipid Bilayers - Theory and Possible Experiments.* Zeitschrift Fur Naturforschung C-a Journal of Biosciences, 1973. **C 28**(11-1): p. 693-703.

18. Lipowsky, R., *The Conformation of Membranes.* Nature, 1991. **349**(6309): p. 475-481.

Chapter 6

Phosphorene nanoribbons

6.1 Background

Many of phosphorene's exciting properties are the result of quantum confinement effects, with phosphorene's wavefunction confined perpendicular to the 2D plane on which the compound lies. As has been demonstrated through investigations of other 2D materials such as graphene and monolayer MoS_2, further interesting electronic properties arise when 2D compounds are terminated to form quasi-1D nanoribbons [1, 2]. Furthermore, the fact that graphene nanoribbons can now be synthesised and isolated on a large scale suggests that the routine use of such heavily nanostructured materials is close to becoming a reality [3].

We have studied the change in phosphorene's electronic structure when it is terminated to form phosphorene nanoribbons (PNRs), investigating two different orientations along which phosphorene can be cut in order to form 'armchair' PNRs (a-PNRs) and 'zigzag' PNRs (z-PNRs). We have shown that z-PNRs in particular demonstrate strong quantum confinement effects which increase the magnitude of the band gap relative to monolayer phosphorene. We explain the origins of these effects by applying periodic boundary conditions to monolayer phosphorene, and ultimately derive a formula relating phosphorene's band edge effective masses to the band gap of PNRs. We also demonstrate that both the band gap and transport properties of PNRs can be modified by applying uniaxial strain along the length of the ribbon.

6.1.1 Graphene nanoribbons

The properties of graphene nanoribbons have been widely investigated. Unlike phosphorene, graphene is a semi-metal with no intrinsic band gap, severely limiting its usage in electronic devices. Two types of graphene nanoribbons exist, namely zigzag graphene nanoribbons (ZGNRs) and armchair graphene nanoribbons (AGNRs).

The electronic properties of AGNRs depends on the ribbon's width, measured in terms of the number of atoms (*m*) along the cross-ribbon direction. Using the tight binding approximation, when $m = 3p + 2$ (where p is any integer) AGNRs are metallic [4], with all other widths semiconducting. However, when using DFT or the GW approximation to calculate electronic structure, all AGNRs are semiconducting with band gaps following the hierarchy $3p+1 > 3p > 3p+2$ [5, 6]. In all cases, there is a consistent inverse relationship between the band gap and ribbon width, with the band gap opening primarily a result of quantum confinement. Meanwhile, ZGNRs have localised electronic states at their edges [7]. Nearest neighbour sites are coupled antiferromagnetically throughout the lattice, giving rise to a small band gap which varies inversely with ribbon width [1].

The most common way to make GNRs is by top-down plasma etching, where resists, metals or nanowires are used as masks and plasma is used to etch away exposed graphene regions. Using this technique, sub-20 nm GNRs can be made, with Bai *et al*. producing 8 nm wide GNR [8]. However, the edge quality of etched nanoribbons can be poor, degrading the electronic properties of sub- 20nm GNRs [9]. Furthermore, chemical approaches have been used to synthesize nanoribbons as narrow at 2 nm with band gaps approaching 400 meV [10]. High quality GNRs have also been made by unzipping carbon nanotubes CNTs by means of plasma etching, sonication, metal nanoparticle cutting and oxidation and reduction.

Experimentally, there is good agreement with theoretically predicted band gaps and their width dependence. The opening of a band gap is vital if graphene is to be used in logic devices, with sub-5nm GNRs required to obtain a reasonable on/off ratio. GNRs produced through chemical sonication deliver an on/off ratio of 10^6, although mobility is limited by edge scattering and is less than 200 $cm^2 V^{-1} s^{-1}$, somewhat defeating the object of using graphene in logic devices [10]. However, research into the field is still very much ongoing, with a multitude of other quantum devices currently under investigation.

6.1.2 MoS_2 nanoribbons

While GNRs remain by far the most widely studied 1D nanostructures, MoS_2 nanoribbons have been well theoretically characterized [2] . As with GNRs, MoS_2 nanoribbons can exist in two forms depending on their edge termination, zigzag MoS_2 nanoribbons and armchair MoS_2 nanoribbons. Armchair nanoribbons are non-magnetic and semiconducting, with band gaps rising as ribbon width is increased. Interestingly, the band gap of nanoribbons does not rise steadily, fluctuating below the band gap of monolayer MoS_2. Meanwhile, zigzag nanoribbons show ferromagnetic and magnetic behaviour, irrespective of the ribbon's width.

6.1.3 Un-passivated phosphorene nanoribbons

Prior to the publication of our work on passivated phosphorene nanoribbons, Guo *et al*. reported the behaviour of un-passivated PNRs [11]. Their study investigated 'zigzag' un-passivated PNRs (z-PNRs) and armchair un-passivated PNRs (a-PNRs). While z-PNRs are metallic regardless of ribbon width [12], a-PNRs have an indirect band gap which decreases as the width of ribbon is increased. In z-PNRs, it is edge states that result in metallic behaviour. In a-PNRs, the CBM is an edge state whereas the VBM is located towards the ribbon's interior.

6.2 Methodology

Density functional calculations were performed using the VASP code. We used a plane-wave basis set truncated at 400 eV and PAW pseudopotentials to treat core electrons. More information about plane-wave DFT and pseudopotentials can be found in Chapter 2. Given the size of the largest PNRs studied, we used the same approach as in Section 5.3, with the PBE functional in combination with the DFT-D3 dispersion correction scheme used not only to perform structural relaxations but also to investigate electronic structures. While we acknowledge that this method is likely to underestimate the absolute size of band gaps, we are confident that the effect is relatively consistent and that the reported trends are representative of the true behaviour. When relaxing crystal lattices and internal atomic positions, we used a conjugate gradient algorithm until all interatomic forces fell below 0.01 eV/Å. A vacuum region of over 20 Å was maintained perpendicular to the *xy* plane, with an additional 20 Å vacuum region separating the periodic images of PNRs within the plane. The geometries obtained were fully converged when *k*-space was sampled using a 9×1×1 Monkhorst-Pack mesh for z-PNRs and a 1×9×1 Monkhorst-Pack mesh for a-PNRs. For electronic structure calculations, a *k*-point density equivalent to that of a 100×1×1 Monkhorst-Pack mesh was used for z-PNRs and that of a 1×100×1 Monkhorst-Pack mesh was used for a-PNRs. Absolute band energies were obtained by subtracting the total local potential found directly in the middle of the vacuum region from the eigenvalues computed using DFT.

6.3 Simulations of Phosphorene Nanoribbons

6.3.1 Geometry of z-PNR and a-PNR

We identified two different directions along which monolayer phosphorene can be cut in order to form nanoribbons. As shown in Figure 6.1, cutting along the [010] direction results in zigzag nanoribbons, z-PNRs, while cutting along the [100] direction results in armchair nanoribbons, a-PNRs. The formation of each nanoribbon involves breaking one P-P bond per edge phosphorus atom, leaving dangling bonds. Given that dangling bonds are highly reactive and will bond with impurities, we passivated edge phosphorus atoms with atomic hydrogen.

We relaxed the structure of 12 different widths of each PNR, containing between 4 and 16 unit cells corresponding to widths of between 13 and 75 Å. The internal geometry of PNRs remained very close to that of the bulk, with central regions of all but the narrowest PNRs indistinguishable from monolayer phosphorene. The lattice parameters along the length of PNRs, a_0 in z-PNRs and b_0 in a-PNRs, also remained similar to those of bulk monolayer phosphorene. Compared to the bulk values of a_0 = 3.298 Å and b_0 = 4.619 Å, z-PNR$_4$ had a length of 3.301 Å and y-PNR$_4$ had a length of 4.620 Å.

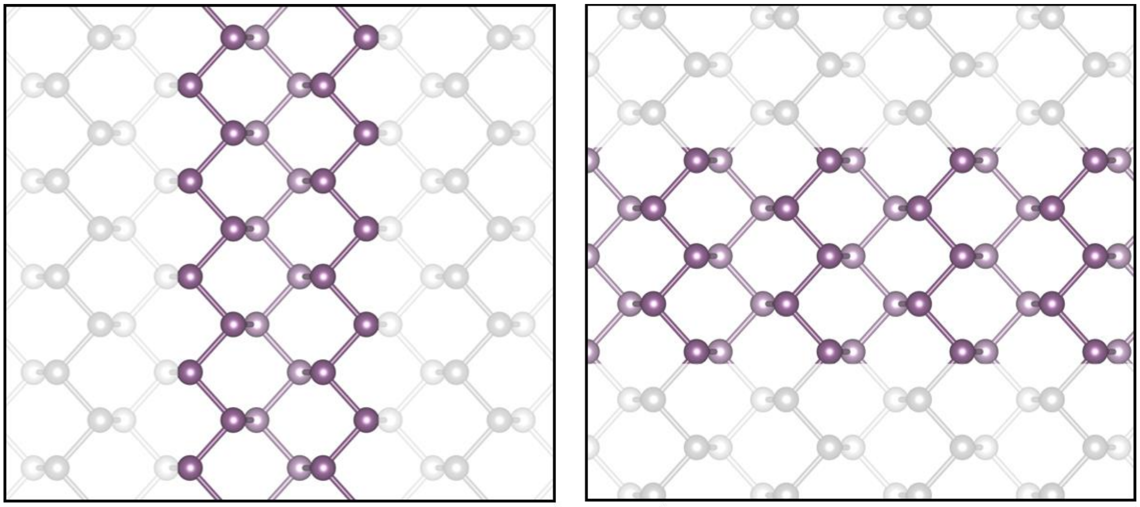

Figure 6.1: A representation of the structure of z-PNRs (left) and a-PNRs (right) with respect to phosphorene.

We checked the stability of both a-PNRs and z-PNRs with respect to Peirels distortions, which are symmetry breaking distortions of the one dimensional periodic lattice. For ribbon widths of 4, 6 and 10 unit cells, we compared the ground state energies of supercells containing one, two and four unit cells along the ribbon's length. Supercells containing two and four unit cells were not stabilised with respect to the unit cell, and we therefore conclude that passivated PNRs do not undergo Peirels distortions.

6.3.2 Formation Energy

For each PNR, we calculated the formation energy per unit edge using the following formula:

$$E_{form} = \frac{1}{2}\left(E^{ribbon} - N_P E^{bulk} - \frac{N_H}{2} E_{H_2}\right)$$

where E^{ribbon} is the energy of the PNR, E^{bulk} is the atomic energy of monolayer phosphorene, E_{H_2} is the energy of a H_2 molecule, N_P is the number of phosphorus atoms in the ribbon and N_H is the number of hydrogen atoms. As can be seen in Table 6.1, formation energies of z-PNRs are slightly exothermic whereas formation energies of a-PNRs are slightly endothermic. We propose that there are two dominant contributions to E_{form}: E_{conf} and E_{chem}.

Wavefunctions confined within the width of a PNR are energetically different to unconfined wavefunctions in the bulk, with the difference between the two equal to E_{conf}. One would expect an unconfined wavefunction to be more stable than a confined one, and we indeed found that E_{form} becomes more exothermic with increasing ribbon width. In other words, as the extent of confinement decreases E_{form} also decreases, proving that confinement has an endothermic effect.

Meanwhile, E_{chem} is simply the change in bond energies which occurs when PNRs are formed from monolayer phosphorene and H_2. For every two P – H bonds formed, $E_{chem} = 2 \times E_{P-H} - (E_{H-H} + E_{P-P})$. Extrapolating to find E_{form} for a PNR of infinite width results in an exothermic formation energy for both z-PNRs and a-PNRs. This approach effectively sets E_{conf} to zero, and assuming that $E_{form} = E_{conf} + E_{chem}$, this means that E_{chem} is exothermic for both types of PNR. This finding is supported by reference data, where E_{P-P} = 2.08 eV, E_{H-H} = 4.48 eV and E_{P-H} = 3.34 eV, giving the net formation energy of a P – H bond in -0.05 eV.

	z-PNRs			a-PNRs		
Width, uc.	**Width, Å**	**E_{form}, eV**	**Gap, eV**	**Width, Å**	**E_{form}, eV**	**Gap, eV**
4	18.69	-0.051	1.554	13.32	0.056	1.077
5	23.29	-0.051	1.393	16.64	0.054	1.017
6	27.89	-0.051	1.290	19.96	0.052	0.985
7	32.49	-0.052	1.213	23.28	0.050	0.966
8	37.08	-0.053	1.156	26.6	0.048	0.952
9	41.68	-0.054	1.114	29.92	0.046	0.944
10	46.28	-0.054	1.082	33.24	0.044	0.938
11	50.88	-0.055	1.057	36.56	0.042	0.933
12	55.48	-0.055	1.037	39.88	0.040	0.929
13	60.07	-0.056	1.021	43.2	0.038	0.926
14	64.67	-0.057	1.007	46.52	0.036	0.923
15	69.27	-0.058	0.996	49.84	0.035	0.920
16	73.87	-0.058	0.986	53.16	0.033	0.917

Table 6.1: The width in Å, formation energy and band gap of z-PNRs and a-PNRs with widths of between 4 and 16 unit cells.

In addition to E_{conf} and E_{chem}, we also acknowledge that E_{form} will include contributions due to geometry relaxations and changes in local potential. However, we assume that these contributions are small given the similarity of the internal geometries of PNRs and monolayer phosphorene. We emphasize that the energies calculated are zero temperature electronic energies only and do not account for entropy. We would expect Gibbs free energies to be significantly endothermic given the high entropy of gaseous H_2, which is in excess of 0.4 eV under standard conditions.

6.3.3 Band Gaps

For each width of PNR investigated, we calculated the electronic band gap. In all a-PNRs, both band edges are located at the Γ-point whereas in z-PNRs the VBM is offset slightly in the X direction. As seen in Figure 6.2, the band gaps of both a-PNRs and z-PNRs increase with decreasing ribbon width. This effect is more dramatic when narrowing z-PNRs (confining wavefunctions in the armchair direction) than it is when narrowing a-PNRs (confining wavefunctions in the zigzag direction). For example, the band gap of 18.7 Å wide z-PNR is 1.55 eV whereas the band gap of 16.6 Å wide a-PNR is 1.02 eV. Given that we are using the PBE functional to investigate electronic structure, the reference band gap for bulk monolayer phosphorene is that which is calculated using the PBE functional, 0.89 eV, rather than that which is calculated using HSE06, 1.55 eV. This means that ~2 nm passivated a-PNR has a band gap which is 0.66 eV higher than that of the monolayer, whereas ~2nm passivated z-PNR has a band gap which is only 0.13 eV higher than that of the monolayer.

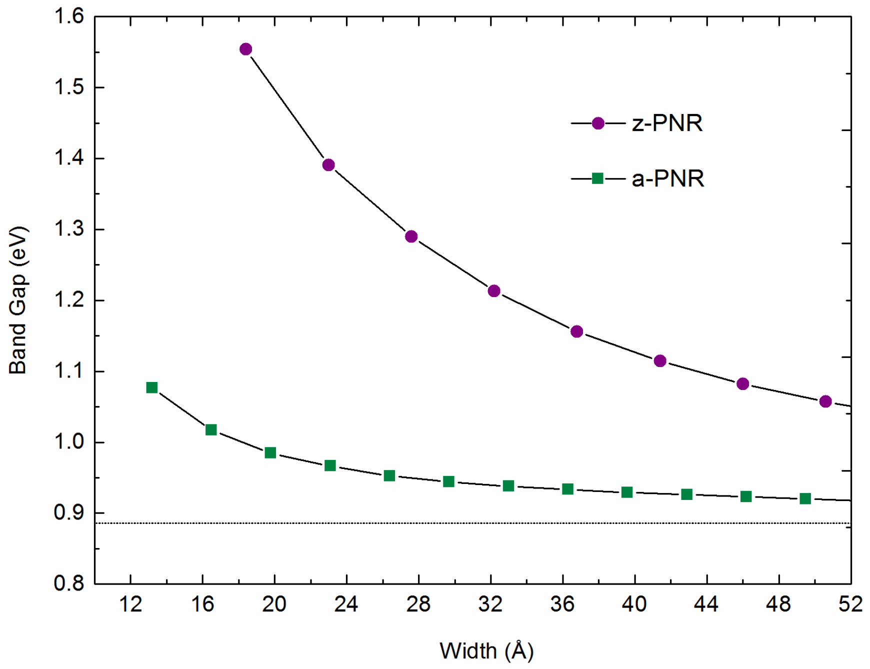

Figure 6.2: The band gaps of a-PNRs and z-PNRs of various widths. The dotted line at ~0.89 eV represents the band gap of 'bulk' monolayer phosphorene.

Examining the absolute band energies of PNRs relative to the vacuum level, we see that the VBM is stabilised and the CBM is destabilised in equal measure relative to the bulk. Stabilising the VBM and destabilising the CBM has a significant effect on stability and reactivity, with PNRs stabilised with respect to both oxidation and reduction. Furthermore, the changes in the absolute band edge energies also increase photocatalytic power. Electrons excited to a less stable CBM have more reductive power and the resulting holes left in a more stable VBM have more oxidative power.

6.3.4 Density of states

We calculated the density of states (DoS) for 10 unit cell wide PNRs, decomposing the contributions of 'middle' and 'edge' phosphorus atoms, as shown in Figures 6.3 and 6.4. We found that for both z-PNR and a-PNR, the inner twenty phosphorus atoms contribute to both band edges more than the outer twenty phosphorus atoms. Hydrogen orbitals, meanwhile, do not contribute to any near edge electronic states.

The unequal contribution of middle and edge phosphorus atoms is also demonstrated by the site decomposed contribution of phosphorus atoms to the band edge electronic states. Figures 6.3(c) and 6.4(c) show the relative contribution of phosphorus atoms to electronic states at the CBM and VBM versus their position along the ribbon's width. While data are only reported to 3 significant figures in the VASP code, the plots clearly follow a half sinusoidal wave, with atomic contributions tending towards zero at either edge of the ribbon. This observation is important given that it defines the boundary conditions which can be used to explain quantum confinement effects, see Section 6.3.5.

Furthermore, the DoS calculated for passivated PNRs are in contrast to those of un-passivated PNRs reported in the literature. The literature reports that un-passivated z-PNRs are metallic, with states around the Fermi level consisting entirely of edge phosphorus character, with the CBM of un-passivated a-PNRs also being located towards the ribbon's exterior. Meanwhile, the nature of the VBM in un-passivated a-PNRs appears similar to the VBM in passivated a-PNRs. We also looked at the spd- decomposed DoS of passivated PNRs, finding that the relative contributions phosphorus *s* and $p_{x/y/z}$ orbitals are very similar to those reported for monolayer phosphorene in Section 3. Electronic states at both band edges appear to predominantly consist of p_z orbitals which appear to be bonding in the *z* direction at the VBM and anti-bonding in the *z* direction at the CBM.

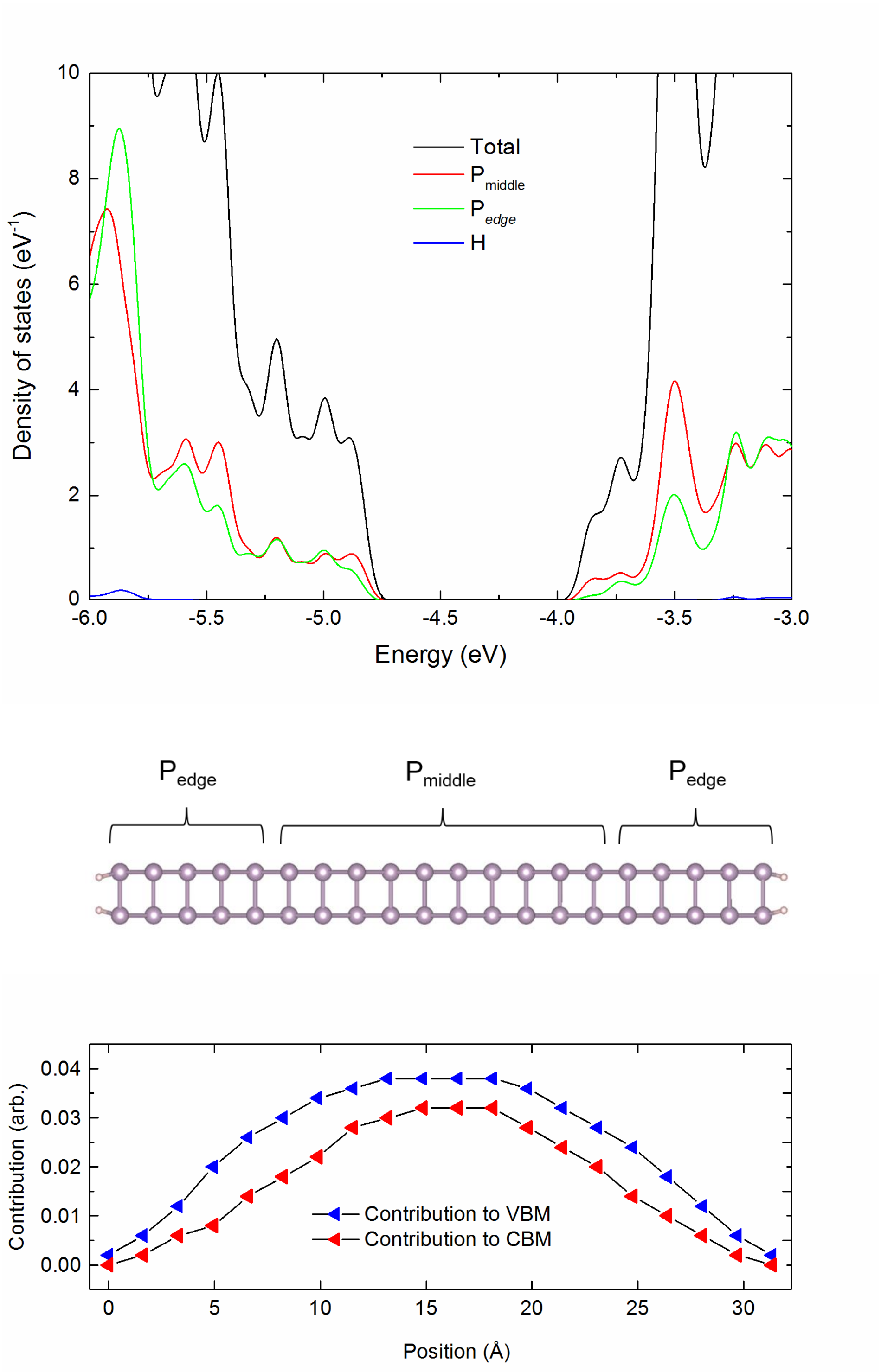

Figure 6.3: The density of states of a-PNR$_{10}$, with the contributions ‘edge’ and ‘middle’ phosphorus atoms decomposed (top), the structure of a-PNR$_{10}$ with ‘edge’ and ‘middle’ regions labelled (middle) and the contribution of phosphorus atoms to the VBM and CBM versus the atomic position (bottom).

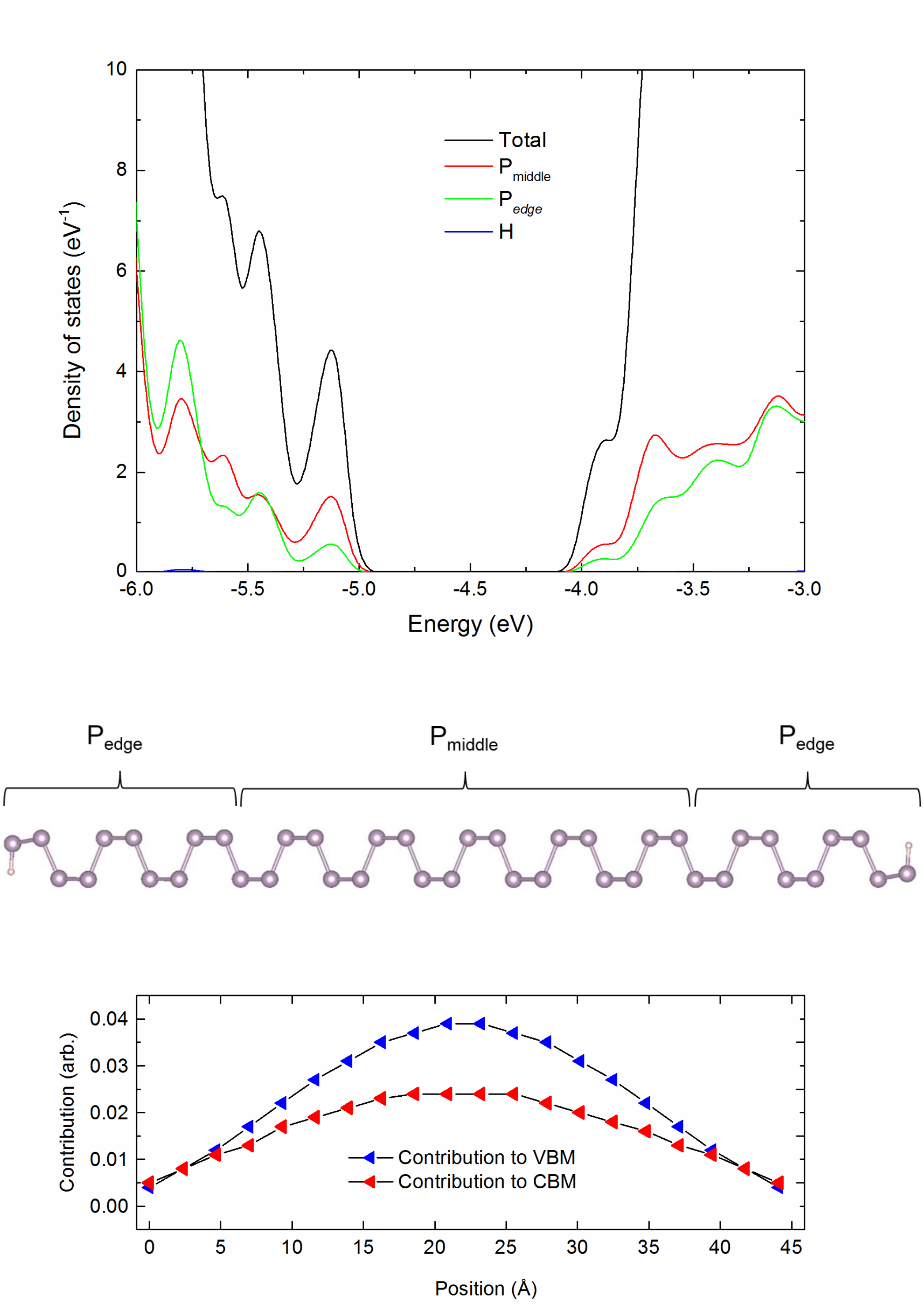

Figure 6.4: The density of states of z-PNR$_{10}$, with the contributions 'edge' and 'middle' phosphorus atoms decomposed (top), the structure of z-PNR$_{10}$ with 'edge' and 'middle' regions labelled (middle) and the contribution of phosphorus atoms to the VBM and CBM versus the atomic position (bottom).

6.3.5 Band gap prediction

Under the assumption that the charge density falls to zero beyond the edges of PNRs, we can assume that that their wavefunctions are confined within the ribbon's width. Therefore, periodic boundary conditions can be applied to deduce the bulk wavefunctions corresponding to the electronic states that can exist in PNRs. In the below formula, k_n is the set of allowed k-points when wavefunctions are confined within the width $N \times l_0$, where l_0 is a bulk lattice vector and N is an integer [13].

$$k_n = \frac{\pi}{l_0} \cdot \frac{n}{\mathrm{N}} \qquad n = 1 \ \ldots \mathrm{N}$$

We sampled the Brillouin zone of bulk phosphorene at the k-points allowed according to the above condition. In each instance, both the highest energy valence state and the lowest energy conduction state sampled were found when n = 1. This is unsurprising given that both the VBM and CBM of phosphorene are located at the Γ-point ($k = 0$), and that k_n is minimised when n = 1. The Bloch wave returned when $k = k_1$ has the form of a half sinusoidal wave spanning $N \times l_0$, and therefore the implied contribution of phosphorus atoms along the length $N \times l_0$ bears a striking resemblance to the band edge contributions of phosphorus atoms shown in Figures 6.3 and 6.4.

By taking the difference between the valence and conduction band energies when $k = k_1$, we calculated the band gaps of wavefunctions confined within $N \times l_0$. We assume that these wavefunctions resemble the wavefunctions of PNRs with a width of N unit cells, and therefore can be used to predict their band gaps. As can be seen in Figure 6.5, the band gaps predicted follow a similar trend to the actual band gaps of PNRs, and are particularly accurate for ribbons with a width greater than 10 unit cells.

The differences between the band gaps calculated for PNRs directly and those calculated by applying PBCs are, however, significant for narrow ribbons. Bulk wavefunctions confined within $N \times l_0$ and wavefunctions found in PNRs of a similar width differ in a number of ways. Perhaps most importantly, PNR wavefunctions are not truly confined within the ribbon's width, but instead tend to zero as the vacuum level is approached. Furthermore, the geometries and local potentials found in the bulk are different from those found in nanoribbons. In the bulk, there are infinite periodic repetitions of the unit cell beyond the area of confinement, whereas PNRs are terminated with hydrogen, which not only affects the local potential felt by electrons close to the PNR's edge, but also leads to subtle geometry changes in the same region.

The above factors primarily affect the wavefunction close to the edge of PNRs, and are therefore more important for narrow PNRs where edge regions make up a larger proportion of the total wavefunction. For wider PNRs, these edge effects are relatively insignificant, and therefore the band gap can be accurately predicted by applying PBCs to the bulk.

It follows that the band gaps obtained using the PBC method can be predicted formulaically if we assume that both of phosphorene's band edges are parabolic around the Γ-point. The valence and conduction band energies of phosphorene at $k = \frac{\pi}{Nl_0}$ can be estimated formulaically as follows:

$$E_{\boldsymbol{k},VB/CB} = A_{VB/CB}.\boldsymbol{k}^2 + E_{VBM/CBM}$$

$$A_{VB/CB} = \frac{1}{2}.\frac{d^2E_{\boldsymbol{k},VB/VB}}{d\boldsymbol{k}^2}$$

where $E_{VBM/CBM}$ are the energies of the VBM and CBM. We recall that the second differential of $E_{\boldsymbol{k}}$ with respect to $\boldsymbol{k}$ also appears during the calculation of effective mass. Therefore, we can express $A_{VB/CB}$ in terms of the corresponding band edge effective mass,

$$m_{h/e} = \hbar^2.\left(\frac{d^2E_{\boldsymbol{k},VB/VB}}{d\boldsymbol{k}^2}\right)^{-1}$$

$$A_{VB/CB} = \frac{1}{2}.\frac{d^2E_{\boldsymbol{k},VB/VB}}{d\boldsymbol{k}^2} = \frac{\hbar^2}{2.m_{h/e}}$$

Furthermore, $E_{\boldsymbol{k},VB/CB}$ and ultimately $E_{gap,\boldsymbol{k}}$ can also be expressed in terms of the effective mass,

$$E_{k,VB/CB} = \frac{\hbar^2}{2.m_{h/e}}.\boldsymbol{k}^2 + E_{VBM/CBM}$$

$$E_{gap,\boldsymbol{k}} = E_{k,CB} - E_{k,VB} = \left(\frac{\hbar^2}{2.m_e}.\boldsymbol{k}^2 + E_{CBM}\right) - \left(\frac{\hbar^2}{2.m_h}.\boldsymbol{k}^2 + E_{VBM}\right)$$

$$E_{gap,\boldsymbol{k}} = E_{gap,phos} + (m_e{}^{-1} + m_h{}^{-1}).\frac{\hbar^2}{2}.\left(\frac{\pi}{Nl_0}\right)^2$$

where $E_{gap,phos}$ is the band gap of bulk phosphorene. When tested, the above formula reproduced the band gaps predicted using PBCs to within 5% for the thinnest nanoribbons and to a far higher degree of accuracy for wider ribbons, as can be seen in Figure 6.5. The overestimation of the band gap of the thinnest ribbons occurs because the valence and conduction bands are not parabolic further away from the band edges.

Given that effective masses at phosphorene's band edges are consistent to within 10% when calculated using different density functionals, the above equation allows E_{gap} to be estimated for any functional provided that $E_{gap,phos}$ is known. It also implies that the absolute additive effect on the band gap as a result of quantum confinement is consistent regardless of the functional used. Given that the electronic and optical band gaps of phosphorene have been found to be around 2.2 and 1.6 eV respectively when calculated using state of the art GW calculations [14], our results suggest that E_{gap} can be moved throughout the optical region.

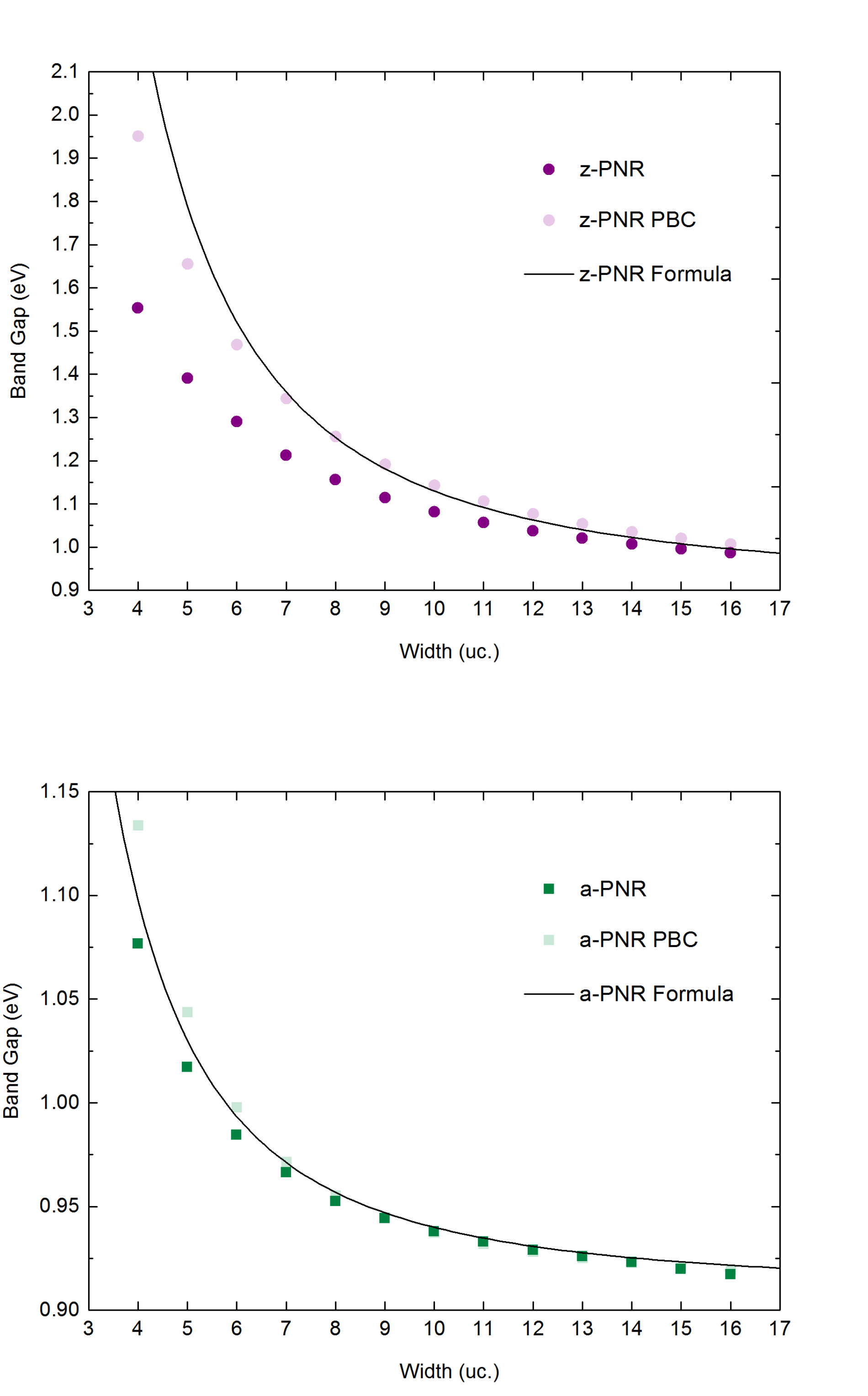

Figure 6.5: The band gaps of z-PNRs (top) and a-PNRs (bottom) consisting of between 4 and 16 unit cells predicted using three methods; direct modelling of the PNR using DFT, applying PBC to the band structure of monolayer phosphorene.

6.3.6 Effective mass

Given that the band edge electronic states of PNRs are different from those found in monolayer phosphorene, their electron and hole effective masses along the length of the ribbon are also different. We found that the effective masses for the majority of the a-PNRs are similar to those along the analogous armchair direction in phosphorene, where when calculated using PBE, m_h = 0.146 m_0 and m_e = 0.156 m_0. However, for narrow a-PNRs, m_e and m_h both increase exponentially with decreasing ribbon width, as show in Figure 6.6. For example, in a-PNR$_4$, m_e = 0.187 m_0 and m_h = 0.173 m_0, both approaching 20% higher than in monolayer phosphorene.

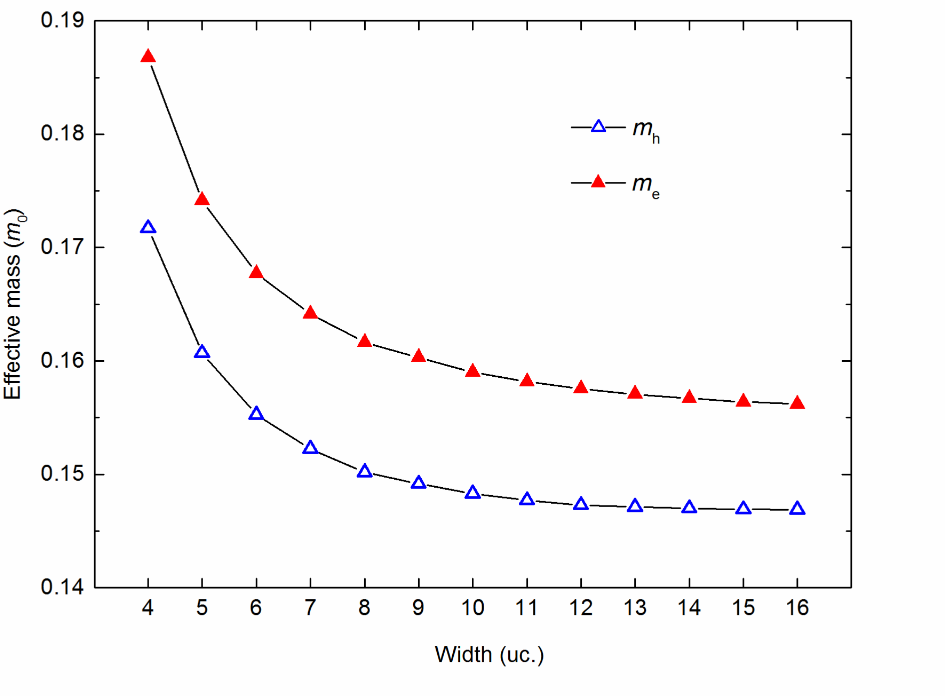

Figure 6.6: The hole and electron effective masses of a-PNRs consisting of between 4 and 16 unit cells.

We found the calculation of m_h in z-PNRs to be considerably more troublesome. While the VBM in phosphorene and in a-PNRs is located directly at the Γ-point, the VBM in z-PNRs is slightly offset from the Γ-point in the X direction. The thinner the nanoribbon, the more sizeable this offset: in z-PNR$_4$, the VBM is located at [0.086, 0, 0] $2\pi/l$, whereas in z-PNR$_{16}$ it is located at [0.038, 0, 0] $2\pi/l$. The displacement of the VBM towards X in z-PNRs is consistent with the band structure of phosphorene; Figure 6.7 compares phosphorene's band dispersion between [0,

$\frac{\pi}{10b_0}$, 0] $2\pi/l$ and [0.1, $\frac{\pi}{10b_0}$, 0] $2\pi/l$ to that of z-PNR$_{10}$ between [0, 0, 0] $2\pi/l$ and [0.1, 0, 0] $2\pi/l$. In both cases the band maximum is displaced towards X, and while the exact band dispersions differ, the origin of the indirect band gaps seen in z-PNRs is clearly demonstrated.

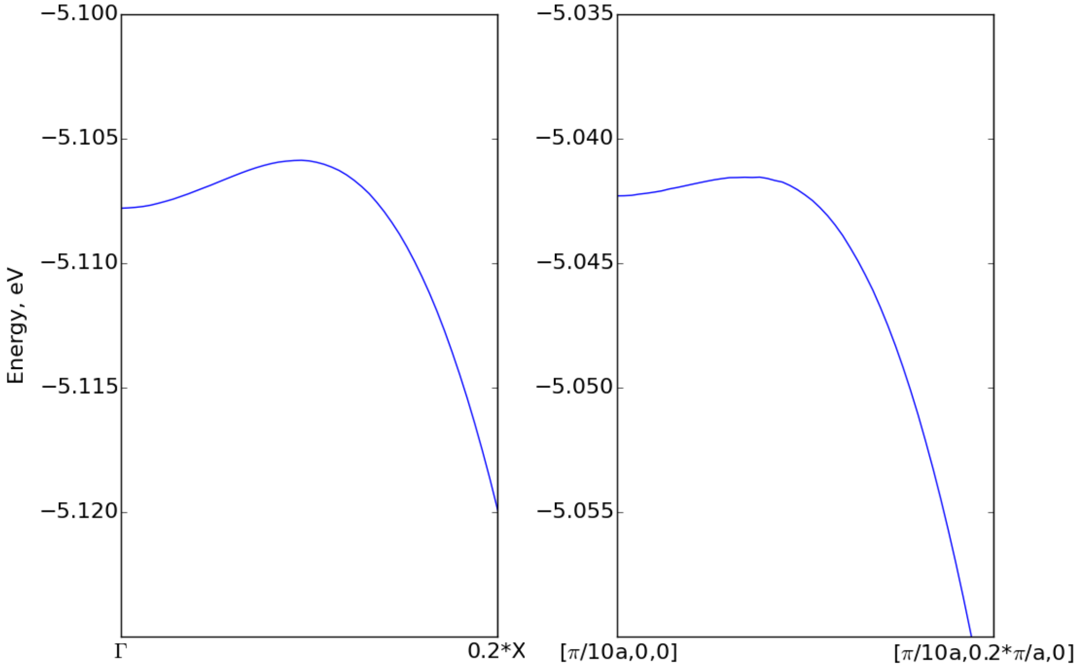

Figure 6.7: The valence band dispersion of z-PNR$_{10}$ (left) compared to that of phosphorene between Γ and 0.2 ×X (right).

While the differences between the energy of valence band of z-PNRs at Γ and the VBM are minimal (typically < 5 meV), the band dispersion about the VBM is asymmetric. Given that effective mass theory is based around the assumption that band edges are parabolic, this brings into question the suitability of the method and makes the calculation of m_h difficult. To compromise, we sampled points between the VBM and X only, ignoring the asymmetric band dispersion between Γ and the VBM. While this compromise allowed us to treat each z-PNR consistently, we believe that the results obtained should be viewed with a degree of caution.

We found that m_h increases exponentially with decreasing ribbon width, rising to around 3.1 m_0 in z-PNR$_4$ compared to 2.2 m_0 in z-PNR$_{16}$. Both of these values are significantly lower than the effective mass calculated for bulk phosphorene in Chapter 3. However, this difference could be considered a misleading result given the way that we calculated m_h in z-PNRs compared to phosphorene. In phosphorene, the high value of m_h is a result of the extremely flat valence band around Γ. In z-PNRs, this flat region is slightly stabilised, and so the point defined as the VBM is no longer located at Γ. Instead, the VBM is located at the point in k-space equivalent to the edge of the flat region in the band structure of bulk phosphorene. If we were to calculate phosphorene's hole effective mass at this point, m_h would be in agreement with the trends seen in Figure 6.8. Given that the energy difference between the two points in the bulk is less than 1 meV, both will be occupied at non-zero temperatures and therefore there is limited meaning in distinguishing between them.

Meanwhile, m_e remains fairly constant with ribbon width, ranging from 1.27 m_0 in z-PNR$_{16}$ to 1.31 m_0 in z-PNR$_4$. These values are similar to m_e in bulk phosphorene, 1.25 m_0, suggesting that *n*-type transport is unaffected by nanostructuring in the *y*-direction.

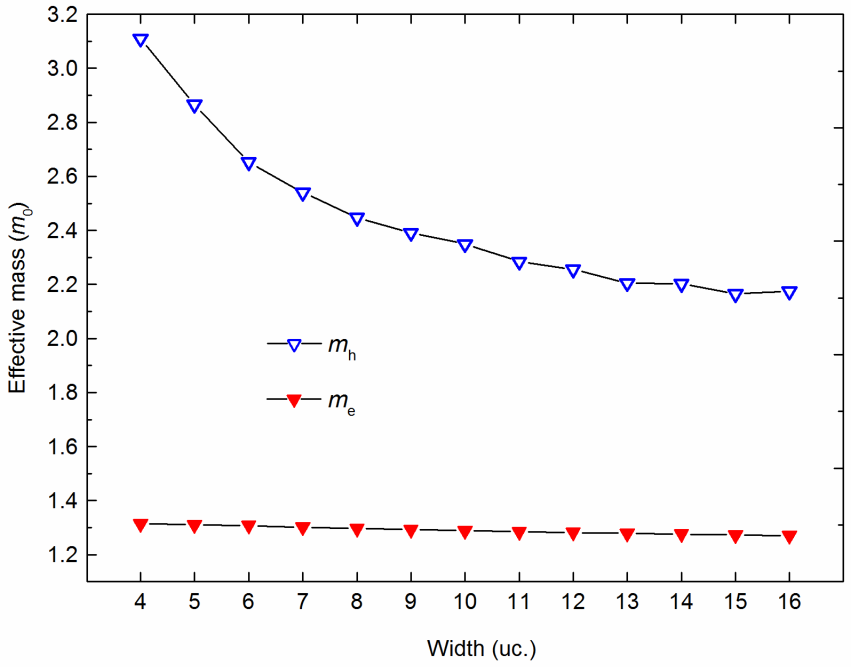

Figure 6.8: The hole and electron effective masses of z-PNRs of widths between 4 and 16 unit cells.

6.4 Phosphorene nanoribbons under strain

Given the remarkable effects of straining monolayer phosphorene, see Chapter 5, we investigated the effects applying uniaxial strain along the length of PNRs. In the interests of computational cost, we only studied 10 unit cell wide PNRs consisting of 40 phosphorus atoms per unit cell and assume that our findings can be extrapolated to PNRs of all widths. We investigated strains, ε, of between 0.90 and 1.10, well within the theoretical strain limit of phosphorene. To do this, we relaxed atomic positions within a fixed unit cell expanded by a factor of ε along the lattice parameter corresponding to the ribbon's length.

6.4.1 Stiffness

We quantified the stiffness of PNRs by calculating the 2D Young's modulus, C_{2D}, as discussed in Chapter 5. C_{2D} is defined in a similar manner as the conventional Young's modulus, C_{3D}.

$$C_{2D} = \frac{1}{A_0}\left(\frac{\partial^2 E}{\partial \varepsilon^2}\right)$$

where E, ε and A_0 correspond to energy, linear strain and the equilibrium surface area of the nanoribbon respectively. While C_{3D} has units of N/m^2 (Pa), C_{2D} has dimensionality of N/m (Pa.m), and is related to ε^{3D} through the relationship $C_{3D} = \frac{C_{2D}}{c_0}$, where c_0 is the lattice parameter perpendicular to the plane on which the 2D material lies.

We noticed that plots of E vs. ε are asymmetric around ε = 1.00, and therefore we calculated two values of C_{2D}: C_{ext}, for $\varepsilon > 1.00$ and C_{comp}, for $\varepsilon < 1.00$. We found that for both extensive ($\varepsilon > 1.00$) and compressive ($\varepsilon < 1.00$) strains, C_{2D} is significantly lower for a-PNR than for z-PNR. This finding was entirely expected; Chapter 5 and other recent studies have shown that it is far easier to strain phosphorene along the armchair direction than along the zigzag direction.

	C_{ext} (N/m)	C_{comp} (N/m)
a-PNR$_{10}$	19.2	23.3
z-PNR$_{10}$	139.65	93.54

Table 6.2: The young's 2D moduli of a-PNR$_{10}$ and z-PNR$_{10}$ for both compressive strain C_{comp} and extensive strain C_{ext}.

Regardless of the difference between a-PNRs and z-PNRs, values of C_{2D} are low. For a-PNR$_{10}$, C_{2D} is an order of magnitude lower than it is for graphene nanostructures. As with bulk phosphorene, we suggest that compression and extension leads mainly to a P-P-P bond angle change rather than more energetically demanding changes in bond length.

6.4.2 a-PNR

Under no strain, the band gap of a-PNR$_{10}$ is 0.93 eV, just 0.04 eV higher than the band gap of bulk phosphorene. However, uniaxial straining can induce large changes in the band gap, see Figure 6.9. For strains of between ε = 0.90 to 1.07, tensile strain is associated with a steadily increasing band gap, while compressive strain is associated with a steadily decreasing band gap. The band gap peaks at 1.16 eV when ε = 1.07, and falls to 0.36 eV when ε = 0.90. When ε > 1.07, the band gap begins to fall with further compressive strain, reaching 1.07 eV when ε = 1.10.

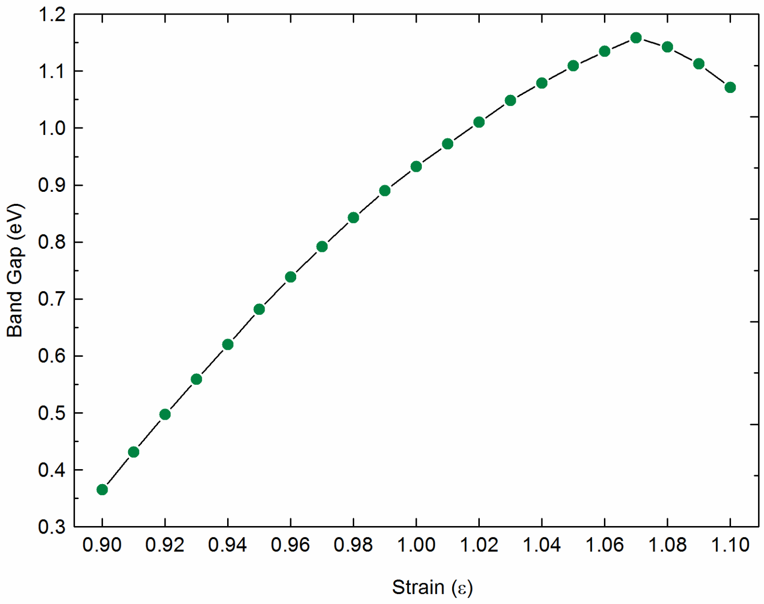

Figure 6.9: The band gap of a-PNR$_{10}$ at strains of between ε = 0.90 to 1.10.

The changes in band gap with strain can be understood by looking at the absolute changes in the energies of conduction and valence bands. Figure 6.10 shows that as a-PNR is stretched from ε = 0.90 to 1.07, the band gap increases as a combined result of the stabilisation of the VBM and the destabilisation of the CBM. The VBM is stabilised from around -4.5 eV to -4.9 eV as ε is increased from 0.90 to 1.07, while the CBM is destabilised from -4.2 eV to -3.75 eV.

The stabilisation of the VBM with extensive strain suggests that the state's constituent atomic orbitals are arranged in an anti-bonding manner along the ribbon's length. Figure 6.10, which shows that the spd- and site-projected phase factors of the electronic state at the VBM, confirms that the VBM consists of p_z orbitals arranged in an anti-bonding manner along the length of the ribbon. Meanwhile, the CBM of a-PNR$_{10}$ also consists of p_z orbitals, but arranged in bonding manner along ribbon's length, explaining why the CBM is destabilised as a-PNR is stretched between ε = 0.90 and 1.07.

Past a critical strain of ε = 1.07, the band gap falls with further tensile strain. While the energy of the VBM plateaus, the emergence of a new CBM which is stabilised with tensile strain causes the band gap to fall. The emergent CBM consists of p_y orbitals arranged in an antibonding manner along the armchair direction, explaining its stabilisation with extensive strain.

We also note the presence of competing valence band which is rapidly destabilised with compressive strain. This valence band has its maximum away from the Γ-point at approximately [0.3, 0, 0] $2\pi/l$, and is just 40 meV more stable VBM when ε = 0.90. At strains of ε < 0.90, the band gap of a-PNR becomes indirect, from [0.3, 0, 0] $2\pi/l \rightarrow \Gamma$, with the overall band gap rapidly decreasings thereafter. Indeed, preliminary investigations indicate that z-PNR$_{10}$ becomes metallic at strains of ε < 0.85.

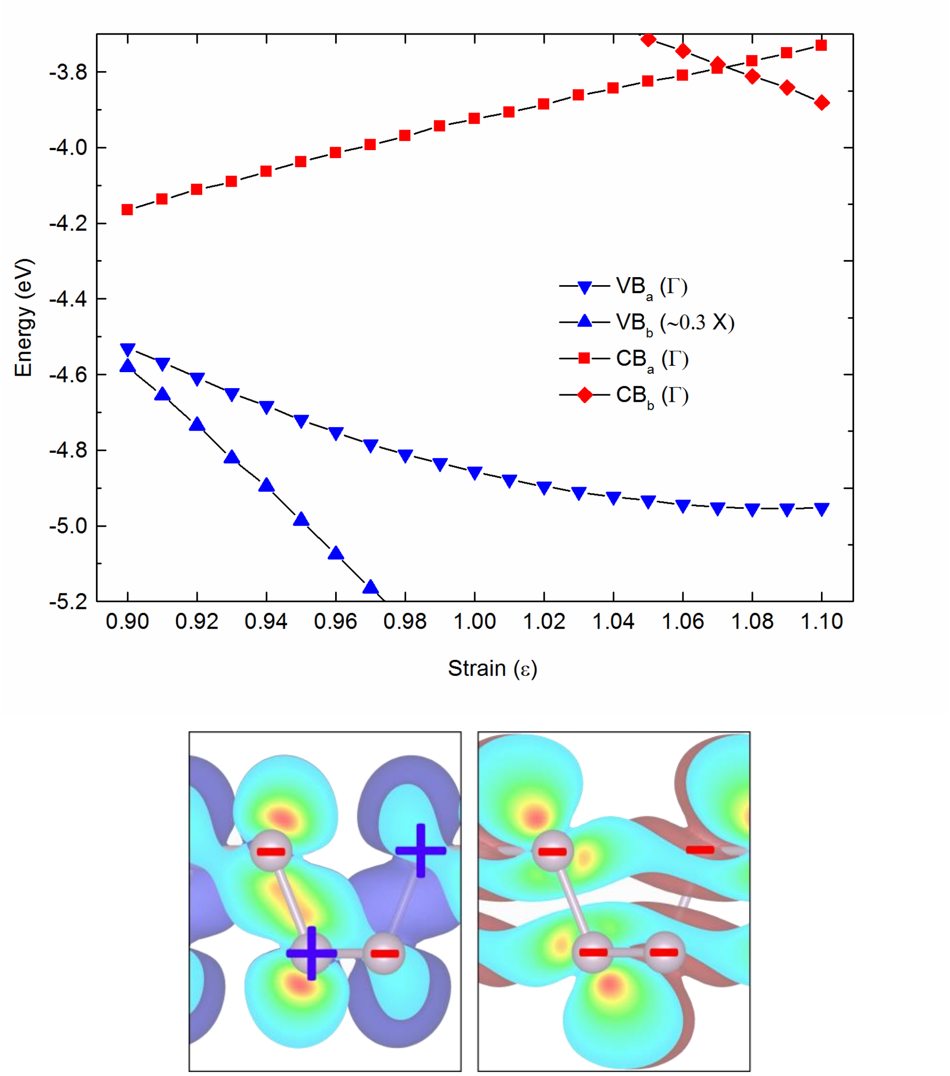

Figure 6.10: Absolute band energies (relative to the vacuum level) of the first and second valence and conduction bands in a-PNR$_{10}$ at strains of between ε = 0.90 to 1.10 (top) and the charge density of electronic states at VB$_a$ (bottom left), CB$_a$ (bottom right), with the phase factors of the constituent and dominating p_z orbitals shown. Isosurfaces are 0.001 e/Å^3.

Unstrained a-PNR$_{10}$ has hole and electron effective masses of 0.158 m_0 and 0.147 m_0 respectively. The phase factors at the VBM shown in Figure 6.10 suggest that there is a continuous region of electron density 'inside' the sheet, while the phase factors of orbitals making up the CBM suggest that there is a continuous region of electron density on the top and bottom surfaces of the sheet. The presence of continuous electron density, i.e. without nodes, aids charge carrier transport and explains the low effective masses calculated.

Between strains of ε = 0.90 and 1.07, the ordering of valence and conduction bands stays constant, and thus so do the electronic states at the VBM and CBM. Both hole and electron effective masses rise gradually upon extension as overlap between neighbouring atomic orbitals decreases; m_h rises from 0.114 m_0 when ε = 0.90 to 0.158 m_0 when ε = 1.07, while m_e rises from 0.125 m_0 when ε = 0.90 to 0.160 m_0 when ε = 1.07. While this behaviour is ordinary, much more dramatic changes in effective mass occur past a critical strain of ε > 1.07.

The band structure around the new CBM that emerges when ε > 1.07 is highly un-dispersive, as can be seen by comparing the band structure of a-PNR$_{10}$ when ε = 1.00 to the band structure when ε = 1.10, see Figure 6.11. The result is a dramatic increase in m_e, from 0.160 m_0 to over 8 m_0 when ε = 1.07, an increase of over 50× which effectively quenches *n*-type transport in highly strained a-PNR. The fact that m_h remains relatively constant could have important implications for *p*-type devices where concurrent *n*-type transport is undesirable. Meanwhile, the VBM that emerges when ε < 0.90 has a slightly lower effective mass compared to the ground state, m_0.

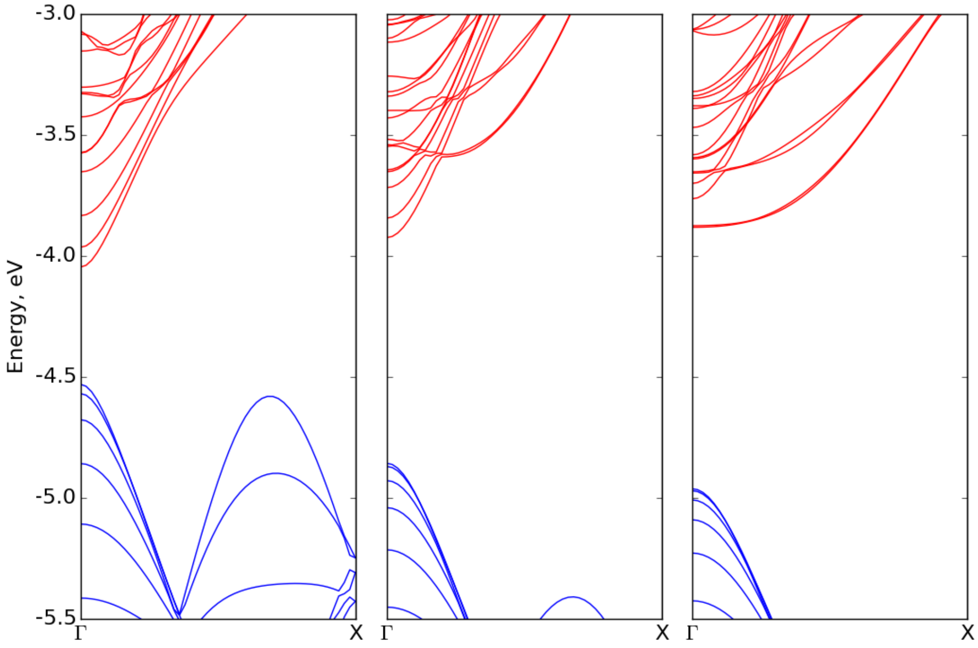

Figure 6.11: The effective mass at the conduction (m_e) and valence (m_h) band edges of a-PNR under strains of between ε = 0.91 and 1.03 (top) and the band structure of a-PNR$_{10}$ at strains of ε = 0.90 (bottom left), ε = 1.00 (bottom midde) and ε = 1.10 (bottom right).

6.4.4 z-PNR

The band gap of unstrained z-PNR_{10} is 1.08 eV. Between ε = 0.91 and 1.03 the band gap rises from 0.75 to 1.23 eV, and between ε = 1.04 and 1.10 the band gap falls from 1.25 to 0.73 eV. As z-PNR_{10} is compressed from ε = 0.91 and 0.90, the band gap falls sharply from 0.75 to 0.54 eV.

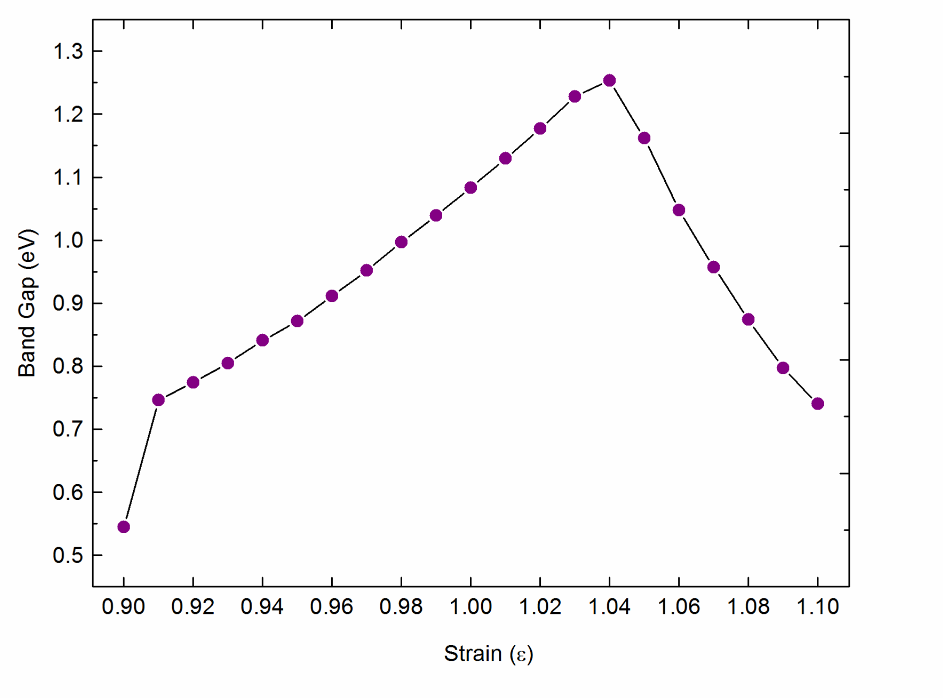

Figure 6.12: The band gap of z-PNR_{10} under uniaxial strains of between ε = 0.90 to 1.10.

To understand these trends, we consider at the absolute band energies of z-PNR_{10} under various strains, see Figure 6.13. Changes in the band gap between ε = 0.91 and 1.03 are driven mainly by the destabilisation of the CBM, which is destabilised from around -4.5 eV when ε = 0.91 to over -4.0 eV when ε = 1.03. Examining the charge density and site decomposed phase factors, we see that the CBM of z-PNR consists of p_z orbitals arranged in a bonding manner along the length of the ribbon. As the ribbon is extended these electronic states are destabilised, increasing the band gap between ε = 0.91 and 1.03.

Changes in the band gap between ε = 1.03 and 1.10, which falls from 1.25 eV to 0.73 eV, are also driven by changes in the energy of the CBM. At ε > 1.03, a new CBM emerges which is stabilised with extensive strain, from -3.93 eV when ε = 1.04 to -4.35 eV when ε = 1.10. The electronic state at the emergent CBM consists of p_y orbitals arranged in an anti-bonding manner along the length of the ribbon, explaining its stabilisation with extensive strain.

Meanwhile, the energy of the VBM remains relatively constant as tensile strain is applied between ε = 1.00 and 1.10. Upon compression, the VBM is stabilised by approximately 0.2 eV between ε = 1.00 and 0.90. However, examining the charge density and site decomposed phase factors, it appears to consist of p_z orbitals arranged in an antibonding manner along the ribbon's length, suggesting that is should be destabilised with compressive strain. The charge density plot of the VBM suggests that it is dominated by the bonding interaction between atoms on the top and bottom surfaces of the sheet, and given that the distance between these atoms barely changes with strain the energy of the VBM remains fairly consistent. Moreover, from a top view, the anti-bonding interaction between neighbouring phosphorus atoms (e.g. those marked *a* and *b*) is compensated by a bonding interaction between atoms *a* and *c*. This bonding interaction increases as the ribbon is compressed, leading to the stabilisation observed between ε = 1.00 and 0.90. Meanwhile, between ε = 0.91 and 0.90, a new VBM emerges, which is rapidly stabilised upon compression, resulting in a jump in band gap from 0.75 eV to 0.54 eV.

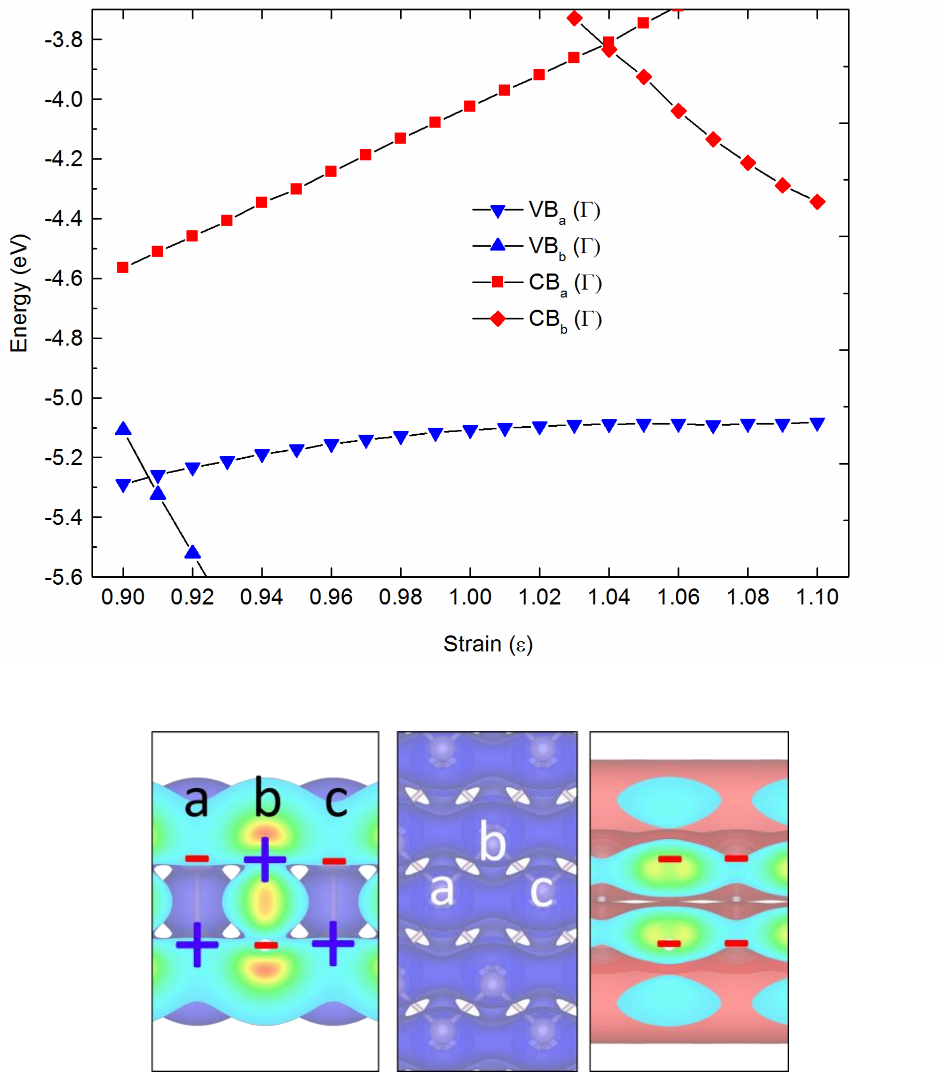

Figure 6.13: The absolute band energies of the first and second valence and conduction bands in a-PNR$_{10}$ at strains of between ε = 0.90 to 1.10 (top) and the charge density of electronic states at VB$_a$, CB$_a$, with the phase factors of the constituent and dominating p_z orbitals shown (bottom left, centre, right).

In unstrained z-PNR$_{10}$, hole and electron effective masses are 2.35 and 1.29 m_0 respectively. As discussed previously, there is only a limited bonding interaction along the length of the ribbon, explaining these high effective masses. Extensive straining between ε = 1.00 and 1.02 m_0 leads to a massive increase in m_h, which reaches 7.63 m_0. This change occurs as VBM moves to the Γ-point, around which the valence band is remarkably flat. The effective mass of 7.63 m_0 is in line with m_h in monolayer phosphorene, where the VBM is also located at the Γ-point. With further extensive strain, m_h quickly decreases, falling to 1.40 m_0 when ε = 1.10. However, as discussed in Section 6.3.6, hole effective masses in z-PNRs should be viewed with some caution given that they are extremely sensitive to the exact position of the VBM. With compressive strain, between ε = 1.00 and 0.91, m_h falls from 2.39 m_0 to 1.21 m_0 as the bonding between atoms *a* and *c* in Figure 6.13 increases. At ε = 0.90, a new VBM emerges which is highly dispersive, and m_h falls to 0.11 m_0, the lowest effective mass reported for any black phosphorus structure.

Meanwhile, m_e slowly rises between ε = 0.90 and 1.03, from 1.21 m_0 to 1.31 m_0. This change is what one would intuitively expect when interatomic distances are increased. Past ε = 1.03, a new CBM emerges around which the band structure is highly dispersive, see Figure 6.14, leading to a sudden fall in m_e to 0.14 m_0. The resulting high m_h/m_e ratio suggests a suitability for *n*-type applications, with the sudden increase in the ratio between ε = 1.03 and 1.04 potentially useful for switching devices.

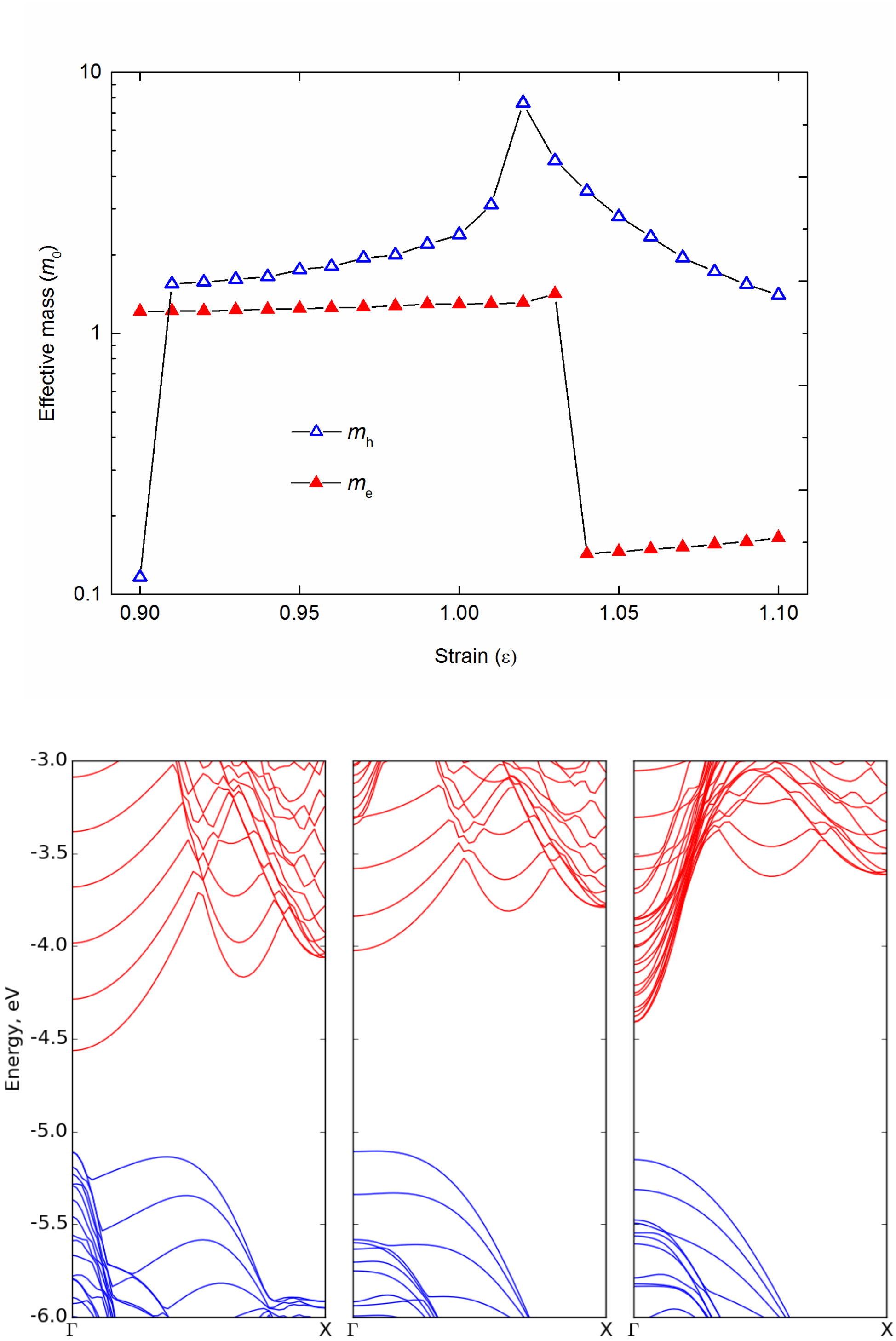

Figure 6.14: The hole and electron effective mass of z-PNR under strains of between ε = 0.91 and 1.03 (top) and the band structure of a-PNR$_{10}$ at strains of ε = 0.90 (bottom left), ε = 1.00 (bottom midde) and ε = 1.10 (bottom right).

6.5 Diagonal phosphorene nanoribbons

Alongside the preceding work investigating a-PNRs and z-PNRs, Dr Xiaoyu Han investigated the properties of a different type of PNR, d-PNRs, which are cut diagonally along the lattice. Her work was published alongside that contained in this chapter. The band gaps of d-PNRs were also increased with respect to bulk phosphorene as a result of quantum confinement. The increases in band gap in d-PNRs are larger than in a-PNRs but smaller than those in z-PNRs. Meanwhile, straining d-PNR led to two direct to indirect band gap transitions as the valence band is stabilised (under compression) and the conduction band is destabilised (under extension) at a k-point lying away from the Γ–point. It is possible that d-PNR structures may be engineered upon straining so that two valleys are energetically degenerate with electrons of widely different momentum able to coexist at the same energy.

6.6 Summary

We investigated the properties of two different types of hydrogen passivated PNR using DFT at the GGA level. We looked at ribbon widths between 13 and 75 Å, corresponding to between 4 and 16 unit cells. There were limited changes in geometry with respect to the bulk, and furthermore we found that the changes in electronic energy associated with the formation of either passivated PNR were minimal. However, we would expect the Gibbs free formation energies to be endothermic due to the entropic losses associated with hydrogen adsorption.

In terms of electronic properties, the band gap of both PNRs increased with decreasing ribbon width as a result of quantum confinement effects. The band gap of the narrowest z-PNR studied was increased by 0.65 eV while the band gap of the narrowest a-PNR was increased by 0.12 eV. We explained the difference in the magnitude of quantum confinement effects by applying periodic boundary conditions to the band structure of monolayer phosphorene. We also derived a formula relating the band gap of PNRs to phosphorene’s band edge effective masses and band gap. This formula demonstrates that the additive effect on the band gap of PNRs with respect to the bulk should be consistent regardless of the methodology used to calculate electronic structure. This shows shown that the band gap of PNRs can be shifted throughout the optical region.

Effective masses are, in general, subtly increased in narrow PNRs with respect to the bulk. As would be expected from the anisotropy seen in monolayer phosphorene, both hole and electron effective masses are significantly lower in a-PNRs than in z-PNRs.

We also investigated the effects of applying strain to PNRs. Stretching a-PNR$_{10}$ between ε = 0.90 and 1.08 leads to an increased band gap due to the simultaneous stabilisation of the VBM and destabilisation of the CBM. At strains of ε > 1.08, a new CBM emerges that is stabilised as further strain is applied, reducing the band gap. The band structure of a-PNR is highly undispersed around the emergent CBM, meaning that m_e dramatically increases. The nature of the VBM, however, remains fairly constant across all strains and thus so does m_h. The dramatic decrease in the m_h/m_e ratio past a critical strain of ε =1.08 suggests that a-PNRs may readily be tuned for *p*-type applications.

Meanwhile, stretching z-PNR$_{10}$ between ε = 0.90 and 1.03 increases the band gap predominantly because of the destabilising effect on the CBM. At ε = 1.04, a new CBM emerges that is stabilised with extensive strain, and so the band gap falls between ε = 1.04 and 1.10. The emerging CBM has a far lower effective mass, leading to a significant increase in the m_h/m_e ratio. This suggests that z-PNRs may be readily tuned for *n*-type applications through the application of uniaxial strain.

References

1. Dutta, S. and S.K. Pati, *Novel properties of graphene nanoribbons: a review*. Journal of Materials Chemistry, 2010. **20**(38): p. 8207-8223.

2. Li, Y.F., et al., *MoS2 Nanoribbons: High Stability and Unusual Electronic and Magnetic Properties*. Journal of the American Chemical Society, 2008. **130**(49): p. 16739-16744.

3. Vo, T.H., et al., *Large-scale solution synthesis of narrow graphene nanoribbons*. Nature Communications, 2014. **5**.

4. Ezawa, M., *Peculiar width dependence of the electronic properties of carbon nanoribbons.* Physical Review B, 2006. **73**(4).

5. Son, Y.W., M.L. Cohen, and S.G. Louie, *Energy gaps in graphene nanoribbons.* Physical Review Letters, 2006. **97**(21).

6. Yang, L., et al., *Quasiparticle energies and band gaps in graphene nanoribbons.* Physical Review Letters, 2007. **99**(18).

7. Son, Y.W., M.L. Cohen, and S.G. Louie, *Half-metallic graphene nanoribbons.* Nature, 2006. **444**(7117): p. 347-349.

8. Bai, J.W., X.F. Duan, and Y. Huang, *Rational Fabrication of Graphene Nanoribbons Using a Nanowire Etch Mask.* Nano Letters, 2009. **9**(5): p. 2083-2087.

9. Ma, L., J.L. Wang, and F. Ding, *Recent Progress and Challenges in Graphene Nanoribbon Synthesis.* Chemphyschem, 2013. **14**(1): p. 47-54.

10. Agar, G., *"Nanofabrication and its Application in Renewable Energy".* Johnson Matthey Technology Review, 2014. **58**(4): p. 221-223.

11. Guo, H.Y., et al., *Phosphorene Nanoribbons, Phosphorus Nanotubes, and van der Waals Multilayers.* Journal of Physical Chemistry C, 2014. **118**(25): p. 14051-14059.

12. Du, Y., et al., *Unexpected magnetic semiconductor behavior in zigzag phosphorene nanoribbons driven by half-filled one dimensional band.* Sci Rep, 2015. **5**: p. 8921.

13. Loh, S.M., et al., *Quantum confinement effect in armchair graphene nanoribbons: Effect of strain on band gap modulation studied using first-principles calculations.* Physical Review B, 2014. **90**(3).

14. Tran, V., et al., *Layer-controlled band gap and anisotropic excitons in few-layer black phosphorus.* Physical Review B, 2014. **89**(23): p. 235319.

Chapter 7

Thesis Summary

The investigations reported in this thesis reveal novel properties of two nanomaterials: phosphorene and titanium metallocarbohedrene. Both have potential applications in important technologies, with Ti_8C_{12} relevant to hydrogen storage and the properties of phosphorene suitable for next generation electronic devices. Given that both materials have been successfully fabricated, our investigations provide a direction for future development. While we recognize that computationally reported behaviours are often difficult to reproduce experimentally, it is important to recall the numerous occasions where theoretical work has preceded experimental realization. For example, graphene was theoretically investigated for several decades before its exceptional properties were confirmed in 2004. Furthermore, a theoretical understanding of a material's properties can useful in overcoming practical challenges and in improving performance in existing applications. This chapter will summarise the findings presented in Chapters 3, 4, 5 and 6 and explain their potential significance.

7.1 Titanium metallocarbohedrene

Chapter 3 investigated the adsorption of hydrogen by titanium metallocarbohedrene in order to assess its potential use as a hydrogenation catalyst. We found that Ti_8C_{12} fulfils the criteria set out in Chapter 1: it is able to dissociate hydrogen with a low kinetic barrier and a moderate change in Gibb's free energy, making it thermodynamically compatible with a wide range of HSMs. We considered the stepwise chemisorption of H_2 to form a variety of hydrogenated products, ranging from $Ti_8C_{12}H_2$ to $Ti_8C_{12}H_8$. We calculated the stability of each compound over a range of temperatures and pressures, concluding that the hydrogenation of Ti_8C_{12} is reversible under mild conditions. Furthermore, different forms of hydrogenated Ti_8C_{12} are preferentially formed under different conditions, with each form thermodynamically compatible with a different range of HSMs.

We studied the kinetics of H_2 dissociation using transition state theory. The electronic activation energy for the heterolytic dissociation of H_2 by Ti_8C_{12} is very low, particularly when considered with the moderate binding energies in mind. Furthermore, the kinetics of H_2 dissociation by Ti_8C_{12} are much faster than in many other materials that heterolytically dissociate H_2. This observation can be attributed to the donation of electron density from titanium species to the anti-bonding σ^* orbital in H_2, the same mechanism that catalyses the dissociation of H_2 by precious metals and their complexes.

Overall, the fast dissociation of H_2 with a moderate binding energy makes Ti_8C_{12} a suitable candidate for use in catalysis. While its gravimetric hydrogen storage capacity falls short of requirements for future HSMs, the near ideal thermodynamic reversibility of hydrogenation reported is thought provoking, with local structure playing a huge role in determining hydrogen binding energies.

While previous studies have shown that Ti_8C_{12} is exceptionally stable and can be formed through plasma reactions, the isolation of significant quantities of Ti_8C_{12} is yet to be achieved. However, given the continued progress in experimental nanochemistry, we are confident that the promising properties of Ti_8C_{12} are realizable. In terms of future work, the investigation of other stable metallocarbohedrenes such as V_8C_{12} and mixed metallocarbohedrenes, $M_xN_{8-X}C_8$, would likely yield interesting results.

7.2 Phosphorene

Just two years after the first reports of phosphorene, more than 250 articles investigating the material have been published. The level of interest in phosphorene is unsurprising given the topicality of 2D materials stimulated by the fabrication of graphene in 2004. Once a field confined to theory, there is a growing possibility that 2D materials will allow for the continued evolution of electronic devices. With silicon based technologies fast approaching their fundamental limits and the demand for faster, smaller and more efficient electronic devices showing no signs of slowing, the emergence of such 2D materials is well timed.

Within the growing family of 2D materials, phosphorene has an appealing set of properties. It holds a key advantage over graphene in that it is inherently semiconducting and is thus better suited for use in integrated circuit devices. Furthermore, phosphorene's high *p*-type conductivity complements the *n*-type conductivity of MoS_2 in terms of building CMOS logic devices.

In Chapter 4, we investigated the basic electronic structure of ground state phosphorene and bulk black phosphorus. The band gap of phosphorene increases as the number of layers is decreased, allowing the properties of phosphorene transistors, including the on-off ratio and threshold voltage, to be modulated. We were able to predict the band gaps of few-layered phosphorenes by applying periodic boundary conditions to the band structure of bulk black phosphorus, with the agreement with results calculated using DFT improving as the number of layers is increased. Therefore, the method presented provides a computationally efficient way of predicting the band gap of *N*-layered phosphorenes when *N* is large. Furthermore, we showed that the anisotropy of phosphorene's effective mass increases as the number of layers is reduced, another factor that requires careful consideration during the construction of phosphorene based devices.

Chapters 5 investigated the effects of strain on the properties of phosphorene. In our opinion, the most important result presented is the huge enhancement of *n*-type mobility induced by applying a relatively modest compression normal to the surface of bilayer phosphorene. The utilisation of the huge *n*-type mobility predicted would likely lead to exceptional device performance, with electrons over two order of magnitude more mobile than those in the ground state. While phosphorene is inherently *p*-type, bulk black phosphorus is *n*-type when doped with tellurium. We therefore suggest that a full charged defect analysis of tellurium doped phosphorenes would be a worthwhile exercise. Furthermore, in order to confirm the high mobility of the electronic state that emerges when bilayer phosphorene is compressed, we suggest a more thorough investigation of electron – phonon coupling in few-layered phosphorenes. In Chapter 5, we also investigated the out-of-plane bending of phosphorene, reporting that it is five times easier to bend phosphorene in the armchair direction than in the zigzag direction. The bending stiffness of phosphorene in the armchair direction is lower than that of graphene, suggesting a highly degree of rippling. Given that bending phosphorene affects phosphorene's band edge positions and band gap, the behaviour reported has implications for phosphorene's susceptibility to both oxidation and reduction. Finally, we found that when armchair direction extensive strain is applied, phosphorene becomes unstable with respect to a phase transition to blue phosphorus. This finding renders previously reported critical strains in excess of 30% unrealistic.

The properties of phosphorene nanoribbons are investigated in Chapter 6. Quantum confinement effects result in the band gap of PNRs being increased with respect to the bulk, with the magnitude of the effect largest when wavefunctions are confined in the armchair direction. By applying PBCs to the electronic structure of ground state phosphorene, we derive a numerical model that can be used to predict the electronic properties of PNRs that are too large to be modelled directly using DFT. We also investigated the changes in the band gap and effective mass of PNRs under uniaxial strain, explaining each response in terms of the composition of band edge electronic states. Of particular interest are the sudden changes in effective mass observed when PNRs are extended past relatively modest critical strains. To investigate these effects further, we suggest future work to predict scattering times, using either the DPA or a full analysis of electron-phonon coupling.

Appendix A

Quaternary Oxynitrides

A.1 Background

In addition to the main body of work reported in Chapters 3, 4, 5 and 6, we investigated the properties of a family of quaternary compounds for their potential suitability as water-splitting photocatalysts. The first water splitting catalyst was discovered by Fujishima and Honda in 1972 and was based on TiO_2 and Pt [i]. Water splitting photocatalysis relies upon the excitation of electrons from the valence band of a semiconductor into the conduction band through the adsorption of solar energy. The excited electron is energetic enough to reduce H^+ while the electron hole oxidises water to form O_2 and H^+. The general scheme of photocatalytic water splitting is shown in Figure A.1, which shows the energy levels of the semiconductor valence and band edges relative to the absolute reduction and oxidation potentials of H^+ and OH^- respectively.

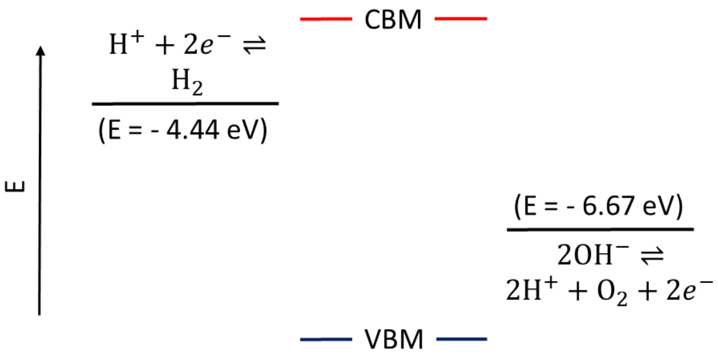

Figure A.1: A schematic diagram depicting the absolute energy levels of a water splitting photocatalyst's band edges alongside the redox potentials of H^+ and OH^-, with energies calculated relative to the vacuum level

Given the mechanism of water splitting photocatalysis, there are several prerequisites that any potential catalyst must fulfil. Their band gap must be greater than 1.23 eV, the difference in the reduction potential of H+/H_2 and O_2/H_2O. More specifically, the absolute potential energy of the conduction band must be higher than the reduction potential of H^+, and the potential energy of the valence band must be lower than the oxidation potential of OH^-. It is important to note that the band edge positions at the material's interface with solution may significantly differ from the bulk band edge positions. Such considerations are, however, beyond the scope of this investigation.

The above prerequisites for water splitting photocatalysis means that the band gap should fall within the visible light region (1.65-3.27 eV). While photocatalysis using ultraviolet photons (>3.27eV) is possible, the intensity of ultraviolet photons at the Earth's surface is far lower than the intensity of lower energy photons, the intensity of which peak between 2.0 and 2.5 eV.

The majority of known photocatalysts are d^0 or d^{10} metal oxides [ii]. Wide band gap semiconductors such as TiO_2 respond only to the UV region [iii], while efforts to dope these semiconductors with N or S have produced limited success [iv]. Hematite (α-Fe_2O_3) is another popular photocatalytic material, but its conduction band is too low to drive H_2 production [v]. A recent publication screening in excess of 130 inorganic materials suggests the potential of Na_5MoO_4N and Li_5MoO_4N as a potential water splitting photocatalysts, claiming their thermodynamic stability, appropriate band-edge positions and estimated band gaps of 3.19 and 2.61 eV respectively [vi]. While the Δ-sol method that was used to estimate the band gap of Na_5MoO_4N and Li_5MoO_4N has been shown to be relatively accurate in estimating the band gaps of transition metal compounds [vii], it is highly empirical and does not provide a detailed picture of the electronic structure of materials. More computationally demanding density functionals such as HSE06 are more widely used and equipped to calculate an accurate electronic band structure and decomposed density of states.

A.2 Methodology

DFT ionic relaxations were carried out using the Vienna Ab initio Simulation Package (VASP) using both PBE and HSE06 functionals to account for exchange and correlation. The electronic energy of Na_5MO_4N (M=Cr,Mo,W) was found to be fully converged when the brillouin zone was sampled at a density of 7 ×7×5 k-points. Wave functions were expanded using a plane wave basis set with a cut-off energy of 500eV. Ionic positions were optimized using a conjugate-gradient algorithm, and the structure was optimized until the change in energy between two consecutive steps fell below 1 meV. In order to ensure the correct cell volume, a Birch-Murnaghan fitting was carried out for each compound [viii]. We used CPLAP to assess the stability of compounds which are yet to be synthesised experimentally [ix]. The electronic properties of Na_5MO_4N were investigated using the results of calculations using both of the HSE06 functional. A further electronic relaxation of the structural ground state derived using the PBE functional was carried out using the mBJ meta-GGA functional [x].

A.3 Metal Oxynitdies

A.3.1 MoO_3

To assess the performance of mBJ and HSE06 in predicting the electronic properties of Mo(VI) semiconductors, we compared the band gaps predicted when the electronic structure of MoO_3 was optimised using both mBJ and HSE06 to experimental results from the literature. The literature suggests that the MoO_3 has an indirect band gap of 2.9 – 3.15 eV [xi-xii]. This compares well to the indirect band gap of 3.01 eV calculated when MoO_3 was relaxed using the HSE06 functional. When the structure of MoO_3 was relaxed using PBE and then the electronic structure was relaxed using mBJ, the indirect band gap of MoO_3 was found to be underestimated at 2.53 eV. Furthermore, throughout our study of group VI-semiconductors we will primarily analyse the electronic properties resulting from optimisation with the HSE06 functional. However, as mBJ is comparatively cheap calculation, we will run mBJ calculations in parallel in case of any useful insights arising from comparisons of the two methods.

A.3.2 M_5MoO_4N (M=Na, Li)

The structure of Na_5MoO_4N obtained from the ICSD database [xiii] was relaxed using both PBE and HSE06 functionals. While the lattice paramaters calculated using PBE more closely resembled experimental lattice parameters published in the literature, the local structure of

$[MoO_4N]^{6-}$ polyhedra calculated using the HSE06 functional matched the literature more closely than when using the PBE functional. In particular, the Mo-N bond length were overestimated by 2.7% when using the PBE functional but were only overestimated by 1.2% when using HSE06.

The structure of Li_5MoO_4N was determined by sustituting each sodium atom present in the structure of Na_5MoO_4N with a lithium atom and relaxing the structure. Both lattice parameters are reduced by around 9% with respect to Na_5MoO_4N when using either exchange correlation functional. This result is to be expected by virtue of the smaller ionic radii and subsequent higher charge density of Li^+ with respect to Na^+. The local structure of the $[MoO_4N]^{6-}$ polyhedra is, however, essentnially unchanged.

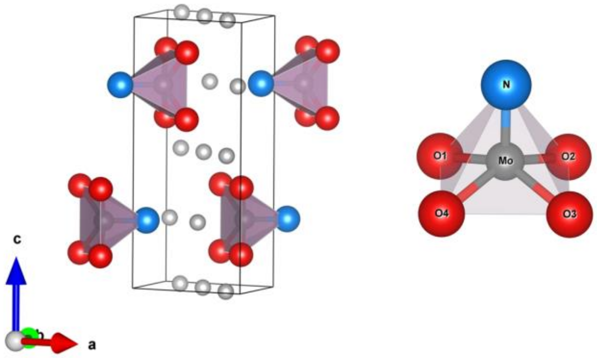

Figure A.2: Unit cell of Na_5MoO_4N (left) and the structure of $[MoO_4N]^{6-}$ relaxed using HSE06.

	Na_5MoO_4N			Li_5MoO_4N	
	Exp	PBE (vs. Exp)	HSE (vs. Exp)	PBE	HSE
a /Å	5.727	5.71	5.67	5.23	5.19
c /Å	10.677	10.70	10.63	9.74	9.67
Mo-N /Å	1.719	1.77	1.74	1.76	1.73
Mo-O /Å	1.958	1.98	1.96	1.96	1.94
O1-Mo-O2 /°	83.68°	83.97°	83.93°	83.20°	83.20°
O2-Mo-O3	87.51°	86.96°	86.96°	87.86°	87.84°
O3-Mo-O4	83.68°	83.97°	83.93°	83.20°	83.20°
O4-Mo-O1	87.51°	86.96°	86.96°	87.86°	87.84°

Table A.1: Structural properties of M_5MoO_4N (M=Na, Li) following relaxation using PBE and HSE06 functionals.

We calculated the electronic band gap of Na_5MoO_4N and Li_5MoO_4N using three different exchange correlation functionals; PBE, mBJ and HSE06. Both direct and indirect band gaps are shown in Table A.2, where we also show the band gaps calculated in the literature using the Δ-sol method.

	Na_5MoO_4N		**Li_5MoO_4N**	
	Indirect	**Direct**	**Indirect/**	**Direct**
PBE	2.38	2.53	2.11	2.25
mBJ	3.30	3.39	2.96	3.10
HSE06	3.89	3.99	3.57	3.86
Δ-sol [xiv]	3.19		2.77	

Table A.2: Electronic band gaps of M_5MoO_4N (M=Na, Li) determined using a range of functionals and methods.

It can be seen that the four methods employed give a wide range of indirect band gaps for Na_5MoO_4N, ranging from 2.38 eV when using PBE to 3.89 eV when using HSE06. It is well known that PBE tends to underestimate band gaps, meaning that these results do not warrant further consideration. While mBJ is far less computationally expensive, we believe that the better established HSE06 functional is likely to produce more accurate results in this investigation, due both to its ability to reproduce both the local structure of $[MoO_4N]^{6-}$ and the indirect band gap of MoO_3 (see Section A.3.1).

In agreement with the trend seen in the band gaps determined using the Δ-sol method, we found the indirect band gap of Li_5MoO_4N (3.57 eV) to be smaller than that of Li_5MoO_4N (3.89 eV) when using the HSE06 functional. However, both of these band gaps are significantly greater than those calculated using Δ-sol, which are in far better agreement with the band gaps calculated using the mBJ functional. The decomposed density of states, as shown in Figure A.3, reveals that the valence band of Na_5MoO_4N is dominated by oxygen orbital character while the conduction band is dominated by molybdenum character.

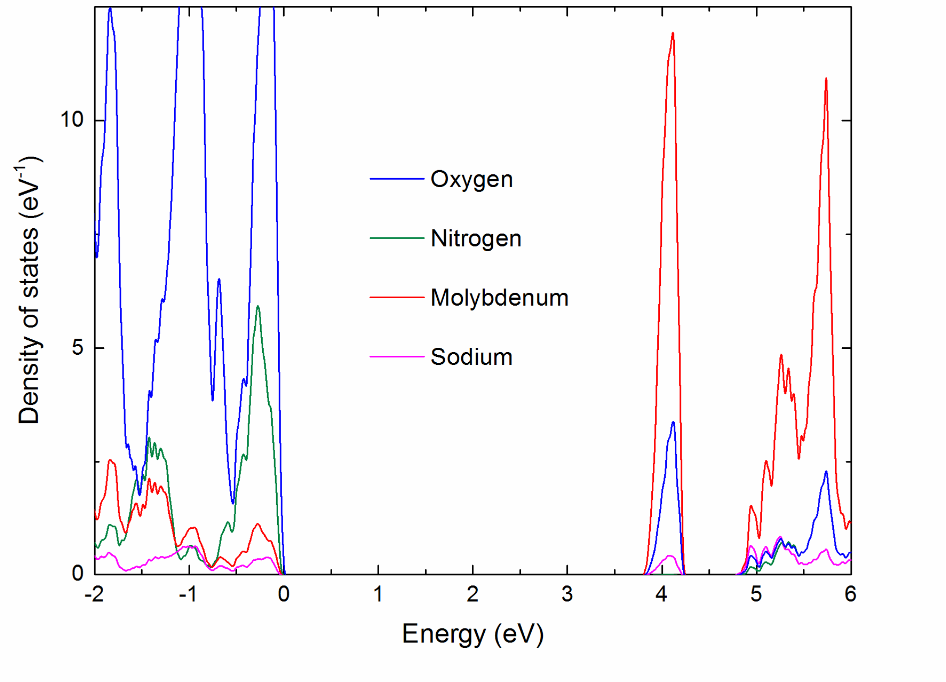

Figure A.4: Decomposed density of states of Na_5MoO_4N

The band structures of Na_5MoO_4N and Li_5MoO_4N was determined by sampling the brillouin zone between highly symmetric k points and is shown in Figure A.4.The first conduction band of both compounds is very flat, suggesting highly localised states conduction states. Furthermore, the anti-symmetric molybdenum environment in both compounds gives rise to distinct conduction bands as the d-orbital energies diverge. The conduction band at around 4 eV is comprised almost exclusively of Mo dz^2 orbital character, while the next distinct band comprises of a combination of Mo dx^2-y^2 and dyz orbitals.

The mobility of electrons excited to the conduction band minimum (CBM) can be qualitatively estimated by calculating the effective mass. The effective mass of conduction band electrons at the CBM in Na_5MoO_4N was found to be 1.88 m_0 and 1.57 m_0 in Li_5MoO_4N. In comparison to rutile TiO_2 where the conduction band contains light electronic states with effective mass of 0.6 – 0.8 m_0 [xv], the conduction band electrons in Na_5MoO_4N and Li_5MoO_4N are predicted to be relatively immobile and localised.

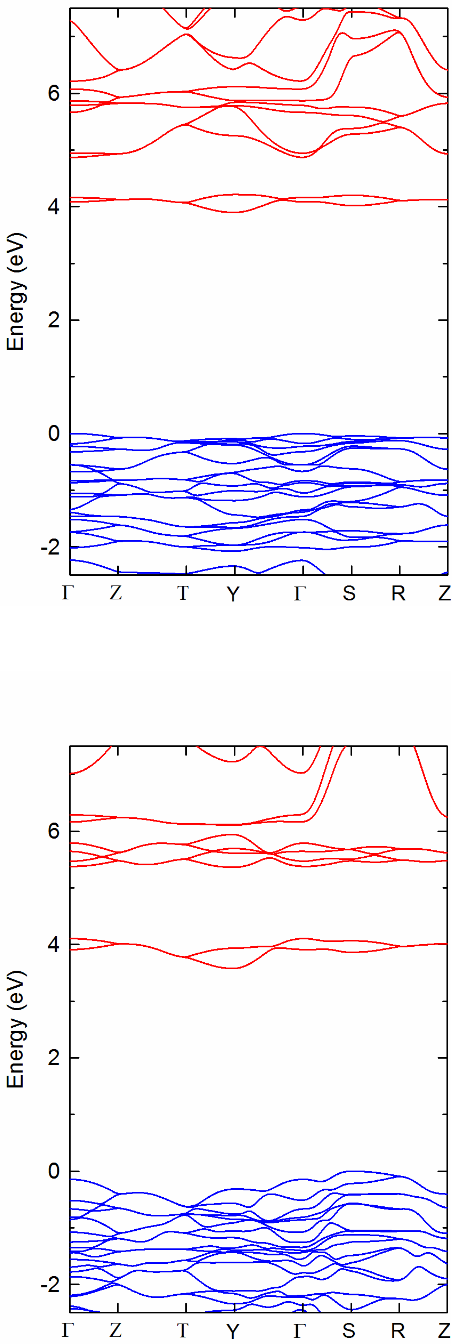

Figure A.3: The band structures of Na_5MoO_4N (left) and Li_5MoO_4N (right) calculated using the HSE06 functional. The VBM is arbitrarily set to zero.

The valence bands of the two compounds are, however, more starkly different. The valence band in Li_5MoO_4N is much more dispersive than in Na_5MoO_4N. Indeed, the relative mass of an electron hole in the valence band of Na_5MoO_4N about the VBM was found to be 9.39 m_0, whereas in Li_5MoO_4N it was found to be 2.59 m_0.

The decreased separation of $[MoO_4N]^{6-}$ units in Li_5MoO_4N is likely to play a role in increasing hole mobility. More specifically, the shortest O-O separation between $[MoO_4N]^{6-}$ polyhedra is reduced from 3.52 Å in Na_5MoO_4N to 3.00 Å in Li_5MoO_4N. Bearing in mind that the valence band in both compounds is dominated by oxygen character, reduced O-O separation is likely to significantly increase hole mobility through the compound. While Mo-Mo distances are also similarly decreased, electron mobility through the anions surrounding Mo(VI) is likely to be extremely low regardless of Mo-Mo separation

The low mobility of both conduction band electrons and electron holes in the valence band means that electron-hole recombination is likely to occur [xvi], reducing potential photocatalytic activity. The higher charge carrier mobility of Li_5MoO_4N means that the compound is likely to be more photocatalytically active that Na_5MoO_4N in terms of recombination kinetics.

A.3.3 M_5CrO_4N (M=Li,Na)

In an attempt to reduce the band gap of M_5MoO_4N, we investigated the electronic properties of M_5CrO_4N. The rationale behind substituting chromium species into the structure in place of molybdenum was to stabilise the conduction band while keeping the same number of valence electrons. The unoccupied 4d states of Mo(VI) are likely to be significantly higher in energy than the unoccupied 3d states of the more oxidising Cr(VI).

The initial structures of Li_5CrO_4N and Na_5CrO_4N were based around the analagous molybdenum compounds discussed above. We then relaxed both structures using the PBE and HSE06 functionals. The size of the unit cells of both Na_5CrO_4N and Li_5CrO_4N are reduced with respect to Na_5MoO_4N and Li_5MoO_4N, while Cr-O and Cr-N bonds were also shorter then in either of the analogous molybdenum compounds. Both of these observations can be explained by the smaller ionic radius and higher charge density of Cr(VI) compared to Mo(VI). As was the case when studying Na_5MoO_4N and Li_5MoO_4N, Cr-O and Cr-N bond distances were shorter when using the HSE06 functional compared to the PBE functional.

	Na_5CrO_4N		**Li_5CrO_4N**	
	PBE	**HSE**	**PBE**	**HSE**
a_0	5.566	5.520	5.056	5.010
c_0	10.537	10.438	9.522	9.454
M-N /Å	1.636	1.560	1.620	1.584
M-O /Å	1.885	1.861	1.860	1.837

Table A.3: Structural properties of M_5CrO_4N (M=Na, Li) following relaxation using PBE and HSE06 functionals.

We calculated the band gaps of Na_5CrO_4N and Li_5CrO_4N, with the results shown in Table A.4. As predicted, the band gaps for M_5CrO_4N were significantly lower than for M_5MoO_4N, with the HSE06 functional predicting indirect band gaps of 2.55 eV and 2.43 eV for Na_5CrO_4N and Li_5CrO_4N respectively. While both compounds have a significantly smaller band gap than the analogous molybdenum compounds, it is interesting to note that substituting sodium for lithium has far less of an effect on the size of the band gap than it does in M_5MoO_4N compounds. Both band gaps are well within the visible light region, suggesting an excellent potential for photocatalysis.

	Na_5CrO_4N		**Li_5CrO_4N**	
	Indirect	**Direct**	**Indirect**	**Direct**
mBJ	2.06	2.10	1.83	1.94
HSE06	2.55	2.66	2.43	2.62

Table A.4: Electronic band gaps of M_5CrO_4N (M=Na, Li) determined using the mBJ and HSE06 functionals

The band structures of Na_5CrO_4N and Li_5CrO_4N are shown in Figure A.5. The conduction bands of both compounds are similarly undispersed, with the effective mass about the CBM calculated to be 2.68 m_0 and 2.71 m_0 respectively. The valence band of Li_5CrO_4N is again far more dispersive than in Na_5CrO_4N. The effective masses of electron holes about the VBM were calculated to be 3.21 m_0 and 7.40 m_0 respectively. Reasons for this difference are analogous to those discussed for M_5MoO_4N in Section A.3.3.

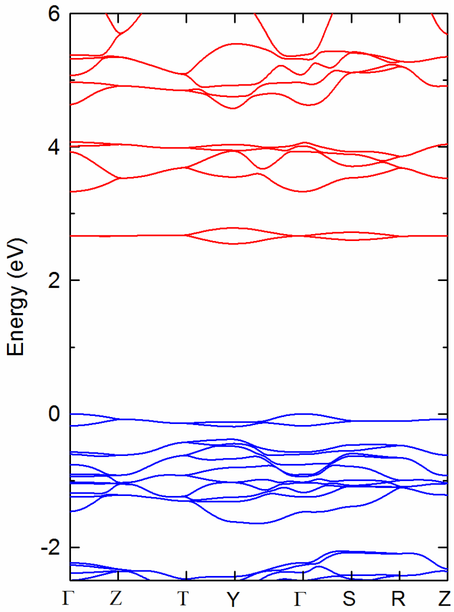

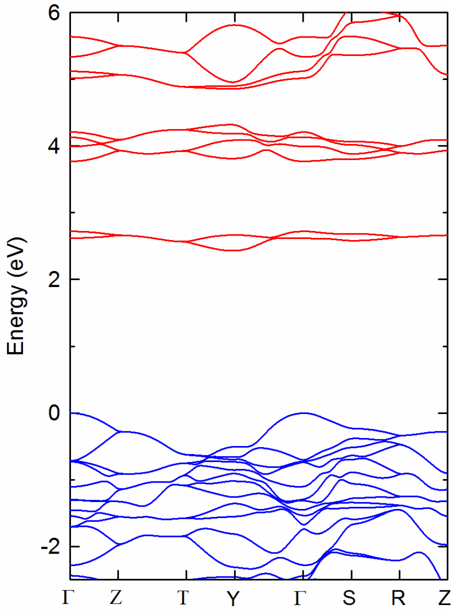

Figure A.5: The band structures of Na_5CrO_4N (left) and Li_5CrO_4N (right) calculated using the HSE06 functional. The VBM is arbitrarily set to zero.

We used CPLAP to assess the likely stability of Na_5CrO_4N and Li_5CrO_4N against competing phases including chromium oxides, tertiary chromium oxides, chromium nitride, sodium oxide, lithium oxide, sodium nitride, lithium nitride and elemental sodium, lithium, chromium, oxygen and nitrogen.

The structures of Na_5CrO_4N relaxed using both the HSE06 and PBE functional were found to be stable with respect to competing phases. The stability region plot calculated using energies calculated using HSE06 is shown in Figure A.6.

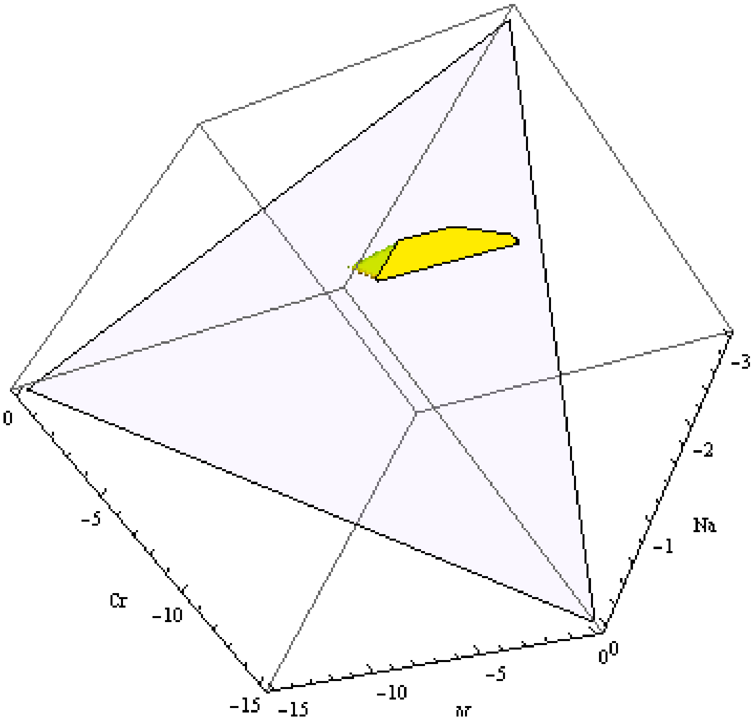

Figure A.6: A representation of the stability region of Na_5CrO_4N, generated using CPLAP.

However, we found that Li_5CrO_4N is unstable with respect to competing phases by an approximated 0.07 eV/atom. We believe that this is down, in part, to the high charge density of Li^+ and resulting stability of Li_2O.

We also investigated some of the likely native point defects of Na_5CrO_4N. Na_5CrO_4N was chosen because its band gap falls within the visible light region and CPLAP predicts that it is stable versus competing phases.

The large number of Na^+ particles surrounding $[CrO_4N]^{6-}$ means that several possible doped structures with either an Na^+ interstitial ($Na_i^{\bullet}$) or an Na^+ vacancy (Na_v') can be formed. We identified three unique Na^+ sites in Na_5CrO_4N and two likely sites for a Na^+ interstitial.

We relaxed each defective structure using the HSE06 functional, and found that a 2×2×1 supercell with a volume of 1122.5 Å^3 was sufficient to converge defect energies to within 0.005 eV. The formation energy, E_f of a defect with charge q was calculated using the following equation [xvii].

$$E_f(q) = E_d(q) - E_p - N\mu + q(E_v + E_f + \Delta)$$

The term needed to align the Fermi level, Δ, was calculated using sxdefectalign [xviii,xix]/

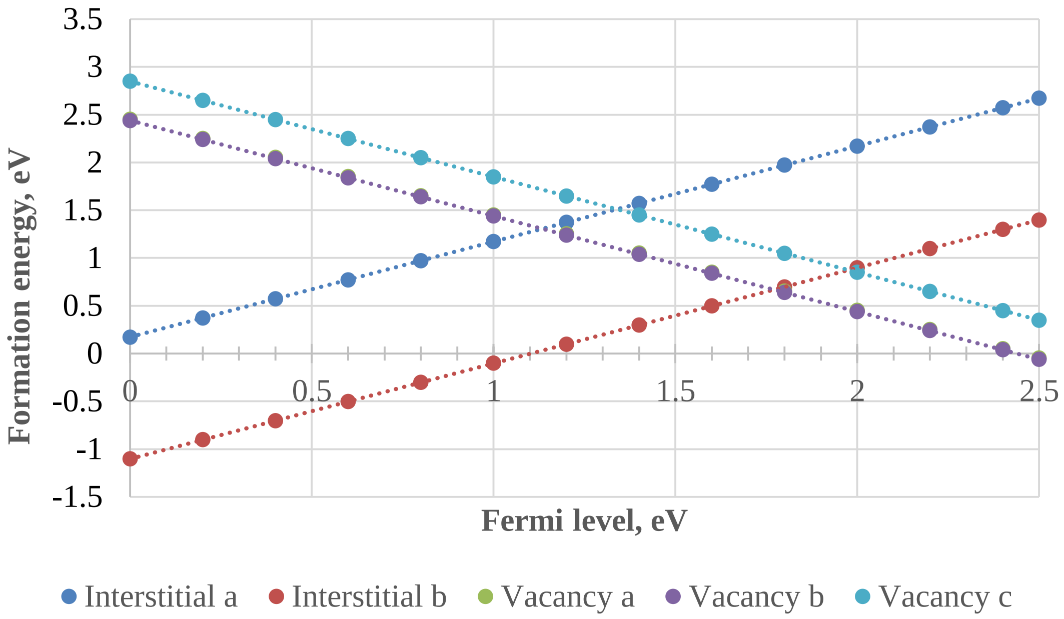

Figure A.7: The formation energy of charged defects in a 2x2x1 supercell of Na_5CrO_4N

By combining $Na_i^{\bullet}$ and Na_v', the energy of an infinitely separated frenkel defect can be calculated. The lowest energy $Na_i^{\bullet}$ / Na_v' pair has a total formation energy of 1.34 eV, suggesting that stoichiometric Na_5CrO_4N is likely to contain relatively few infinitely separated Na^+ Frenkel defects.

A.3.4 M_5WO_4N (M=Li, Na)

In order to test our reasoning behind the smaller band gap of M_5CrO_4N compared to M_5MoO_4N, we also investigated the electronic structure of M_5WO_4N. The tungsten 5d dominated conduction band of M_5WO_4N should, in theory, be higher in energy than the 4d and 3d dominated conduction bands of Na_5MoO_4N and Na_5CrO_4N respectively leading to a larger band gap.

Our calculations found the band gap of M_5WO_4N to be significantly higher than either M_5CrO_4N or M_5MoO_4N; using the HSE06 functional, their indirect band gap of Na_5WO_4N was found to be 4.46 eV while the indirect band gap of Li_5WO_4N was found to be 4.14 eV.

	Na_5CrO_4N		**Li_5WO_4N**	
Method	**Indirect Band Gap /eV**	**Direct Band Gap /eV**	**Indirect Band Gap /eV**	**Direct Band Gap /eV**
mBJ	4.42	4.45	3.96	4.05
HSE06	4.46	4.54	4.14	4.26

Table A.5: Electronic band gaps of M_5WO_4N (M=Na, Li) determined using the mBJ and HSE06 functionals

A.4 Conclusions

M_5CrO_4N compounds were found to have band gaps extremely well suited to photocatalysis; Li_5CrO_4N had a band gap of 2.43 eV and Na_5CrO_4N was found to have a band gap of 2.55 eV. However, the low charge carrier mobility of Na_5CrO_4N suggests that electron-hole recombination would significantly hinder the compounds catalytic activity. While the charge carrier mobility of Li_5CrO_4N was found to be slightly higher, phase stability calculations predicted that the compound is unstable with respect to competing phases.

References

1. Fujishima A, Honda K. Electrochemical Photolysis of Water at a Semiconductor Electrode. Nature. 1972;238(5358):37.

2. Osterloh FE. Inorganic materials as catalysts for photochemical splitting of water. Chem Mater. 2008;20(1):35-54.

3. Linsebigler AL, Lu GQ, Yates JT. Photocatalysis on TiO2 Surfaces - Principles, Mechanisms, and Selected Results. Chem Rev. 1995;95(3):735-58.

4. Daghrir R, Drogui P, Robert D. Modified TiO¬¬¬2 For Environmental Photocatalytic Applications: A Review. Ind Eng Chem Res. 2013;52(10):3581-99.

5. Kamat PV, Bisquert J. Solar Fuels. Photocatalytic Hydrogen Generation. J Phys Chem C. 2013;117(29):14873-5.

6. Wu YB, Lazic P, Hautier G, Persson K, Ceder G. First principles high throughput screening of oxynitrides for water-splitting photocatalysts. Energ Environ Sci. 2013;6(1):157-68.

7. Chan MKY, Ceder G. Efficient Band Gap Prediction for Solids. Phys Rev Lett. 2010;105(19).

8. Murnaghan FD. The compressibility of media under extreme pressures. P Natl Acad Sci USA. 1944;30:244-7.

9. Buckeridge J, Scanlon DO, Walsh A, Catlow CRA. Automated procedure to determine the thermodynamic stability of a material and the range of chemical potentials necessary for its formation relative to competing phases and compounds. Comput Phys Commun. 2014;185(1):330-8.

10. Tran F, Blaha P. Accurate Band Gaps of Semiconductors and Insulators with a Semilocal Exchange-Correlation Potential. Phys Rev Lett. 2009;102(22).

11. Krylov O. Catalysis by nonmetals. New York: Academic Press; 1970.

12. Erre R, Legay MH, Fripiat JJ. Reaction of Molecular-Hydrogen with the 100 Face of MoO3: II. Kinetics Initiated by Atomic-Hydrogen and Characterization of the Surface Electronic State. Surf Sci. 1983;127(1):69-82.

13. Bergerhoff, G, Brown, ID. in “Crystallographic Databases”, F.H. Allen et al. (Hrsg.) Chester, International Union of Crystallography; 1987.

14. Wu YB, Lazic P, Hautier G, Persson K, Ceder G. First principles high throughput screening of oxynitrides for water-splitting photocatalysts. Energ Environ Sci. 2013;6(1):157-68.

15. Perevalov TV, Gritsenko VA. Electronic structure of TiO¬2 rutile with oxygen vacancies: Ab initio simulations and comparison with the experiment. J Exp Theor Phys+. 2011;112(2):310-6.

16. Ikeda S, Sugiyama N, Pal B, Marci G, Palmisano L, Noguchi H, et al. Photocatalytic activity of transition-metal-loaded titanium(IV) oxide powders suspended in aqueous solutions: Correlation with electron-hole recombination kinetics. Phys Chem Chem Phys. 2001;3(2):267-73.

17. Lany S, Zunger A. Accurate prediction of defect properties in density functional supercell calculations. Model Simul Mater Sc. 2009;17(8).

18. Freysoldt C, Neugebauer J, Van de Walle CG. Fully Ab Initio Finite-Size Corrections for Charged-Defect Supercell Calculations. Phys Rev Lett. 2009;102(1).

19. Freysoldt C, Neugebauer J, Van de Walle CG. Electrostatic interactions between charged defects in supercells. Phys Status Solidi B. 2011;248(5):1067-76.

---

iFujishima A, Honda K. Electrochemical Photolysis of Water at a Semiconductor Electrode. Nature. 1972;238(5358):37-+.

ii Osterloh FE. Inorganic materials as catalysts for photochemical splitting of water. Chem Mater. 2008;20(1):35-54.

iii Linsebigler AL, Lu GQ, Yates JT. Photocatalysis on TiO2 Surfaces - Principles, Mechanisms, and Selected Results. Chem Rev. 1995;95(3):735-58.

iv Daghrir R, Drogui P, Robert D. Modified TiO2 For Environmental Photocatalytic Applications: A Review. Ind Eng Chem Res. 2013;52(10):3581-99.

v Kamat PV, Bisquert J. Solar Fuels. Photocatalytic Hydrogen Generation. J Phys Chem C. 2013;117(29):14873-5.

vi Wu YB, Lazic P, Hautier G, Persson K, Ceder G. First principles high throughput screening of oxynitrides for water-splitting photocatalysts. Energ Environ Sci. 2013;6(1):157-68.

vii Chan MKY, Ceder G. Efficient Band Gap Prediction for Solids. Phys Rev Lett. 2010;105(19).

viii Murnaghan FD. The compressibility of media under extreme pressures. P Natl Acad Sci USA. 1944;30:244-7.

ix Buckeridge J, Scanlon DO, Walsh A, Catlow CRA. Automated procedure to determine the thermodynamic stability of a material and the range of chemical potentials necessary for its formation relative to competing phases and compounds. Comput Phys Commun. 2014;185(1):330-8.

x Tran F, Blaha P. Accurate Band Gaps of Semiconductors and Insulators with a Semilocal Exchange-Correlation Potential. Phys Rev Lett. 2009;102(22).

xi Krylov O. Catalysis by nonmetals. New York: Academic Press; 1970.

---

xii Erre R, Legay MH, Fripiat JJ. Reaction of Molecular-Hydrogen with the 100 Face of MoO_3: II. Kinetics Initiated by Atomic-Hydrogen and Characterization of the Surface Electronic State. Surf Sci. 1983;127(1):69-82.

xiii Bergerhoff, G, Brown, ID. in “Crystallographic Databases”, F.H. Allen et al. (Hrsg.) Chester, International Union of Crystallography; 1987.

xiv Wu YB, Lazic P, Hautier G, Persson K, Ceder G. First principles high throughput screening of oxynitrides for water-splitting photocatalysts. Energ Environ Sci. 2013;6(1):157-68.

xv Perevalov TV, Gritsenko VA. Electronic structure of TiO_2 rutile with oxygen vacancies: Ab initio simulations and comparison with the experiment. J Exp Theor Phys+. 2011;112(2):310-6.

xvi, Ikeda S, Sugiyama N, Pal B, Marci G, Palmisano L, Noguchi H, et al. Photocatalytic activity of transition-metal-loaded titanium(IV) oxide powders suspended in aqueous solutions: Correlation with electron-hole recombination kinetics. Phys Chem Chem Phys. 2001;3(2):267-73.

xvii Lany S, Zunger A. Accurate prediction of defect properties in density functional supercell calculations. Model Simul Mater Sc. 2009;17(8).

xviii Freysoldt C, Neugebauer J, Van de Walle CG. Fully Ab Initio Finite-Size Corrections for Charged-Defect Supercell Calculations. Phys Rev Lett. 2009;102(1).

xix Freysoldt C, Neugebauer J, Van de Walle CG. Electrostatic interactions between charged defects in supercells. Phys Status Solidi B. 2011;248(5):1067-76.